

DISS. ETH NO. 14720

# ANODIC PLASMA-CHEMICAL TREATMENT OF TITANIUM IMPLANT SURFACES

A dissertation submitted to the

SWISS FEDERAL INSTITUTE OF TECHNOLOGY ZURICH

for the degree of

DOCTOR OF TECHNICAL SCIENCES

presented by

VINZENZ MAX FRAUCHIGER

Diploma in Materials Engineering (ETH Zürich) 1999

born on August 12, 1973

citizen of Wyssachen BE

accepted on the recommendation of

Prof. Dr. M. Textor, examiner

Prof. Dr. N. D. Spencer, co-examiner

Dr. F. Schlottig, co-examiner

Dr. B. Gasser, co-examiner

Zürich, 2002



---

## *Prologue*

---

If I have seen further than others, it is by  
standing upon shoulders of giants. - *Sir Isaac  
Newton*

I can't see any further, giants are standing on  
my shoulders. - *unknown*



---

# *Acknowledgments*

---

I would like to thank Prof. Nicholas D. Spencer and Prof. Marcus Textor for giving me the possibility to carry out my thesis project at the Laboratory for Surface Science and Technology (LSST) of the ETH Zurich.

Dear Nic, I appreciated very much that you always took your time to discuss with me the thesis work in a very motivating way. Marcus, in your lab I learned to wait, to calm down, some things about diplomacy, some things about politics, the things about Mankell's crime stories, how to make fondue out of cheese and water, not to die from electric shock and how to repair a XPS, how to cope with weird people, and finally, how to survive and carry out a PhD thesis. I am deeply grateful that you gave me full responsibility for my research.

Many thanks to Dr. Falko Schlottig, STRATEC Medical, and Dr. Beat Gasser, Dr. h. c. Robert Mathys Foundation (RMS), for their constant support and their interest in my work. Dear Falko, thanks for introducing the ANOF-process to LSST, which made this PhD thesis possible and the fruitful and constructive discussions we had. Dear Beat, whenever I called somebody at RMS I got help and support, thanks very much. I would also like to thank people at STRATEC Medical for their support, especially Dr. Andrea Montali, Dr. Christian Frei, Simon Möschberger and all the others. Many thanks to Dr. Lukas Eschbach and Werner Hirsiger at RMS who supported me concerning calcium phosphate materials and stereo-SEM respectively.

Many thanks to Dr. R. Geoff Richards, Patrick Schlegel and the whole Interface Biology Group at AO Research Institute, for the good collaboration and the many fruitful discussions. Patrick, I very much appreciated the collaboration with you. Also, I would like to thank Prof. Berton Rahn for his support concerning the histology during the *in vivo* study.

Thanks to Prof. R. Thull, Dr. Angela Hauck and Ursula Rummel, University of Würzburg, for carrying out the cell culture study and the given possibility to actively help during the experiments. Many thanks to Dr. Caroline Sittig and Ruedi Christ for giving me the opportunity to use the SEM at Institute Straumann. Also, many thanks to Franz Hochleitner and Erwin Sutter and their team at Alcan, for doing all the ICP-OES measurements and the support with chemical digestion procedure. Thanks to Max Aeberhard, EMPA Thun, for the GD-OES spectra.

Thanks to Dr. Joachim Schreckenbach, TU Chemnitz, for sharing his know-how of the ANOF-process with me. Many thanks to Diethard Butte who took care of me during my stay at the TU Chemnitz. Also, many thanks to Dr. Norbert Meyer for the support with the Raman measurements.

Many thanks to Dr. Martin Müller, Labor f. EM I at ETH Zürich, for introducing me to the art of electron microscopy. Dear Martin, thank you very much for all the things I was able to learn at your lab and the long discussions we had. Also, many thanks to Prof. Peter Uggowitzer, ETH Metals, for the very interesting discussions and the support with the experiments on titanium foil. Thanks to Prof. Jürg Dual and Dr. Daniel Baechi, Inst. of Mechanics at ETH Zürich, for the possibility to use the laser profilometer. I would also like to acknowledge KTI-MedTech Initiative for the funding of the project 4729.1.

Furthermore, I would like to thank *all* the people from LSST for the good atmosphere in Schlieren and Zürich, especially Irene Klingenfuss for the good collaboration concerning computers, Jaroslav Vanicek for the technical support, Dr. Janos Vörös for the many fruitful discussions, Dr. Susan De Paul for helping me with the american way of writing english. Many thanks to Michael Eglin, Samuele Tosatti, and Roger Michel for the great time we had during the diploma studies and our PhD projects. I would like to thank my diploma student, Markus Müller, for having chosen me as his supervisor and the significant input he made to the project during his diploma work.

---

---

Many thanks also to the former members of LSST, who were a big help at the beginning of my work in this lab: Dr. Marco Wieland for convincing me to stay for a PhD project, Dr. Rolf Hofer for sharing his invaluable knowledge about chemistry.

Many, many thanks to all my friends, my family, and Melanie Hoffmann who have always supported me.





---

# Table of Contents

---

*Prologue* **i**

---

*Acknowledgments* **iii**

---

*Abstract* **xi**

---

*Zusammenfassung* **xv**

---

**CHAPTER 1** *General Introduction* **1**

---

Hard-Tissue Implant Materials **1**  
Aim of the Thesis **3**

**CHAPTER 2** *Biocompatible Materials and Surfaces* **5**

---

Metallic Implant Materials - History **5**  
Titanium as an Implant Material **6**  
    *Pure Titanium and Its Physico-Chemical Properties* **6**  
    *CP Titanium and Titanium Alloys* **9**  
    *Titanium Surfaces in Contact with Tissue* **11**  
    *Wear on Titanium Implant Surfaces* **16**  
Calcium Phosphate and Calcium Phosphate Containing Ceramics - An Overview **17**  
Hydroxyapatite and Its Relatives **18**  
    *The Chemistry of Calcium Phosphate Bioceramics* **19**  
    *The Biological Performance of Calcium Phosphate Ceramics* **22**

**CHAPTER 3** *Methods for Producing Ceramic Coatings on Medical Implants* **25**

---

Overview **25**  
    *Thermal Spray Coatings* **25**  
    *Physical-Vapour-Deposition Coatings (PVD)* **27**  
    *Chemically Prepared Layers (Densified by Sintering)* **28**  
    *Enamelling and Sol-Gel Techniques* **28**  
    *Cathodic Deposition* **29**  
    *Anodic Oxidation* **29**  
The Anodic Plasma-Chemical Treatment **31**  
    *Introduction* **31**  
    *Theoretical Background of the Breakdown Process* **35**

**CHAPTER 4** *Materials & Sample Pretreatment* **41**

---

Substrate Materials **41**

---

---

## Table of Contents

---

	<i>Commercially Pure Titanium Disks</i>	41
	<i>Cortex Screws for the Unloaded in Vivo Study</i>	41
	Sample Pretreatment	42
<b>CHAPTER 5</b>	<b><i>Methods I: The APC Coating Procedure</i></b>	<b>45</b>
<b>CHAPTER 6</b>	<b><i>Methods II: Characterization Methods</i></b>	<b>49</b>
	Characterization of the Chemical Composition	49
	<i>X-ray Photoelectron Spectroscopy (XPS or ESCA)</i>	49
	<i>Glow Discharge Optical Emission Spectroscopy (GD-OES)</i>	50
	<i>Inductively Coupled Plasma Optical Emission Spectroscopy (ICP-OES)</i>	54
	Characterization of the Crystal Structure	54
	<i>Raman Spectroscopy</i>	54
	Characterization of the Surface Topography	56
	<i>Scanning Electron Microscopy (SEM)</i>	56
	<i>Laser Profilometry (LPM)</i>	58
	Characterization of the Mechanical Coating Properties	61
	<i>Tensile Tests</i>	61
	<i>Scratch Tests</i>	62
<b>CHAPTER 7</b>	<b><i>Basic Investigations on Standard Electrolytes</i></b>	<b>63</b>
	Orthophosphoric Acid as an Electrolyte	64
	<i>Experimental</i>	64
	<i>Results</i>	64
	<i>Conclusions</i>	70
	Samples for in the Vitro Study Coated in Phosphoric Acid	71
	<i>Experimental</i>	71
	<i>Characterization</i>	71
	Calcium Dihydrogen Phosphate as an Electrolyte	77
	<i>Experimental</i>	77
	<i>Results</i>	77
	<i>Conclusions</i>	85
	Discussion of the Standard Electrolytes	86
<b>CHAPTER 8</b>	<b><i>Development of a New Electrolyte System for Titanium Implant Surfaces</i></b>	<b>89</b>
	Approach	89
	Parameter Screening on the New Electrolyte System (ESOC)	91
	<i>Experimental</i>	91
	<i>Results</i>	92
	<i>Conclusions</i>	100
	Cell-Culture Samples Coated in ESOC	100
	<i>Experimental</i>	100

---

---

## Table of Contents

---

	<i>Results</i>	<b>101</b>
	Discussion of the New Electrolyte System	<b>107</b>
<b>CHAPTER 9</b>	<b><i>Chemical and Biological Properties of APC-coated CP Titanium Surfaces 111</i></b>	
	Dissolution Experiments in Diluted EDTA-solution	<b>111</b>
	<i>Introduction</i>	<b>111</b>
	<i>Experimental</i>	<b>112</b>
	<i>Results</i>	<b>113</b>
	<i>Discussion</i>	<b>117</b>
	A Standard Osteoblast Cell-Culture Study	<b>119</b>
	The Unloaded in Vivo Study	<b>122</b>
	<i>Experimental</i>	<b>122</b>
	<i>Results</i>	<b>125</b>
	<i>Conclusions</i>	<b>129</b>
<b>CHAPTER 10</b>	<b><i>Investigations on the APC Process Mechanism 131</i></b>	
	Process Mechanism: What is Known	<b>131</b>
	High-Resolution SEM Study of the different stages of the APC Process	<b>132</b>
	<i>Experimental</i>	<b>132</b>
	<i>Results</i>	<b>134</b>
	<i>Discussion</i>	<b>145</b>
	A Proposal for the APC Process Mechanism	<b>147</b>
<b>CHAPTER 11</b>	<b><i>Summary and Outlook 151</i></b>	
<b>CHAPTER 12</b>	<b><i>References 157</i></b>	

---

---

## Table of Contents

---

---

# *Abstract*

---

Metallic titanium and calcium phosphate materials are both used as implant materials in contact with bone. While titanium, covered with a passive oxide film, is a rather bioinert material, calcium phosphate materials are similar to the inorganic proportion of bone and normally react to some extent with the biological environment and, therefore, are very well accepted by the surrounding tissue. Additionally, some of these materials are partly soluble in the biological environment and can therefore accelerate the re-calcification of bone after the implantation procedure. The principal drawback of calcium phosphate materials, such as hydroxyapatite or tricalcium phosphate, is their brittleness, which does restrict their use as load bearing materials, whereas titanium and its alloys have high enough strength and toughness to bear loads, but are passive materials. In order to combine the favorable properties of both material classes, titanium implant surfaces are coated with calcium phosphate materials. A number of different coating methods have been invented and developed, of which many suffer from brittleness and relatively low adhesion of the calcium phosphate coating on the metal substrate.

In this thesis, the anodic plasma-chemical surface modification method (APC) is evaluated as a technique to combine the favorable properties of titanium and calcium phosphates with improved coating integrity and adhesion. APC, an advanced anodization method, allows for anodic oxide layer formation and incorporation of calcium phosphate phases in one single process step. The method exploits the dielectric breakdown of anodic oxide films at high electrical field strength to produce a

porous oxide layer with a thickness of a few micrometers that contains significant amounts of electrolyte components. A major advantage is the interfacial integrity as a result of the electrochemical reaction between titanium metal and electrolyte. Additionally, APC is a fast single-step process that is less expensive and much more suited to coat complex 3D-shaped implants than deposition processes such as plasma spraying.

The thesis focusses on two main topics:

- The investigation of the anodic plasma-chemical surface modification process, also known as anodic spark deposition or spark anodization, in terms of process mechanism and the influence of process parameters on the resulting APC coating properties.
- The development of a bioactive coating consisting of a titanium oxide matrix with incorporated calcium phosphate phases with a Ca/P ratio as close as possible to that of hydroxyapatite (1.67) by using the APC process.

Firstly, the influence of the process parameters on the dielectric breakdown properties, the coating structure and chemical composition were investigated by using electrolytes based on orthophosphoric acid and calcium orthophosphate. Both electrolyte systems are well known from literature. Electrolyte concentration and solution temperature as well as process duration were varied while the applied current was kept constant (galvanostatic regime). The resulting coatings were characterized using XPS<sup>1</sup>, SEM, GD-OES<sup>2</sup>, and Raman spectroscopy. It turned out that the most important parameter is the electrolyte concentration. The higher the electrolyte concentration the lower the breakdown voltage. The relation between breakdown voltage and concentration could be described with an exponential decay fit. The electrolyte concentration was also found to substantially influence the resulting coating structure, while the effect on the chemical composition of the APC coating was comparatively weak. Secondly, electrolytes were screened in terms of their ability to produce calcium phosphate containing APC coatings. The standard calcium orthophosphate electrolyte was found to produce coatings with low amounts of calcium (a few atom-%) resulting in Ca/P ratios of less than 0.4. Further attempts to increase the calcium content and the Ca/P ratio using

---

1. X-ray photoelectron spectroscopy

2. Glow-discharge optical emission spectroscopy

---

a number of different calcium compounds were unsuccessful due to two reasons: Firstly, the solubility of calcium in aqueous electrolytes is generally low. Secondly, the calcium ions are positively charged in solution and are, therefore, repelled by the positively polarized implant surface (during the anodization process).

A novel approach in the design of the electrolyte proved to be successful based on the use of a  $\text{Ca}^{2+}$ -chelating agent (EDTA) to increase the concentration of calcium of the electrolyte solution. Additionally, the pH of the electrolyte was increased in order to maximize the net-negative charge of the chelate complex. The resulting APC coatings had Ca/P ratios of up to 1.3 and calcium contents of up to 14 atom-% at the surface of the coating. GD-OES depth profiles indicated that both calcium and phosphorus are nearly homogeneously distributed across the coating thickness. The new electrolyte system called 'electrolyte system for osteointegrative coatings', ESOC, contains calcium orthophosphate, calcium acetate, EDTA as a chelating agent, and sodium hydroxide to adjust the pH in the electrolyte solution. A process-parameter screening using the ESOC showed that the process parameters current, duration, and electrolyte temperature have only a weak influence on the chemical composition at the surface and the crystal structure of the APC coating. The surface topography of the coating can be varied by changing either the amount of applied current or the process duration. Raman measurements indicated that the main crystalline phase of all APC coatings is the anatase modification of titania. The calcium phosphate phases in the APC coatings are most probably amorphous. Only one single Raman band (at  $955\text{ cm}^{-1}$ ) typical for calcium phosphate was detected. The mechanical adhesion strength of the coatings produced in the ESOC is at least a factor 4 higher than the minimal adhesion strength required for plasma-sprayed hydroxyapatite coatings according to ISO 13779-2. The adhesion strength was found to decrease with increasing coating process duration and increasing current applied to the sample, i. e. with increasing coating thickness.

The chemical solubility of the coating is relevant to the bioactivity and was assessed in a dissolution experiment using a dilute EDTA solution. Within the 14 d of the experiment the calcium phosphate incorporated in the APC coating was released to a large extent. After the dissolution experiment the structure of the coatings produced in ESOC had become grainy indicating that an amorphous or glassy matrix had been dissolved around small anatase crystals.

A cell-culture study was carried out with human fetal osteoblasts (hFOB 1.19) in order to test the biocompatibility of the new coating in comparison to uncoated CP titanium surfaces and commercial hydroxyapatite coatings. The results indicated that the APC coatings produced in ESOC are not less biocompatible than the commercially available implant surfaces with respect to cell growth, cell viability, total amount of proteins on the surfaces, and alkaline phosphatase activity. Furthermore, in collaboration with the AO Research Institute, Davos, a first animal study was carried out. Standard cortex screws with different surface modifications were implanted into the tibiae of White Alp sheep for 12 weeks. APC-coated screws coated in ESOC were compared to APC-coated screws coated in phosphoric acid, uncoated CP titanium screws, and two commercially available hydroxyapatite coatings. The amount of newly formed bone as well as the bone growth rate adjacent to the screws coated in the ESOC APC process was comparable to that of the commercial calcium phosphate coatings.

Finally, the APC process was investigated by means of a high-resolution SEM study. To study the mechanism of film formation, the process was stopped after different coating times with the aim of locating the first breakdown events. In literature, first breakdown events for aluminum as a substrate material have been reported to be located at flaws, such as small gas inclusions in the anodic oxide. The results suggest that titanium and aluminum behave differently. On titanium, already during the first phase of the APC anodization, the anodic oxide delaminates locally and forms blister-like structures. In this study, the first dielectric breakdown events were found to be located at these blister-like structures, which weakened the anodic oxide film. The blisters are believed to originate from high compressive stresses in the anodic oxide and/or from excessive formation of molecular oxygen at the interface between substrate and anodic oxide layer. In comparison to published data the voltages corresponding to the first breakdown events were found to be substantially lower. Furthermore, there is good evidence that breakdown events, oxide growth and healing processes occur simultaneously at different locations of surface.



---

# *Zusammenfassung*

---

Metallisches Titan und Calciumphosphate (CaP) werden beide für die Herstellung von Implantaten, welche in Kontakt mit Knochen kommen, verwendet. Titan ist normalerweise mit einer Passivschicht bedeckt und verhält sich deshalb bioinert. CaP sind dem inorganischen Anteil des Knochens sehr ähnlich und reagieren zu einem gewissen Grad mit der biologischen Umgebung im Körper. Aus diesem Grund werden CaP sehr gut vom menschlichen Körper akzeptiert. Ein Teil dieser CaP-Materialien ist so konzipiert, dass sie sich teilweise im Körper auflösen und so die Neubildung von Knochen nach der Operation beschleunigen. Der Hauptnachteil der CaP ist ihre Sprödigkeit, da die fehlende Zähigkeit eine Anwendung von CaP-Werkstoffen als lastragende Implantatmaterialien verhindert. Titan und seine Legierungen hingegen weisen eine genügend hohe Festigkeit und Zähigkeit auf, um Lasten zu tragen, sind jedoch nicht bioaktiv. Um die guten Eigenschaften der beiden Materialklassen zu vereinen, werden Titansubstrate mit CaP beschichtet. Zahlreiche Methoden wurden dafür entwickelt. Die meisten Methoden ergeben aber Schichten, die eine geringe Haftfestigkeit auf dem Titansubstrat aufweisen und spröde sind.

Als mögliche neue Methode für die Kombination (mittels Beschichtung) der positiven Eigenschaften beider Werkstoffklassen wird in dieser Dissertation die anodisch plasmachemische Oberflächenmodifikationsmethode (APC) untersucht. APC ist eine Weiterentwicklung der klassischen Anodisation von Ventilmaterialien. APC erlaubt den Einbau von Bestandteilen des Elektrolyts in die anodische Oxidschicht. Die Methode nutzt dabei dielektrische Durchbrüche bei

hohen Feldstärken im Oxidfilm aus, um einen neuen porösen Oxidfilm zu bilden, der einige Mikrometer dick ist und zu einem bestimmten Anteil aus Elektrolytbestandteilen besteht. Als Resultat der elektrochemischen Reaktion zwischen Substratmetall und Elektrolyt entsteht eine stabile Grenzfläche zwischen Schicht und Substrat, was eine gute Haftfestigkeit der APC-Schicht auf dem Substrat zu Folge hat. Der APC-Prozess ist schnell, einfach (da nur ein Prozess-Schritt), aufgrund der einfachen Prozess-Infrastruktur billig und geeignet, um komplexe dreidimensionale Formen zu beschichten (im Gegensatz zum Plasma sprayen).

Die Dissertation konzentriert sich auf zwei Aufgaben:

- Die Untersuchung des APC-Prozesses, welcher auch unter der Bezeichnung „anodische Oxidation unter Funkenentladung“ bekannt ist, bezüglich Prozessmechanismus und des Einflusses von Prozessparametern auf die resultierenden APC-Schichteigenschaften.
- Die Entwicklung einer bioaktiven Schicht, welche aus einer Titanoxidmatrix und eingelagertem Calciumphosphat besteht. Dabei ist ein Ziel, das Ca/P-Verhältnis in den Bereich desjenigen von Hydroxylapatit zu bringen.

Als erstes wurde der Einfluss der Prozessparameter auf das Durchbruchverhalten, die Beschichtungsstruktur, und die chemische Zusammensetzung der Schicht untersucht. Dabei wurden Phosphorsäure und Calciumdihydrogenphosphat als Elektrolyte verwendet. Beide Elektrolyte sind in der Literatur schon ausführlich untersucht worden. In den galvanostatisch durchgeführten Versuchen wurden die Elektrolytkonzentration und die Beschichtungsdauer variiert. Die Stromstärke wurde für alle Versuche gleich gewählt. Die so erhaltenen Beschichtungen wurden mittels XPS, REM, GD-OES und Raman-Spektroskopie untersucht. Es stellte sich heraus, dass die Elektrolytkonzentration den wichtigsten Prozessparameter darstellt. Je höher die Elektrolytkonzentration, desto niedriger die Durchbruchsspannung. Die Beziehung zwischen Elektrolytkonzentration und der Durchbruchsspannung konnte mit einer exponentiellen Zerfallsfunktion beschrieben werden. Die Elektrolytkonzentration beeinflusst auch erheblich die Struktur der Beschichtung, während die chemische Zusammensetzung der Schicht nur schwach von der Elektrolytkonzentration beeinflusst wird.

---

In einem zweiten Schritt, wurden verschiedene Elektrolyte bezüglich des Einbaues von Calciumphosphaten in die APC-Schicht untersucht. Wenn Calciumdihydrogenphosphat als Elektrolyt verwendet wurde, konnten nur kleinere Mengen Calcium (ein paar Atomprozent) in der APC-Schicht nachgewiesen werden. Das resultierende Ca/P-Verhältnis lag im Maximum bei etwa 0.4. Weitere Beschichtungsversuche mit einer grösseren Anzahl Calciumsalze führten ebenfalls zu keinen befriedigenden Resultaten. Das wurde vor allem auf zwei Gründe zurückgeführt: Erstens ist die Löslichkeit von Calcium in wässrigen Elektrolyten eingeschränkt. Zweitens sind Calcium Ionen in Lösung positiv geladen und werden deswegen von der während der Beschichtung positiv polarisierten Implantatoberfläche abgestossen.

In der hier präsentierten Arbeit wurde erfolgreich ein neues Elektrolytdesign eingeführt. Dieses Design basiert auf der Komplexierung von  $\text{Ca}^{2+}$ -Ionen mittels EDTA, um die Löslichkeit von Calcium zu erhöhen. Zusätzlich wurde der pH der Elektrolytlösung erhöht, damit die Gesamtladung des Calciumkomplexes möglichst negativ wird. Die in diesem Elektrolytsystem produzierten APC-Schichten wiesen Ca/P-Verhältnisse von bis zu 1.3 auf bei Calciumgehalten von etwa 14 Atomprozent nahe der Oberfläche. Chemische Tiefenprofile (gemessen mit GD-OES) zeigten, dass Calcium und Phosphor relativ homogen über die ganze Schichtdicke verteilt sind. Das neue Elektrolytsystem mit dem Namen „Elektrolytsystem für osteointegrative Beschichtungen“ (Abkürzung in Englisch: ESOC) enthält Calciumdihydrogenphosphat, Calciumacetat, EDTA als Komplexierungsmittel und Natriumhydroxid, um den pH-Wert der Elektrolytlösung einzustellen. Bei einem Prozessparameter-Screening mit ESOC konnte gezeigt werden, dass die Prozessparameter Stromstärke, Prozessdauer und Elektrolyttemperatur die chemische Zusammensetzung der Schicht und die Schichtstruktur nur wenig beeinflussen. Die Oberflächentopographie der Schicht kann mittels Stromstärke oder Prozessdauer variiert werden. Mittels Ramanmessungen konnte Anatas als wichtigste Kristallphase identifiziert werden. Nur eine Bande (bei  $955\text{ cm}^{-1}$ ), welche spezifisch für amorphe Calciumphosphate ist, konnte in den Spektren identifiziert werden. Die Haftfestigkeiten der APC-Schichten auf dem Substrat waren mindestens um einen Faktor vier höher als vorgeschrieben für plasma-gesprayte Hydroxylapatitschichten nach ISO 13779-2. Es konnte gezeigt werden, dass die Haftfestigkeit mit steigender Prozessdauer oder steigender Stromstärke sinkt. Das heisst, die Haftfestigkeit sinkt mit steigender Schichtdicke.

Die Löslichkeit der APC-Schichten in wässriger Umgebung ist wichtig, um eine Abschätzung der Bioaktivität der Schicht machen zu können. Die Löslichkeit der Schichten wurde in einer verdünnten EDTA-Lösung bestimmt. Ein grosser Teil des eingelagerten Calciums ist nach 14 Tagen aus den Schichten, welche in ESOC produziert worden waren, herausgelöst worden. Nach dem Auflösungsversuch zeigte sich im REM, dass die Struktur der Schicht sehr körnig geworden ist. Eine amorphe oder glasige Matrix könnte also um die mit Raman nachgewiesenen Anataskristalle herausgelöst worden sein.

Um die APC Schichten hinsichtlich Zytotoxizität zu testen, und sie mit unbeschichteten Titanoberflächen sowie kommerziellen CaP-Schichten zu vergleichen, wurden Zellkulturversuche mit menschlichen Osteoblasten (HFOB 1.19) durchgeführt. Bezüglich Zellwachstum, Zellvitalität, Proteingehalt auf den Oberflächen und der alkalinen Phosphataseaktivität waren alle APC Schichten nicht-zytotoxisch, also biokompatibel. In einer 12 Wochen dauernden Tierstudie an Schafen mit APC-beschichteten Schrauben konnte gezeigt werden, dass an die in ESOC produzierten APC-beschichteten Schrauben in etwa gleich viel Knochen angelagert wird wie an kommerzielle CaP-Schichten. Ebenfalls vergleichbar war die Knochenanwachstumsrate.

In einem letzten Teilprojekt wurde der APC-Prozess mit dem Elektronenmikroskop untersucht. Um den Mechanismus der APC-Filmbildung untersuchen zu können, wurde der Prozess zu verschiedenen Zeitpunkten mit dem Ziel unterbrochen, die Orte der ersten dielektrischen Durchbrüche zu lokalisieren. In der Literatur wurde beschrieben, dass erste Durchbrüche in Oxidschichten auf Aluminium an Fehlstellen wie Gaseinschlüssen im Oxid stattfinden. Die Resultate der Studie auf Titan zeigen Differenzen zwischen Titan und Aluminium auf. Schon während der ersten Anodisationsphase delaminiert die Oxidschicht auf Titan lokal, was aussieht wie Blasen. Diese blasenartigen Strukturen könnten auf hohe Kompressionsspannungen im anodischen Oxid oder die Bildung von molekularem Sauerstoff an der Grenzfläche zwischen Oxidschicht und Substrat zurückzuführen sein. Die ersten dielektrischen Durchbrüche wurden an diesen blasenartigen Strukturen gefunden. Im Vergleich zu publizierten Daten über die Spannung, bei welcher erste Durchbrüche stattfinden, wurden in dieser Studie tiefere Werte gefunden. Weiter wurden

---

---

Anhaltspunkte dafür gefunden, dass Oxidschichtwachstum, dielektrische Durchbrüche und APC-Schichtbildung an verschiedenen Orten der Probenoberfläche gleichzeitig stattfinden können.



---

*Biocompatibility means the ability of a material to perform with an appropriate host response in a specific application, D. F. Williams, 1987 [23].*

---

### *1.1 Hard-Tissue Implant Materials*

Different classes of materials have been used for joint replacement and osteosynthesis. Both kinds of applications require not only sufficient biocompatibility but also mechanical strength. Titanium has high strength and high toughness; its biocompatibility has been established by many studies [1-3]. However, the biological properties of titanium are often described as bioinert [4]. Bioinert means in this case that titanium is not releasing any toxic compound but also no components accelerating or improving the healing and integration process. Another class of materials used as hard tissue (bone) implants consists of calcium phosphate materials, in particular hydroxyapatite. Their outstanding property is the similarity to the inorganic portion of bone allowing for good acceptance by the human body. Additionally, this similarity stimulates the ongrowth of bone tissue and if the material exhibits a certain chemical reactivity with the bodily fluids, it can accelerate the healing process significantly [5,6]. A lack of mechanical strength and toughness prevented the use of calcium phosphate materials as load-bearing implant materials [7]. Furthermore, their reactivity with the bodily fluids can make them susceptible to dissolution, which can lead to a complete loss of implant integrity [8,9]. As non-load-bearing materials they are commonly used as well-established bone cements [10] and solid bone-void-filling materials [11,12]

Coating of high-strength materials (such as steel and titanium alloys) with biologically more favorable calcium phosphate materials has been found to be a valuable way of combining the good

properties of both material classes [13]. Calcium phosphate materials are applied to the metallic substrate by many different methods such as plasma spraying [14] or enamelling techniques [15]. However, mechanical properties and solubility of the coating as well as the quality of the interface between the coating and the substrate are delicate factors often decisive for the *in vivo* performance of the implant system (refer to Section 2.4.2). Moreover, many of the coating methods fail if complex 3D-shaped implants have to be coated (in particular all 'line-of-sight methods') or they may be costly and time-consuming (e. g. in case of plasma spraying [16] and chemically prepared layers [17]).

An approach, whereby a coating is produced that grows in the course of a chemical or electrochemical reaction of the substrate could possibly allow the coating of complex-shaped implants. At the same time good adhesion could be achieved, since the coating has grown by conversion of the metallic substrate. A drawback of this kind of coating is that the chemical composition is not independent of the chemical composition of the substrate material.

This thesis deals with a coating method that was derived from the classic anodic oxidation process. Anodic oxide coatings grown from the substrate exhibit excellent adhesion properties. These oxide films are harder and chemically more inert than the substrate metal and are therefore employed to reduce wear and corrosion problems [18]. The chemical composition of the anodic oxide film is determined by the substrate material [19]. The method presented in this thesis (anodic plasma-chemical treatment, APC) converts this anodic oxide film into a porous and inert oxide layer that contains large amounts of electrolyte constituents [20]. Thus, not only the chemical composition can be varied but also the crystallinity and crystal structure can be adapted by changing the electrolyte constituents [20]. The coating method, APC, has been known for more than 50 years [21] and first attempts to use this kind of coating for biomedical purposes were made in the 1980s [22].

During the last few years, interest in the APC process as a coating process for biomedical applications has faded for several reasons:

- The mechanism of the APC process is not yet understood, which exacerbates the tailoring of the coating properties.



- The low amount of calcium incorporated in the APC coatings yields only low calcium-to-phosphorus ratios in the resulting APC coating.
- The influence of APC process parameters on the resulting coating composition and the coating morphology are only reported for special examples.

Nevertheless, the APC process could be of much interest for the future since it allows the modification of complicated 3D-shaped implants (such as cages for spinal fusion), coatings on implants can be achieved within minutes, and the infrastructure needed for carrying out the APC process is relatively simple.

---

## 1.2 Aim of the Thesis

My PhD thesis is part of a KTI-MedTech project (No. 4729.1). This thesis has two main objectives:

1. It is intended to use the APC coating method in order to produce a bioactive coating containing calcium and phosphates on commercially pure titanium implant surfaces.

The resulting coating should induce a response by the surrounding tissue similar or better than that of hydroxyapatite coatings. Moreover, the mechanical stability of the resulting APC coating has to be better than the stability of plasma-sprayed hydroxyapatite coatings. Finally, the coating properties shall be achieved in the course of one single process step.

To reach this aim, the current status of the technique is analyzed on the basis of well-known electrolyte systems. The analysis is done by means of process-parameter screening and subsequent characterization of the APC coatings with scanning electron microscopy (SEM) and X-ray photoelectron spectroscopy (XPS). Secondly, measures will be taken to overcome the present restrictions in terms of the degree of calcium incorporation. For example the success of the measures taken will be monitored by thorough characterization of the APC coatings. Final testing of the produced coatings will be carried out *in vitro* and *in vivo*.

2. The mechanism of the APC process is investigated with the aim of understanding the influence of coating process parameters and electrolyte properties on the resulting coating properties.

Based on the results found in literature, the process mechanism will be investigated with a phenomenological approach. The process will be stopped at various process stages and the intermediate states will be characterized by SEM at magnifications up to  $> 10^5$ . Subsequently, the findings will be compared and discussed with theoretical and empirical models reported in the literature.

---

*2.1 Metallic Implant Materials - History*

The successful use of biomaterials goes back to the early 20th century, following the development of aseptic surgical techniques in the second half of the 19th century. The earliest implants used with a limited success were in the skeletal system, e. g., bone plates for fracture fixation. Many of these implants failed because of poor mechanical design. The plates were too thin or suffered from stress-concentration at edges, inducing cracks. A second problem was related to the material chosen for bone plates. Vanadium steels that have advantageous mechanical properties exhibited unsatisfactory chemical resistance to the environment in the human body. The 1930s brought stainless steels and cobalt chromium alloys (CoCr) with better corrosion resistance. These materials were also used for the first successful joint replacements [24]. Titanium was first used as a biomaterial in the 1950s for parts with low mechanical stresses, such as heart valves. An increasing number of clinical reports of proximal bone resorption due to excessively stiff CoCr stems led to an increased interest in elastic and high-strength titanium alloys in Europe and North America in the second half of the 1970s [25]. Additionally, titanium alloys offered excellent corrosion properties in the biological environment. Stainless steel, CoCr and titanium alloys are chosen nowadays, depending on the patient condition (e. g., obesity) and on the surgeon's prejudice [26].

---

## 2.2 *Titanium as an Implant Material*

### 2.2.1 **Pure Titanium and Its Physico-Chemical Properties**

**Occurrence and fabrication.** Titanium is the fourth most frequently occurring structural metal on Earth, being exceeded only by aluminum, iron, and magnesium. Its concentration within the Earth's crust is about 0.06 %. Titanium is mainly extracted from ores such as rutile (almost pure  $\text{TiO}_2$ ) and ilmenite ( $\text{FeO}\cdot\text{TiO}_2$ ), with a content of 50 to 65 %  $\text{TiO}_2$ . Due to the high reactivity of titanium towards hydrogen, oxygen and nitrogen, the process for producing titanium metal from ores requires sophisticated and costly handling, in order to prevent contact with reactive compounds. In the common Kroll process, the ores are chlorocarbonated first to form  $\text{TiCl}_4$ . The titanium chloride is subsequently reduced with liquid magnesium in an airtight vessel under an argon atmosphere to avoid contamination with air and moisture. The result is titanium sponge with magnesium and magnesium chloride inclusions. In order to purify the titanium, the sponge is crushed into small particles and acid leached or vacuum distilled. Compared to the energy needed to produce a ton of steel, a ton of titanium needs a sixteen-fold larger amount. Further melt processes and heat treatments have to be carried out under vacuum or inert atmosphere conditions [27].

**Properties.** With a density of  $4.5 \text{ g/cm}^3$ , titanium belongs to the category of light metals. The two outstanding properties are its high corrosion resistance to various compounds and its high strength with respect to its low specific weight [28].

Titanium belongs to the group of refractory metals and has an atomic number of 22. Its atomic weight is 47.90, which is the average value of its five stable isotopes: 7.95 atom-%  $^{46}\text{Ti}$ , 7.75 atom-%  $^{47}\text{Ti}$ , 73.45 atom-%  $^{48}\text{Ti}$ , 5.51 atom-%  $^{49}\text{Ti}$ , and 5.34 atom-%  $^{50}\text{Ti}$ . Its valence electron configuration is  $3d^24s^2$ ; stable oxidation states are +4 (electron configuration of argon), +3, and +2 [28].

At ambient temperature the crystal structure of pure titanium is hexagonally close-packed (hcp,  $\alpha$ -titanium). At 882 °C, an allotropic transition to a body-centered cubic structure (bcc,  $\beta$ -titanium) takes place. Titanium melts at 1668 °C, and has a Young's modulus of 106-108 GPa [28].

**Passive layer.** Titanium is highly reactive with hydrogen, nitrogen, and especially oxygen. In an oxidative environment (such as air, water or blood) it immediately forms a natural oxide layer on the surface. The thickness of this layer is 4 to 6 nm. The amorphous oxide layer consists of different oxides of titanium: mainly  $\text{TiO}_2$ , as well as minor amounts of  $\text{Ti}_2\text{O}_3$  and  $\text{TiO}$  [29,30]. According to the literature the formation of the passive layer in acidic solutions starts with the reaction from Ti to a non-protective  $\text{Ti}_2\text{O}_3$  layer, followed by a not completely protecting  $\text{Ti}_3\text{O}_5$ -layer, and finally a layer of  $\text{TiO}_2$  is formed [31,32]. The growth with time is shown in Fig. 2.1. After about 50 d the growth rate decreases drastically. The formation of the oxide layer leads to passivation of the metal and protects it from further corrosion as well as oxidation since titanium dioxide is very inert [29].

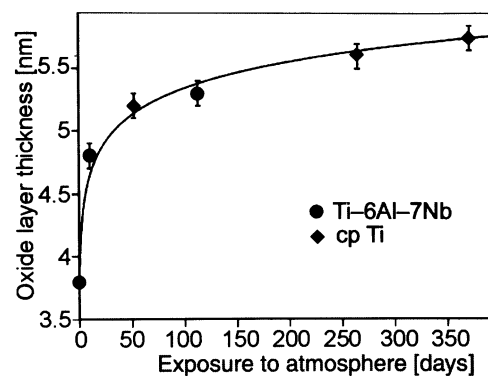


**Fig. 2.1.** The dependence of the oxide film thickness of polished commercially pure Ti and Ti-6Al-7Nb surfaces on time of exposure to ambient room temperature atmosphere [29,33].

**Titanium dioxide.** Titanium dioxide exists in three allotropic modifications: rutile, brookite, and anatase. Rutile is thermodynamically the most stable modification [34]. In titanium dioxide layers on titanium metal, rutile and anatase are important modifications. Thermal oxidation of titanium metal leads mainly to the rutile modification, while anodic oxidation generally leads to a mixed amorphous/anatase oxide layer [34]. Table 2.1 gives a brief overview of the structure and physical properties of the three modifications.

**TABLE 2.1.** Crystal structure and some physical properties of the three stable titanium dioxide modifications [34].

	<b>Rutile</b>	<b>Brookite</b>	<b>Anatase</b>
Elementary cell	Tetragonal	Orthorhombic	Tetragonal
Density [g/cm <sup>3</sup> ]	4.245	4.119	3.893
Heat of formation $\Delta H_{298}^0$ [kJ/mol]	945	942	939
Dielectric constant	110	78	48

The solubility of titanium dioxide is very low in aqueous environments between pH 3 and pH 12 (see Fig. 2.2). The main dissolution species in this pH range are uncharged, which is important, because uncharged hydrolysis products have no tendency to react with organic molecules [4].

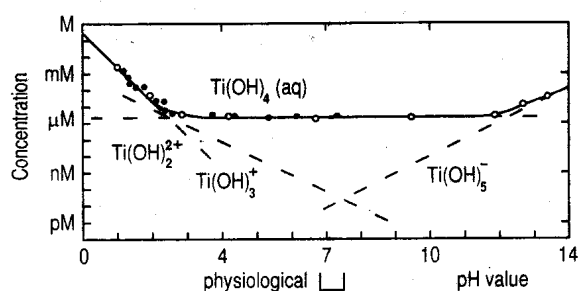


**Fig. 2.2.** Dissolution behavior of hydrous titanium dioxide measured in sodium chloride and chlorate electrolytes. The solid line is the solubility limit and the dashed lines are the partial concentrations for the named species indicated [4].

Titanium dioxide surfaces in contact with water are believed to be strongly hydroxylated. At or around physiological pH the surface charge is slightly negative. This is due to the fact that the hydroxides of multivalent titanium cations are amphoteric. Depending on the pH of the contacting solution the reaction of  $\text{TiO}_2$  with water can result in a net positive (in an acidic environment) or net negative (in a basic environment) surface charge. Since the isoelectric point (IEP) of  $\text{TiO}_2$  is around pH 6 [35], the resulting surface charge at physiological pH is negative. This negative charge is partially compensated in the body environment due to cations found in the body fluids (such as  $\text{Na}^+$  or  $\text{Ca}^{2+}$ ) interacting with the titanium oxide surface and inducing an increase in the IEP. The charge is therefore only slightly negative. The absence of strong charges on the surface of titanium oxide (including titanium implant surfaces) is believed to be one of the reasons for their excellent

biocompatibility. Such implants do not interact excessively with proteins, causing less denaturation of proteins in comparison to surfaces with higher surface charge [29].

### 2.2.2 CP Titanium and Titanium Alloys

Commercially pure (CP) titanium and titanium alloys are very commonly used as implant materials. They are used in dental and orthopedic applications and in traumatology. All titanium implant materials have several properties that make them interesting for biomedical use: corrosion resistance (due to passive film formation), high strength-to-specific-weight ratio, relatively low stiffness (with respect to steel and cobalt chromium alloys), and little or no tendency to cause adverse tissue reactions.

CP titanium is mainly used as dental implant material and in osteosynthesis, because the strength of CP titanium is too low for orthopedic applications. CP titanium is available in four different purity grades (according ISO 5832-2:1993), which are listed in Table 2.2.

**TABLE 2.2.** Purity grades of CP titanium according to ISO 5832-2:1993 [36,37].

Grade	Ti [wt-%]	O [wt-%]	N [wt-%]	Fe [wt-%]	C [wt-%]	H [wt-%]
Ti CP-1	>99.5	max. 0.18	max. 0.03	max. 0.15	max. 0.1	max. 0.015
Ti CP-2	>99.4	max. 0.25	max. 0.03	max. 0.20	max. 0.1	max. 0.015
Ti CP-3	>99.2	max. 0.35	max. 0.05	max. 0.25	max. 0.1	max. 0.015
Ti CP-4	>99.0	max. 0.45	max. 0.05	max. 0.3	max. 0.1	max. 0.015

For orthopedic load-bearing implants alloying elements are added to titanium to increase the strength of the material. Titanium alloys are categorized into  $\alpha$ -, near  $\alpha$ -,  $\alpha + \beta$ , near  $\beta$ -, and  $\beta$ -alloys based on their room temperature crystalline structure. Ti-6Al-4V ( $\alpha + \beta$ -type), which was developed for the aircraft industry, was one of the first alloys used as implant material [37]. More recent developments include near  $\beta$ - and  $\beta$ -alloys with a high strength and a decreased stiffness. They can be produced without the use of aluminum or vanadium, which have cytotoxic properties (vanadium) or are suspected to cause Alzheimer's disease (aluminum) [38]. The lower stiffness of the  $\beta$ -alloys is of interest, since it can reduce the stress-shielding effect present in very stiff load-bearing implants [39,40]. Furthermore,  $\beta$ -alloys are of interest because of their improved ductility possibly allowing for intraop. shape adaption. Ti-15Mo and Ti-13Zr-13Nb are two examples from this new class of

alloys. The chemical compositions of a number of commonly used titanium alloys are given in Table 2.3.

**TABLE 2.3.** Chemical composition of different titanium implant alloys [37]. bal: balance.

<b>Alloy (standard)</b>	<b>Type</b>	<b>Nominal chemical composition [wt-%]</b>
Ti-6Al-4V (ISO5832-3)	$\alpha + \beta$	<b>Al</b> 6.0; <b>C</b> 0.1 max; <b>Fe</b> 0.2; <b>H</b> 0.015 max.; <b>N</b> 0.03; <b>O</b> 0.20 max.; <b>Ti</b> bal; <b>V</b> 4.0
Ti-6Al-7Nb (ISO5832-11)	$\alpha + \beta$	<b>Al</b> 6.0; <b>C</b> 0.08 max; <b>Fe</b> 0.15; <b>H</b> 0.009 max.; <b>Nb</b> 7.0; <b>N</b> 0.03; <b>O</b> 0.20 max.; <b>Ta</b> 0.5 max.; <b>Ti</b> bal
Ti-15Mo (ASTM F 2066)	b	<b>C</b> 0.05 max; <b>Fe</b> 0.1; <b>H</b> 0.015 max.; <b>Mo</b> 15.0; <b>N</b> 0.01; <b>O</b> 0.15; <b>Ti</b> bal
Ti-13Nb-13Zr (ASTM F 1713)	b	<b>C</b> 0.08 max; <b>Fe</b> 0.1; <b>H</b> 0.02 max.; <b>Nb</b> 13.0; <b>N</b> 0.01; <b>O</b> 0.10; <b>Ti</b> bal; <b>Zr</b> 13.0
Ti-12Mo-6Zr-2Fe (ASTM F 1813)	b	<b>C</b> 0.02 max; <b>Fe</b> 2.0; <b>H</b> 0.02 max.; <b>Mo</b> 12.0; <b>N</b> 0.01; <b>O</b> 0.18; <b>Ti</b> bal; <b>Zr</b> 6.0

An important issue with titanium alloys is the chemical composition of the passive film. The composition of the passive film on Ti-6Al-4V and Ti-6Al-7Nb was investigated by Sittig and coworkers [29,41]. They studied the chemical composition as a function of different surface treatments such as mechanical polishing, passivating in nitric acid and acid pickling in a mixture of hydrofluoric and nitric acid. A general finding of their studies was that aluminum (in both alloys) is slightly enriched in the passive layer with respect to the bulk composition, independent of the surface treatment. On Ti-6Al-4V, the vanadium content is depleted. It was found that pickling leads to a significant enrichment of niobium in the passive film of Ti-6Al-7Nb. However, the alloying elements are not homogeneously distributed over the surface of the  $\alpha + \beta$  alloy. Aluminum ( $\alpha$ -stabilizer) is enriched in the oxide film above the  $\alpha$  grains, while vanadium and niobium (both  $\beta$ -stabilizers) are enriched in the oxide film above the  $\beta$  phase. Even though  $\text{Al}_2\text{O}_3$  and  $\text{Nb}_2\text{O}_5$  have highly different IEPs it was found that the surface charges at physiological pH seem to be distributed homogeneously over the surface, similar to pure titanium oxide. The stability of the passive layer of titanium alloys in a physiological environment in the absence of wear is comparable to that of passive films on CP titanium [42-44].



Titanium alloys exhibit a higher strength than CP titanium. A comparison of the mechanical properties of the titanium implant materials together with the properties of cortical bone is presented in Table 2.4.

**TABLE 2.4.** Mechanical properties of titanium implant materials and cortical bone [37,45].

<b>Alloy (condition)</b>	<b>Young's modulus [GPa]</b>	<b>Ultimate tensile strength [MPa]</b>	<b>0.2%-Yield Strength [MPa]</b>	<b>Elongation [%]</b>
Ti CP-1 (annealed)	106-108	241	172	24
Ti CP-4 (annealed)	106-108	552	483	15
Ti-6Al-4V (annealed)	88-116	931	862	15
Ti-6Al-7Nb (annealed)	108	862	793	10
Ti-13Nb-13Zr (aged)	79	860	725	8
Ti-12Mo-6Zr-2Fe	74-85	1000	965	15
Cortical bone	18	140	130	1

### 2.2.3 Titanium Surfaces in Contact with Tissue

The first contact of an implant, e. g., a bone plate or artificial hip joint, with the body environment is through the surface (in the case of titanium its passive oxide layer). Therefore, it is believed that the topography, the chemical composition, and the physical properties of the surface all strongly influence the formation of an implant/tissue interface and the long-term stability of the implant [46]. A further very important factor is the primary mechanical fixation of the implant in the bone tissue. If the implant is able to move at the implantation site after surgery (so-called micromotion), the bone will not grow onto the implant. Instead, a fibrous tissue layer will form between the implant and the bone, which firstly leads to a weak fixation, and secondly hinders the vascularization at the interface [47]. If the interface region is not supplied with sufficient blood, potential infections located at the implant surface are difficult to be treated with antibiotics.

The extent to which biomolecules interact with an implant surface depends on surface chemistry, and on physical properties such as surface charge, surface roughness, and surface contamination [48]. Cells do not respond to the surface properties directly, but to the biomolecules adsorbed on the

implant surface. Of particular relevance are proteins, which strongly interact with bone cells through integrin-peptide interactions, in particular fibronectin and vitronectin [39]. In the following paragraphs, the influences of the implant surface on the tissue reactions will be divided into three parts: influence of chemical composition, influence of surface topography, and influence of surface physical properties.

**Influence of the surface chemical composition.** Before cells reach the surface of the implant, biomolecules and other constituents of the bodily fluids (such as ions) interact in many different ways with the surface [47]. Reactions can be of either a temporary (e. g. van der Waals interactions) or a permanent nature (ionic or covalent bonds). An overview of the possible reactions is given in Fig. 2.3.

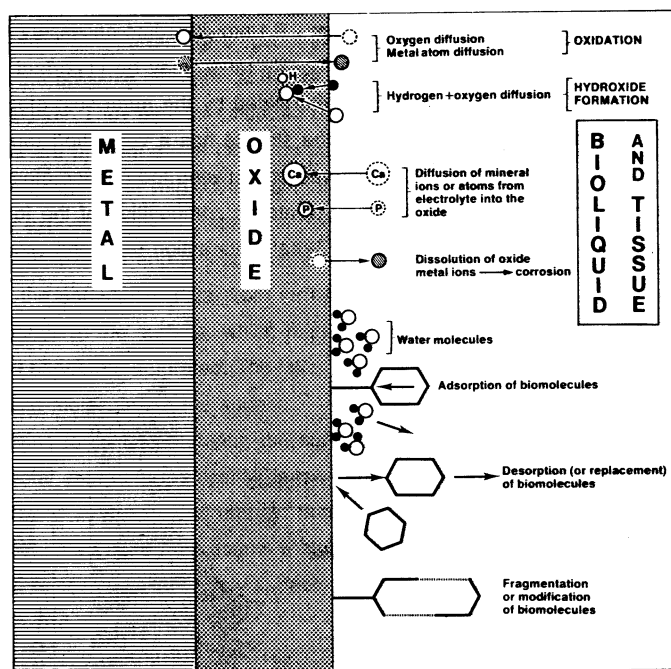


**Fig. 2.3.** Schematic illustration of some molecular surface processes that may occur at the interface between biomaterial and tissue [49].

Adsorbed biomolecules mediate the interaction between cells and the implant surface [50]. Therefore it is crucial that proteins do not denature excessively in order to still be able to guide and attach cells to the surface and to reduce the risk of strong sustaining inflammatory response. Titanium oxide surface are only slightly negatively charged at physiological pH and thus interact

only weakly with proteins [29]. From *in vitro* investigations it is also known that the interaction of titanium surfaces with important cell-attachment-mediating proteins (such as fibronectin and vitronectin) is weaker than that of hydroxyapatite surfaces, i. e., fewer molecules attach to titanium surfaces than to hydroxyapatite surfaces [51].

During the first few days to weeks after implantation, the tissue responds with a more or less pronounced inflammation reaction mediated by cells such as leukocytes or macrophages. These cells are able to produce peroxides or peroxy-nitrites in response to the foreign body [52,53]. Frangos and Suzuki showed that titanium dioxide has the ability to chemically crack these aggressive chemicals *in vitro*, which reduces the overall inflammatory response to titanium with respect to fluoropolymers and polyethylene [52]. This positive effect of titanium surfaces has already been reported by Tengvall. He found that in presence of hydrogen peroxide, a titanium peroxide gel is formed, which traps the chemically aggressive peroxide and therefore improves the biological properties of titanium in comparison to other materials [54,55].

An *in vitro* investigation with osteoblast-like cells showed that these cells are able to discriminate between CP Ti and Ti-6Al-4V surfaces although the main component of the passive layer is TiO<sub>2</sub> in both [56]. Stainless steel surfaces induce the formation of more connective tissue with respect to titanium implant surfaces [57]. Osteoblasts were also shown to be sensitive to the ionic composition at the surface of the implant and to the grade of crystallinity of the oxide layer on titanium implants [58,59].

Surface contamination of titanium implants and its origin in the fabrication process chain are important issues. Some chemical elements are always present on titanium surfaces exposed to air: oxygen, which forms the passive layer with titanium; adsorbed nitrogen; hydrogen (i. e. water); carbon in the form of hydrocarbons, which are present in air [30]. As measured with X-ray photoelectron spectroscopy (XPS), the concentration of carbon was found to exceed 20 atom-% on commercially available titanium implant surfaces [48]. A typical contaminant introduced by implant cleaning processes is silicone oil. Silicone oil or siloxanes are often used as a cleaning detergent additive or as a lubricant. The influence of contaminants that are present on the implant surface on the biological reaction is not well known. Other contaminants including iron, zinc, tin and lead are

reported to contribute to failure of implants, as was shown by a study on non-osseointegrated retrieved dental implants [60].

**Influence of the surface topography.** The surface topography is believed to significantly influence the biological response [61]. Many studies have been published investigating the influence of surface topography features of different sizes on both reactions of cells *in vitro* and on the biological response *in vivo*.

Ratner and coworkers have shown that the topographical modification of surfaces on the nanometer scale influences the adsorption of proteins and subsequently the response of the cells to the surface [62]. *In vitro* studies by Curtis and others showed that cells can sense topographical steps on the nanometer scale [63-65].

The geometric dimensions of microstructured surfaces [66-69] and random surfaces [70,71] with features in the micrometer range are known to influence cell adhesion, orientation, morphology, motility, proliferation, differentiation and expression of local factors *in vitro*. Martin and coworkers have shown that the proliferation of osteoblasts on rough surfaces is lower than on smooth ones [72]. Additionally, the response of osteoblasts to vitamin D<sub>3</sub> is improved if the R<sub>a</sub><sup>1</sup> value of the surface exceeds 2 μm. At this roughness, the expression of the transforming growth factor β-1 and prostaglandin E<sub>2</sub> is increased significantly [73]. If, however, the feature size exceeds the size of the cell (osteoblasts: 20 μm [39]), the cell will react as if it is on a smooth surface [74]. In a biomechanical context, features in the range of 100 μm to several millimeters can improve the mechanical interlocking between implant and tissue.

*In vivo* studies demonstrate that the surface topography of titanium implants influences the properties of the tissue/implant interface (such as new bone formation) and the foreign body response to the implant [75]. Wennerberg et al. described the optimal surface topography for titanium implants in the micrometer range with three parameters: the R<sub>a</sub> value should be between 1 and 1.5 μm, the spacing parameter should be around 10 μm, and the area ratio should be around 1.5

---

1. R<sub>a</sub>: Measure of the roughness of the surface; the arithmetic average of the absolute values of all points of a surface profile.

to maximize bone ongrowth onto the implant surface [75]. However, Buser and coworkers reported excellent bone apposition for dental implants with even higher  $R_a$  values [76]. Wennerberg and Buser used different roughness measurement methods, which could be the reason for the discrepancy between the conclusions [61]. Furthermore, the two authors used different animal models (rabbit and pig), which may have influenced the outcome of the experiments.

Wieland developed a new approach for correlating surface roughness with *in vitro* and *in vivo* results. He introduced the concept of window roughness [61,77,78]. Via Fourier transformation he extracted roughness parameters in three different size ranges, 3-10  $\mu\text{m}$ , 10-50  $\mu\text{m}$  and 50-500  $\mu\text{m}$ . He was able to show that in the range between 3 and 10  $\mu\text{m}$  an increase of surface roughness increased the cell differentiation of rat bone marrow cells *in vitro*. No correlation was found for the other size ranges. Correlation of the size ranges with *in vivo* data showed that with increasing surface roughness in the range of 50 to 500  $\mu\text{m}$ , the bone/implant contact area was increased [61].

**Influence of the surface physical properties.** It has been postulated that a high surface energy has a positive influence on the integration of the implant in the tissue. Baier found that proteins form an advantageous primary coat prior to the arrival of the cells, which improves the ongrowth of cells on the implant [79,80]. The surface tension of the implants was increased by a glow discharge treatment prior to implantation. Nevertheless, Wennerberg and coworkers were not able to confirm the positive effects of the glow discharge treatment *in vivo* [81].

The charge on the implant influences protein adsorption [29] as well as the cells in contact with the charged surface [82]. A negative surface charge was shown *in vitro* to be advantageous for bone-cell survival compared to positive charge. The cells expressed a stand-off morphology with very localized adhesion sites on negatively charged surfaces [83]. Davies and coworkers found a very strong attachment and spreading of osteoblast cells on positively charged surfaces as well as an intimate contact between the ventral cell membrane and the surface [83].

### **2.2.4 Wear on Titanium Implant Surfaces**

Wear may occur on any implant that undergoes dynamic loading. All implants are somehow fixed in the body and may articulate against natural tissue or another synthetic material (e. g. a metal head of an artificial hip joint articulating against a polyethylene cup). The severeness of the wear depends on the implant and counterface material, its surface properties, the presence of third-body material causing wear (i. e., particles), the medium around the implant, and the mechanical conditions (load, amplitude etc.). An example of a fixed implant with virtually no movements are bone plates, which are fixed on the bone with screws. Small movements on the micrometer scale may occur between the screw heads and the walls of the holes in the bone plate, while the movement of ball and cup of a hip joint is in the range of centimeters.

Titanium, in comparison to steel and cobalt chromium alloys a rather soft material, is more susceptible to wear and fretting than harder metals like steels or cobalt chromium alloys [84]. The wear resistance of titanium can be increased by strengthening the oxide film or hardening of the metal region near the surface. This can be done by increasing the thickness of the oxide film, by ion implantation [85] or by application of other coatings such as PVD-coatings [86,87] onto the titanium substrate.

Severe wear may eventually lead to failure of the implant function. Additionally, during the abrasion process small particles from the implant are released. La Budde and coworkers investigated patients with knee joint prostheses, with titanium as load bearing, articulating material [88]. They found accumulation of wear particles in the lymphatic system. In the case of severe wear they reported an intense immune response, possibly leading to osteolysis and implant loosening. The size of the wear particles were found to have an aspherical shape with a diameter of up to 4  $\mu\text{m}$  or a flake-like form with a size of up to 20  $\mu\text{m}$ . These findings were confirmed by a study of Willert [89]. Willert found abrasive and third body wear in a study performed on patients who had to undergo revision surgery. If the wear debris consisted mainly of metallic particles, the particles were internalized by macrophages. Willert did not observe a toxic effect of the wear debris. The wear debris is transported into the surrounding tissue generating blackish staining of the tissue [89]. Zeiler and Thull suggest to

avoid titanium for applications, where mechanical load and rubbing of the titanium surface against a counterface occur simultaneously [90].

No tribological investigations have been performed on the anodic plasma-chemically treated surface during this thesis project. As a qualitative test, the coating surfaces were scratched with one of the tips of polystyrene tweezers and the effects were examined with light microscopy.

---

### *2.3 Calcium Phosphate and Calcium Phosphate Containing Ceramics - An Overview*

Ceramic materials for use in the biomaterials field can be categorized into two broad groups: the non- calcium phosphate ceramics and the calcium and phosphate containing ceramics. The first group consists mainly of oxidic ceramics, which are nearly inert ceramic materials (e. g.,  $\text{Al}_2\text{O}_3$  or  $\text{ZrO}_2$ ). Such materials are used as load bearing bulk material implant parts with a good long-term stability [5]. The second group contains all ceramic compounds that incorporate calcium and phosphates to a certain extent and the pure calcium phosphates (CaP). Since hydroxyapatite ( $\text{Ca}_{10}(\text{PO}_4)_6(\text{OH})_2$ ) is the main inorganic compound of bone [39] such materials are used to produce so-called bioactive<sup>1</sup> implants [91]. A material with similar properties as the calcium phosphates is calcium sulfate (e. g. gypsum or plaster of Paris). Calcium sulfate is also referred to be bioactive and is used as resorbable filling material in large bone defects [92].

**TABLE 2.5.** Categories of calcium and phosphate containing and pure CaP compounds for use as biomaterials [7]

---

<b>Category</b>	<b>Example</b>
hydroxyapatite (HA)	HA coatings on hip prostheses
other calcium phosphates	tricalcium phosphate, tetracalcium phosphate
silicates	Bioglass
glass ceramics	Apatite/Wollastonite (A/W)
ceramic-matrix composites	A/W ceramic with a tetragonal zirconia dispersion

---

1. A bioactive material elicits a specific biological response at the interface with the tissue, that results in the formation of a bond between the tissue and the material [91].

The group of the calcium phosphate containing and CaP-materials can be subdivided into further groups according to Table 2.5. These materials are used as bone void fillers, cements for metal implant fixation [12], and for bioactive coatings on inert metals.

A very interesting subcategory consists of calcium- and phosphate-containing glasses and glass ceramics. In contact with a physiological environment these compounds undergo surface dissolution and induce the formation of a hydroxy carbonate apatite (HCA) layer. In the human body, growth factors adsorbing on this HCA-layer and induce the differentiation of nearby stem cells into bone forming cells (such as osteoblasts). Subsequently, new bone that is tightly bound to the surface of the implant is formed due to the biological equivalence of the HCA layer with the inorganic portion of bone [91] resulting in a high interfacial adhesion strength, which is about 5 to 7 times stronger than that of natural bone [7]. A typical example for a bioactive glass is the 45S5 Bioglass with chemical composition given in Table 2.6.

**TABLE 2.6.** Chemical composition of Bioglass 45S5 [91]. In order to be bioactive as described in the text, the portion of SiO<sub>2</sub> has to be below 60 wt-% for melt derived glasses.

Na <sub>2</sub> O	CaO	SiO <sub>2</sub>	P <sub>2</sub> O <sub>5</sub>
24.5 wt-%	24.5 wt-%	45 wt-%	6 wt-%

The chemical properties and the biological performance of hydroxyapatite and other pure CaP compounds will be discussed below. The main problem of all more or less bioactive ceramics are their unfavorable mechanical properties, with relatively low strength and low toughness. This has prevented a more widespread application as bulk structural materials [7].

---

## 2.4 Hydroxyapatite and Its Relatives

About 70 wt-% of bone consists of inorganic materials, mainly calcium phosphates in the form of carbonated apatite [39]. This is the reason why synthetic calcium phosphate materials (CaP), especially hydroxyapatite, are of great interest as biomaterials in contact with bone. CaP materials are used for repairing large bone defects (in combination with collagen and bone marrow [93]) or as thin coating on a large variety of materials in order to promote the ongrowth of bone and the formation of a high strength interface between bone and implant [5,6].



Focusing now on thin CaP-coatings one can formulate several requirements for CaP coatings used on implants in contact with bone. They should

- be bioactive (or even bioreactive<sup>1</sup> to some extent [6,13]); bone should grow faster and in larger proportions onto the coating relative to the bare implant [94],
- adhere strongly to the substrate, in order to be able to express advantageous bioactivity and not to cause 3rd body wear problems,
- not disintegrate completely during the lifetime of the implant, which could otherwise lead to a weak interface between tissue and implant, and
- be applicable at reasonable time/costs (see Chapter 3)

The chemical properties of the calcium phosphate bioceramics will be discussed in Section 2.4.1 and the biological performance will be reviewed in Section 2.4.2.

#### **2.4.1 The Chemistry of Calcium Phosphate Bioceramics**

In clinical applications CaP-materials are in contact with an aqueous environment (i. e., bodily fluids). Therefore, it is important to know about the stability of CaP-materials in the presence of water. Their stability at ambient and physiological temperature determines if an implant will fail or not. Solid-state reactions occur mostly at elevated temperatures, so that unstable solid phases will react mainly at their surface. An unstable solid CaP-phase may dissolve continuously and vanish completely. If the surface dissolution leads to the formation of a second stable phase, the dissolution will be stopped due to the virtual absence of solid-state reactions at ambient conditions [8]. Subsequently, the interface between implant and tissue is stabilized.

The CaP-phases that are of most interest in the biomaterials field are listed in Table 2.7. When in contact with water at ambient temperature, only two phases of the CaO-P<sub>2</sub>O<sub>5</sub>-H<sub>2</sub>O-system are thermodynamically stable. At pH values below 4.2 dicalcium phosphate is the most stable phase; above pH 4.2 hydroxyapatite (HA) is the most stable phase [8].

---

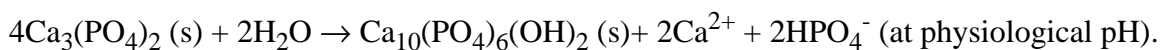
1. bioreactive: a materials, which chemically reacts/dissolves to certain extent in order to improve the biological reaction.

---

**TABLE 2.7.** Common CaP-phases with chemical formulas and solubility product [95-98].

Name	Formula	Crystal structure	Ca/P ratio	Solubility product at 37 °C, pH 7.3
Dicalcium hydrogen phosphate	CaHPO <sub>4</sub> ·2H <sub>2</sub> O	triclinic, P1	1.00	1.87·10 <sup>-7</sup> (mol <sup>2</sup> ·l <sup>-2</sup> )
β-Tricalcium phosphate	Ca <sub>3</sub> (PO <sub>4</sub> ) <sub>2</sub>	rhombohedral, R3c	1.50	2.83·10 <sup>-29</sup> (mol <sup>15</sup> ·l <sup>-15</sup> )
Octacalcium phosphate	CaH <sub>2</sub> (PO <sub>4</sub> ) <sub>6</sub> ·5H <sub>2</sub> O	triclinic, P1̄	1.33	2.5·10 <sup>-99</sup> (mol <sup>16</sup> ·l <sup>-16</sup> )
Hydroxyapatite	Ca <sub>10</sub> (PO <sub>4</sub> ) <sub>6</sub> (OH) <sub>2</sub>	monoclinic, P2 <sub>1</sub> /b	1.67	5.5·10 <sup>-118</sup> (mol <sup>18</sup> ·l <sup>-18</sup> )
Tetracalcium phosphate	Ca <sub>4</sub> O(PO <sub>4</sub> ) <sub>2</sub>	monoclinic, P2 <sub>1</sub>	2.00	insoluble

If an unstable calcium phosphate phase is in contact with water, it tends to react with water to form the thermodynamically stable phase. For example, β-tricalcium phosphate (β-TCP) reacts with water as follows:



The dissolution of β-TCP reduces the pH of the solution. Since the stability of the CaP phases depends on the pH in solution, the above-mentioned dissolution reaction is also influenced by changes in pH induced by the reaction itself. The drastic changes in solubility are depicted in Fig. 2.4. In conclusion, one can say that hydroxyapatite is the most stable phase in a physiological environment [99].

In the HA crystal lattice, calcium and phosphate ions as well as the hydroxy group can be partly substituted by other ions without a change of the crystal structure. Such modifications are of interest to the biomedical field in the following cases:

- The substitution of phosphate groups by carbonate groups, the so-called carbonated apatite is very similar to bony apatite.
- The substitution of hydroxy groups by fluoride, resulting in the so-called fluoroapatite with a decreased solubility under physiological conditions.

In addition, the level of calcium vacancies can be increased, so that the Ca/P ratio decreases from 1.67 to 1.5, resulting in the so-called calcium-deficient apatite. In its X-ray amorphous form this compound is called amorphous calcium phosphate.

In  $\beta$ -TCP, the calcium ions can be substituted by magnesium ions in order to increase the stability of  $\beta$ -TCP with respect to the pure  $\beta$ -TCP [97],[8]. The high temperature form of TCP,  $\alpha$ -TCP<sup>1</sup>, has a very similar crystallographic structure to HA and can therefore be transformed to calcium deficient HA via hydrolysis [100].

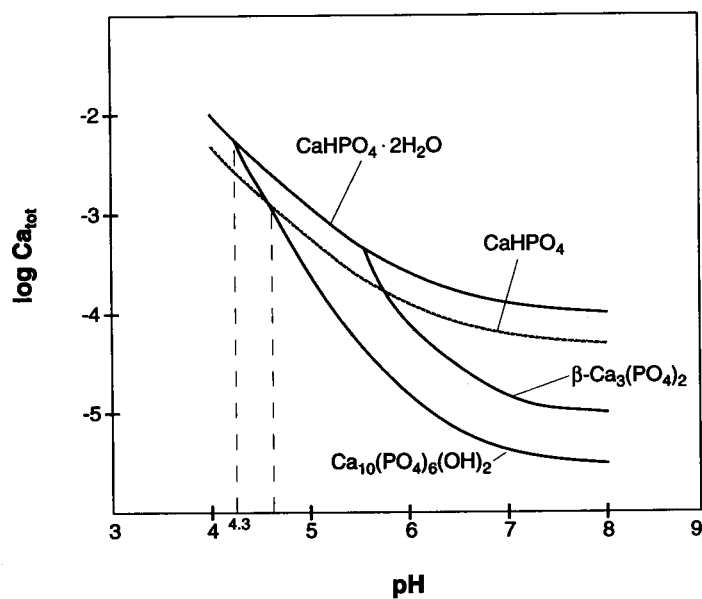


**Fig. 2.4.** Solubility of various CaP-phases as a function of pH. Below pH 4.2 DCP is the most stable phase, above hydroxyapatite is more stable [8,39]; the calcium concentration in solution has the units moles/L.

There are many different routes to produce CaP-compounds. The most simple way is to coprecipitate 1 M  $NH_4H_2PO_4$  and 1 M  $Ca(NO_3)_2$  in water at room temperature, which results in a fine HA-powder with a specific surface area of 116-119  $m^2/g$  [97].

1.  $\beta$ -TCP transforms at 1150 °C into  $\alpha$ -TCP [97].

### **2.4.2 The Biological Performance of Calcium Phosphate Ceramics**

CaP-bioceramics are used as coatings for bone implants (and bone defect repair materials) because they have several advantages over non-CaP-materials (such as titanium or steel). Since they hinder the formation of a fibrous capsule around the implant, the ongrowth of bone is faster than with other materials. They form tight bonds between implant and tissue due to direct bone contact, they reduce the dissolution rate of metal ions from the underlying substrate. CaP bioceramic coatings provide a faster overall healing process with respect to metallic implant materials [101]. This section focusses on CaP coatings, even though some examples of bulk materials and their properties will be given as well.

**Explanation for superior biological performance.** Several different arguments can be given to explain the advantageous biological behavior of CaP materials under loaded and unloaded conditions [102]. The most simple one is to consider the chemical similarity between HA to bony apatite [39]. A more sophisticated explanation deals with the bioreactivity of several CaP materials (such as bioglass). CaP materials, which chemically react to a certain extent with the biofluids around the implant, i. e. dissolve and saturate the level of calcium and phosphate around the implant, may induce the formation of a carbonated apatite layer on the implant surface. This natural layer is responsible for the good bonding of the tissue to the implant [6,91]. Hydroxyapatite exhibits a reduced bioactivity *in vivo* compared to Bioglass [103]. This can be explained by the inertness of crystalline HA in physiological environment. In contrast to the mentioned positive effect of bioreactivity, it has been shown in a recent study that dissolution of partly crystalline HA can lead to a significant increase of pH around the coating surface, possibly inhibiting DNA and protein synthesis in tissue culture [104]. However, the increase in pH due to dissolution affects not only the cell DNA, but also the reprecipitation of calcium. An increase in pH reduces the solubility of  $\text{Ca}^{2+}$  and therefore accelerates the natural reprecipitation of CaP on the surface (see Fig. 2.4) [105]. In a recent study defined proportions of TCP were added in an attempt to improve the biological performance of crystalline HA. Even though extensive dissolution of the plasma-sprayed mixed HA/TCP-coatings occurred after 12 weeks, the authors could not find significant differences with respect to bone healing, bone apposition, and shear strength of the implant/bone interface in comparison to coatings of pure plasma-sprayed HA [106].

A third explanation for the bioactive properties of CaP bioceramics may be found in the adsorption of biomolecules at a very early stage after implantation. It was shown by Kilpadi and coworkers that hydroxyapatite binds increased amounts of serum proteins and purified integrins relative to titanium or steel surfaces. In particular, fibronectin and vitronectin, which are responsible for osteoblast cell attachment, bind better to HA than to titanium or steel [51].

**Long-term stability.** The major problem of CaP coatings on implants is their lack of long-term stability. Much scientific effort has been put into the investigation of the stability of CaP coatings (esp. hydroxyapatite coatings with different crystallinity). Plasma-sprayed HA coatings, for example, always contain a certain amount of amorphous CaP next to HA because of the plasma-spray process (see Chapter 3) [16]. The amorphous parts in the coating are susceptible to dissolution, and as was showed by Ogiso and coworkers, the amorphous part tends to recrystallize *in vivo*. Recrystallisation leads to a volume change of the coating and to stress accumulation, thereby weakening the coating [107].

A study by de Groot and coworkers investigated the solubility of four different CaP coatings on Ti-6Al-4V in simulated physiological solutions at different pH values. They found that the following order of decreasing solubility at pH 7.3 (normal physiological pH): amorphous carbonated apatite (ACCP) > HA > carbonated HA (CHA) > octacalcium phosphate (OCP). At pH 5 (inflammatory conditions) they found: CHA > HA > OCP > ACCP [9]. The authors explain the different dissolution rates with specific solubilities (of the different CaP-phases), crystal size and microstructure of the coatings. However, both pH values reflect reality *in vivo* since inflammation is a general and nonspecific reaction to the tissue damage produced by the implantation surgery. A further investigation by Fulmer et al. showed that the solubility in tris(hydroxymethyl) amino methane buffer solution (pH 7.4 at 37 °C) depends on the crystallinity of the HA phase. They investigated three commercially available HA coatings and found that the higher the crystallinity, the lower the dissolution rate [12]. Experiments in a cell-culture medium supplemented with bovine serum performed by another group gave less distinctive results. HA coatings with low crystallinity dissolved only slightly faster than highly crystalline HA coatings. This slower dissolution, they claim, could be the consequence of buffering effects of the serum proteins [104]. *In vivo*, the

dissolution rate has also been shown to depend on the crystallinity [108]. In the same study, the researchers could not find any influence of the HA crystallinity on the biocompatibility (up to 26 weeks). Koerten and van der Meulen investigated the degradation of three different CaP materials *in vivo*. They injected  $\beta$ -TCP, HA and fluorinated apatite (FA) spheres into mouse peritoneal cavities. They found that  $\beta$ -TCP degrades faster than HA and that HA degrades faster than FA, which is consistent with the findings presented in Section 2.4.1. They further claim that the degradation *in vivo* starts between the grain boundaries of the CaP crystals in the spheres where they could locate amorphous CaP material [109]. The degradation of  $\beta$ -TCP seems strongly dependent on crystallinity and crystal size of the  $\beta$ -TCP crystals. However, contradictory results are reported in literature. A recent review by Shackelford describes TCP as, in general, being resorbable [5], but Cleries and coworkers find that only  $\alpha$ -TCP may be resorbable, while  $\beta$ -TCP dissolves only slowly [110].

Frayssinet and coworkers investigated the degradation of HA coatings in humans. They retrieved HA coated hip prostheses post mortem from patients deceased for reasons not directly related to the hip surgery. The crystallinity of the coatings was about 60 %, and the initial coating thicknesses were  $100 \pm 50 \mu\text{m}$ . They noted a decrease of coating thickness after a few months of implantation. They reported both dissolution and degradation by cells. A very important finding was that the degradation of the coating depended very strongly on the patient. Due to this dependency, no tendency could be found for the degradation rate of the HA coatings [111].

# *Methods for Producing Ceramic Coatings on Medical Implants*

---

---

## *3.1 Overview*

### **3.1.1 Thermal Spray Coatings**

Thermally sprayed coatings are produced by heating fine powders of an inorganic substance beyond its melting temperature and propelling them onto a substrate. Melting, vaporization, crystallization on the substrate and decomposition are the main processes occurring during the formation of the coating. Plasma spraying and flame spraying are hitherto the most common methods of thermal spraying [16,112]. Two types of energy are very important in thermal spraying processes.

- *Thermal energy* is needed to soften or melt the coating materials
- *Kinetic energy* is required to accelerate the liquid droplets towards the substrate. The velocity upon impact determines the final coating density.

The optimal setting of both energies influences the mechanical interlocking of coating and substrate surface, the activation of chemical bonds, and the formation of an inter-diffusion zone between substrate and coating.

**Plasma-sprayed coatings.** During the last twenty years, plasma spraying of hydroxyapatite (HA) has become a standard method of titanium surface modification for implants designed to come into contact with bone. HA powder is injected into a inert gas plasma jet. During the short exposure to a

very high temperature of about 15'000 K, the particles melt on their surfaces and are deposited on the cooler titanium substrate (see Fig. 3.1). Owing to the quenching effect, the re-solidified particles are partly amorphous. To avoid reaction with air, the spraying process can be performed under vacuum conditions [16]. The applied thickness of the layer (from 30 to 250  $\mu\text{m}$ ) is a compromise between coating strength<sup>1</sup> (thin coatings) and resistance to complete resorption/dissolution (thicker coatings). In order to optimize the adhesion properties of the coatings, the substrates surfaces are roughened (e. g., sandblasted), and the natural oxide layer of titanium is removed under vacuum conditions [16].

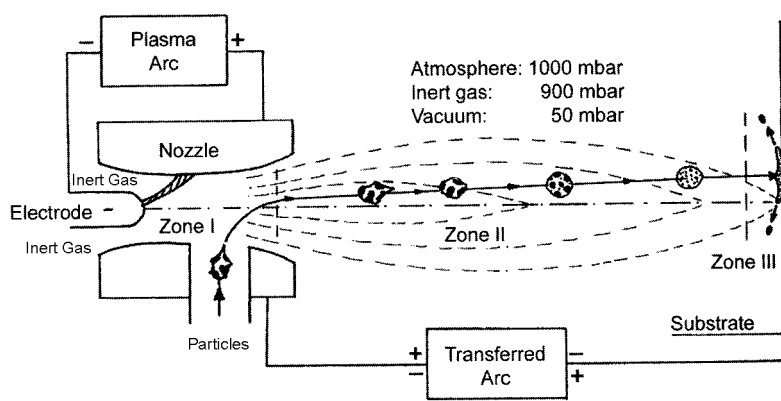


**Fig. 3.1.** Process scheme of the plasma spraying process. Melting (Zone I), accelerating (Zone II), and depositing (Zone III) are achieved using a plasma torch [16].

HA tends to decompose at high temperatures so that tetracalcium phosphate (TTCP) and tricalcium phosphate (TCP) can also be present in the plasma-sprayed coating. Above 850 °C, HA dehydrates first to oxy-hydroxyapatite (with variable content of  $\text{OH}^-$ ). Further heating leads to pure oxyapatite and at about 1350 °C oxyapatite decomposes to TCP and TTCP [16]. The chemical reaction of the HA particle with the titanium substrate to  $\text{CaTi}_2\text{O}_5$  is reported in the literature [113]. The authors of this study conclude that the chemical reaction might have a positive effect on the adhesion of the coating. In order to increase the crystallinity of the coating the implants can be heat treated after the coating process [112].

1. Coating strength: adhesive strength between coating and substrate as well as cohesive strength inside the coating.



Instead of pure HA powder, several other calcium phosphate (CaP) powders have been successfully evaluated as coating materials [112,114,115] (see also Section 2.4.1) for applications in the field of biomedical materials:

- Fluoroapatite (FA) with decreased solubility in aqueous environments. Additionally, FA has a congruent melting point in contrast to HA that decomposes below its melting temperature.
- $\beta$ -TCP to produce a resorbable  $\alpha$ -TCP coating.
- Bioglass and bioactive glass ceramics.
- $\text{Ca}(\text{Ti,Zr})_4(\text{PO}_4)_6$

**Flame-sprayed coatings.** Flame spraying, i. e. heating and partial melting of particles to be deposited by a combustion process, is an alternative to plasma spraying. Typical fuels are hydrogen, acetylene, or propane. In contrast to the plasma spraying process the flame temperature is much lower (3100 K), and the kinetic energy of the particle is about 5 times lower. Flame spray coatings are therefore typically porous and have significant oxide content due to the presence of oxygen. Porosity and oxide content can be decreased under high-pressure combustion, since the particle velocity is increased by a factor of 5 [16]. Thus, the kinetic energy is increased 25 times. This modified flame spraying process is called high-velocity oxy-fuel flame spraying.

Thermal-spray methods are line-of-sight methods. Complicated geometrical shapes (especially hollow structures) are difficult and expensive (since time consuming) to coat.

### 3.1.2 Physical-Vapour-Deposition Coatings (PVD)

**Beam Techniques.** These techniques use a beam of electrons, ions or light to evaporate material from a target with the desired chemical composition under ultra-high vacuum conditions. The evaporated atoms coat the substrate (implant) in a line-of-sight process at typical deposition rates of 25 Å per minute (HA coatings) [116] up to a thickness of several micrometers [117]. The crystallinity varies from amorphous to partly crystalline depending on substrate temperature and gas pressure during the coating process. The resulting coatings are dense [87].

**Magnetron sputtering.** High-energy gas ions from a radio-frequency plasma impinge upon a target with the desired chemical composition under vacuum conditions. The atoms of the target are released (sputtered) and transferred to the substrate. The resulting coating is dense and well-adherent. The thickness of the coating can be up to tens of microns [112]. The technique is suitable for coating more complex shapes.

### **3.1.3 Chemically Prepared Layers (Densified by Sintering)**

A recently developed method to produce HA on CP titanium is the following. By soaking CP titanium in 5 to 10 M NaOH at 60 °C for 24 h, a titanium hydrogel is formed on the surface. After washing and drying a heat treatment at 600 °C is applied to densify the gel, resulting in a well adhering and mechanically stable amorphous sodium titanate layer. When this layer is soaked in simulated body fluid (SBF) it is reactive enough to form a 5 to 10 micrometer thick HA layer [118]. The resulting HA layer is firmly bound to the substrate. During the exposure to SBF the alkali ions from the titanate layer dissolve. The titanate transforms into a hydrogel, while the alkali ions increase the pH and supersaturate the solution. The titania hydrogel then induces the nucleation of apatite. The process also works without the densification step, but the resulting HA layers are mechanically unstable and exhibit poor adhesion properties [17,112].

### **3.1.4 Enamelling and Sol-Gel Techniques**

Enamelling techniques apply a mixture of the desired raw, inorganic coating components by dipping, spraying or using other methods, followed by firing in order to densify the coating (the densification may be accompanied by chemical consolidation) and to establish a strong bond between the two materials.

The most important prerequisites for the enamelling process are the following [112]:

- equal or similar coefficients of thermal expansion between substrate and coating material to prevent high mechanical stresses at the interface during the firing, and
- and the capability of the substrate and coating materials to form a strong adhesive or chemical bond at the interface.

The first point is particularly important in the case of thick coatings (tenths of millimeters). The range of feasible thicknesses spans from a few micrometers (sol-gel methods) to millimeters (traditional enamelling techniques).

For biomedical purposes titania, HA, bioglass and bioactive glass ceramics have been applied to metal substrates. HA can be applied to titanium surfaces by various enamelling techniques. The titanium substrate can be simply dipped into a colloidal suspension of HA particles, dipped into a HA/Ti sol [119,120] or coated by electrophoretic deposition of HA particles, followed by a heat treatment [112].

Depending on the method chosen for the application of the coating precursor, even complicated implants with complex geometries can be coated easily and in a reasonable amount of time.

The deposition of HA onto titanium can cause significant stresses as a consequence of the difference of the thermal expansion coefficients ( $87 \cdot 10^{-7} \text{ K}^{-1}$  for titanium and  $133 \cdot 10^{-7} \text{ K}^{-1}$  for HA) [112]. In order to improve the adhesion strength, several authors prepared a mixed titania/CaP layer via a sol-gel route [15,121]. After the firing process, the coating consists not only of HA but also of TCP and other decomposition products of HA [99,112].

### **3.1.5 Cathodic Deposition**

CaP layers on metal surfaces can also be produced via an electrochemical route. In this approach the metal substrate is slightly cathodically polarized in a calcium phosphate solution. The resulting coating can consist of either amorphous calcium phosphate [122] or nanophase HA [123]. Eventually, the amorphous layer can be transformed to HA through a hydrothermal treatment [124]. The thickness of such CaP coatings can be several micrometers. The adhesion of the CaP layer can be improved by inverting the polarization temporarily in order to anodize the substrate, resulting in mixed and mechanically well interlocked layers consisting of HA and titania [125].

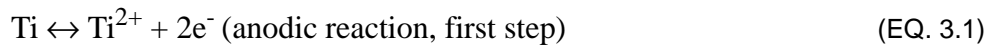
### **3.1.6 Anodic Oxidation**

**Anodic Oxidation.** The anodic oxidation process for passivating metals is used to form an oxide layer, which is thicker than the natural passive film, on the metal surface. It is mainly used in the

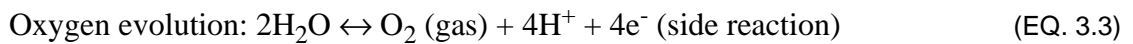
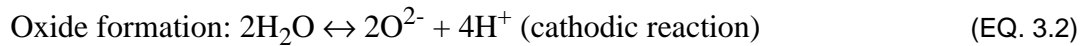
biomaterials field for corrosion protection and reduction of ion release, but it can also be used to change the surface topography. The structural and chemical properties can be changed by controlling the process parameters. Typical electrolytes are diluted acids, such as sulphuric or phosphoric acid [19].

The main reactions at a titanium anode (substrate) are the following [19]:

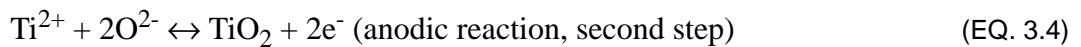
At the titanium/titanium interface oxide:



At the titanium oxide/electrolyte interface:



At both interfaces:



Titanium oxide has a high electrical resistivity compared to the electrolytes. Therefore the voltage drop will mainly occur across the oxide layer. The titanium and oxygen ions will migrate through the film driven by the electric field of the voltage drop. As long as the electric field is strong enough to force the ions through the oxide, the oxide layer will thicken. The final thickness of the oxide layer will be proportional to the applied voltage. Typical thickening rates lie between 1.5 and 3 nm per volt. This relation is only true below the breakdown limit of the oxide layer, which depends on the electrolyte composition and other parameters such as the electrolyte temperature. For typical electrolytes breakdown occurs at about 100 V. Anodic oxidation above the breakdown limit will be discussed in Section 3.2. If the anodization process is carried out at constant voltage, it is called the potentiostatic regime, if the current is constant, the regime is called galvanostatic. During the anodic oxidation process the growing oxide layer incorporates minor amounts of anions present in the electrolyte, thus influencing the properties of the resulting coating [19]. Anodic oxide films

generally consist of anatase and amorphous titanium oxide. In thick anodic oxide films, rutile can be found as well [126].

**Anodic plasma-chemical treatment.** The anodic plasma-chemical treatment process is an advanced and more extreme form of anodic oxidation that works above the breakdown voltage of a conventional anodic oxide film and produces a porous oxide layer. Details of this method are discussed in Section 3.2.

---

## 3.2 *The Anodic Plasma-Chemical Treatment*

### 3.2.1 Introduction

The anodic plasma-chemical treatment, APC, (also known as anodic spark deposition, ASD, [20], spark anodization [19], or anodic oxidation by spark discharge [127]) is a ceramic coating process, which exploits the dielectric breakdown of an insulating passive oxide layer of a valve metal<sup>1</sup> anode [128]. The APC process is carried out in an electrolyte solution that can be water-based or organic-solvent-based. APC usually includes the incorporation of electrolyte constituents into the forming layer, producing crystalline or amorphous phases in the film [20]. A typical example is the deposition of  $\text{WO}_3$  from a  $\text{Na}_2\text{WO}_4$  [20] solution on aluminum or the deposition of barium titanate from an  $\text{Ba}(\text{OH})_2$  solution [129] on titanium. The spark is a visual sign of the dielectric breakdown of the barrier oxide layer. APC as a process has been known for many years. Güntherschulze and Betz first reported an anodization process that uses the dielectric breakdown for the formation of an insulating film [21]. They also reported the occurrence of sparks, their appearance, decay, and disappearance during the process, as they travel over the surface of the anode. In the late 1930s APC found its first practical application. It was used to form a corrosion protective oxide layer on magnesium alloys [130]. Since then much research has been performed on applications on many different valve metals [20]. A recent study showed the possibility of incorporating Me(II)- and Me(III)-ions into APC coatings on aluminum and titanium via complexation of the metal ions with

---

1. *valve metal*: valve metals are metals that form a very stable passive oxide film on their surface when in contact with air, moisture or water. Under moderate conditions the reverse reaction from oxide to metal is thermodynamically not possible (therefore, they are called valve metals) [128].

polyphosphates [131]. Mg, Zn, Ba, Mn, Ni, Pb, Y, and Eu were deposited. Resulting levels of up to 40 wt-% of metal ions incorporated from the electrolyte were reported. The authors suggested that during the breakdown of the oxide layer, adsorbed metal chelates would undergo hydrolysis, and that the insoluble hydrolysis products would stay on the surface of the anode, being incorporated in the APC layer. Another interesting experiment performed by Koshkarian and Kriven deals with the incorporation of molybdenum disulfide particles into an aluminum oxide APC layer to reduce friction and wear [132]. By including molybdenum sulfide particle they were able to reduce wear by a factor of about two, using a dimple grinder for the determination of the wear rate.

The idea of using the APC process to modify metal implant surfaces emerged in the 1980s, when Kurze and coworkers made first attempts to produce CaP-containing coatings, including the first animal studies [22]. They concluded that the APC method is suitable for rendering titanium surfaces very corrosion resistant and bioactive. In the 1990s Ishazawa and coworkers coated titanium implants with APC in electrolytes containing calcium acetate and calcium  $\beta$ -glycerophosphate. They crystallized HA out of the APC coating via a hydrothermal process, thus forming a layer of small single crystals of HA on top of the APC coating [133-139]. The authors report a low solubility of the crystallized HA *in vivo* with respect to plasma sprayed HA. It was shown, however, that the hydrothermal treatment reduced the mechanical integrity of the APC coating. Schreckenbach and Schlottig investigated the properties of APC coatings produced in a  $\text{Ca}(\text{H}_2\text{PO}_4)_2$  electrolyte [140]. They proposed a glassy coating morphology for the phosphate containing coating. It was concluded that such coatings could be of potential interest due to their good abrasion resistance, corrosion resistance and biocompatible composition.

**Process Description.** The APC process consists of three phases [20]:

1. Anodization phase.
2. Local breakdown of the anodic oxide film.
3. Healing and layer formation phase.

In the first phase, usually within the first 10 to 30 seconds of the anodization treatment, an anodic oxide layer is formed on the anode surface as described in Section 3.1.6. During anodic oxide

formation anions of the electrolyte are incorporated [141] and other flaws such as gas bubbles may become incorporated in the layer as observed in some investigations on aluminum [142]. Typically, the required electrical field strength is very near the breakdown field strength [20]. The incorporated anions work as impurity centers and deliver electrons into the conduction band of the oxide film. Electrons present in the conduction band gain sufficient energy from the anodization field to be able to ionize surrounding ions if the oxide film thickness exceeds the mean free path of the electrons. This kind of ionization not only leads to a multiplication of mobile electrons but also breaks ionic bonds between the oxide constituents. As soon as the electron current locally reaches a critical current density, the oxide layer breaks down (phase 2). Light is emitted by the accelerated electrons as they recombine with atoms in the breakdown site. Electrolyte constituents enter into the breakdown site and mix with substrate material and the anodic oxide layer. Local fusion and further oxidation occur due to the intense Joule heating of the breakdown. The newly formed oxidic melt leads to a healing of the breakdown site, and subsequently solidifies and produces a new oxide coating with a thickness of around one micrometer (phase 3). Solidification and cooling at the breakdown location cause thermal stresses in the surrounding oxide layer. Subsequently, these stresses weaken the oxide film, leading to electrical breakdown in the neighborhood of the first site [20]. This process is repeated spontaneously until the surface is completely covered with a new thick oxide film. According to Krysmann and coworkers, a single breakdown takes place within 10 to 20  $\mu\text{s}$ . The same authors found a single spark (i. e., breakdown) power of 0.2 to 1 W with melting spot diameters of about 1  $\mu\text{m}$  [143].

The newly formed film consists of a metal oxide, mixed phases of substrate and electrolyte constituents, or phases formed exclusively from the electrolyte constituents. According to current knowledge the breakdown starts at weak points of the anodic oxide [20]. A prediction of where the first breakdown will happen is, however, difficult, since the exact mechanism is not known and many factors can influence the breakdown event. Shimizu, Thompson and Wood investigated single breakdowns on aluminum and they conclude that the breakdown could also be of thermal nature triggered by highly localized processes taking place at flaws/impurities in the oxide layer. This process could include also electron avalanching processes as discussed above [144]. Several authors found the oxygen evolution reaction to be a key process for the breakdown of anodic oxide films

[142-144]. However, the oxygen evolution does not take place on all valve metals that are used for the APC process [145]. Vijn postulated that the oxygen evolution reaction depends on the distance, which has to be tunneled by electrons from surface states into the conduction band of the oxide during the oxygen formation. For example aluminum exhibits a high tunneling distance; oxygen evolution is therefore not observed.

Fig. 3.2 shows a titanium surface before and after the APC treatment. In the example shown, the titanium surface was sandblasted prior to the APC treatment. The structure of a typical breakdown event consists of a pore created by evaporating electrolyte solution and surrounding material, which is temporarily molten and re-solidified during the breakdown event (circle on the SEM micrograph).

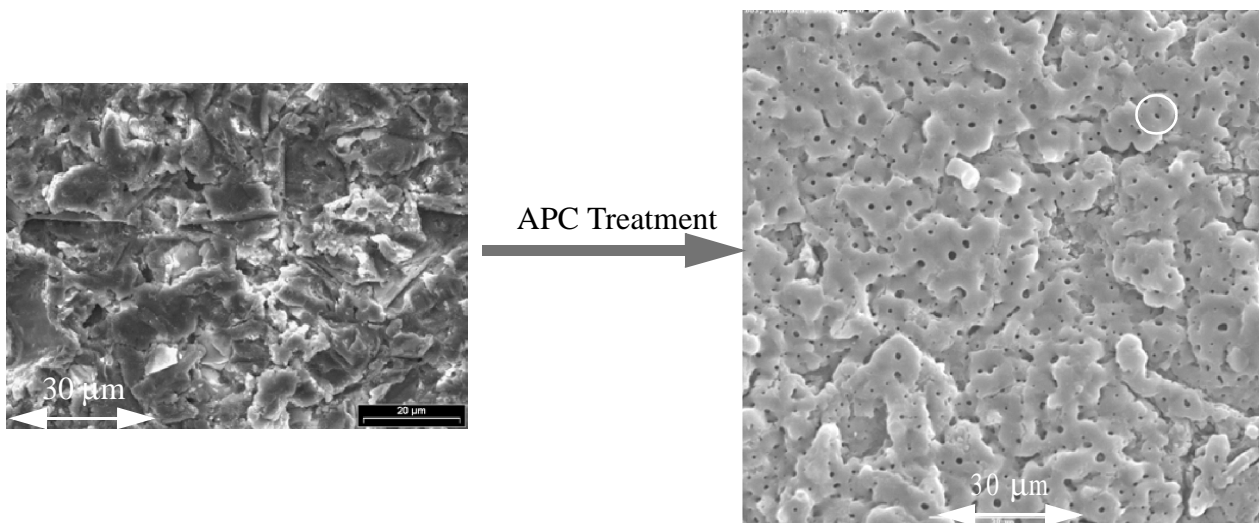


**Fig. 3.2.** CP titanium surface before (left) and after (right) APC treatment. Prior to the APC treatment the surface was sandblasted. The coated surface on the right side of the figure shows the typical characteristics of APC coatings (circle). A breakdown event has usually a pore in the middle from evaporating electrolyte solution. Around the pore a zone with molten and re-solidified material can be found.



### 3.2.2 Theoretical Background of the Breakdown Process

Several theories have evolved to describe the breakdown phenomena that occur during anodic oxidation of valve metals [22,127,146-149]. The following section reproduces one of them [148], while pointing out the influences excluded from the theory at the end of the section. The presented theory represents one of the most logical explanations for the breakdown of anodic oxide films as a consequence of the incorporation of ions from the electrolyte.

**The theory of electron avalanche breakdown during anodic oxidation.** The theory discussed in the following paragraphs is taken from the basic work of Albella, Montero, and Martínez-Duart, published in the late 1980s. They developed this model for tantalum oxide, but they claim that it can be easily adapted to other valve metal oxides (e. g., titanium oxide). Their model includes the following assumptions:

(i) During the first phase of the APC process (assuming a galvanostatic regime), the barrier-layer anodization, electrolyte constituents such as anions are incorporated into the forming oxide. This incorporation process consumes a certain current density,  $j_2$ . The incorporation current density,  $j_2$ , is considered to be a constant fraction,  $\gamma$ , of the total oxidation current,  $j_1$ . This assumption is based on experimental results published by other authors [150], who showed that on tantalum oxide, different mass amounts are deposited when the concentration of electrolyte is changed.

(ii) As soon as the electrolyte species are included into the oxide, they behave as impurity centres. A strong electric field,  $E$ , is able to ionize these impurity centers. They release a number of electrons into the conduction band of the oxide via a Poole-Frenkel mechanism [148]. If the field,  $E$ , is assumed to be constant, the corresponding electronic current density,  $j_0$ , is a defined fraction,  $\eta$ , of the incorporation current density,  $j_2$ . This gives the following relation between  $j_0$  and  $j_1$ :

$$j_0 = \eta j_2 = \gamma \eta j_1 \quad (\text{EQ. 3.5})$$

(iii) According to earlier theories of the breakdown process [147], the released electrons are accelerated by the electric field,  $E$ , over a mean free path,  $\lambda$ , producing an electron avalanche by impact ionization. Due to this electron multiplication process the electron avalanche current can be written as

$$j_e = j_0 e^{(\alpha d)} = \gamma \eta j_1 e^{(\alpha d)}, \tag{EQ. 3.6}$$

where  $\alpha$  is the impact ionization coefficient ( $\alpha = 1/\lambda$ ) and  $d$  the oxide thickness. If the anodization is carried out in a galvanostatic regime (i.e., constant current),  $d = V/E$ . The electron avalanche current can thus be written as:

$$j_e = \gamma \eta j_1 e^{\left(\frac{\alpha V}{E}\right)}. \tag{EQ. 3.7}$$

For tantalum oxide, Equation 3.7 is in good agreement with experiments of Kadary and Klein [151], who measured fast electronic current fluctuations during anodization.

If side reactions such as oxygen evolution are neglected, the (constant) total current density is distributed among  $j_1$ ,  $j_2$ , and  $j_e$ . The distribution is qualitatively depicted in Fig. 3.3.

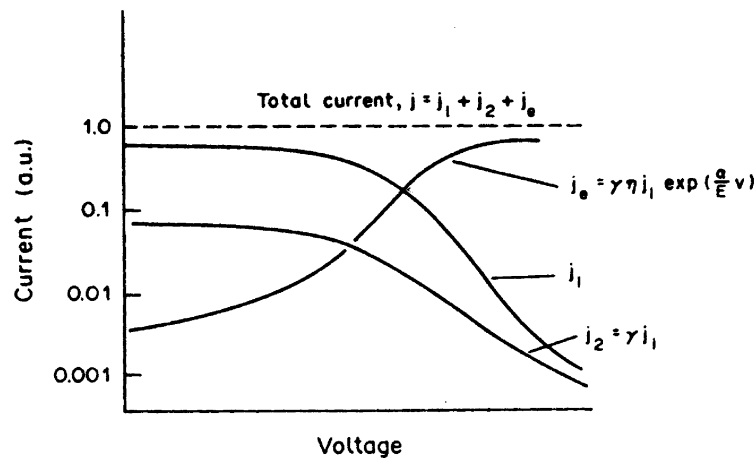


**Fig. 3.3.** Distribution of the ionic currents  $j_1$ ,  $j_2$ , and the electronic avalanche current  $j_e$  with increasing anodization voltage in the galvanostatic regime [148]. With increasing voltage, which means increasing thickness, the number of impact ionizations increases, and consequently the electronic avalanche current rises as well.

Since the number of impact ionizations increases with the thickening of the anodic oxide film, the electronic avalanche current becomes the dominant contribution to the total applied current. In the above equation it is assumed that the anodization field is constant with time. The strength of the anodization field is then determined by the ionic current during the oxidation process until the oxide film breaks down. Field effects, produced by positive space charge left by the electrons, as described by O’Dwyer [152], are assumed to be negligible. Neither the stochastic nature of the avalanches nor

the fluctuations over time of the avalanches, formerly discussed by Kadary and Klein [151] are taken into account.

(iv) Finally, the film breakdown occurs at a critical electron avalanche current density [147]. Albella and coworkers have introduced now the condition that the effective ionization collision rate cannot be larger than the oxide formation rate. If only one type of atom were ionized, e. g., the cations M of the oxide  $M_xO_y$ , then the avalanche electronic current should be a fraction of the formation current; thus

$$j_e = zj_1, \text{ with } z \leq 1/y. \quad (\text{EQ. 3.8})$$

The condition of Equation 3.8 can be substituted into Equation 3.7, which leads to an equation for the breakdown voltage,  $V_B$ :

$$V_B = \frac{E}{\alpha} \ln\left(\frac{z}{\gamma\eta}\right) \quad (\text{EQ. 3.9})$$

It is possible to assume other breakdown criteria than the one used above, such as a critical electron avalanche charge [153]. It is claimed by Albella, that the critical electron avalanche charge criterion is in good qualitative agreement with the criterion discussed previously. Using tantalum as the anode material and diluted phosphoric acid as the electrolyte, the experimental value of  $V_B$  turned out to be in good agreement with the calculated value for the breakdown voltage [154].

Albella, Montero, and Martínez-Duart also discuss the consequences of their theory. First of all, they consider the anodization voltage-time curves. The electron avalanche current increases with an increasing thickness of the oxide layer (increasing voltage under galvanostatic conditions) since more impact ionizations can take place. This directly gives rise to a decreasing anodization rate so that for constant current anodization the slope of the anodization voltage-time curve decreases. This deviation from the linear voltage-time relation has been expressed by the authors as:

$$V = \frac{1+A\gamma}{1+\gamma} k_j t - \Delta V \quad (\text{EQ. 3.10})$$

with  $\Delta V$  expressed as

$$\Delta V = \frac{E}{\alpha} \frac{\gamma \eta}{1+\gamma} \left( \exp\left(\frac{\alpha V}{E}\right) - 1 \right) \quad [155]. \quad (\text{EQ. 3.11})$$

$A$  is the ratio of the equivalent weight of incorporated species to the equivalent weight of the pure oxide, and  $k$  denotes the anodization rate of the pure oxide. The first factor in Equation 3.10,  $(1+A\gamma)/(1+\gamma)$ , is a correction for the anodization rate depending on the incorporation of electrolyte species. If  $A$  is greater than 1, the anodization rate will be greater than that of the pure oxide and vice versa. The first factor in Equation 3.10 therefore explains the dependence of the electrolyte concentration on the anodization rate and the specific oxide weight as reported by the authors in a further publication [154].

Using the above theory, the dependence of a number of experimental conditions on the breakdown voltage can be explained. From Equation 3.9 a logarithmic relation between the breakdown voltage and  $\gamma$  is predicted.  $\gamma$  itself is directly related to the number of electrolyte species incorporated into the oxide layer. For tantalum, within certain restrictions, it was found that the relation between  $\gamma$  and the electrolyte concentration can be described with a power law [155]. After replacing  $\gamma$  with the power law in Equation 3.9, a logarithmic dependence of the breakdown voltage on the electrolyte concentration results:

$$V_B \sim -\ln(C) \quad (\text{EQ. 3.12})$$

Additionally,  $E$ ,  $\alpha$ , and  $z$  may also depend on the electrolyte concentration [154], and they probably are not independent from each other. Therefore, a change of anodization conditions will induce a complex variation of the breakdown voltage, which is not straightforward to explain completely. Experiments also support this view [147,156].

Several authors have reported that if they performed an anodization experiment in a solution with a high electrolyte concentration up to a voltage just below the breakdown voltage, then interrupted the anodization, and subsequently reduced the electrolyte concentration in the solution. A repetition of the anodization experiment with the same sample gave a higher breakdown voltage [147,149,155]. This behaviour can now be explained with the theory introduced above. First, the breakdown voltage

---

decreases as the electrolyte concentration increases. From the theory one knows, furthermore, that the electron avalanche current depends on the incorporation rate of the electrolyte species. Therefore a decrease of electrolyte concentration in the solution causes a decrease in the incorporation rate, lowering the electron avalanche current as well. Since the critical electron avalanche current (where the breakdown occurs) stays constant, the voltage will rise again to the point where the incorporation rate (which is now lower) induces the critical current density. Consequently, the breakdown voltage becomes higher because fewer electrons start an avalanche at a given time (due to the reduced incorporation rate) [148].

**Important factors omitted from the theory.** The theory excludes side reactions during the anodization. One of the side reactions is oxygen evolution at the anode during the anodization phase. On titanium oxide oxygen evolution is more probable than on tantalum oxide. Vijn describes this difference in relation to electron tunneling from the electrolyte/oxide interface into the oxide. On tantalum oxide, the tunneling distance for electrons is higher than on titanium oxide, which is an estimate for the probability of the oxygen evolution reaction to occur, as claimed by the author. Vijn calculated the tunneling distances based on typical anodization field strengths and the band gap between valence and conduction band in the stoichiometric oxides [145]. The theory fails for electrolytes that dissolve the oxide layer [148].

Finally, the influence of mechanical stresses induced by the change of the ratio between the specific volume of the consumed, i. e., oxidized, metal and the newly formed oxide is not taken into account [146]. Influences from electrostrictive forces, i.e., forces in the growing oxide layer induced by the high electric field, are also not considered in the presented theoretical approach [149].



# *Materials & Sample Pretreatment*

---

---

## *4.1 Substrate Materials*

All substrate materials were supplied by either STRATEC Medical AG, Oberdorf, Switzerland, or Dr. h. c. Robert Mathys Foundation, Bettlach, Switzerland. Data concerning purity and composition of the bulk materials were supplied by the named companies.

### **4.1.1 Commercially Pure Titanium Disks**

Disk shaped samples were used throughout the thesis with the exception of the animal study. The disks had diameters of 7 and 13 mm and a thickness of 1 mm. The surface quality was 'machined'. The CP titanium was of purity grade 4 (see Table 2.2), although with reduced iron and oxygen concentration (Fe: <0.05 wt-%, O: <0.2 wt-%).

### **4.1.2 Cortex Screws for the Unloaded *in Vivo* Study**

The animal study screws, 4.5 mm in diameter and 16 mm long, were fabricated from grade 4 CP titanium (Synthes Cortex Screw Ref. 414.016).

## 4.2 Sample Pretreatment

Both the disks and the screws were ultrasonically degreased with acetone for 25 minutes. Subsequently, they were etched in a mixture of hydrofluoric and nitric acid (0.4 M HF/1 M HNO<sub>3</sub>) for 2 minutes under constant agitation and rinsed with ultra pure water (18.3 MΩ/cm). Finally, the samples were ultrasonically cleaned in ultra pure water for 25 minutes and allowed to dry in air. The dry samples were wrapped in aluminum foil for storage. The surface chemical composition after cleaning is documented in Table 4.1. X-ray photoelectron spectroscopy, XPS, (method and measurement parameters are described in Section 6.1.1) indicated that no other elements than oxygen (binding energy for O<sub>1s</sub>: 530.2 eV), titanium (binding energy for Ti<sub>2p3/2</sub>(metal): 458.7 eV) and carbon were present at the surface.

**TABLE 4.1.** Surface chemical composition of cleaned CP titanium disks, measured with XPS. The values are average values resulting from three measurements on three different samples ± standard deviation.

Element	Concentration [atom-%]
Titanium	25.9 ± 0.2
Oxygen	59.7 ± 0.5
Carbon	14.4 ± 0.4

A scanning electron microscope (SEM) image of a cleaned surface is shown in Fig. 4.1 (method and measurement parameters are described in Section 6.3.1). The grain structure is visible after the cleaning procedure (dashed line) since the etching rate depends on the grain orientation [30].



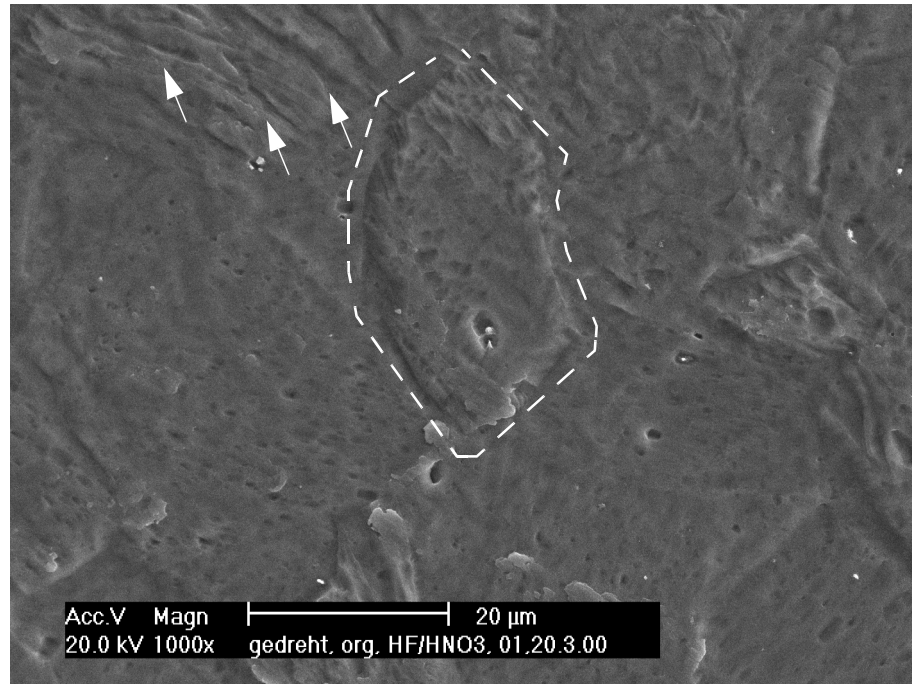


**Fig. 4.1.** Scanning electron micrograph of a CP titanium surface after cleaning. The etching rate depends on the grain orientation (dashed line marks a grain boundary) [30]. The grain inside the polygon is etched more slowly than the surrounding grains. The arrows mark locations inside the grains where the etching rate is increased (e. g. where dislocations penetrate the surface)

---



---

## *Methods I: The APC Coating Procedure*

---

The coating setup used for the APC process is very similar to that used for conventional anodic oxidation. The most apparent difference is the DC power supply, which has to supply voltages of up to 500 V and high currents at the same time (up to 1-2 A). The sample to be coated is immersed into a conductive liquid electrolyte and polarized positively. Another metal electrode serves as counter cathode. A cylindrical platinum mesh was used as cathode throughout the thesis, offering the advantage of the chemical inertness of platinum and the possibility to surround the sample completely with the cylindrical mesh. CP titanium wire (Goodfellow, Huntingdon, England; diameter: 0.5 mm, purity:  $\geq 99.6$  wt-%) was used to contact the sample in the electrolyte. The wire was bent to clamp the sample on its edges.

As DC power supply (Hewlett Packard 6035A) was used and controlled via a GP-IB interface with LabView software running on a personal computer. For the independent measurement of voltage and current a Schlumberger/Solartron 7150plus multimeter was used (also controlled via GP-IB). Time vs. voltage diagrams were acquired with a frequency of 10 measurements per second. Alternatively, the coating procedure was carried out directly by increasing the voltage manually on the power supply with the maximum current set to a constant value. The coating procedure was carried out in a double walled glass beaker (with inside volumes of 0.5 and 2 L respectively) that allows water-cooling of the walls with an external thermostat (Lauda Ecoline E119, IG Instrumenten Gesellschaft, Zurich, Switzerland). The thermostat used allowed for temperature control in the beaker in the range

of tap water temperature (between 10 and 15 °C) up to approximately 80 °C. The samples were coated galvanostatically and at constant electrolyte solution temperature. The used setup is shown in Fig. 5.1.

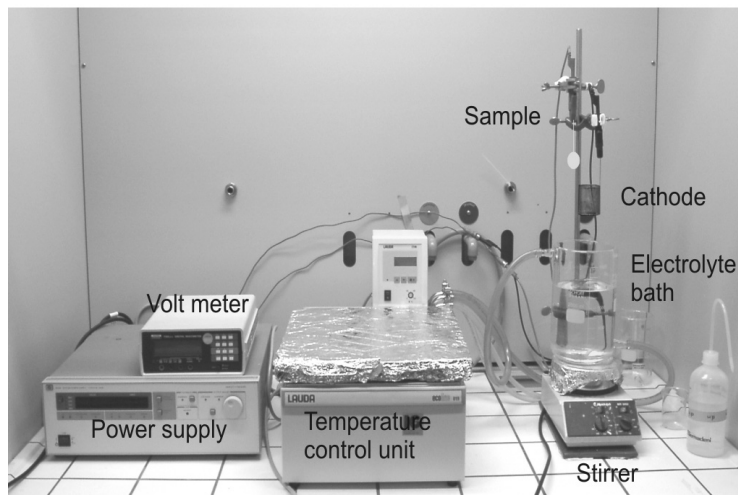


**Fig. 5.1.** Coating setup used for the APC process. The electrolyte solution is contained in a double walled beaker in order to enable temperature control via an external control unit. Power supply and volt meter are connected to a personal computer using a GP-IB interface. A cylindrical platinum mesh served as cathode. The coating experiments were carried out in a hood with closed windows, for safety reasons.

#### Standard coating procedure:

1. The electrolyte solution is filled into the beaker and the temperature control unit is set to the desired temperature. A magnetic stirrer is used to achieve a homogeneous temperature distribution.
2. As soon as the desired temperature is reached, the platinum cathode is immersed into the solution and connected to the negative output of the power supply.
3. The disc shaped sample is clamped with a piece of titanium wire, immersed into the electrolyte, and connected to the positive output of the power supply.
4. Current density, coating duration and maximum voltage are set in the LabView program (see Appendix).
5. The program (and hence the process) is started. The set current is kept constant while the voltage is allowed to float as long as the voltage is lower than the maximum voltage.

- 
6. The process is stopped by the personal computer after the preselected coating duration or when the maximum voltage is exceeded. Current and Voltage are set to zero by the LabView program.
  7. The sample is taken out of the solution, detached from the wire and carefully rinsed with ultra pure water (18.3 M $\Omega$ /cm).
  8. The sample is immersed into ultra pure water for 5 more minutes and then allowed to dry in air.
  9. The sample is wrapped in aluminum foil for storage.

The same procedure was applied to the cortex screws for the animal study. The screws were contacted with titanium wire at the head.



---

*6.1 Characterization of the Chemical Composition*

---

**6.1.1 X-ray Photoelectron Spectroscopy (XPS or ESCA)**

**Principle.** X-rays ( $h\nu$ ) are used to illuminate the sample surface. The X-rays excite electrons in the material. If the transferred energy exceeds the binding energy ( $E_{\text{bind}}$ ) of the electron and the work function it will leave the surface with a certain kinetic energy ( $E_{\text{kin}}$ ). Hence, the  $E_{\text{kin}}$  can be written as

$$E_{\text{kin}} = h\nu - \Phi - E_{\text{bind}} \quad \text{or} \quad E_{\text{bind}} = h\nu - \Phi - E_{\text{kin}}, \quad (\text{EQ. 6.1})$$

where  $\Phi$  corresponds to a combined work function (influenced by the physical work function and the spectrometer).  $\Phi$  depends on the spectrometer and has to be determined by calibration with well-known high-purity materials (such as gold, silver and copper). The electrons are commonly excited with  $\text{AlK}_\alpha$  or  $\text{MgK}_\alpha$  radiation (with an energy of 1486.6 eV and 1253.6 eV, respectively). Even though the X-rays penetrate deeply into the material, photoelectrons (with a typical kinetic energy of 100 to 1000 eV) can escape without loss of energy only from the top 2 to 10 nm nearest the surface. To avoid interactions of the escaping electron with the environment, XPS measurements have to be performed under ultra high vacuum (UHV) conditions. XPS spectra provide qualitative and (semi-) quantitative information on the elemental chemical composition. The spectra also contain information on the chemical oxidation state and surface contamination. Conductive and insulating

materials can be investigated with XPS. Charging on insulating materials results in a linear energy shift of the spectra and can usually be corrected after the measurement [30,157].

**Experimental conditions.** All XPS spectra were recorded on a SAGE 100 (SPECS, Berlin, Germany) using non-monochromatic MgK $\alpha$  radiation with an energy of 240 W (12 kV, 20 mA), an electron take-off angle of 90°, and an electron detector pass energy of 50 eV for survey and 14 eV for detail spectra. The measured area was typically 2 x 3 mm<sup>2</sup>. For the high-resolution spectra, a reference Ag 3d<sub>5/2</sub> full width at half maximum (FWHM) corresponds to 1.0 eV. During analysis, the base pressure remained below 1 x 10<sup>-7</sup> mbar. All peaks were referenced to the C<sub>1s</sub> (hydrocarbon C-C, C-H) contribution at 285.0 eV [158]. Quantification using the detail spectra was carried out with a first-principle model [159]. Absolute percentages are based on the quantification of oxygen, titanium, phosphorus and calcium.

### **6.1.2 Glow Discharge Optical Emission Spectroscopy (GD-OES)**

Glow-discharge optical emission spectrometry combines sputtering of a surface with atomic emission spectrometry. It enables the rapid analysis of bulk and surface composition as well as chemical depth profiling of conducting and non-conducting coatings and bulk materials. The GD-OE spectrometer consists of two main parts, viz a glow discharge source and an optical spectrometer [160].

**Principle.** A scheme of a glow-discharge source is given in Fig. 6.1. The sample is tightly attached to the cathode blocks to achieve vacuum conditions and electrical contact. A small metal tube in the middle of the plasma chamber works as anode (inner diameter 2 to 4 mm). The plasma chamber is closed by a MgF<sub>2</sub> window, which is transparent for wavelengths from 110 to 800 nm. Argon is bled through the chamber at pressures ranging from 300 to 1300 Pa. The radio frequency (rf) power supply is used at a power of 20 to 50 W giving potentials of 400 to 1200 V at the inner sample surface. During the glow discharge between anode and cathode, argon atoms are ionized in the region near the cathode and bombard the surface [160]. The argon ions contain sufficient energy to disrupt chemical bonds and eject atoms and electrons from the sample. Some of the released atoms are excited to higher energy states by electrons or metastable argon ions in the plasma. When they



de-excite, a photon with a wavelength characteristic of the species is emitted. The emitted light is analyzed by an optical spectrometer. The used type of spectrometer used is shown in Fig. 6.2.

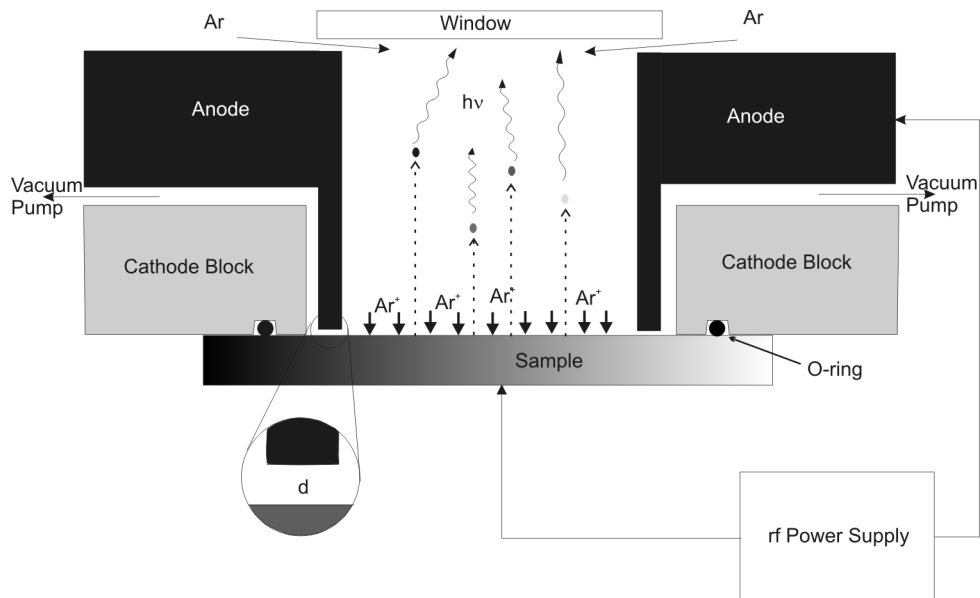


**Fig. 6.1.** Schematic drawing of a GD-OES sputter source (after [160]).

The rf source used for GD-OES allows continuous sputtering of the sample and thus chemical depth profiles can be recorded with GD-OES. Typical sputter rates on metals are 10-50 nm/s [161]. However, quantitative information with respect to concentration and depth is difficult to extract. On conducting and homogeneous samples the concept of emission yield has been developed. This method is based on the assumption that the emitted light per sputtered mass unit, the so-called emission yield, is a matrix-independent constant for each element (with the source operated at constant conditions) [162]. Hence, if the number of photons per atom is assumed to be constant, the frequency of a species can be determined by simply counting of the number of photons at a certain wavelength.

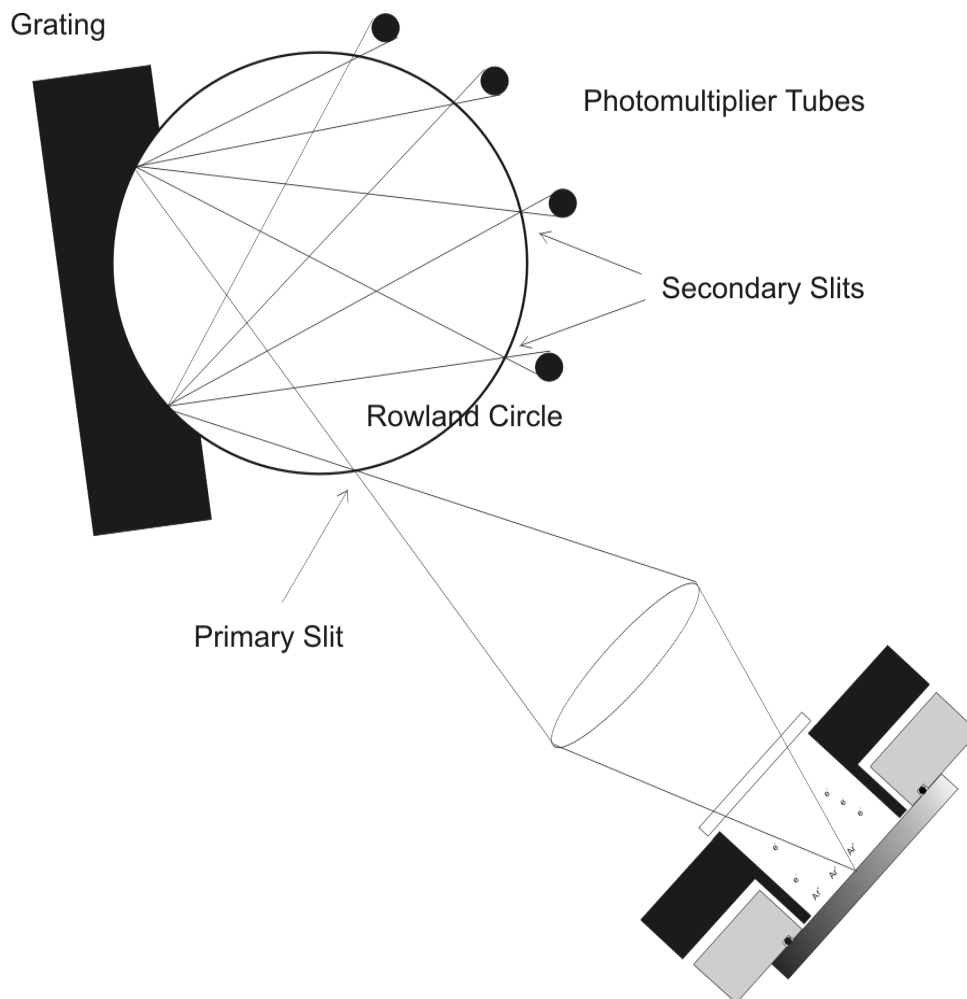


**Fig. 6.2.** Schematic drawing of an optical spectrometer (polychromator). The light emitted at the glow discharge source is focussed by lens onto the primary slit of the rowland circle. A grating diffracts the incoming light according to its wavelength. The light intensity at specific wavelengths is measured with photomultiplier tubes.

Since the sample acts as cathode of the rf system, the source conditions (voltage, current, and power) change significantly as zones of different chemical composition are sputtered. State-of-the-art GD-OES accounts for this problem by stabilization of the plasma conditions via adapting the argon pressure in the source. The variations of the argon pressure have much less influence on the signal than changes in current or voltage [163]. The influence of varying sputter rates is taken into account by appropriate calibration samples of known composition and sputter rate. Separate calibration has to be performed for each set of excitation conditions. Since sputter rate and plasma conditions are not

independent of each other, the quantification of the chemical depth profiles for complex matrix systems may be a too complex a task.

Moreover, other influences on the emitted light and, thus, the quantification are found that directly depend on the emission intensity. Non-excited atoms of a species, which are present in the source, tend to absorb the light emitted by other atoms of the same species. This so-called self-absorption process is likely to occur because most of the atoms present in the source are in their ground state. A recent object of discussion has been hydrogen as a contamination source and its influence on the signal intensities. Bengtson and Hånström have reported that small traces of hydrogen (< 0.1 % partial pressure) added to the argon gas in the glow discharge source or embedded in the sample significantly altered the emission yields [164]. They were, however, not able to establish correlations between the hydrogen partial pressure and the emission yields, since the influence varies from species to species. Some spectral lines are attenuated and others are amplified in the presence of hydrogen. This complicated influence may be based on the numerous possible reactions that can occur in the presence of hydrogen. Bogaerts and Gijbels have compiled a thorough overview of the different reactions likely to occur in the argon plasma [165].

GD-OES is an emerging technique for the chemical analysis of surfaces with the outstanding ability to record depth profiles of insulating layers. In order to enable the quantification of insulating and heterogeneous layers, more sophisticated software for the correction of listed influences still has to be developed. A more extensive review of state-of-the-art GD-OES can be found in the diploma thesis of Müller [166].

**Experimental conditions.** GD-OES chemical depth profiles were recorded with a JY 5000 RF instrument, manufactured by Jobin-Yvon Horiba, Longjumeau, France. The impedance between the radio frequency (rf) generator and the GD-source was balanced using a matching box. All experiments were performed at 600 Pa argon pressure and at a rf power of 30 W. For all measurements, the same calibration was used. After mounting the sample to the rf source, the source volume was flushed with argon for 30 s.

### 6.1.3 Inductively Coupled Plasma Optical Emission Spectroscopy (ICP-OES)

**Principle.** The principle of ICP-OES is very similar to the principle of GD-OES. The differences are found in the method of atom excitation and the form of the sample to analyze. The sample for ICP-OES has to be a liquid. This liquid is injected into an argon plasma torch via a concentric nozzle with argon as carrier gas. The high temperatures in the plasma torch (about 10'000 K) cause the atomization of refractory metals and even small particles present in the liquid can be analyzed. The argon plasma excites partly the atoms present in the liquid. The emitted light is analyzed with an optical spectrometer (see Fig. 6.2).

**Experimental conditions.** ICP-OES measurements were performed with an Applied Research Laboratories ARL Accuris 180 device, the quantifications were calibrated with standard solutions and the signal drift was corrected by repeated calibration measurements during the analysis of the samples. No sample preparation was necessary for the solutions of the dissolution experiment. Two times 3 mL of each solution were analyzed.

**Chemically digested samples.** The APC coatings were dissolved in a dipotassium sulfide melt (500 mg  $K_2S$  per sample). After the complete dissolution of the coating the sample was removed from the salt melt and 1 mL of concentrated sulfuric acid was added to the melt. The re-solidified melt was dissolved in ultra pure water to a volume of 25 mL. 3 mL of the solution per measurement were used and the measurement was repeated three times.

---

## 6.2 *Characterization of the Crystal Structure*

### 6.2.1 Raman Spectroscopy

**Principle.** Raman spectroscopy uses the information contained in light that has been inelastically scattered by a sample surface. The Raman effect relies upon the electric field of the incident electromagnetic radiation. The incident radiation induces a dipole moment in the electron clouds of the sample material. The dipole moment is time dependent due to molecule vibrations. Therefore, the

polarizability rather than the dipole moment is the important molecular parameter that determines the Raman intensities. The Raman effect was first observed by Sir C V Raman in 1928 [167].

An incident light quantum induces a dipole moment in the sample and thus energy is transferred from the light quantum to the molecule. The light quantum is re-emitted with a reduced energy (so-called Stokes photons). The excited molecule can subsequently transfer the energy back to another light quantum, which is scattered by the molecule (so-called anti-Stokes photons). The excited state is not generally a true electronic state of the molecule but a complex composite of the vibrational, rotational, and electronic states. If the excitation energy coincides with a true state of the molecule the Raman intensity increases drastically (up to a factor of  $10^6$ ). The Raman effect is, however, a weak effect. Only 1 of  $10^{11}$  photons is inelastically scattered by molecules. Both Stokes and anti-Stokes photons can be analyzed in the emission spectrum of the sample. Usually, only the Stokes emission is shown in the spectra. The wavenumber shown in the spectra are relative shifts with respect to the excitation wavelength.

A laser with a wavelength of 633 nm is frequently used as light source. This laser is coupled into a light microscope so that the light reflected from the sample surface can be analyzed. The emitted light is detected through the objective lens of the light microscope. The elastically scattered light is filtered by a notch filter and the inelastically scattered portion is divided into its spectral components with a grating. The grating scans the wavelengths and the intensities are measured with photomultiplier tubes. Using a laser as light source allows a lateral resolution of about 2  $\mu\text{m}$ . The information depth depends on the material analyzed and ranges from nanometers to several micrometers [168].

In the case of titania and calcium phosphate phases, Raman spectroscopy has been found to be a valuable tool for providing information about the crystal phases that are present in the samples and the degree of crystallinity of the phases [110,169-174].

**Experimental conditions.** A Dilor Labram spectrometer (Jobin Yvon, Bensheim, Germany) with a HeNe-Laser (5 mW, 1  $\mu\text{m}$  spot size) and a grid with 1800 lines/mm was used for all measurements. The spectral resolution was  $1.5\text{ cm}^{-1}$ . Spectra were integrated over 30 to 60 seconds.

### 6.3 Characterization of the Surface Topography

#### 6.3.1 Scanning Electron Microscopy (SEM)

**Principle.** A focussed beam of primary electrons is scanned across a sample surface. The impact of the primary beam induces secondary electron (SE) and photon emission from the sample. Furthermore, the primary electrons are scattered within the sample material and a portion escapes again from the sample as backscattered electrons (BSE). An electron detector collects the electrons that are emitted from the sample surface. The signal of the electron detector is used to influence the brightness of a cathode ray tube (CRT). In order to localize the emitted electrons on the sample surface, the scan generator controlling the primary electron beam is coupled to the scan deflectors of the cathode ray tube. Thus, the primary electron beam and the electron beam in the CRT are scanned synchronously. A schematic diagram of the principle of a scanning electron microscope is shown in Fig. 6.3.

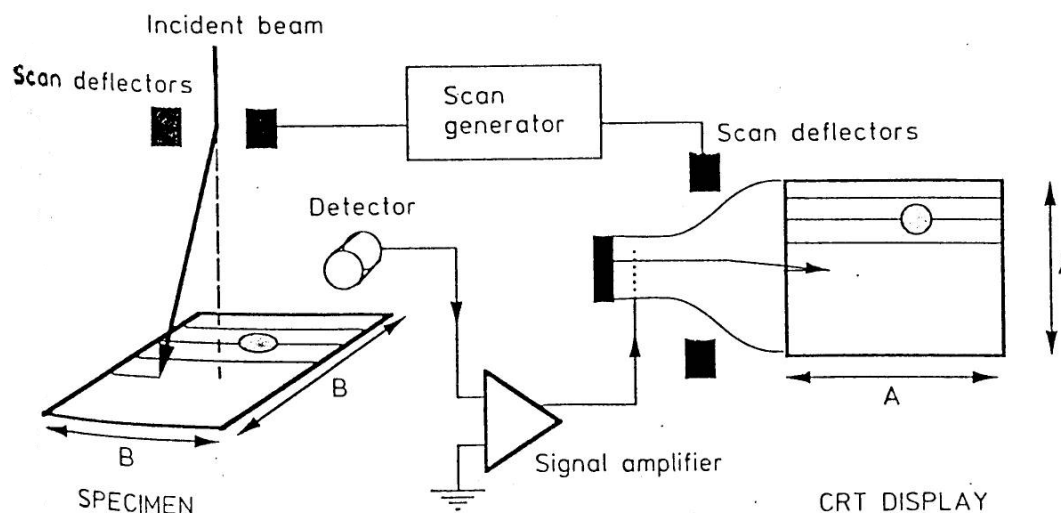


**Fig. 6.3.** Schematic diagram of a scanning electron microscope [175]

By definition, any electron escaping from the sample with a kinetic energy of less than 50 eV is called a secondary electron, the others being called backscattered electrons. SEs typically have a kinetic energy of 5 to 10 eV. This corresponds to an attenuation length inside matter of about 8 nm (the pear-shaped interaction volume is shown in Fig. 6.4). The minimum lateral resolution will be in

the same order of magnitude if the primary beam diameter is smaller than the attenuation length. Thus, the SE signal is very surface sensitive. The SE yield depends strongly on the tilt of the surface and is therefore used to image the surface topography. The SE signal (and subsequently the image contrast), however, cannot be used to image smooth surfaces since the contrast is very low.

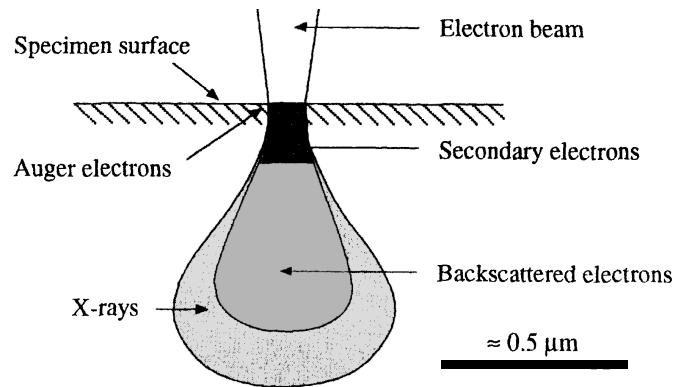


**Fig. 6.4.** Interaction of a high energy primary electron beam with a sample [61].

BSEs have a kinetic energy of typically half the energy of the primary electrons [175]. As a consequence, their attenuation length is higher than that of SEs. It is expected to be of 100 to more than 1000 nm. Hence, the lateral resolution of the BSE signal at constant primary electron energy is lower than for the SE signal. The backscattering yield depends on the density and atomic number of the material investigated [176]. Consequently, the BSE signal is not only used for imaging the surface topography but also to obtain material contrast. The higher the density and the atomic number of the material the higher the BSE yield. Bright regions in a BSE micrograph can be associated with heavy elements.

The primary electrons also induce the emission of X-rays from the sample due to inelastic scattering processes. These X-rays are element characteristic and can be used to identify the atomic species that are present in the sample with energy dispersive X-ray analysis (EDX).

**Experimental conditions.** An Hitachi S-700 field emission SEM was used for all cylindrically shaped samples with 7 mm diameter as shown in Chapter 7 and 8. The energy of the primary electrons was 25 keV and the emission current was between 1 and 2  $\mu\text{A}$ . The working distance was 5

mm. The samples with a diameter of 13 mm were investigated with a Philips XL 30 SEM at 20 kV and a working distance of 10 mm. Prior to the investigation, these samples were sputter coated with gold in order to increase the electronic conductivity of the sample surface. The titanium foils used for the investigations on the process mechanism (Chapter 10) were investigated with a Hitachi S-900 in-lens SEM with a field-emission gun. The primary electron energy was 30 keV and the emission current was 10  $\mu$ A. Prior to the investigation, the foils were sputter coated with 1 nm of tungsten.

### 6.3.2 Laser Profilometry (LPM)

**Principle.** Laser profilometry uses the auto-focus principle [177] to measure quantitatively the height profile of a sample. A laser beam is focused on the sample surface by minimizing the spot size of the reflected beam by moving a collimator lens. A scheme of the auto focus sensor (microfocus™ sensor) is shown in Fig. 6.5.

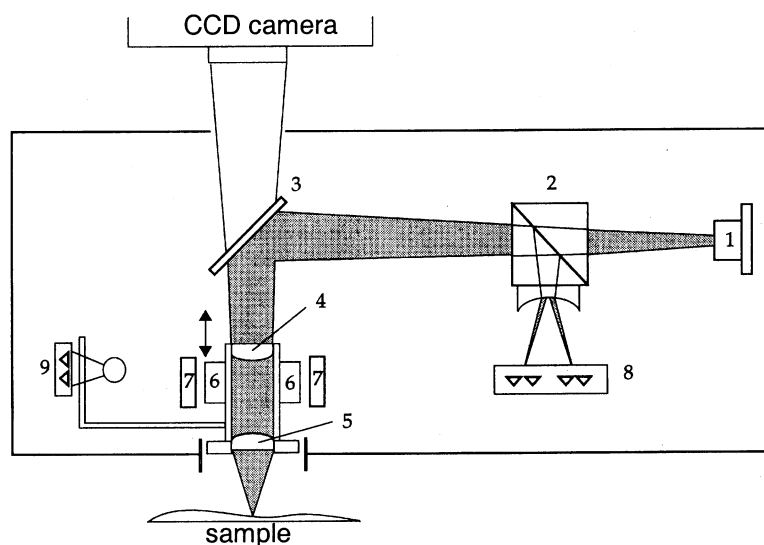


**Fig. 6.5.** Schematic drawing of a microfocus™ sensor for roughness determination [61].

The light produced by the laser diode (1) passes through the prism with beam splitter (2) and is deflected by the beam splitter (3). The light reaches the sample surface through the collimator lens (4) and the objective (5). The position of the collimator lens is controlled by a magnet-coil system (6):



permanent magnet, 7: coil). The light reflected from the probe surface runs along the way back to the beam splitter (2) and is led to the photodiodes (8). The illuminated point on the probe surface is in focus when the output of the photodiodes (8) is minimal. Thus, the photodiodes signal represents the input signal of the regulator controlling the current in the coil (7). The position of the collimator lens is monitored with a light detector (9). The read-out of the light detector is proportional to the Z-coordinate of the illuminated point on the sample surface. Line profiles and area measurements can be carried out by moving the sample with translation stages. The method has two important advantages: firstly, the method is non-destructive and secondly, the measurement can be performed under ambient air [61].

**Experimental conditions.** In this thesis, a UBM laser profilometer, UBM Messtechnik, Germany, with a microfocus<sup>TM</sup> sensor was used. The vertical resolution was 10 nm with a measurement range of  $\pm 50 \mu\text{m}$ . The scan length for each recorded profile was 5.6 mm and density of the measured points was 1000 p/mm, which corresponds to the maximum lateral resolution of the microfocus<sup>TM</sup> sensor. Prior to the roughness calculations, a linear regression to eliminate surface inclinations was performed on each profile. Subsequently, the waviness of the profile was subtracted with a Gauss filter with an attenuation factor of 50 % according to DIN 4768. The cut-off wavelength in the Gauss filter was set to 0.58 mm in accordance with Wieland [61].

The calculated roughness parameters are listed in Table 6.1. The definitions of the parameters are taken from the DIN 4768 standard.

**TABLE 6.1.** Definition and description of the measured roughness parameters according to DIN 4768 and [61].

Roughness parameter	Definition	Description
<i>Amplitude:</i>		
$R_a$	$R_a = \frac{1}{m} \sum_{i=1}^m  z(x_i) $	The arithmetic average of the absolute values of all points of the profile.
$R_q$	$R_q = \sqrt{\frac{1}{m} \sum_{i=1}^m z^2(x_i)}$	The root mean square of the values of all points of the surface; also called RMS-roughness
$R_{zDIN}$	$R_{zDIN} = \frac{1}{5} \sum_{i=1}^5 z(x_i)$	The arithmetic average of maximum peak-to-valley height of the roughness values $z(x_1)$ to $z(x_5)$ of five consecutive sampling sections over the filtered profile.
$R_{max}$		The maximum individual roughness depth encountered as determining $R_{zDIN}$ .
$R_t$		The maximum peak-to-valley height of the entire measurement trace.
<i>Spacing:</i>		
$S_m$	$S_m = \frac{1}{m} \sum_{i=1}^m S_i$	Arithmetic average spacing between the falling flanks of peaks on the meanline.
<i>Hybrid:</i>		
$S_k$	$S_k = \frac{1}{m} \sum_{i=1}^m \frac{z^3(x_i)}{R_q^3}$	Amplitude distribution skew.
$L_r$	$L_r = \frac{L_0}{L_m}$	The relation of the stretched length of the profile $L_0$ to the scanned length $L_m$ .

## 6.4 Characterization of the Mechanical Coating Properties

### 6.4.1 Tensile Tests

**Principle.** A schematic drawing of the setup for the tensile tests is shown in Fig. 6.6. The cylindrical sample is attached to the stamps (with the stamps attached to the clamps of the tensile tester) of the tensile tester by glueing the circular areas to the stamp with a standardized glue. The force is applied in parallel to the rotational axis of the sample. Failure is expected to occur either between the oxide layer and the substrate (adhesive failure) or within the oxide coating (cohesive failure). A further kind of failure that can occur is between the glue and the oxide coating. This happens if adhesive and cohesive strength of the coating exceed the strength of the glue.

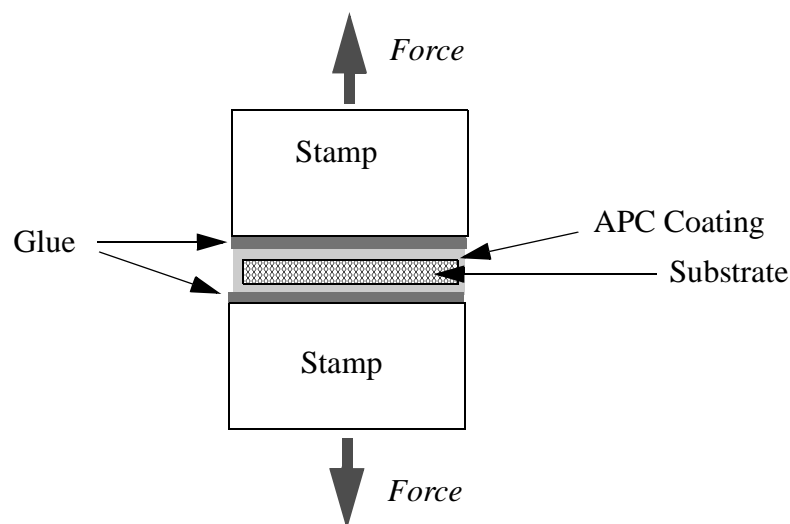


**Fig. 6.6.** Schematic drawing of the setup used for the tensile tests (according to ISO 13779-4). The cylindrically shaped samples were fixed on the stamp with glue.

**Experimental conditions.** The tensile adhesion test was carried out following ISO 13779-4 and using a material testing machine (Zwick UPM with a maximum force of 200kN, Zwick, Ulm, Germany) at a head speed of 0.5 mm/min and a preliminary load of 10 N. The coated samples were fixed to the sample holder with glue (FM 1000 adhesive film, Cytec Industries, West Paterson, USA) on their top and bottom sides.

### **6.4.2 Scratch Tests**

Throughout this thesis a simple scratch test was applied to any new APC coating produced. One of the tips of polystyrene tweezers was manually scratched over the surface. Subsequently, the scratch track was investigated with a light microscope. When the APC coating was damaged by the tweezer the APC coating was rejected. The idea behind this test was that a coating of a good quality must not be damaged by bone during the implantation procedure. In a first approach, the polystyrene tweezers were used. The coatings that withstood the tweezer test were tested with a polyurethane foam (which serves as an artificial bone substitute for surgeon training) prior to the animal study. Therefore, screws were coated with the APC method and inserted into pre-drilled and pre-tapped holes and removed again. After removal, the screws were investigated with light microscopy. Additionally, some screws were applied to bovine cadaver bone in order to simulate the *in vivo* situation. None of the coatings documented in this thesis were damaged by either of the scratch tests.

---

## *Basic Investigations on Standard Electrolytes*

---

The breakdown phenomena during the anodization of valve metals and, related to it, the APC process, have been known for some 60 years [21] (refer to Section 3.2). Electrolytes used for APC vary from simple electrolytes, such as phosphoric acid [19], to sophisticated mixtures containing MoS<sub>2</sub> particles [132] for the production of self-lubricating coatings. Because many specific processes have been developed and patented as proprietary technologies<sup>1</sup> since the first publication of Güntherschulze and Betz on APC and related processes, only little information on the influence of the process parameters on the coating properties has been published so far.

As a first step in the course of the development of an APC coating containing calcium and phosphates for biomedical purposes, the APC process was studied in detail. The first step was to investigate orthophosphoric acid as an electrolyte containing phosphate only. The second step was to introduce calcium with the calcium to phosphorus ratio (Ca/P-ratio) kept constant at 0.5. The electrolyte used for this investigation was Ca(H<sub>2</sub>PO<sub>4</sub>)<sub>2</sub>. The process parameters varied were the electrolyte concentration and the electrolyte temperature during the APC process. The influence of the two parameters on the chemical composition of the resulting coating and on surface morphology was assessed by X-ray photoelectron spectroscopy (XPS) and scanning electron microscopy (SEM). This chapter also includes additional characterization of samples coated in phosphoric acid and

---

1. Medical purposes: US 5,478,237; EP 0,277,622 B1; US 4,846,837; EP 0,232,791 A2; EP 0,224,890 B1. Other Applications: US 5,811,194; US 5,385,662; US 5,225,069; SU 1,156,410; SU 1,788,793; EP 0,280,886; DD 198,008,022405,5. The list gives the more recent patents, which are still valid.

calcium orthophosphate solution, which were performed in the context of the cell culture study on samples with increased size.

## 7.1 Orthophosphoric Acid as an Electrolyte

### 7.1.1 Experimental

Cleaned CP titanium, disk-shaped samples, 7 mm in diameter and 1 mm thick were coated in orthophosphoric acid of varying concentrations and temperatures between 25 and 75 °C. The current was kept constant at 150 mA, while the coating process duration was chosen to be between 45 and 90 s. A detailed list with all the process parameters is shown in Table 7.1.

**TABLE 7.1.** Parameter matrix for the APC coatings produced in orthophosphoric acid. ●: used parameter set. □: planned experiment where process did not work.

Concentration of H <sub>3</sub> PO <sub>4</sub>	Temperature (Duration)					
	25 °C	35 °C	45 °C	55 °C	65 °C	75 °C
0.01 M	●(90 s)		●(90 s)		●(90 s)	
0.025 M	●(90 s)	●(90 s)	●(90 s)	●(90 s)	●(90 s)	●(90 s)
0.05 M	●(60 s)		●(60 s)		●(60 s)	
0.1 M	●(45 s)	●(45 s)	●(45 s)	●(45 s)	●(45 s)	●(45 s)
0.25 M	●(90 s)	●(90 s)	●(90 s)	□	□	□
0.5 M	□		□		□	

The coating procedure was performed manually, without computer control. The temperature was measured before each experiment with a mercury thermometer. The process duration was monitored with a stop watch and the anodization was stopped after the time period shown in Table 7.1. Voltages indicated in the results part were directly read out of the power supply.

### 7.1.2 Results

**General.** APC coatings were produced at a wide range of electrolyte concentrations up to 0.25 M phosphoric acid. At 0.5 M phosphoric acid the voltage rose only very slowly with time or even stayed constant due to extensive oxygen evolution, which consumed most of the applied current. Therefore, dielectric breakdown of the anodic oxide could not be achieved. A further observation was that at high concentrations of phosphoric acid the titanium surface did not passivate completely.

Normally, if a constant positive voltage is applied to the sample, the current will rise and immediately return to very low values (passive current density) as soon as the surface has become passivated. In the case of 0.5 M phosphoric acid as the electrolyte, the passivation behavior changed, i. e., in some experiments the surface had depassivated causing local oxide dissolution.

The APC process in 0.25 M phosphoric acid at temperatures of 55 °C and higher was suppressed by oxygen evolution. The voltage at which the first sparks became visible (not identical to the breakdown voltage; refer to Section 10.2) strongly depended on the concentration of the electrolyte. At a higher electrolyte concentration sparks became visible at lower voltage in comparison to lower electrolyte concentrations. With increasing temperature, the voltage where sparks became visible increased as well. Similar observations could be made for the voltage measured just before the end of the process. Table 7.2 lists the process parameters as well as the voltage and time at which first sparks became visible as well as the final voltage at the end of the process.

**TABLE 7.2.** Comparison between the coating parameters and occurrence of first sparks (voltage and time) as well as the voltage just before process was ceased.

Concentration of H <sub>3</sub> PO <sub>4</sub>	Temperature	Current	Duration	First sparks	Time to first sparks	Voltage at end
[M]	[°C]	[mA]	[s]	[V]	[s]	[V]
0.01	25	150	90	324	14	412
0.025	25	150	90	286	12	410
0.05	25	150	60	270	9	420
0.1	25	150	45	255	7	405
0.25	25	150	90	220	5	400
0.025	35	150	90	283	12	420
0.25	35	150	90	225	5	420
0.01	45	150	90	330	16	423
0.025	45	150	90	290	13	430
0.05	45	150	60	275	10	430
0.1	45	150	45	255	8	410
0.25	45	150	90	225	5	428
0.025	55	150	90	300	14	430
0.1	55	150	45	260	9	415
0.01	65	150	90	350	19	425
0.025	65	150	90	305	15	450
0.05	65	150	60	280	11	450
0.1	65	150	45	265	9	420

---

**TABLE 7.2.** Comparison between the coating parameters and occurrence of first sparks (voltage and time) as well as the voltage just before process was ceased.

Concentration of H <sub>3</sub> PO <sub>4</sub>	Temperature	Current	Duration	First sparks	Time to first sparks	Voltage at end
[M]	[°C]	[mA]	[s]	[V]	[s]	[V]
0.025	75	150	90	320	16	450
0.1	75	150	45	270	8	430

Equation 3.12 (refer to Chapter 3) suggests a logarithmic relation between breakdown voltage and electrolyte concentration. This relation seems to be equally true for the voltage at which the first sparks can be observed (see inset diagram in Fig. 7.1).

Fig. 7.1 depicts the dependency of the voltage at which first sparks were observed on the electrolyte concentration and temperature for 25, 45, and 65 °C. The values are averages resulting of 5 identical coating procedures. The error of the values is about 5 V (estimated).

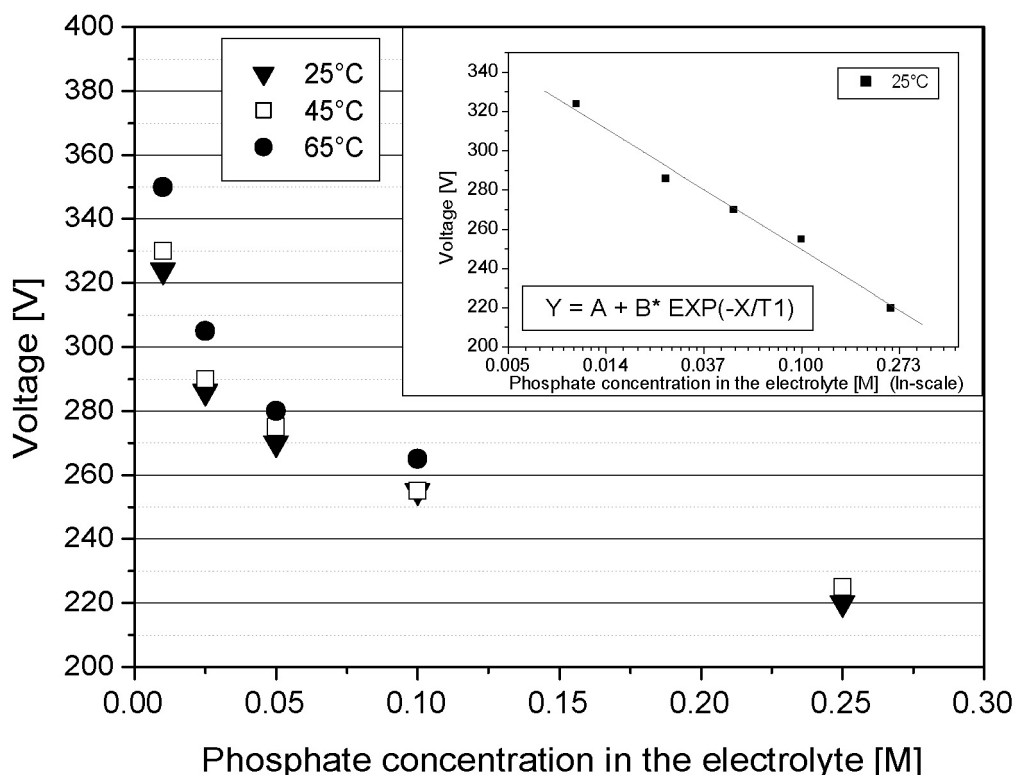


**Fig. 7.1.** Dependence of voltage at which first sparks were observed on the electrolyte concentration and temperature. The inset graph shows a curve fit for the voltages measured at 25 °C. The predicted relation (Equation 3.12) for the breakdown voltage is also found for the voltage at which the first sparks become visible.



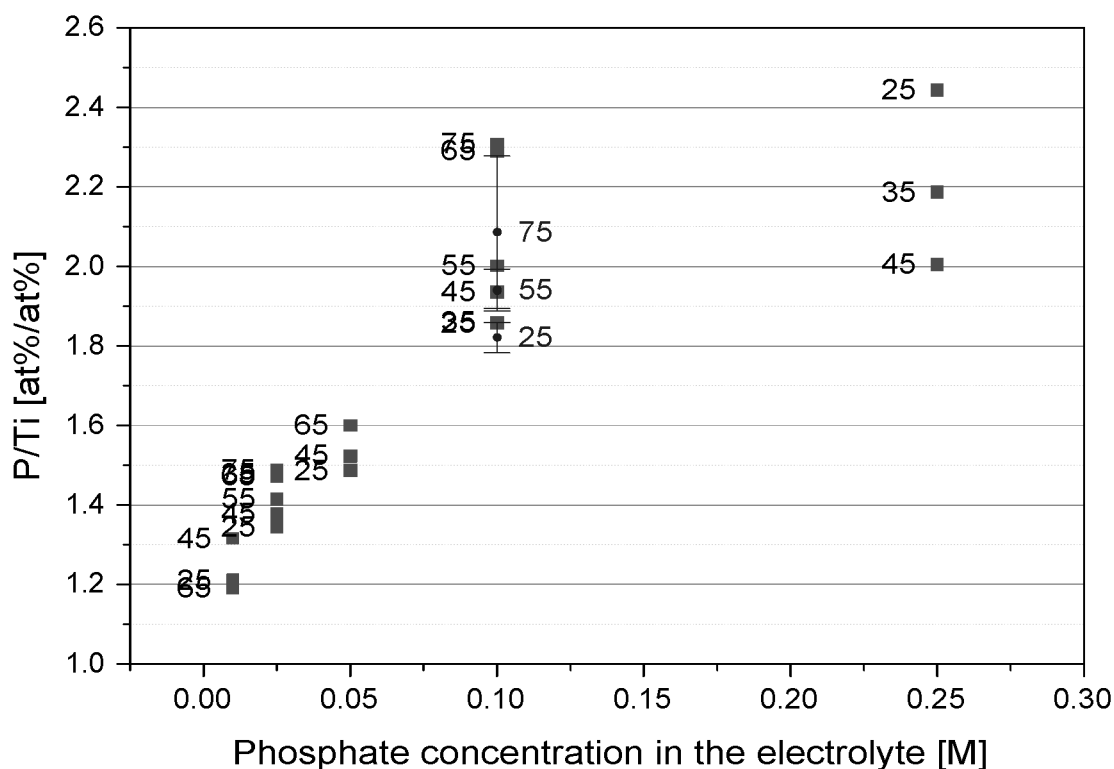
**Chemical Composition.** The chemical composition of the outermost few nanometers was determined semi-quantitatively using XPS. The chemical compositions of the different coatings are compiled in Table 7.3. As expected, titanium, oxygen, phosphorus, carbon, and traces of nitrogen were found at or near the surface. The titanium oxide as produced during the anodization contains up to 20 atom-% of phosphorus, the latter depending more on the electrolyte content than on the electrolyte temperature. The presence of carbon is due to adventitious contamination from the ambient air and is present as soon as the surface is exposed to air. The same is probably true for the nitrogen traces.

**TABLE 7.3.** Chemical composition of coatings produced in phosphoric acid at different concentrations and temperatures. The values are single point XPS measurements. Where a standard deviation is shown the values are averages of three single point measurements  $\pm$  standard deviations on three samples coated under identical conditions.

Electrolyte concentration	Electrolyte temperature	Process Duration	Titanium	Phosphorus	Oxygen	Carbon	Nitrogen
[M]	[°C]	[s]	[atom-%]	[atom-%]	[atom-%]	[atom-%]	[atom-%]
0.01	25	90	13	16	63	8	-
0.01	45	90	13	17	62	8	-
0.01	65	90	13	15	60	10	1
0.025	25	90	12	16	59	11	1
0.025	35	90	10	15	58	15	2
0.025	45	90	12	17	61	10	-
0.025	55	90	11	16	58	13	2
0.025	65	90	12	18	61	8	1
0.025	75	90	11	16	57	15	1
0.05	25	60	12	18	62	8	1
0.05	45	60	12	18	61	8	1
0.05	65	60	11	17	57	13	2
0.1	25	45	10	19	59	11	1
0.1	35	45	10	18	57	13	2
0.1	45	45	10	19	61	10	1
0.1	55	45	10 $\pm$ 0	19 $\pm$ 1	61 $\pm$ 1	10 $\pm$ 2	1
0.1	65	45	9	20	59	11	1
0.1	75	45	9 $\pm$ 2	19 $\pm$ 2	59 $\pm$ 5	10 $\pm$ 7	2
0.25	25	90	9 $\pm$ 1	21 $\pm$ 1	60 $\pm$ 2	9 $\pm$ 3	1
0.25	35	90	10	21	60	8	1
0.25	45	45	10 $\pm$ 1	20 $\pm$ 1	62 $\pm$ 1	7 $\pm$ 1	1

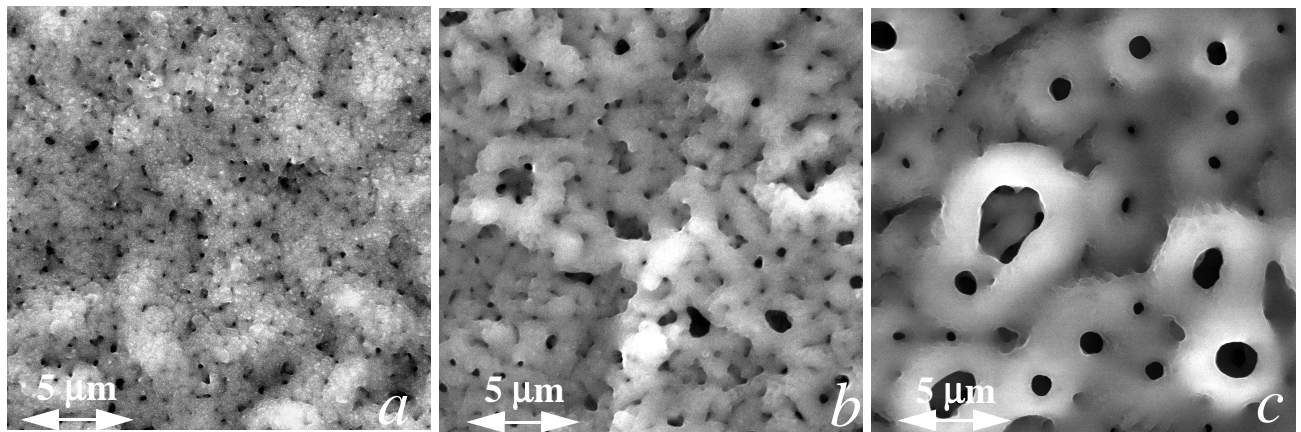
Noticeable is the ratio between the phosphorus and the oxygen content. If the phosphorus was present as stoichiometric phosphate in the coating, the oxygen content would have to be four times higher than the phosphorus content. Since there is obviously too little oxygen in the APC coatings, the phosphorus might be part of a glassy titanium/phosphorus/oxygen-structure as proposed by Schreckenbach, Schlottig and coworkers [140].

Fig. 7.2 shows the phosphorus-to-titanium (P/Ti) ratio as a function of the phosphate concentration in the electrolyte solution. The ratio was chosen rather than the absolute phosphorus concentrations because ratio depends less on the degree of carbon contaminations on the surface. The ratio is rising with increasing concentration of phosphate in the electrolyte. The P/Ti-ratio seems to saturate at higher phosphate concentrations. A very important finding is the fact that even at the low concentration of 0.01 M phosphoric acid in the electrolyte, more phosphorus than titanium is present near the surface.



**Fig. 7.2.** The phosphorus-to-titanium ratio (measured with XPS) vs. the electrolyte concentration and temperature. With increasing electrolyte concentration the P/Ti-ratio increases as well, whereas the influence of the electrolyte temperature is not significant. The squares are single point XPS measurement; the dots with error bars are averages and standard deviations from three samples coated with the same parameter set. The number next to each data point is the electrolyte temperature in °C.

**Surface Morphology.** Scanning electron microscopy was used to investigate qualitatively the morphology of the coating surfaces coated under the different coating conditions. Three examples of coatings produced at three different concentrations of phosphoric acid at 25 °C are shown in Fig. 7.3. The morphological differences between the coatings are clear. The surface morphology gets coarser as the concentration of phosphoric acid is increased. The coating produced in 0.25 M phosphoric acid has pore sizes of more than a micrometer. The coating produced in 0.025 M has very small pores in comparison to the two other samples. Each pore represents one breakdown event and originates from evaporating electrolyte. On samples coated in 0.1 and 0.25 M phosphoric acid, the region between the pores is comparatively smooth. In contrast, the sample coated at the lowest electrolyte concentration has additional bumps between the pores or breakdown sites.



**Fig. 7.3.** SEM Micrographs of APC coatings coated at different concentrations of phosphoric acid at 25 °C. a: 0.025 M; b: 0.1 M; c: 0.25 M. The surface structures get coarser with increasing electrolyte concentration.

The local temperatures during a breakdown have been estimated to be around 8000 °C [143]. A change in electrolyte temperature of 45 °C seems to be very small compared to 8000 °C. However, the surface of the sample coated at 25 °C has a rougher surface with respect to the sample coated at 65 °C (see Fig. 7.4). The area per breakdown event (circles on the micrograph) is smaller on the coating coated at lower temperature. The reason for the differences in surface topography can be found in the first phase of the APC process, the anodization phase. If the temperature change in the electrolyte reduces the adsorption and incorporation rate of anions into the oxide film (refer to Section 3.2), the breakdown voltage will rise (Equation 3.9). The energy impact caused by a single

breakdown becomes larger with increasing voltage and consequently the area per breakdown increases.

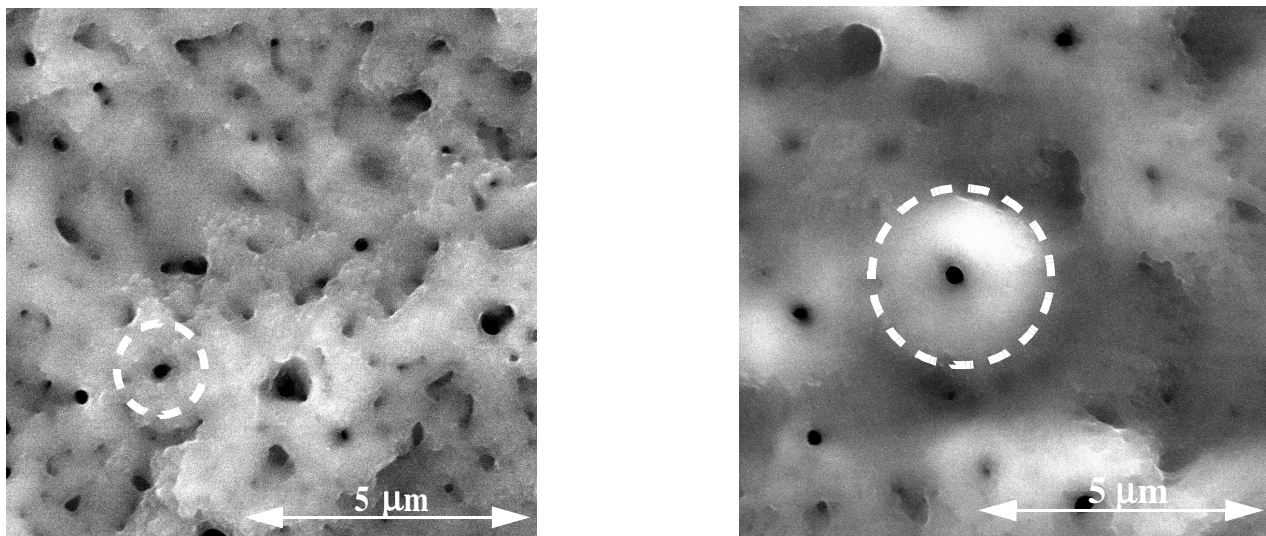


**Fig. 7.4.** SEM Micrographs coated in 0.1 M phosphoric acid at 25 °C (left) and 65 °C (right). The surface topography on the left image is rougher and the APC structure (area per breakdown event) is smaller than on right image.

### 7.1.3 Conclusions

The influence of the electrolyte concentration and electrolyte temperature on the surface chemical composition and the surface morphology have been investigated by XPS and SEM, respectively. The findings suggest the following conclusions:

- Coatings produced at higher concentrations of phosphoric acid contain more phosphorus near the surface and are characterized by coarser surface structures than APC coatings produced at lower concentrations.
- Higher temperatures of the electrolyte solution at constant electrolyte composition lead to coarser surface structures, while no influence of temperature on the chemical composition could be found.
- The voltage at which sparks become visible increases with decreasing electrolyte concentration and with increasing temperatures of the electrolyte solution.

## 7.2 Samples for in the Vitro Study Coated in Phosphoric Acid

### 7.2.1 Experimental

For the cell culture experiments, coatings produced in dilute phosphoric acid were chosen as a standard APC coating. The resulting APC should consist only of titania and as low a level as possible of electrolyte constituents. Orthophosphoric acid was chosen as an electrolyte, because it is a well-known APC electrolyte [156,178,179] and does not contain any metal cations. For technical reasons, the electrolyte concentration was chosen to be 0.01 M phosphoric acid since lower concentrations could lead to voltages above 500 V, which is the present limit of the power supply used. One coating was produced at an electrolyte temperature of 75 °C and another at 25 °C.

For the cell-culture study the diameter of the disk-shaped samples had to be increased from 7 to 13 mm in order to make them fit into the wells (diameter: 15 mm) of a cell-culture multidish. The electrical current was increased up to the value of 290 mA (and a process duration of 90 s). At this particular sample current the final voltage as well as the time and voltage at which first sparks became visible, matched with the values of the 7 mm samples. Since the APC process is a process localized at small spots on the sample surface, the current does not scale linearly the surface areas to coat.

### 7.2.2 Characterization

**Chemical composition.** The chemical composition of the entire coating was determined by chemical digestion (i.e. specific dissolution) of the coating and subsequent measurement of the phosphorus concentration in the resulting solution using ICP-AES. The results presented in Table 7.4 indicate that slightly more phosphorus is incorporated into the APC coating at higher temperatures.

**TABLE 7.4.** Integral phosphorus content in two different coatings produced in 0.01 M phosphoric acid with a current of 290 mA. The process duration was 90 s for both samples. The error in the values is about 3 %.

Electrolyte temperature	Phosphorus content
[°C]	[ $\mu\text{g}/\text{mm}^2$ ]
25	0.11
75	0.17

The surface chemical composition was determined by XPS (results are shown in Table 7.5). In accordance with Section 7.1 the elements found near the surface are titanium, phosphorus, oxygen, and carbon. 16 atom-% of phosphorus would correspond to an oxygen content of about 64 atom-% for stoichiometric phosphate. Since the oxygen concentration is only around 55 atom-%, phosphorus may be present as metaphosphate rather than as phosphate. The binding energy of the P2p electrons for all APC coatings produced in phosphoric acid was 133.8 eV, which also fits better to metaphosphate than to phosphate. No effect of the electrolyte temperature on the chemical composition near the coating surface could be found. The carbon content results from adventitious contamination.

**TABLE 7.5.** Chemical composition of the cell culture samples coated in 0.01 M orthophosphoric acid determined by XPS. The values are averages  $\pm$  standard deviation of three measurements on three samples coated under identical conditions. The chemical composition near the surface is not affected by the change in electrolyte temperature. The nitrogen content was below 1 atom-% and therefore not quantified.

Electrolyte temperature	Titanium	Phosphorus	Oxygen	Carbon
[°C]	[atom-%]	[atom-%]	[atom-%]	[atom-%]
25	12 $\pm$ 1	16 $\pm$ 2	56 $\pm$ 4	16 $\pm$ 6
75	11 $\pm$ 1	15 $\pm$ 1	53 $\pm$ 1	22 $\pm$ 1

Further information about the chemical composition and the distribution of the elements across the coating cross thickness was provided by GD-OES depth profiles of a coating produced at 25 °C.

The depth profile presented in Fig. 7.5 shows that phosphorus is not only adsorbed at the surface of the coating but distributed over the whole coating cross-section. The peaks in the phosphorus signal at the surface and at the interface between oxide and metal are most probably artefacts. At the surface (i. e., at the beginning of the sputter process) the plasma may still be unstable. Another even more important factor is the influence of hydrogen. Hydrogen present in hydrocarbon contamination on the surface influences the light emission of many elements [180] in different ways. The phosphorus signal is amplified by hydrogen. At the interface between the APC layer and metal substrate the peak in the phosphorus signal could arise from a changing sputter rate (change of plasma conditions due the change from oxide to metal) or from an increased interfacial hydrogen content.

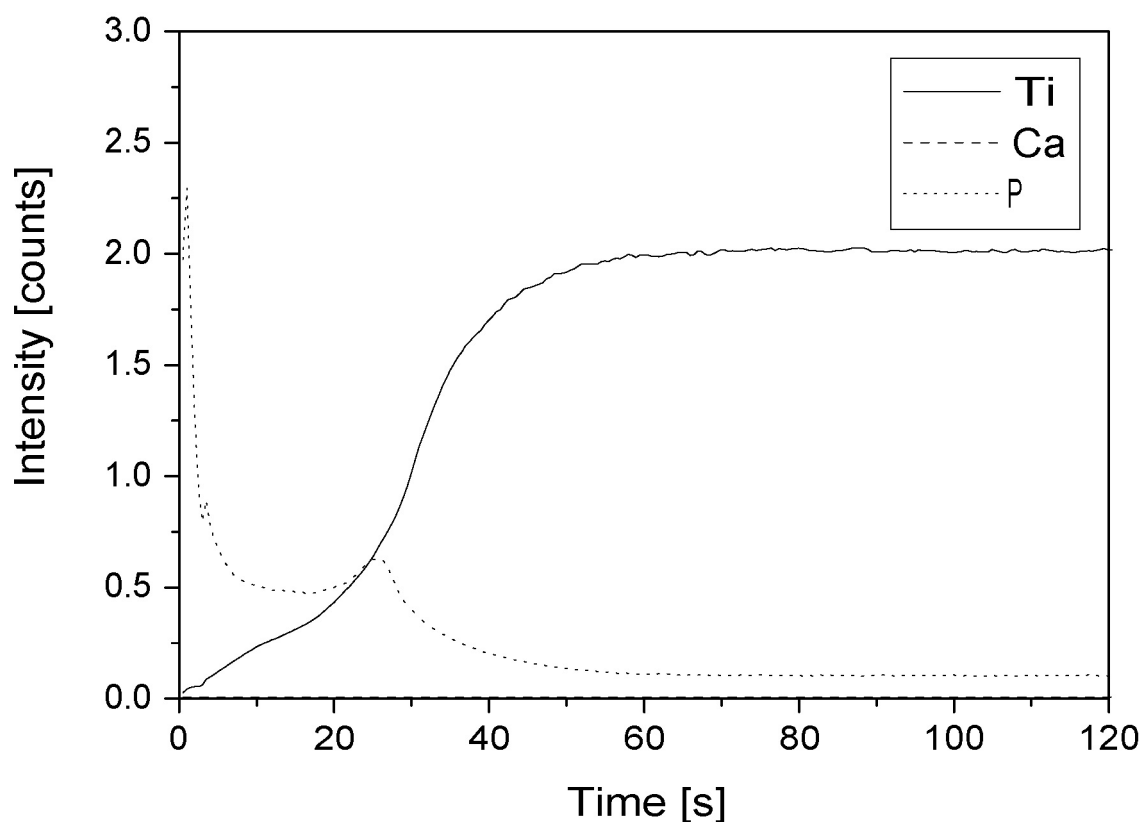


**Fig. 7.5.** Chemical depth profile recorded by GD-OES of an APC coated sample produced in 0.01 M orthophosphoric acid at 25 °C. The profile starts at the surface of the sample (0 s), the interface between oxide and metal corresponds to about 30 s, where the titanium signal increases steeply. The intensities of the elements are purely qualitative and do not reflect the actual concentrations. The element phosphorus is distributed over the whole coating thickness. The distinct phosphorus peak at the very beginning is most probably an artefact produced by interference with hydrogen atoms or by the feedback-loop of the instrument, while the broad peak near the interface could be due to changes in the sputtering rate (changing from oxide to metal).

The XPS results indicate no change in chemical composition of the outermost few nanometers of the coating if the electrolyte temperature is changed from 25 °C to 75 °C. The integral composition, however, shows a higher phosphorus content for coatings produced at the higher electrolyte temperature. It is known that phosphate adsorbs fast and irreversibly to titanium oxide surfaces [181,182]. Thus, the chemical composition of the outermost surface (measured by XPS) may be dominated by adsorbed phosphate species. By measuring the integral content, the influence of the surface is eliminated because of the much higher volume that is analyzed. Both results provide

relevant information, since the surface-near composition is of significance right after the implantation of a device into the biological environment, while the integral composition becomes more important on a larger time scale.

**Crystal structure.** The crystal phases present in the APC coating produced in phosphoric acid were determined by Raman spectroscopy. The aim of using diluted phosphoric acid as an electrolyte was to achieve a highly crystalline titania coating without calcium phosphate phases. Fig. 7.6 shows spectra of the two different coatings used for the cell culture tests. On both surfaces only titanium dioxide (anatase) was found. The identification of the bands was based on published reference spectra of titanium dioxide layers [183] and of bulk anatase [170]. Even though point measurements on many different locations of the sample surface were performed, no phosphate bands were found on the surfaces coated in phosphoric acid. Even though the presence of phosphorus could be confirmed by the measurements of the chemical composition, the accumulations of phosphorus in the coating seem to be too low (or not crystalline enough) for the observation of distinct sharp bands in the Raman spectra.



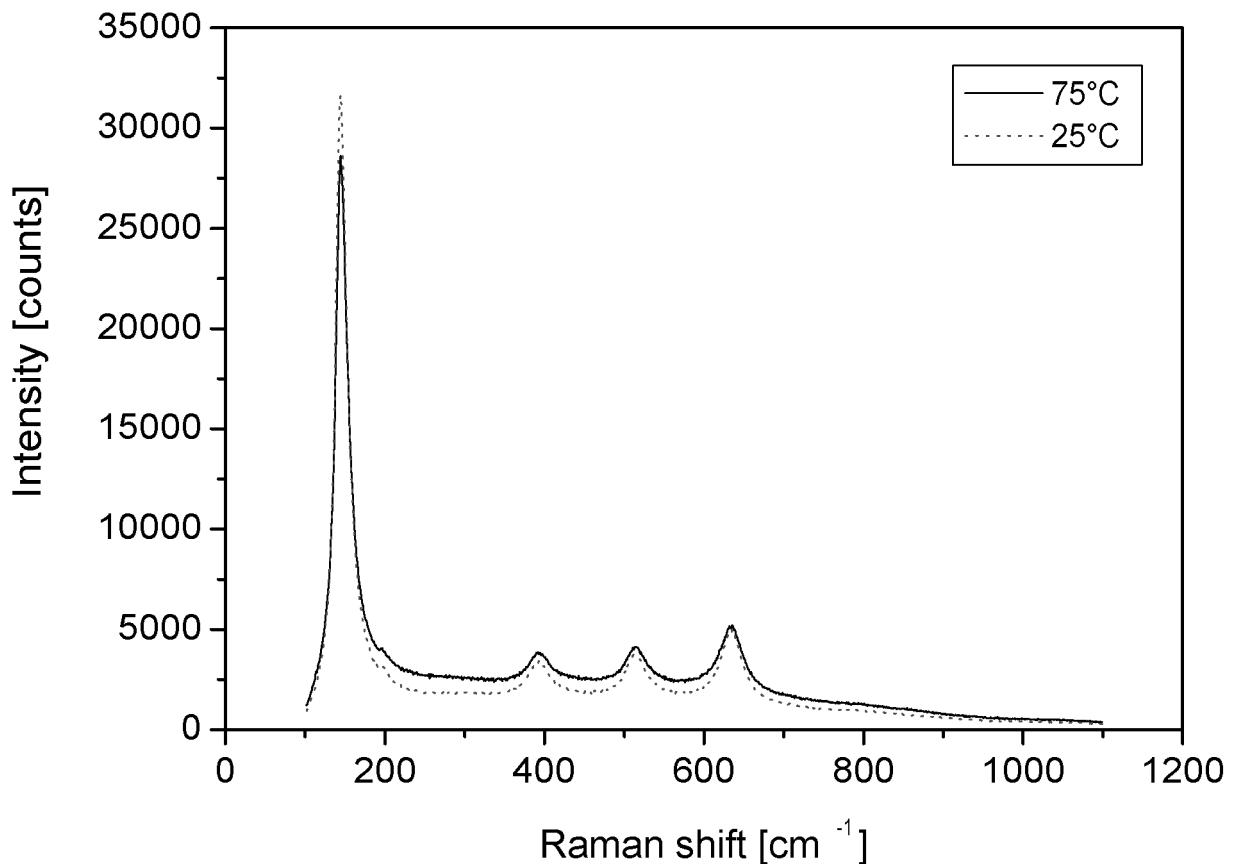


**Fig. 7.6.** Raman spectra of APC coatings produced in 0.01 M phosphoric acid at 25 °C and 75 °C respectively. The only crystalline phase found on these APC coatings was anatase with peaks at 144, 197, 400, 519, and 640  $\text{cm}^{-1}$  [170,183].

**Surface morphology.** The importance of surface topography with respect to the biological performance of an implant surface has been reported by several authors (refer to Section 2.2.3) [61,75]. The surface topography has been investigated qualitatively by SEM and quantitatively by laser profilometry (LPM). In addition, the thickness of the coating produced at 25 °C was determined by cross sectioning and subsequent measurement of the coating thickness by light microscopy (average value of ten measurements on two identically coated samples).

A comparison of the two different surfaces is shown in Fig. 7.7. The sample coated at 75 °C exhibits coarser surface structures in comparison to the that coated at 25 °C. This is in good agreement with the tendencies found in the parameter screening series. The roughness values have been determined on the sample coated at 25 °C; Table 7.6 presents the results. However, these values do not represent

the coating structures shown in the SEM images, since the laser profilometer does not resolve features with a lateral size below 1.5  $\mu\text{m}$  [61]. The thickness of the APC coating produced in 0.01 M at 25  $^{\circ}\text{C}$  was determined to be  $2.4 \pm 0.3 \mu\text{m}$ .

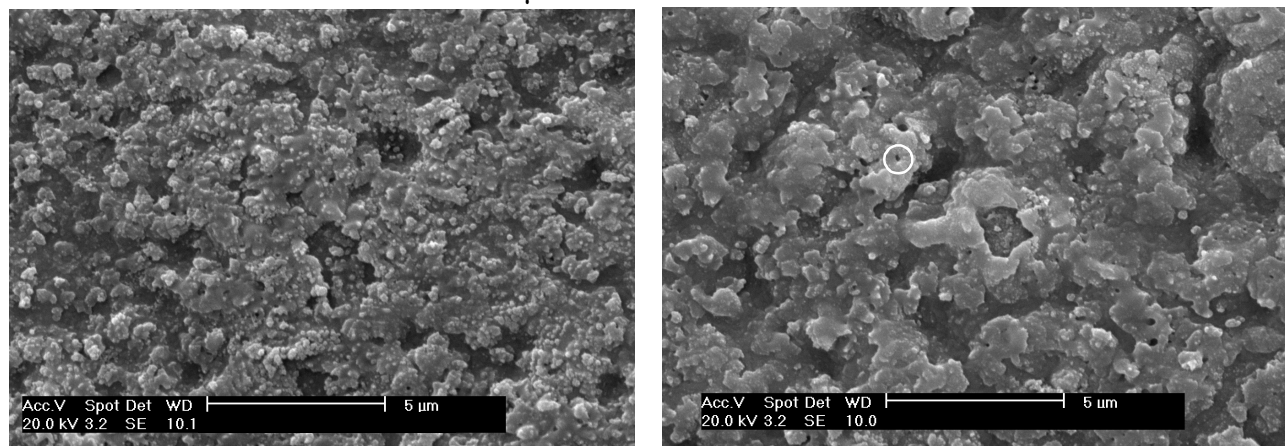


**Fig. 7.7.** SEM Micrographs of coatings produced in 0.01 M orthophosphoric acid at 25  $^{\circ}\text{C}$  (left) and 75  $^{\circ}\text{C}$  (right) electrolyte temperature. As predicted in Section 7.1, the surface topography contains coarser structures if coated at higher temperature. Since the concentration of the electrolyte is low, the typical pores arising from evaporating electrolyte become very small (circle).

**TABLE 7.6.** Roughness parameters of a coating prepared in 0.01 M orthophosphoric acid at 25  $^{\circ}\text{C}$ . The values were obtained using an UBM laser profilometer and are average values and standard deviation of 4 measurements on one sample.

	$R_a$	$R_q$	$R_{zDIN}$	$R_t$	$S_m$	$L_r$	$S_k$
	[ $\mu\text{m}$ ]	[ $\mu\text{m}$ ]	[ $\mu\text{m}$ ]	[ $\mu\text{m}$ ]	[mm]		
Average	0.65	0.83	5.51	6.80	0.02	1.19	-0.10
Std. deviation	0.01	0.01	0.26	0.82	0	0.01	0.1

### 7.3 Calcium Dihydrogen Phosphate as an Electrolyte

#### 7.3.1 Experimental

Cleaned CP titanium disk-shaped samples 7 mm in diameter and 1 mm thick were coated in solutions of calcium orthophosphate ( $\text{Ca}(\text{H}_2\text{PO}_4)_2$ )<sup>1</sup> of varying concentrations and temperatures ranging from 25 to 75 °C. The current was kept constant at 150 mA, while the coating process duration was varied between 30 and 90 s. A detailed list with all the process parameters is shown in Table 7.7. The maximum concentration used was 0.07 M, corresponding to the solubility limit [184]

**TABLE 7.7.** Parameter matrix for the APC coatings produced in calcium orthophosphate. ●: used parameter set. The current was kept constant at 150 mA. At 0.07 M  $\text{Ca}(\text{H}_2\text{PO}_4)_2$  the maximum solubility in water is reached.

Concentration of $\text{Ca}(\text{H}_2\text{PO}_4)_2$	Temperature (Duration)					
	25 °C	35 °C	45 °C	55 °C	65 °C	75 °C
0.0125 M	●(90s)	●(90s)	●(90s)	●(90s)	●(90s)	●(90s)
0.025 M	●(45s)		●(45s)		●(45s)	
0.05 M	●(30s)	●(30s)	●(30s)	●(30s)	●(30s)	●(30s)
0.07 M	●(30s)		●(30s)		●(30s)	

The coating parameters were controlled manually. The temperature was measured before every experiment with a mercury thermometer. The duration was monitored with a stop watch and the process was stopped after the period shown in Table 7.1. Voltages documented in the results part were directly read off the power supply.

#### 7.3.2 Results

**General.** The range of concentrations used for the APC parameter screening was constrained by the limited solubility of  $\text{Ca}(\text{H}_2\text{PO}_4)_2$  in water. No problem with the APC process arose due to depassivation or dominating side-reactions up to the solubility limit of 0.07 M  $\text{Ca}(\text{H}_2\text{PO}_4)_2$ . As for phosphoric acid as the electrolyte, the voltages at which the first sparks become visible decrease with increasing electrolyte concentration (see Table 7.8). As shown in Fig. 7.8, the logarithmic relation

1. orthophosphate is used here as short version of 'primary phosphate of the orthophosphoric acid'.

observed for the phosphoric acid system is also observed for the calcium orthophosphate electrolyte system.

**TABLE 7.8.** Comparison between the coating parameters and occurrence of the first sparks (voltage and time) as well as the final voltage. The values for the last three columns are averages of at least five coating experiments. The error is around 5 V for the voltages and about 1 s for the time to first sparks.

Concentration of $\text{Ca}(\text{H}_2\text{PO}_4)_2$	Temperature	Current	Duration	First sparks	Time to first sparks	Final voltage
[M]	[°C]	[mA]	[s]	[V]	[s]	[V]
0.0125	25	150	90	320	11	423
0.025	25	150	45	300	10	420
0.05	25	150	30	270	8	420
0.071	25	150	30	265	7	397
0.0125	35	150	90	325	13	435
0.05	35	150	30	280	9	425
0.0125	45	150	90	337	15	447
0.025	45	150	45	304	12	432
0.05	45	150	30	280	9	420
0.071	45	150	30	265	7	395
0.0125	55	150	90	325	13	450
0.05	55	150	30	285	9	425
0.0125	65	150	90	332	13	455
0.025	65	150	45	315	13	443
0.05	65	150	30	285	9	425
0.071	65	150	30	272	7	398
0.0125	75	150	90	350	16	457
0.05	75	150	30	285	9	428

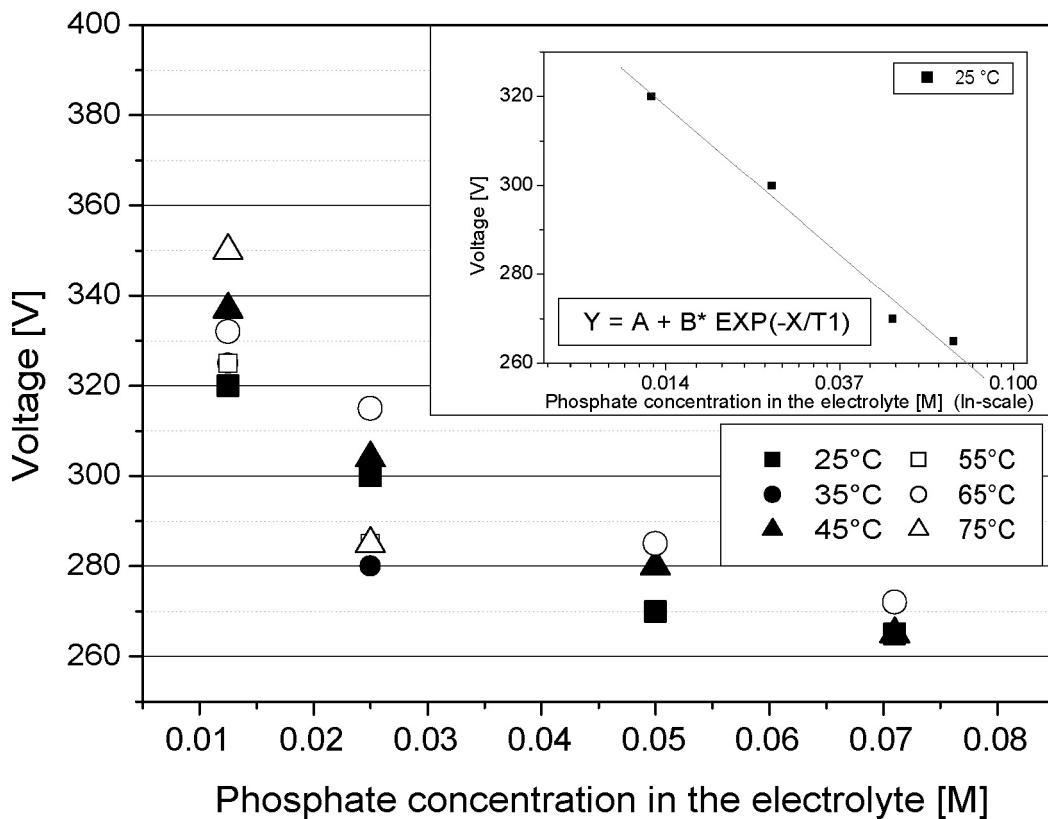


**Fig. 7.8.** Dependence of the voltage, at which the first sparks were observed on electrolyte concentration and temperature. The inset graph shows a curve fit for the voltages measured at 25 °C. The predicted relation (Equation 3.12) for the breakdown voltage is found to hold for the voltage at which the first sparks become visible as well.

**Chemical Composition.** The chemical composition of the APC coatings produced in the calcium orthophosphate electrolyte was determined semi-quantitatively by XPS. The detailed chemical compositions are listed in Table 7.9. Fig. 7.9 and Fig. 7.10 show the calcium-to-phosphorus ratio and the phosphorus-to-titanium ratio, respectively versus the phosphate concentration in the electrolyte solution. The ratio between calcium and phosphorus in the electrolyte solution was at a fixed value of 0.5. It is found that both the Ca/P-ratio and the P/Ti-ratio in the coatings are increasing with increasing electrolyte concentration. The increase in P/Ti-ratio has been expected (refer to Section 7.1) from the experiments with phosphoric acid, while the increase in Ca/P-ratio is

unexpected. However, even at the solubility limit the Ca/P-ratio is lower in the coating than in the electrolyte solution. A correlation of temperature and chemical composition in the APC coating could not be established. The tendency is for higher temperatures to result in higher Ca/P-ratios, but the variations among the identically coated samples are too large for a distinct statement.

**TABLE 7.9.** Chemical composition of coatings produced in calcium orthophosphate solutions of different concentrations and temperatures. The values are single point XPS measurements. Where a standard deviation is shown, the values are averages from three single point measurements  $\pm$  standard deviations on three samples coated under identical conditions.

Electrolyte concentration	Electrolyte temperature	Process duration	Titanium	Phosphorus	Calcium	Oxygen	Carbon	Nitrogen
[M]	[°C]	[s]	[atom-%]	[atom-%]	[atom-%]	[atom-%]	[atom-%]	[atom-%]
0.0125	25	90	12	17	2	63	5	1
0.0125	35	90	11	16	3	60	9	1
0.0125	45	90	11	16	3	58	10	2
0.0125	55	90	11	16	3	58	11	-
0.0125	65	90	11	16	3	60	10	-
0.0125	75	90	11	17	3	61	7	1
0.025	25	45	10	16	4	58	12	-
0.025	45	45	10	19	5	61	5	-
0.025	65	45	10	18	5	61	7	-
0.05	25	30	9 $\pm$ 1	18 $\pm$ 1	4 $\pm$ 0	58 $\pm$ 3	10 $\pm$ 4	1
0.05	35	30	7	16	3	48	24	2
0.05	45	30	8	19	4	59	8	1
0.05	55	30	8 $\pm$ 0	18 $\pm$ 2	5 $\pm$ 0	57 $\pm$ 4	12 $\pm$ 6	1
0.05	65	30	9	19	5	60	6	1
0.05	75	30	8 $\pm$ 0	20 $\pm$ 0	6 $\pm$ 0	61 $\pm$ 0	5 $\pm$ 0	-
0.071	25	30	8	20	6	60	6	-
0.071	45	30	7	20	7	59	6	-
0.071	65	30	8	20	6	59	6	-

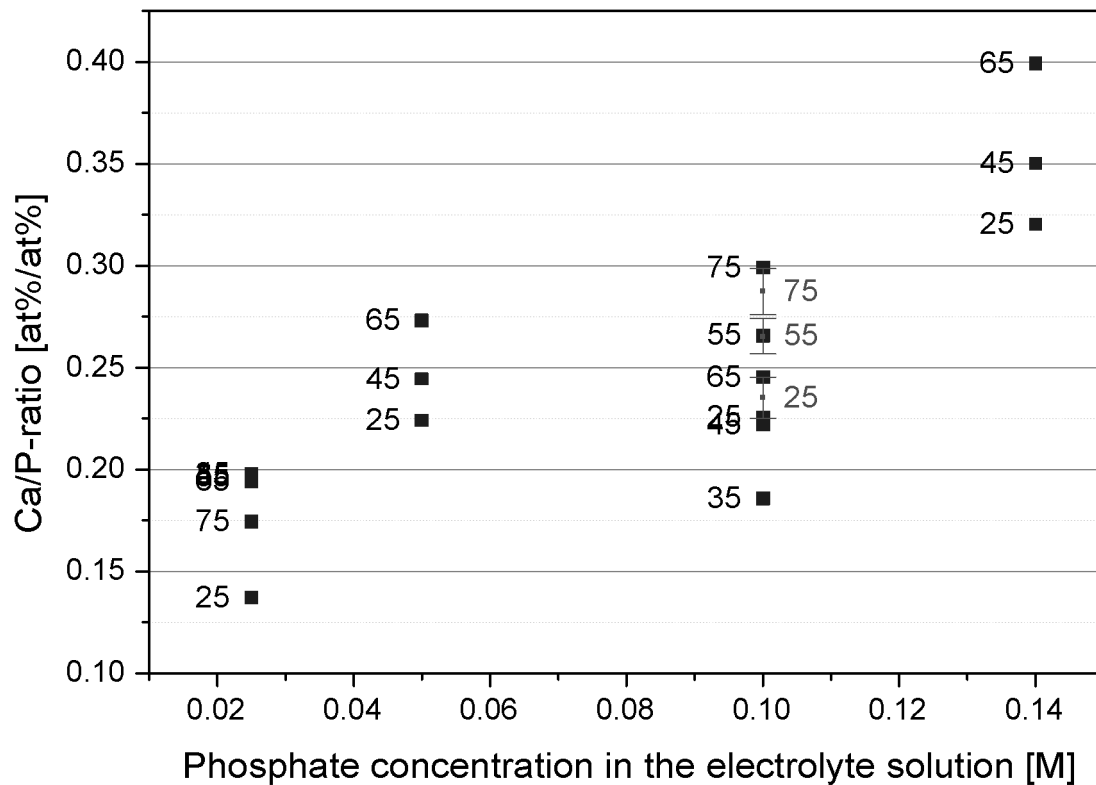


**Fig. 7.9.** Calcium-to-phosphorus ratio of coatings produced in  $\text{Ca}(\text{H}_2\text{PO}_4)_2$  at different concentrations and different temperatures (label next to data points) measured with XPS. The squares are single point measurements, while the dots with error bars are averages of three measurement performed on three samples coated with the same parameters. The x-axis shows the phosphate concentration in solution, which corresponds to twice the calcium concentration, in order to make the graphs comparable to Section 7.1.2.

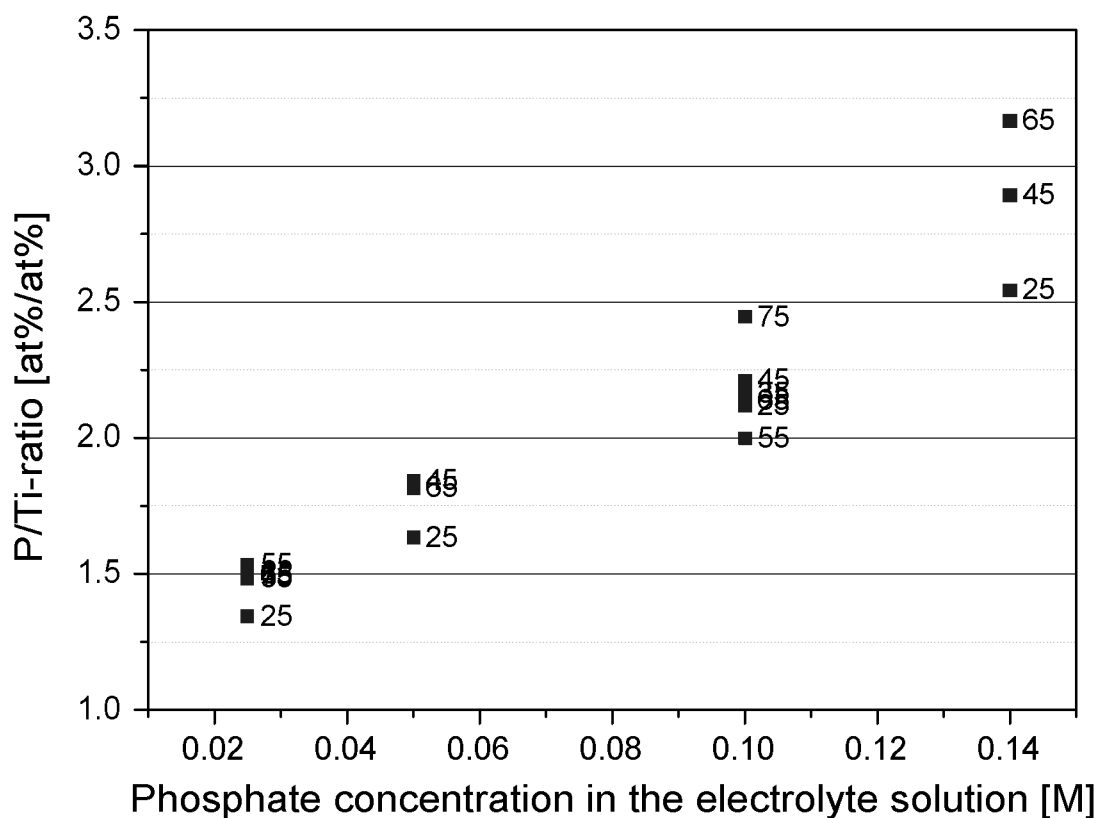


**Fig. 7.10.** Phosphorus-to-titanium ratio of coatings produced in  $\text{Ca}(\text{H}_2\text{PO}_4)_2$  in different concentrations and at different temperatures (label next to data points) measured with XPS. The data points are single measurements. The x-axis shows the phosphate concentration in solution, which is twice the calcium concentration in order to make the graphs comparable to Section 7.1.2.

**Surface Morphology.** One of the interesting results from Section 7.1 is that the structure of the surface becomes coarser as the electrolyte concentration is increased. The same trend is found for  $\text{Ca}(\text{H}_2\text{PO}_4)_2$  as electrolyte when varying the electrolyte concentration. Fig. 7.11 shows surfaces coated at three different concentrations of  $\text{Ca}(\text{H}_2\text{PO}_4)_2$ , namely 0.025, 0.05 and 0.07 M. The difference between 0.025 and 0.05 M is evident. If coated in 0.025 M  $\text{Ca}(\text{H}_2\text{PO}_4)_2$ , the coating has a very fine structure compared to coatings prepared in 0.05 and 0.07 M  $\text{Ca}(\text{H}_2\text{PO}_4)_2$ . No difference can be found between the two coatings prepared at higher concentrations, since the difference in concentration is rather small (in contrast to the wide range of concentrations used for phosphoric acid).



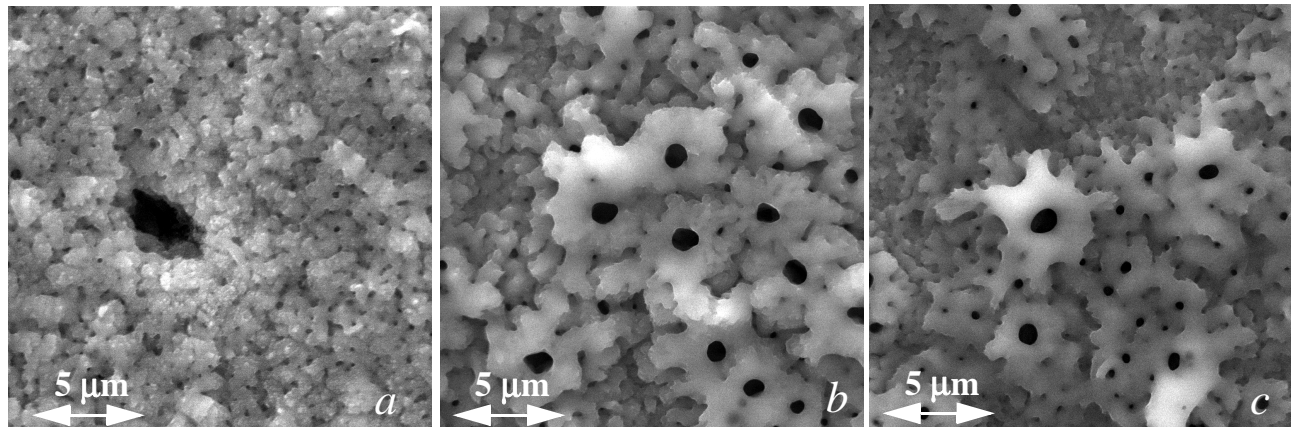


**Fig. 7.11.** SEM Micrographs of APC coatings prepared in different concentrations of calcium orthophosphate at 25 °C. a: 0.025 M; b: 0.05 M; c: 0.07 M. From low to high concentration of calcium orthophosphate the surface structures get coarser.

Furthermore, a dependence of surface morphology on electrolyte temperature during the coating procedure, could not be found in the calcium orthophosphate system (Fig. 7.12). The coating structures, i. e., the APC structures, have the same size. The qualitative impression of the surface roughness is the same.

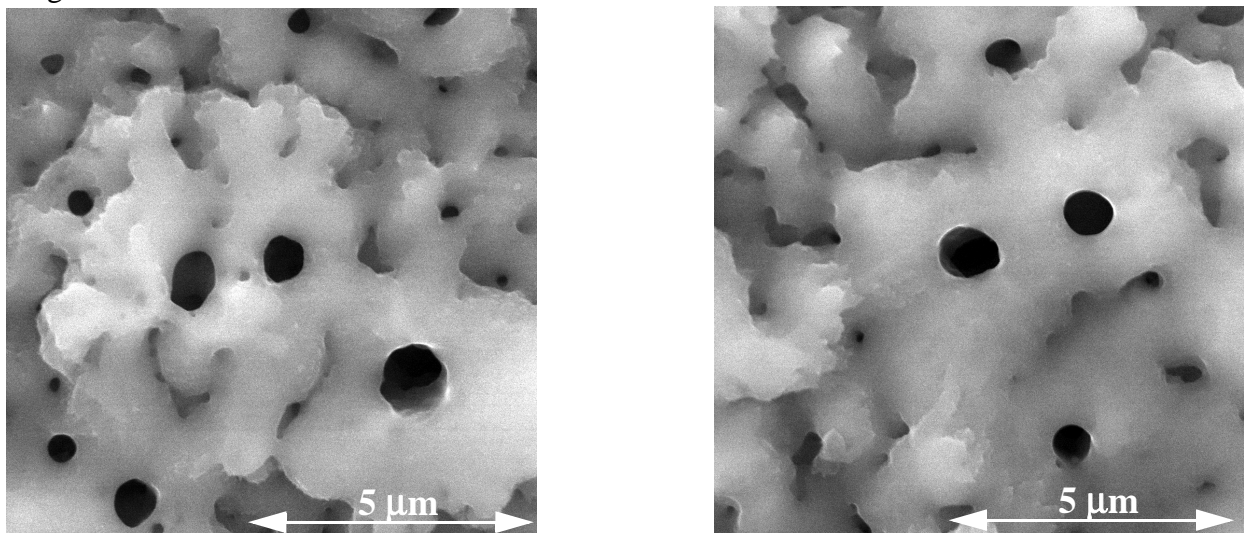


**Fig. 7.12.** SEM Micrographs coated in 0.05 M calcium orthophosphate at 25 °C (left) and 65 °C (right). No distinct difference can be found for the morphologies of the two surfaces.

**Additional characterization.** Additional characterization was carried out on samples with larger geometrical dimensions (same as in Section 7.2). The integral composition, a chemical depth profile,

and the coating thickness were determined for samples coated in 0.07 M calcium orthophosphate for 30 s at 25 °C and 290 mA. The methods and settings used for the characterization were the same as described in Section 7.2.

The integral composition was determined by chemical digestion of the oxide layer in a salt melt and subsequent optical emission spectroscopic analysis of the resulting solution. The total amount of calcium incorporated in the coating is  $0.04 \mu\text{g}/\text{mm}^2$  and the total amount of phosphorus  $0.63 \mu\text{g}/\text{mm}^2$ . This results in a Ca/P-ratio of 0.05 atom-%/atom-% for the entire coating. The chemical depth profile is shown in Fig. 7.13.

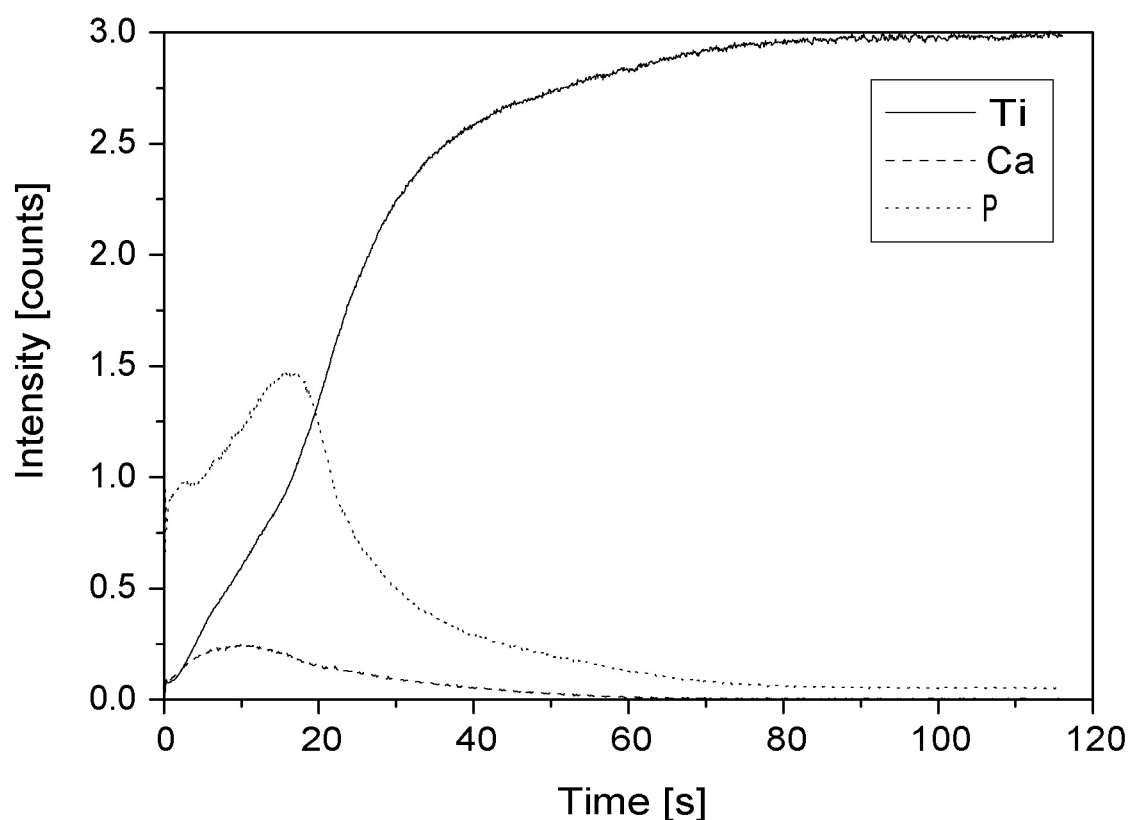


**Fig. 7.13.** Chemical depth profile (recorded by GD-OES) of an APC coated sample that was produced in 0.07 M calcium orthophosphate at 25 °C. The surface of the coating is at 0 s while the interface between APC layer and substrate metal can be found at about 30 s. Most interestingly, the phosphorus signal is much higher at the inner part of the layer.

While the chemical depth profile for the coating produced in phosphoric acid (see Fig. 7.5) had a constant signal intensity in the range between coating surface and interface substrate/coating, the phosphorus signal for the coating prepared in calcium phosphate shows a pronounced maximum inside the APC layer. This maximum could indicate that the concentration of phosphorus inside the layer is higher than at the surface or the interface and thus explains the difference of the Ca/P-ratio between surface and integral chemical composition. The calcium signal is weak throughout the APC layer, but the distribution of calcium is over the whole coating cross-section. The coating thickness was determined on cross-sections of two samples and turned out to be  $3.0 \pm 0.8 \mu\text{m}$ . The crystalline structure of coatings produced in a calcium phosphate electrolyte was investigated during the authors diploma thesis and is not shown in here [185]. The only phase found on the investigated APC films was anatase.

### **7.3.3 Conclusions**

Calcium orthophosphate has been investigated as an electrolyte for the APC process. The influence of the electrolyte concentration and the electrolyte temperature on the resulting coating composition and morphology was determined by XPS and SEM. Additionally, the integral composition was investigated with wet chemical analysis (ICP-OES), the distribution of elements with GD-OES, and the coating thickness by metallographic techniques on a coating produced in 0.07 M calcium orthophosphate. The following conclusions are drawn from the results:

- With increasing electrolyte concentration, the content of calcium and phosphorus in the coating increases. The increase of calcium content is bigger than the that of the phosphorus content since the Ca/P-ratio rises as well.
- The lower the electrolyte concentration, the finer the surface morphology.
- No influence of electrolyte temperature on the chemical composition of the coating and the coating topography could be found.
- The voltage at which sparks become visible increases with decreasing electrolyte concentration.

---

#### *7.4 Discussion of the Standard Electrolytes*

Phosphoric acid was used as a simple electrolyte system in order to investigate the influence of electrolyte concentration and electrolyte temperature on the anodic plasma-chemical surface modification process. In a second step, a calcium containing electrolyte (i. e.,  $\text{Ca}(\text{H}_2\text{PO}_4)_2$ ) was investigated in the same manner as the phosphoric acid system.

The main influence on the breakdown voltage of the anodic oxide film seems to originate from the electrolyte concentration. During the APC experiments, the voltage at which first sparks occur (as an indicator for breakdown) was monitored. For both electrolyte systems, this voltage was found to depend on the electrolyte concentration through a logarithmic relation as predicted by Albella and coworkers [148]. On the other hand, the influence of the electrolyte solution temperature was comparatively weak. As a tendency, the values of the breakdown voltage increased with increasing electrolyte temperature.

The chemical composition near the surface of the APC coatings was found to mainly depend on the concentration of the electrolyte. For both, phosphoric acid and calcium orthophosphate, the amount of phosphorus incorporated becomes larger at the higher electrolyte concentrations. The same is true for calcium in case of the calcium phosphate electrolyte.

For APC coatings produced in calcium orthophosphate, the comparison between the integral and the surface-near chemical composition of the coatings is very interesting. In the case of the Ca/P-ratio, the results demonstrate an important difference between the bulk and the surface composition. The bulk ratio (via chemical digestion) turned out to be 0.05, the XPS surface ratio approx. 0.33. The reason for this difference can be found in the distribution of calcium and phosphorus across the coating thickness (GD-OES depth profile) with phosphorus accumulated near the interface between APC layer and substrate and calcium showing a maximum in the signal near surface of the coating. Therefore, the Ca/P-ratio at the surface is higher in comparison with the average ratio for the bulk coating. Interestingly enough, the depth profile obtained on a coating produced in phosphoric acid showed a rather flat distribution (except for the surface and interface between oxide and substrate, see Section 7.2.2).

The only crystal phase found by Raman spectroscopy was anatase (a modification of  $\text{TiO}_2$ ). In the literature, rutile was reported to be present in thick anodic oxide films [126]. The measured thickness of the APC layers is more than 2  $\mu\text{m}$ . Nevertheless, no rutile was found in the APC coatings. The difference in crystal structure must be due to the different genesis of titania in APC layers and in classical anodic oxide films. The anodic oxide is growing slowly out of the metal substrate, while the titania in APC is temporarily fused and subsequently quenched to electrolyte temperature within milliseconds. The fast cooling hinders the proper crystallization and the formation of the thermodynamically stable rutile phase. Crystallization ends at the stage of the more loosely packed anatase phase, the metastable phase between the amorphous state and the stable rutile phase [169]. Pure anatase transforms irreversibly into rutile at temperatures above 500 °C [186]. Impurities in the anatase lattice influence the transformation to rutile. If the impurities are of lower oxidation state than  $\text{Ti}^{4+}$ , the oxygen vacancy concentration increases, making the transformation easier. The opposite happens if the impurities are of higher oxidation state than 4. During the APC process electrolyte constituents are incorporated in the oxide film. If  $\text{P}^{5+}$ -ions are incorporated in the anatase lattice, the concentration of oxygen vacancies in the lattice is reduced, which hinders the transformation from anatase to rutile [187]. This suggests that anatase remains the stable crystal phase even at extended heat impacts, e.g. during dielectric breakdown events in the proximity.

Surface topography is one of the key features for a successful integration of implants in contact with bone. The surface topography of surfaces coated by the APC process in phosphoric acid and calcium orthophosphate has been investigated qualitatively with SEM. Problems arise when trying to quantify the surface roughness. Laser profilometry has a resolution limit of 1.5  $\mu\text{m}$  [61]. Since the typical structures of the coating are in the size range close to the resolution limit of the laser profilometer, the surface roughness can only be described inadequately. The second method evaluated for the APC coatings was stereo-SEM, which is described in detail by Wieland [61]. Stereo-SEM also yielded unsatisfactory results. APC structures have smooth structures and rounded edges due to the temporary fusing of the oxide. SEM images therefore generally lack contrast, preventing the complete correlation between left and right hand images by the computer software. However, just recently new approaches have been found ([www.alicon.com](http://www.alicon.com)), where the surfaces are described as a set of mathematical functions.

The electrolyte concentration has a strong influence on the surface topography of the resulting APC coating. As the electrolyte concentration is increased the topography becomes coarser suggesting that more energy is contained in a single breakdown event. Suppose, that the energy,  $W$ , contained in one breakdown event is expressed as

$$W = V \cdot I \cdot t \quad (\text{EQ. 7.1})$$

where  $V$  is the breakdown voltage,  $I$  the electronic current at the breakdown location causing Joule heating, and  $t$  the duration of the breakdown event. The breakdown voltage decreases as the electrolyte concentration increases. The electronic current in the anodic oxide depends on the incorporation rate of impurity centers (Equation 3.6). The incorporation rate of anions out of the electrolyte into the anodic oxide is likely to increase with increasing electrolyte concentration, because the decrease in breakdown voltage has to be more than compensated by the current,  $I$ , if the energy contained in a breakdown increases (assuming identical duration). An increased incorporation rate suggests higher levels of electrolyte constituents in the anodic oxide film. This *in situ* stage, however, cannot be examined by the methods used to determine the chemical composition of the APC films since the chemical composition of the films was always determined after a completed breakdown, thus after fusing and re-solidification of the oxide. It would be necessary to determine the chemical composition just before the breakdown event as well.

With regard to the use as electrolyte for bioactive implant surfaces, APC coatings produced in calcium orthophosphate are not too promising. They contain only small amounts of calcium and the Ca/P-ratio is very low, much lower than e. g. in hydroxyapatite (1.7) or tricalcium phosphate (1.5). New electrolyte systems will have to be developed in order to overcome the low solubility of calcium in aqueous solutions and the low amount of calcium incorporated into the APC layer.

---

# *Development of a New Electrolyte System for Titanium Implant Surfaces*

---

---

## *8.1 Approach*

The aim of this thesis was to develop a titanium dioxide coating containing calcium phosphate phases. These phases should at least partly be soluble in order to supply the healing bone tissue with calcium and phosphate immediately after implantation in the host tissue. The well-known calcium orthophosphate electrolyte system [140] only allows the incorporation of minor calcium amounts, as was shown in Section 7.3. Two reasons were assumed to be responsible for the low amount of calcium incorporated into the APC layer:

1. The low solubility of calcium in aqueous solutions.
2. The positive charge of the calcium anion, which hinders the incorporation into a positively polarized oxide layer due to electrostatic repulsion.

About 18 g/l  $\text{Ca}(\text{H}_2\text{PO}_4)_2$  can be dissolved in pure water [184]. Many other commercially available calcium salts were tested for possible use as electrolyte in the APC process<sup>1</sup>. The only successful alternative to  $\text{Ca}(\text{H}_2\text{PO}_4)_2$  is calcium acetate,  $\text{Ca}(\text{OOCCH}_3)_2$ , which has a solubility of 347 g/l [184]. Calcium acetate, however, is very well known as an electrolyte for the APC process [136] and,

---

1. The following calcium containing compounds were tested in this work as possible electrolytes for the APC process leading to active dissolution of the metal substrate during the anodization: calcium formiate, lactate, nitrate, oxalate, and cyanamid. Calcium carbonate, citrate, and hydroxide were found to be insoluble, while oxidation of electrolyte constituents during the anodization process took place for calcium iodide and oxide. In the case of the iodide, iodine crystals formed on the anode. In the case of calcium oxide calcium hydroxide precipitated out of the electrolyte solution.

additionally, as soon as phosphates are added to the electrolyte solution, the solubility is again determined by the phosphate group.

In order to increase the solubility of calcium in phosphate solutions, the calcium ion has to be camouflaged against the phosphate anion. This can be achieved by adding a chelating agent to the electrolyte solution that binds to the calcium ion. In this thesis, ethylene diamine tetracetic acid (EDTA) was used as chelating agent. The four acetic acid groups and the two amino groups of EDTA offer potential binding sites for forming a chelate. These binding sites are folded around the calcium cation. The ratio between EDTA and calcium for the chelate is 1. In practice, the chelation works very well, even though EDTA has to be added in a slight surplus in comparison to calcium.

Due to its positive charge the calcium cation is repelled rather than attracted by the positively charged anode. Once the calcium has been chelated by EDTA, the overall charge of the chelate (per calcium cation) in a neutral environment changes from double positive to neutral or slightly negative. If the pH of the solution is increased beyond the point where the last dissociation of EDTA has taken place ( $\gg 10.3$ ), the overall charge of the chelate will become -2. Therefore, a maximum amount of calcium incorporated into the APC layer would be expected at high pH.

A limited series of feasibility experiments was carried out in order to test the above hypothesis. As the base component of the electrolyte  $\text{Ca}(\text{H}_2\text{PO}_4)_2$  was used. Calcium acetate was used to increase the Ca/P-ratio in the solution from 0.5 to the desired value. In order to keep the calcium in solution,  $\text{EDTA}\cdot\text{Na}_2$  was added in slight excess to the calcium concentration. Finally, the pH of the electrolyte solution was varied with sodium hydroxide. Table 8.1 shows XPS results of coatings produced in electrolyte solutions with identical composition but different pH. The phosphorus concentration in the APC coating was not affected by the change in pH. The absolute concentration of phosphorus was around 13 atom-%.

**TABLE 8.1.** Influence of the pH in the electrolyte solution on the Ca/P-ratio in the APC coating. The chemical composition of the APC coating was determined using XPS. The level of incorporated phosphorus was constant. The ratios are given as atom-%/atom-%.

pH	6	11	14
Ca/P-ratio	0.6	0.9	1.3



As predicted, the level of incorporated calcium increases significantly with increasing pH in the electrolyte solution. Secondly, it was found that the calcium level at all pH-values is higher if compared to APC coatings prepared in the calcium orthophosphate electrolyte.

However, the found Ca/P-ratio of 1.3 at pH 14 is still below the desired ratio of about 1.7 (as for hydroxyapatite). An extensive parameter screening was performed in order to find out whether the amount of calcium incorporated into the coating and the Ca/P-ratio could be influenced by the process duration, the applied current, and the electrolyte temperature. For the parameter screening, the electrolyte composition was kept constant. Since the highest ratios were achieved at pH 14, it was kept constant at this value.

The newly developed electrolyte system is named electrolyte system for osteointegrative coatings (ESOC) according to its intended medical application.

## 8.2 Parameter Screening on the New Electrolyte System (ESOC)

### 8.2.1 Experimental

Cleaned CP titanium disk-shaped samples with a diameter of 7 mm and 1 mm thick were coated in ESOC (pH 14) at varying durations, current densities and temperatures. A detailed list with all the coating parameters is presented in Table 8.2. The composition of the electrolyte solution is shown in Table 8.3.

**TABLE 8.2.** Parameter matrix for parameter screening using the ESOC. Coatings were produced at 25 and 45 °C. At 45 °C the duration was 65 s instead of 60 s at 80 mA current.

Current	Process Duration			
	45 s	60 s	90 s	120 s
80 mA		●	●	●
150 mA	●	●	●	

The coating procedure was carried out manually without computer control. The temperature was monitored before and after each coating experiment with a mercury thermometer. A stop watch was

used for monitoring the process duration. After the periods shown in Table 8.2, the process was stopped by setting the applied voltage to zero.

**TABLE 8.3.** Composition of the ESOC (pH 14). The chemicals were dissolved in u. p. water (18.3 M $\Omega$ /cm).

Concentration	Compound
0.025 M	Ca(H <sub>2</sub> PO <sub>4</sub> ) <sub>2</sub>
0.075 M	Ca(OOCCH <sub>3</sub> ) <sub>2</sub>
0.12 M	EDTA·Na <sub>2</sub>
0.9 M	NaOH

### 8.2.2 Results

**General.** APC coatings were produced in ESOC at different current densities, temperatures, and for different durations. At the higher temperature of 45 °C, oxygen evolution became more prominent than at 25 °C. Therefore, no experiments at temperatures higher than 45 °C were carried out. Just recently, Müller has investigated the influence of temperature on APC coatings produced in ESOC more thoroughly in his diploma thesis [166]. As shown in Table 8.4, the voltage at which the first sparks became visible was not really affected by a change in electrolyte temperature. The time span up to the first-sparks-point depended on the temperature of the electrolyte and the current applied to the sample. With increasing temperature or decreasing current, the time span increased from 12 to approximately 50 s. The effect of temperature can be explained by the increasing amount of current consumed by side reactions such as oxygen evolution. Therefore, the anodization efficiency is reduced and the time span needed to reach the breakdown voltage increases. With increasing current per sample, the anodization velocity is increased and thus the time span to the breakdown voltage is reduced.

**TABLE 8.4.** Comparison between coating parameters and occurrence of first sparks (time and voltage) as well as the final voltage. The error in the voltages is about  $\pm 3$  V. Electrolyte: ESOC (pH 14)

Temperature	Current	Duration	First sparks	Time to first sparks	Final voltage
[°C]	[mA]	[s]	[V]	[s]	[V]
25	80	60	115	28	160
25	80	90	115	34	167
25	80	120	115	28	197
25	150	45	115	12	178
25	150	60	112	12	192
25	150	90	115	12	200
45	80	65	114	38	135
45	80	90	115	42	158
45	80	120	115	50	168
45	150	45	116	16	150
45	150	60	116	20	164
45	150	90	115	20	187

**Chemical Composition.** XPS was used to determine the chemical composition of the coatings near the surface. The absolute concentration values are presented in Table 8.5. Titanium, oxygen, calcium, phosphorus, and sodium could be found in all the coatings. Nitrogen, a constituent of EDTA, could not be detected by XPS. The level of carbon is in the normal range for implant surfaces. Again, carbon as a component of EDTA would have been expected to be present in the coating at a level exceeding the level of normal surface contamination. Hence, both carbon and nitrogen seem to merely form volatile compounds during the dielectric breakdown. For all coatings the oxygen content is between 50 and 54 atom-%. If stoichiometric  $\text{TiO}_2$  and  $\text{PO}_4^{3-}$  was assumed, the oxygen concentration would have to be higher than the values measured with XPS. The oxygen concentration would have to be twice the titanium concentration plus four times the phosphorus concentration (refer to Section 7.2.2). The sodium content is underestimated by XPS.  $\text{Na}_{1s}$  electrons are escaping from the coating after the excitation by the X-ray source with a low kinetic energy.

Thus, the escape depth (or information depth) for these electrons is smaller if compared to electrons originating from other elements at higher kinetic energy.

The binding energies for the  $O_{1s}$ -,  $Ti_{2p_{3/2}}$ -,  $Ca_{2p_{3/2}}$ -, and  $P_{2p}$ -electrons remained constant throughout the parameter screening in ESOC. The values are: 530.8 ( $O_{1s}$ ), 458.9 ( $Ti_{2p_{3/2}}$ ), 347.6 ( $Ca_{2p_{3/2}}$ ), and 133.6 eV ( $P_{2p}$ ). The variation of the values remained within 0.2 eV for all elements.

**TABLE 8.5.** Overview over the chemical compositions of coatings produced in ESOC at different temperatures, currents, and process durations. The values are single-point XPS measurements. Where a standard deviation is shown, the values are averages of three measurements on three samples coated under identical conditions.

Temperature [°C]	Current [mA]	Duration [s]	Titanium [atom-%]	Phosphorus [atom-%]	Calcium [atom-%]	Oxygen [atom-%]	Carbon [atom-%]	Sodium <sup>a</sup> [atom-%]
25	80	60	13	9	10	54	13	≥ 1
25	80	90	12 ± 1	10 ± 1	12 ± 1	53 ± 1	12 ± 2	≥ 1
25	80	120	13	10	10	51	15	≥ 1
25	150	45	10	11	11	51	16	≥ 1
25	150	60	12	10	12	54	11	≥ 1
25	150	90	9 ± 1	11 ± 1	14 ± 1	51 ± 1	15 ± 1	≥ 1
45	80	65	14	8	9	53	15	≥ 1
45	80	90	13 ± 1	9 ± 1	12 ± 1	53 ± 1	12 ± 1	≥ 1
45	80	120	13	9	12	51	14	≥ 1
45	150	45	13 ± 1	9 ± 1	12 ± 1	52 ± 1	13 ± 1	≥ 1
45	150	60	14 ± 1	8 ± 1	11 ± 1	53 ± 1	13 ± 1	≥ 1
45	150	90	11 ± 1	10 ± 1	12 ± 1	52 ± 1	13 ± 2	≥ 1

a. The sodium content in the coating is underestimated by XPS. Since the  $Na_{1s}$  electrons have only a very low kinetic energy, their escape depth is smaller than for other elements. Therefore, the sodium content is shown with a  $\geq$ -sign.

The absolute concentrations of calcium are higher than 9 atom-% on all surfaces. On most surfaces, the concentration is around 12 atom-%. Correlations between the coating parameters and the calcium concentration cannot be established, since the values do not differ significantly. This finding is confirmed by the scatter plot shown in Fig. 8.1. The Ca/P-ratio scatters between 1.0 and 1.5. As a tendency, the ratio is higher at the higher electrolyte temperature.

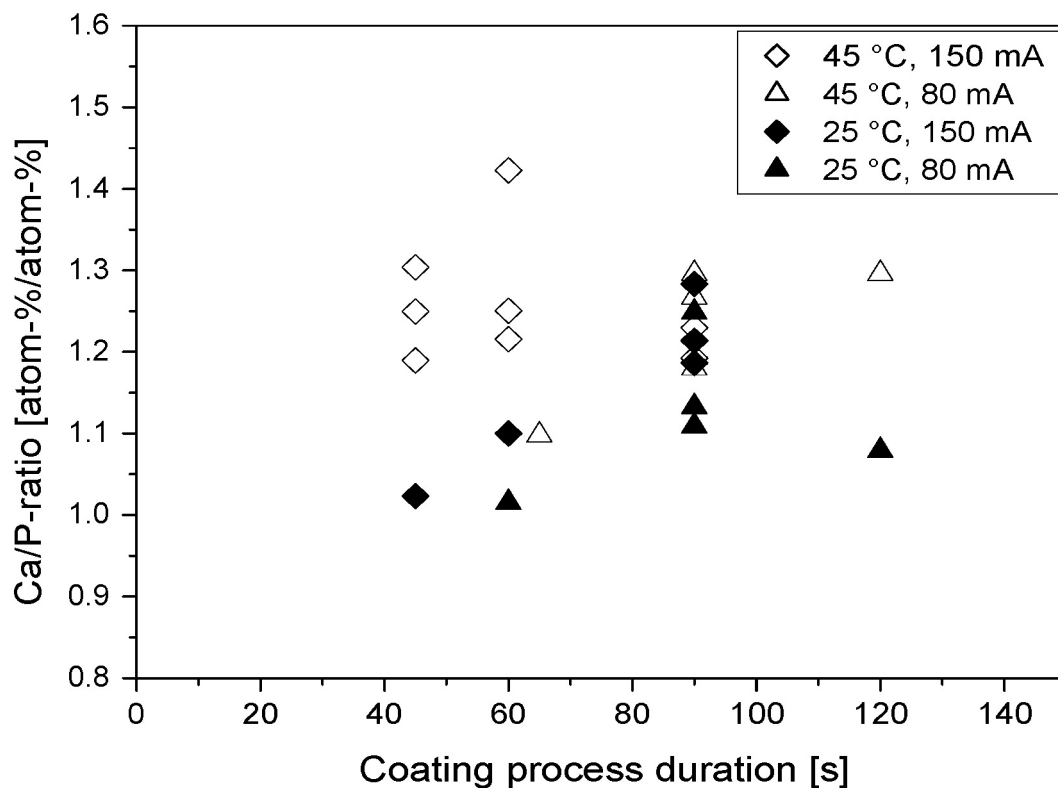


**Fig. 8.1.** Ca/P-ratio for coatings prepared in the ESOC with varying coating parameters. No relations can be established between coating parameters and the Ca/P-ratio. As a tendency, the ratio is higher at 45 °C electrolyte temperature than at 25 °C. The current density does not seem to influence the Ca/P-ratio. The plotted data are single spot XPS measurements.

**Surface Morphology.** The APC coating topography was investigated with SEM and the mechanical integrity with tensile tests (ISO 13779-2/4). Fig. 8.2 shows the comparison of four different coatings produced in ESOC. The micrograph (a) shows a surface coated at 25 °C electrolyte temperature, at a current of 80 mA, and for a duration of 90s. Coating (b) was produced with the same parameters but at a higher current density (150 mA). The increase in current induces two changes, which can be seen on the micrographs. Firstly, the pore density decreases. Secondly, more cracks are found on the surface coated at the higher current density. Micrograph (c) on Fig. 8.2 shows a surface coated with the same parameters as (b) but only for 45 s. The general impression is that the pore density is higher and less cracks are found at shorter durations.

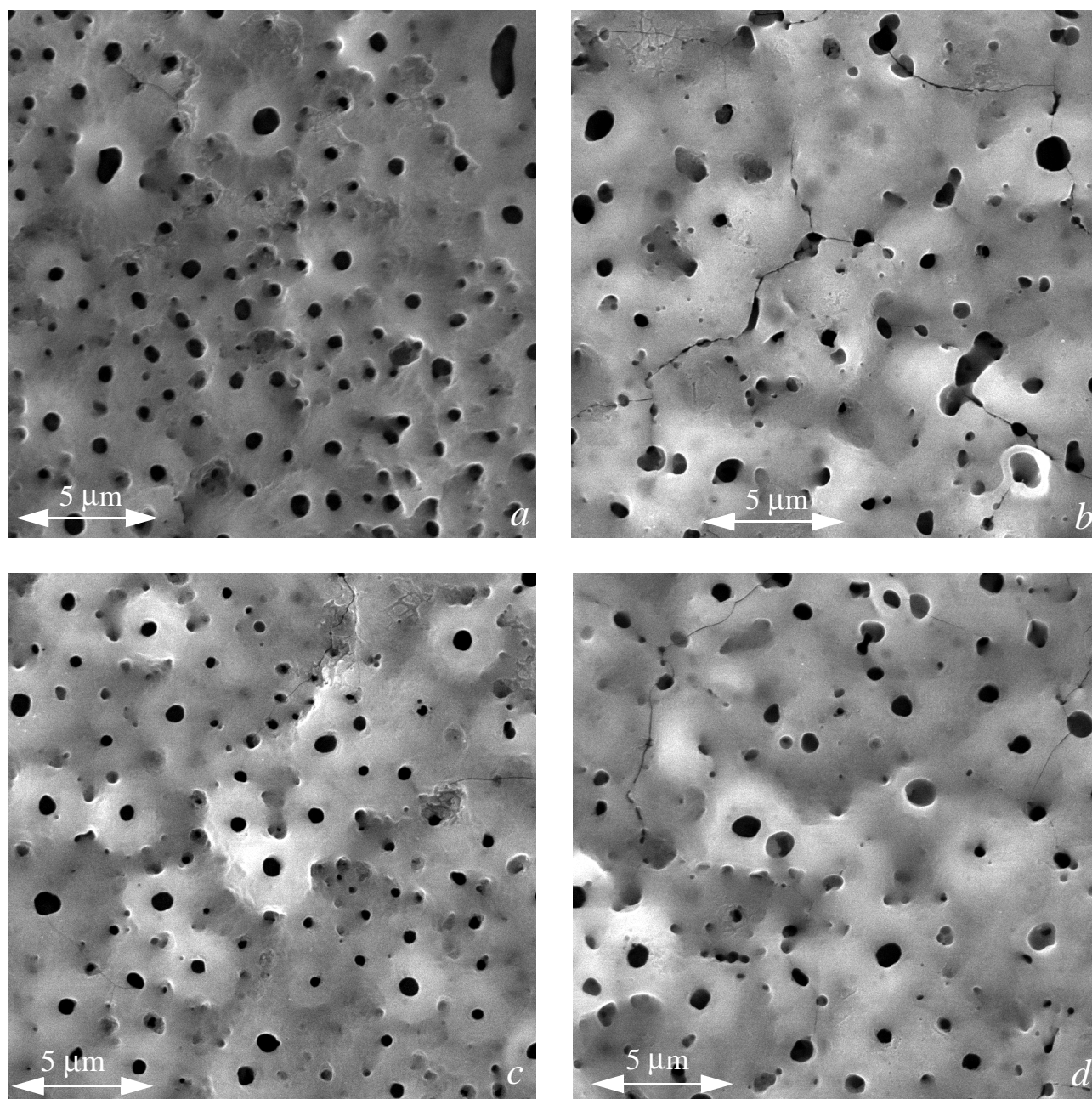


**Fig. 8.2.** SEM micrographs of APC coatings produced in the ESOC with the following parameters (electrolyte temperature; current; process duration): a) 25 °C; 80 mA; 90 s, b) 25 °C; 150 mA; 90 s, c) 25°C; 150 mA; 45 s, d) 45 °C; 150 mA; 90 s.

The coating on micrograph (d) was produced at 45 °C, the other parameters match with the coating on micrograph (b). In comparison to (b), fewer cracks are found on (d). The surface structure of (d) is similar to (b). Magnified 10'000 times, the surfaces of the coating look rather similar. At lower

magnification the influence of coating duration on the surface structure is more obvious. On Fig. 8.3, micrograph (a) shows a coating produced at 25 °C, 80 mA and a coating process duration of 60 s. The surface on micrograph (b) was coated for 120 s (the other parameters matching surface (a)). The surface coated for 120 s has a coarser surface structure. The grooves arising from the machining process are still visible after the shorter coating process duration (micrograph (a)), whereas they cannot be found anymore after longer durations (micrograph (c)). The form of the pores changes with coating duration, too. Their shape after 120 s is circular. If the process is stopped after 60 s seconds, the shape is more elliptical.

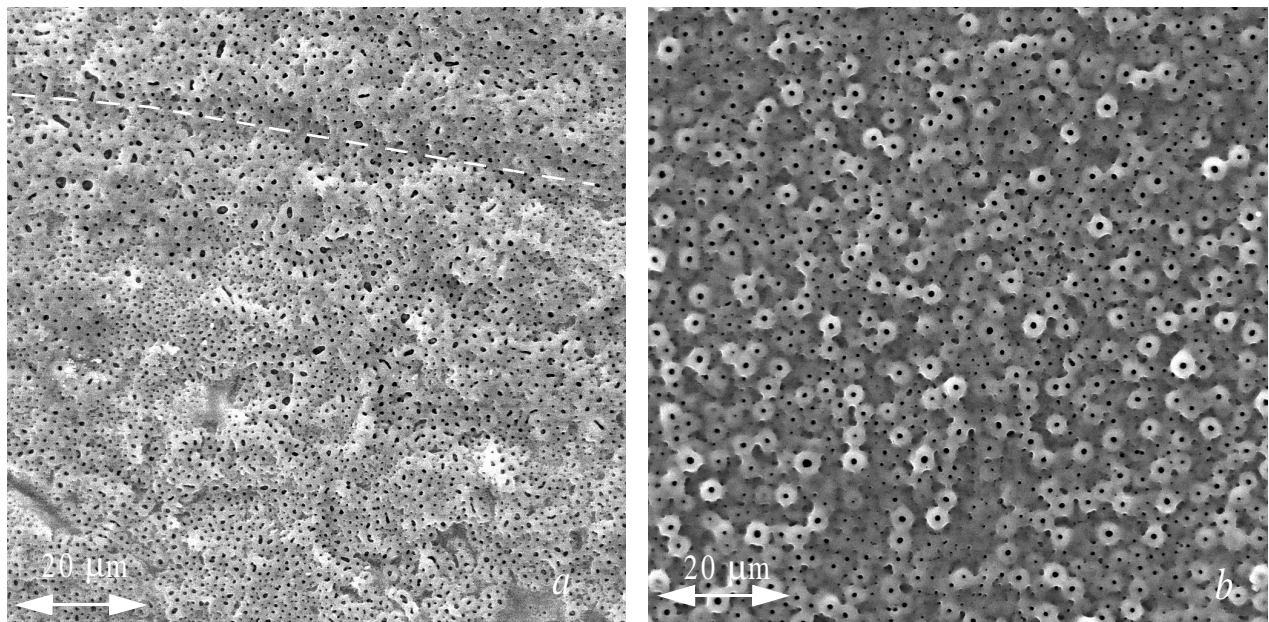


**Fig. 8.3.** SEM micrographs of APC coatings produced in ESOC with the following parameters (electrolyte temperature; current; process duration): a) 25 °C; 80 mA; 60 s, b) 25 °C; 80 mA; 120 s. The influence of the coating process duration is obvious. If only coated for 60 s (a) the pore density on the surface is much higher than on the surface coated for 120s. For the APC coating (a) the grooves of the machining process are still visible (dashed line) indicating a thinner coating than on (b).

**Mechanical properties.** According to the objectives of the thesis, the mechanical properties of the coating need to be significantly better than the properties of plasma-sprayed hydroxyapatite coatings. In order to be able to compare the properties tensile tests according to ISO 13779-4 were performed, which standardizes mechanical testing for hydroxyapatite coatings. The minimal adhesion strength for HA-coatings is 15 MPa (ISO 13779-2). In Fig. 8.4 the results of the tensile tests are plotted as a

function of the total amount of transferred charge (i.e., current · duration). With increasing charge transfer, the mechanical strength of the coating is reduced. As could be seen in Fig. 8.2, the amount of cracks present in the coating is higher if the coating process is performed at higher currents or for longer durations. It is probable that the cracks have an adverse effect on the mechanical properties of the coating. A second reason for the found tendency might be related to the general nature of ceramics. With increasing charge transfer the coatings get thicker. Since the coatings consist of ceramics, the probability to fail at lower stresses increases with an increasing volume of ceramics [188].

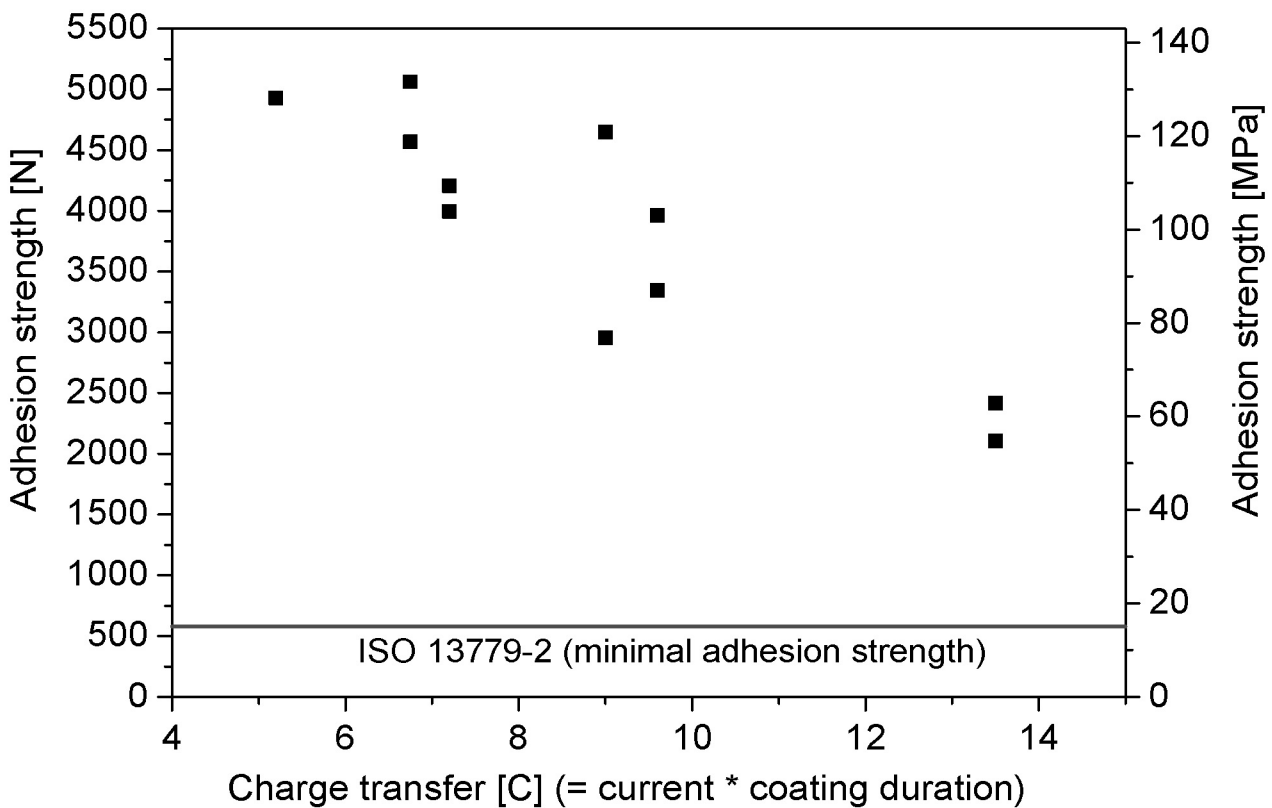


**Fig. 8.4.** Tensile strength of coatings prepared in ESOC. The x-axis contains the current and the process duration as a product (total amount of transferred charge). No correlation with coating temperature was found and, therefore, no label for the temperature was added in the graph. The conversion from force to stress was done by dividing the force by the nominal area of a sample (circle with a diameter of 7 mm).

The horizontal line at 15 MPa shows the minimal adhesion strength for plasma-sprayed HA-coatings as required by ISO 13779-2. All APC coatings produced in ESOC have at least three times higher



adhesion strength than the minimal value. Coatings produced by APC grow as a result of a chemical reaction of the substrate and do not contain an „artificial“ interface as deposited coatings do. Therefore, the adhesion would be expected to be high. From the localized nature of the APC process, it can be assumed that interfaces are formed between the areas of single breakdown events. The measured mechanical strength would not only be determined by the adhesion of the APC layer on the substrate but also by the cohesive strength inside the APC layer. Fig. 8.5 shows an APC coated surface after the tensile test. Region A shows the coating with a layer of glue on top (glue was used to fix the sample in the stamps of the tensile tester). Region B shows intact APC coating without glue and C shows an area where the coating had failed. The surface of region C still contains at least fragments of the oxide layer indicating a partly cohesive nature of the APC layer failure (arrow).

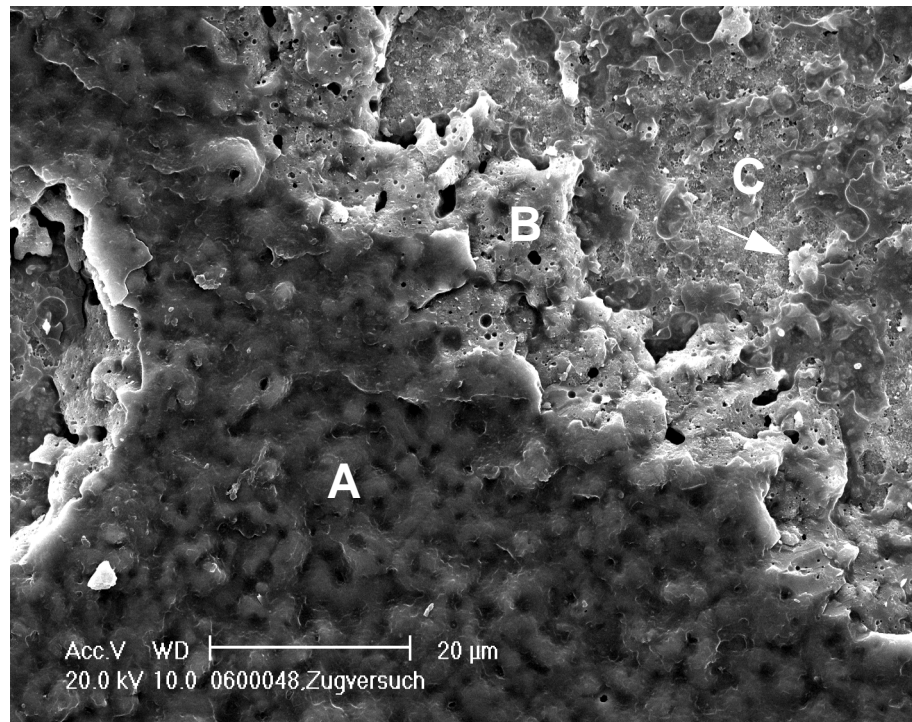


**Fig. 8.5.** SEM micrograph of an APC treated surface after the tensile test. In region A fixation glue is on top of the APC layer. Region B shows intact APC layer and in region C, the coating has failed in a mixed adhesive and cohesive manner (arrow denotes a remaining fragment of the APC layer).

### 8.2.3 Conclusions

The influence of current, coating process duration and electrolyte solution temperature on the surface- chemical composition and the coating morphology have been investigated with XPS, SEM and tensile tests. The results allow the following conclusions:

- The influence of the coating parameters on the surface chemical composition is rather weak. As a tendency, the Ca/P-ratio increases with increasing temperature.
- An increase in current applied to the sample or an extension of the coating process duration leads to coarser surface structures and more cracks in the APC coating.
- The mechanical strength of the coatings is reduced with increasing current or coating duration, indicating a dependence on the amount of cracks contained in the APC coating.

---

## 8.3 *Cell-Culture Samples Coated in ESOC*

### 8.3.1 Experimental

It is one of the main aims in this work to develop a mixed titania/calcium phosphate coating, which exhibits bioactive properties similar to hydroxyapatite coatings but combined with significantly improved mechanical properties in comparison to plasma sprayed hydroxyapatite coatings.

In preparation for the planned animal study, the coatings produced in ESOC were tested for possible toxicity on living organisms with standard cell-culture tests using human osteoblasts. In this section, the production and the characterization of the samples produced for the cell culture study is presented, while the cell culture tests and results themselves are presented in Section 9.2.

In order to meet the geometrical requirements of the cell culture multidishes, the APC process with ESOC as the electrolyte was scaled up from a disc diameter of 7 mm to 13 mm. The thickness was kept constant at 1 mm. The process was adapted so that voltage and time span at which the first sparks occurred as well as the voltage at the process end matched the corresponding values for the smaller samples. Since the APC process is localized to small spots on the surface, the upscaling cannot be done by simply keeping the current density constant. 80 mA for 7 mm samples

corresponds to 200 mA on 13 mm samples, 150 mA on 7 mm to 290 mA on 13 mm. For the cell-culture study, two parameter sets were chosen.

1. Electrolyte temperature: 25 °C, process duration: 90 s, and current: 290 mA
2. Electrolyte temperature: 25 °C, process duration: 90 s, and current: 200 mA

Both combinations should lead to about the same chemical composition of the coating but a different surface topography.

### **8.3.2 Results**

Prior to the *in vitro* tests, the chemical composition, the crystal structure, and the surface topography of the APC coatings were characterized. The chemical composition at the surface was determined by XPS and the averaged coating composition by dissolution and ICP-AES. In addition, chemical depth profiles were acquired using the GD-OES method in order to gather information about the distribution of calcium and phosphorus across the coating thickness. The crystal structure was assessed with Raman spectroscopy, while the topography was investigated qualitatively with SEM and quantitatively with laser profilometry.

**Chemical composition.** The chemical composition near the surface was determined by XPS. Table 8.6 gives the quantifications of the two different surfaces. As expected, the chemical composition near the surface is identical for both parameter sets. The chemical composition is in good agreement with the values during the parameter screening. Sodium has been excluded from this quantification because less than one atom-% has been found on the surfaces (see Section 8.2.2 for detailed explanation)

**TABLE 8.6.** Chemical composition of APC coatings prepared in ESOC for the cell culture study. Sodium was excluded from the quantification because less than 1 atom-% sodium was found. Sodium is present in the ESOC at concentration of 1.14 M. However, the content in the APC layer is underestimated by XPS (refer to Section 8.2.2). The values are averages  $\pm$  standard deviation of three XPS measurements on three samples.

Current	Titanium	Calcium	Phosphorus	Oxygen	Carbon
[mA]	[atom-%]	[atom-%]	[atom-%]	[atom-%]	[atom-%]
290	11 $\pm$ 2	11 $\pm$ 2	9 $\pm$ 1	53 $\pm$ 2	16 $\pm$ 3
200	11 $\pm$ 1	11 $\pm$ 1	9 $\pm$ 1	52 $\pm$ 1	17 $\pm$ 1

Table 8.7 shows the integral contents of calcium and phosphorus in the coatings determined via chemical digestion of the APC layers. The resulting concentrations of calcium and phosphorus were determined using ICP-AES. If coated at higher current density, the APC layer produced in ESOC contains almost twice the amount of calcium than the coating prepared at the lower current density. The Ca/P-ratio calculated in Table 8.7 is lower in comparison to the one determined by XPS. This may be due to irregular distribution of calcium and phosphorus in the APC layer (i. e., accumulation of calcium near the surface).

**TABLE 8.7.** Integral calcium and phosphorus content of coatings produced in ESOC for the *in vitro* study assessed via chemical digestion and determination of concentrations in solution with ICP-AES.

Current	Calcium	Phosphorus	Ca/P-ratio
[mA]	[ $\mu\text{g}/\text{mm}^2$ ]	[ $\mu\text{g}/\text{mm}^2$ ]	(molar ratio)
290	0.64	0.61	0.81
200	0.37	0.38	0.75

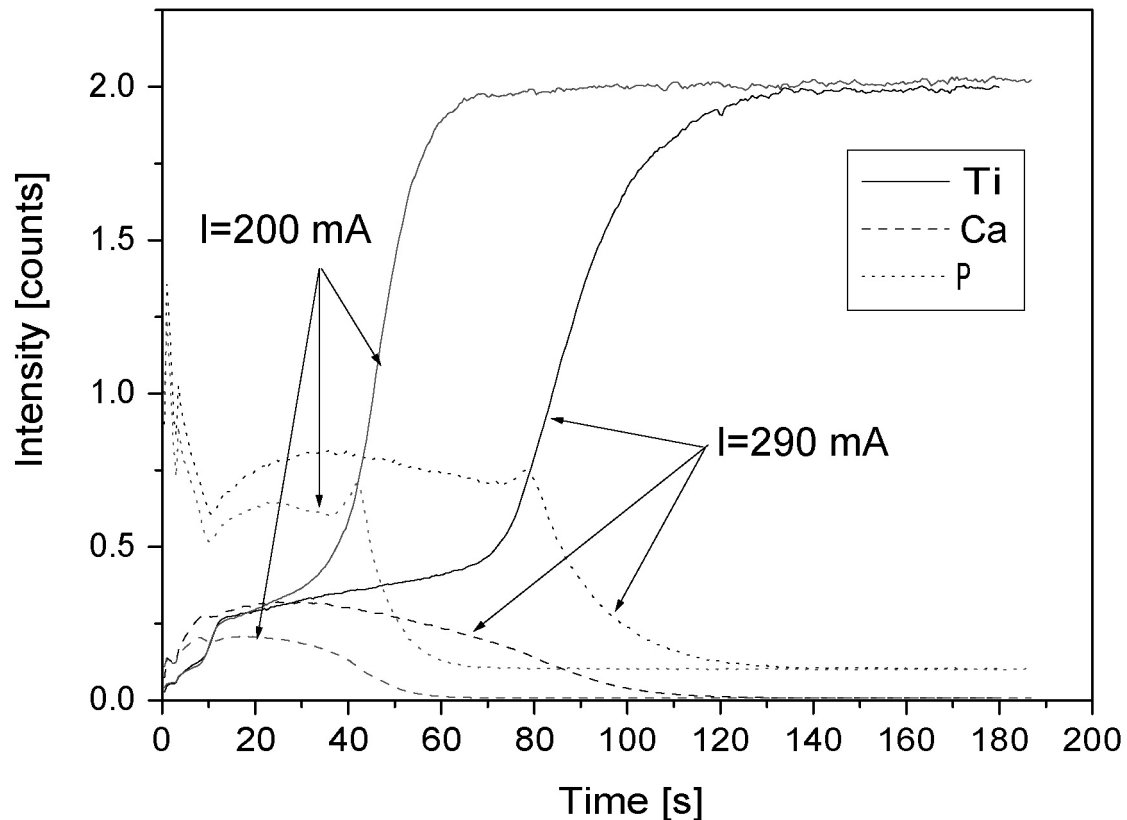


**Fig. 8.6.** Chemical depth profiles (recorded with GD-OES) of APC layers coated in ESOC at 25 °C for 90s. The profile starts at the surface of the coating (0 s); the interface between APC layer and substrate is at 90 s for the coating anodized with 290 mA and at 50 s for the coating anodized at 200 mA. Both calcium and phosphorus are distributed across the whole APC layer. The peaks in the phosphorus signal at the surface and the interface substrate/APC layer may result from artefacts (refer to Section 7.2).

Chemical depth profiles recorded on APC coatings produced in the calcium orthophosphate electrolyte suggested an accumulation of phosphorus near the interface APC layer/substrate. The profiles recorded on APC coatings produced in ESOC do not show this accumulation (Fig. 8.6). This may be due the relatively small difference in the Ca/P-ratio (XPS compared to ICP-AES). Measured by XPS, the Ca/P-ratio for the cell culture sample coated at 290 mA is about 1.2, while the ratio drops to 0.8. Fig. 8.6 shows depth profiles of the two coatings. Calcium and phosphorus are distributed across the whole APC layers. In the coating prepared at 200 mA, the interface between coating and substrate is reached faster than in the coating prepared at 290 mA. The difference in time

until the interface is reached indicates that the coating produced at 290 mA is thicker. The phosphorus peaks at the coating surface may be due to interference with hydrogen resulting from hydrocarbon contaminations. The phosphorus peak at the interface between coating and substrate may stem from the change in sputter rate (see section Section 7.2 for a detailed description).

**Crystal structure.** The crystal phases present in coatings produced in ESOC were determined with Raman spectroscopy. The phase identification has been obtained from reference spectra published in literature. The aim of the ESOC development was to achieve a mixed coating, consisting of titania and calcium phosphates. The Raman spectra plotted in Fig. 8.7 show mainly anatase, a modification of titania. Only on the coating produced at the higher current density an additional band is present. This band at  $960\text{ cm}^{-1}$  is typical for the symmetric stretching vibration of  $\text{PO}_4^{3-}$  [171]. The other vibration modes for phosphate are much weaker than the band at  $960\text{ cm}^{-1}$  and, therefore, they can not be identified. Association of the phosphate band with hydroxyapatite or any other calcium phosphate phase is not possible, since only the most intense of the characteristic bands is found [189-192].

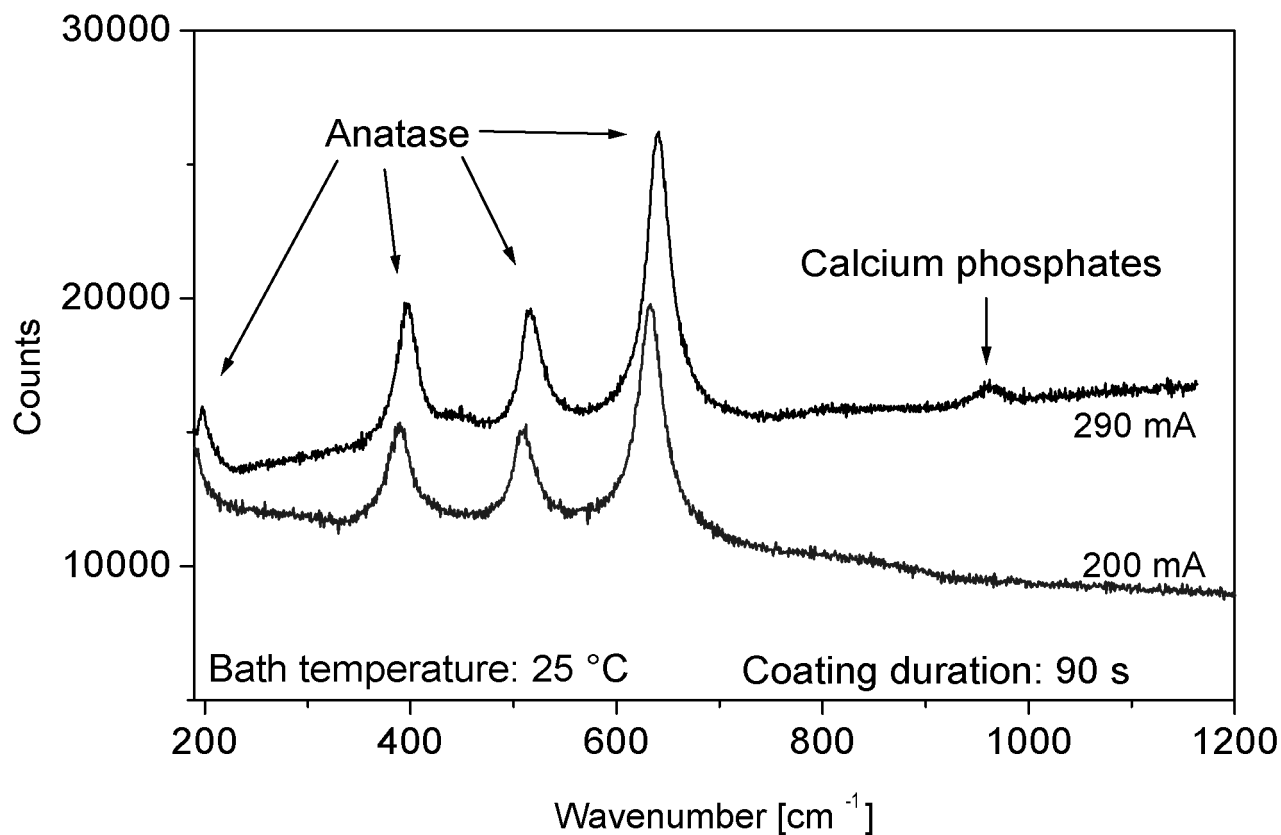


**Fig. 8.7.** Raman spectra of two coatings produced in ESOC. The main crystal phase in the APC coatings is anatase with bands at 144 (not shown), 197, 400, 519, and 640  $\text{cm}^{-1}$  [170,183]. No additional crystal phases could be found on the coating anodized at 200 mA. The surface anodized at higher current expressed an additional band at ca. 960  $\text{cm}^{-1}$ , which can be assigned to the symmetric stretching mode of  $\text{PO}_4^{3-}$  [171,192].

**Surface morphology.** The topography was investigated qualitatively with SEM and quantitatively with laser profilometry. In addition, the thickness of both coatings produced in ESOC used in the *in vitro* study was measured on cross-sections with a light microscope.

Two SEM micrographs are shown in Fig. 8.8. The difference resulting from the two currents applied is not as obvious as the one from the smaller samples coated during the parameter screening (Section 8.2.2). If coated at the higher current density (290 mA), the coating structure is coarser and contains more cracks. This is in agreement with the findings of Section 8.2.2.

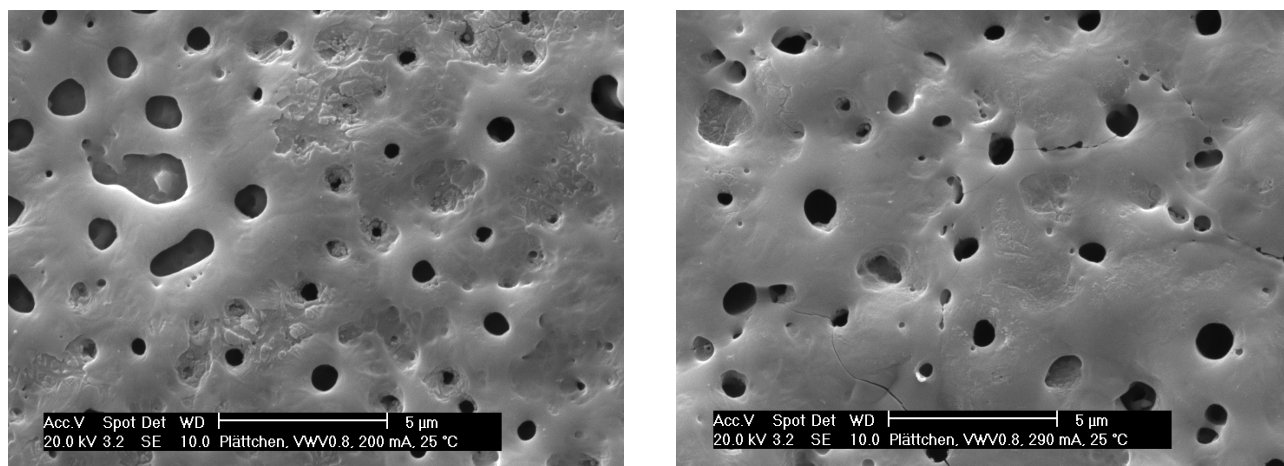


**Fig. 8.8.** SEM micrographs of two surfaces coated in ESOC for the *in vitro* study. The surface on the left was coated at 200 mA and the surface on the right at 290 mA. The surface structure is similar, but the coating on the right side contains more cracks and less pores.

The roughness parameters of the two surfaces coated in ESOC were determined with a UBM laser profilometer. The results are compiled in Table 8.8 and indicate a higher roughness of the coating produced at 290 mA. However, the pore density is higher for the coating produced at 200 mA (Fig. 8.8). Since the UBM profilometer has a lateral resolution of 1 to 2 µm [61], the pores are too small to be detected by this method. The roughness parameters therefore reflect the surface features with a size larger than the detection limit. Within this range, the surface roughness differs only slightly.

**TABLE 8.8.** Roughness parameters measured on surfaces coated in ESOC at two different currents. The values for the roughness parameters are averages and standard deviations of 4 measurements on one sample.

Current	$R_a$	$R_q$	$R_{zDIN}$	$R_t$	$S_m$	$L_r$	$S_k$
[mA]	[µm]	[µm]	[µm]	[µm]	[mm]		
290	$0.70 \pm 0.01$	$0.88 \pm 0.01$	$5.54 \pm 0.18$	$6.29 \pm 0.19$	0.02	$1.16 \pm 0.01$	$-0.09 \pm 0.01$
200	$0.66 \pm 0.02$	$0.82 \pm 0.02$	$5.09 \pm 0.18$	$6.25 \pm 0.79$	0.02	$1.12 \pm 0.00$	$-0.12 \pm 0.06$

In order to determine the coating thickness, the samples were cross-sectioned. The thickness of the coating was then determined with a light microscope at ten positions on two samples coated under the same conditions. The coating prepared at 290 mA was found to have thickness of  $8.5 \pm 1.2$  µm. The coating prepared at the lower current (200 mA) had a thickness of  $6.0 \pm 1.1$  µm.



---

#### *8.4 Discussion of the New Electrolyte System*

A new electrolyte system has been developed. It allows the incorporation of significantly higher amounts of calcium into the APC layer with respect to the standard calcium orthophosphate electrolyte described in literature. This improvement has been achieved by increasing the solubility of calcium in the solution with a chelating agent and subsequent increase of pH in the electrolyte solution leading to a net negative charge of the calcium chelate. The new electrolyte (ESOC) contains calcium orthophosphate as a basis and calcium acetate to increase the Ca/P-ratio in the electrolyte solution. EDTA was used as chelating agent. The pH was increased with sodium hydroxide.

It was found that the APC process is slowed down by an increase in electrolyte temperature. The voltage at which the first sparks can be observed is taken as a measure for the process speed. For the smaller samples coated at a current density of 150 mA, the voltage was reached after about 12 s at 25 °C. At 45 °C, the voltage was reached after about 20 s. The voltages just before the APC process was ceased is lower for coatings prepared at higher electrolyte temperatures. Instead, more oxygen evolution occurred at higher temperatures, consuming an increasing amount of the applied current. This behavior, however, was not found for phosphoric acid and calcium orthophosphate as electrolytes, where the final voltage increased with increasing electrolyte solution temperature. This may be due to the difference in pH of the three electrolyte systems. In the phosphoric acid electrolyte system, the pH was always lower than 2, while for the calcium orthophosphate electrolyte the pH is neutral. For these two electrolyte systems the oxygen evolution reaction can be written as



In ESOC, the pH is 14 and the dominant oxygen evolution reaction will be



The two different reactions leading to oxygen evolution have different kinetics, and it may be that the reaction in the basic environment is faster and preferable to the reaction in the acidic environment. The resistance of the anodic oxide film which was found to be lower in oxide films prepared in basic solutions [193] suggests a second reason for the increased oxygen evolution

reaction. Thus, the oxygen evolution in ESOC is increased due to the higher electron conductivity in oxide layers prepared in basic solutions. However, the influence of temperature cannot be explained by this. More research on the topic of oxygen evolution on titanium during the APC process is needed.

The influences of the current applied to the sample, the APC process duration, and the electrolyte solution temperature on the coating properties have been investigated with parameter screening. The chemical composition near the coating surface is only weakly influenced by the electrolyte temperature, while no influence arising from changes in current or process duration was detected. The integral content of calcium is certainly influenced by the current density. The coatings produced at the higher current density contain more calcium than the coatings anodized at the lower current density. Measured on cross sections, the high current APC layers are thicker, too, but the calculation of the ratio between calcium content and layer thickness still results in a calcium content per micrometer thickness, which is about 18 % higher for the high current APC-layers. The cell culture sample coated in ESOC at 290 mA for 90 s contains  $0.64 \mu\text{g}/\text{mm}^2$  calcium. The sample coated in 0.07 M  $\text{Ca}(\text{H}_2\text{PO}_4)_2$  at the same current contains  $0.04 \mu\text{g}/\text{mm}^2$ . If these values are corrected for the difference in coating thickness, the calcium content of the APC layer produced in ESOC is still 7 times higher than in the coating produced in calcium orthophosphate. This difference impressively demonstrates the beneficial effect of the  $\text{Ca}^{2+}$  chelation and charge inversion.

While the chemical composition near the surface is not sensitive to the amount of current applied to the sample, the surface topography is coarsened by an increase of current or an increase in process duration, making it feasible to tune the surface topography without changing the chemical composition of the coating near the surface.

Problems arose during the characterization of crystal structure of the coatings produced in ESOC. As the amount of calcium phosphate incorporated in the APC coatings was increased by the new electrolyte, calcium phosphate phases were expected to be present in the coating. The Raman spectra shown in Section 8.2.2 did not allow the phases present in the APC coating to be identified. Only one small band, typical for phosphate stretch vibrations, was found in the spectra. Phosphorus with its possible oxidation state of five can be seen as strong glass former. The hypothesis that the calcium

phosphate is present in the coating as a glassy phase does not seem to be too far fetched. Attempts to characterize the crystal phases with transmission electron microscopy were not successful so far. However, if the calcium phosphate was incorporated in an amorphous or glassy phase, its solubility in the biological environment would be higher in comparison to that of crystalline calcium phosphates (refer to Chapter 2). In my opinion, the higher solubility should have positive effects on the ongrowth and mineralization of the newly formed bone tissue around the implant.



---

# *Chemical and Biological Properties of APC-coated CP Titanium Surfaces*

---

---

## *9.1 Dissolution Experiments in Diluted EDTA-solution*

### **9.1.1 Introduction**

Thin coatings made of bioactive materials such as calcium phosphate (CaP) ceramics promote the ongrowth of bone on implants and the formation of a high-strength, bone-implant interface [6,7]. As already discussed in Section 2.4.2, an interesting approach involves partial solubility of the CaP-coating in contact with the biological environment in order to induce bone mineralization by supplying the tissue adjacent to the implant with calcium and phosphate [13].

The coatings produced in the new electrolyte system for osteointegrative coatings (ESOC) were shown to contain significantly higher amounts of calcium than coatings prepared in the known standard electrolyte calcium orthophosphate. Since no distinct crystalline calcium phosphate structures were found during the characterization of the new coatings, a prediction of bioreactivity cannot be made. Therefore, a lab-scale dissolution experiment was set up in order to test the reactivity of the coatings in a model solution.

As a model solution, a diluted ethylene diamine tetracetic acid (EDTA) solution was chosen. Ducheyne and Healy used EDTA to simulate the activity of serum on the assumption that ions released from the implant *in vivo* do not remain in solution, but are chelated by biomolecules (such as proteins) [194]. Additionally, calcium- and phosphate-ions are used by cells for the mineralization

of the tissue by cellular activity. Both effects result in an effective reduction of the calcium and phosphate concentration in the fluid around the implant *in vivo*. A steady state of dissolution and re-precipitation of ions from the CaP-coating may never be reached *in vivo*. Healy, Ducheyne and their coworkers improved their model solution further by adding simulated body fluids (such as HBSS and SIE) to the EDTA-solution in order to have an ionic strength level similar to that of bodily fluids [195-198]. However, they mainly investigated the dissolution kinetics of titanium and not those of calcium and phosphate. In order to avoid interference from other ion species and precipitation from the model solution onto the APC coating during the dissolution experiment, an EDTA-only model environment was chosen. The main reason for this decision was that if only small amounts of the coating dissolved, it would not be possible to measure these amounts of calcium and phosphate since both species are already present in SIE or serum at concentrations of 5 and 2 mM respectively [194]. The pH of a diluted EDTA·K<sub>2</sub>-solution is expected to be slightly acidic. For the experiment, the pH of the solution was not increased to normal physiological pH of 7.4, since the interest of the experiment is focussed on the time right after the implantation. The response of the biological system in the first days to weeks after the implantation includes an inflammation reaction with the possibility of a significant decrease of the pH around the implant [199].

The model experiment was chosen to be as simple as possible. The question related to this experiment was: is the newly developed coating able to supply calcium and phosphate to an environment, which is short of the two mentioned species at a time scale of two weeks? In order to compare the coatings produced in ESOC with standard surfaces, the experiment was also performed with APC coatings produced in orthophosphoric acid and with uncoated clean CP titanium surfaces.

### **9.1.2 Experimental**

The solubility of the CaP-phases in the coating was tested by exposing APC coated samples to a 1.7 mM EDTA·K<sub>2</sub>-solution<sup>1</sup> at 37 °C for 14 days. Cleaned (35 % HNO<sub>3</sub> for 12 hours) 100 mL borosilicate glass flasks were used as containers. These containers were filled with 100 mL of 1.7mM EDTA·K<sub>2</sub> solution and heated to 37 °C in a water bath. Subsequently 5 identical samples

---

1. The concentration of EDTA necessary to chelate all the calcium present in the APC coatings was calculated with the assumption that one coating on a sample of 7 mm size could theoretically contain 0.7 mg calcium.

(7 mm diameter) were added to each container and the flask was tightly closed to prevent evaporation of water. The different parameter sets tested are shown in Table 9.1. In addition, cleaned and uncoated CP titanium served as control. One of the flasks was filled with solution only and served as a further blank control. The containers were under constant agitation in a laminar flow box under sterile conditions. After 6, 24, 72, 168, and 336 hours, 8 mL of each solution were removed with sterile pipettes, filled into polystyrene centrifugal tubes and kept for the determination of the calcium, phosphorus, titanium and sodium content (using ICP-OES). The dissolved mass could then be calculated from the solution concentrations after correcting for the loss of solute volumes used for the elemental analyses. The chemical composition of the APC coatings before and after the dissolution experiment near the surface was determined with XPS. The coating morphology after the dissolution experiment was looked at with SEM.

**TABLE 9.1.** Coating parameters and electrolytes used for the dissolution experiment in 1.7 mM EDTA-K<sub>2</sub>.

Electrolyte	Electrolyte solution temperature	Current	Coating process duration
ESOC	25 °C	150 mA	90 s
ESOC	25 °C	80 mA	90 s
0.01 M H <sub>3</sub> PO <sub>4</sub>	25 °C	150 mA	90 s
0.01 M H <sub>3</sub> PO <sub>4</sub>	75 °C	150 mA	90 s

### 9.1.3 Results

The pH of the EDTA-solutions was measured before and after the dissolution experiment. The pH stayed constant throughout the experiment at 4.2.

**Dissolved mass.** A comparison between the released mass over time of the different surfaces tested is shown in Fig. 9.1 and Fig. 9.2. The highest amount of calcium was released from an APC coating produced in ESOC coated at 150 mA (Fig. 9.1). The coating prepared in ESOC at the lower current released less than half the amount of calcium than the sample coated at the higher current. As expected, no calcium was released by the samples coated in phosphoric acid and the uncoated sample. The release rate for both coatings prepared in ESOC steadily decreases with time.

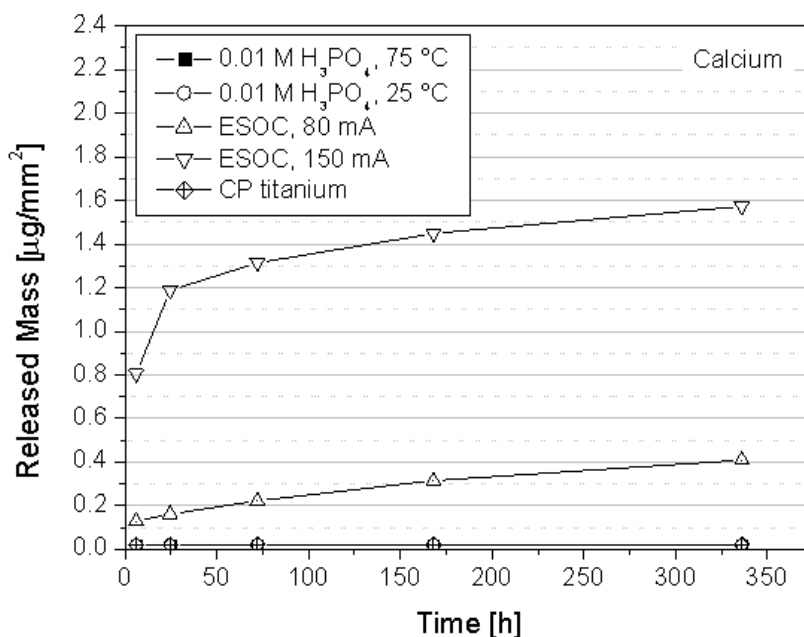


**Fig. 9.1.** Calcium mass released over time by five different surfaces. The highest amount of calcium is released by the APC coating produced in ESOC at 150 mA. As expected, no calcium is found to be released by APC coatings produced in phosphoric acid and the CP titanium surface.

Fig. 9.2 depicts the phosphorus release from the five tested coatings. Again, the highest amount is released by the coating produced in ESOC at high current. The coatings prepared in phosphoric acid release phosphorus, but significantly less than the coating prepared in ESOC. Sodium was released only from the APC coatings prepared in ESOC. After two weeks, about  $0.4 \mu\text{g}/\text{mm}^2$  sodium were released by the coating produced at 150 mA and  $0.15 \mu\text{g}/\text{mm}^2$  from the one produced at 80 mA. The kinetics of the sodium release are very similar to the kinetics of the calcium release. Titanium was released by all APC coatings, while no titanium was found to be released from the uncoated surface. The amount of titanium present in the EDTA-solution increased almost linearly. The total amounts per square-millimeter for the coatings produced in ESOC and exposed to the model solution for 14 d were  $1.45$  (150 mA) and  $0.85 \mu\text{g}/\text{mm}^2$  (80 mA). The coatings prepared in phosphoric acid released less titanium:  $0.3$  (25 °C) and  $0.45 \mu\text{g}/\text{mm}^2$  (75°C).



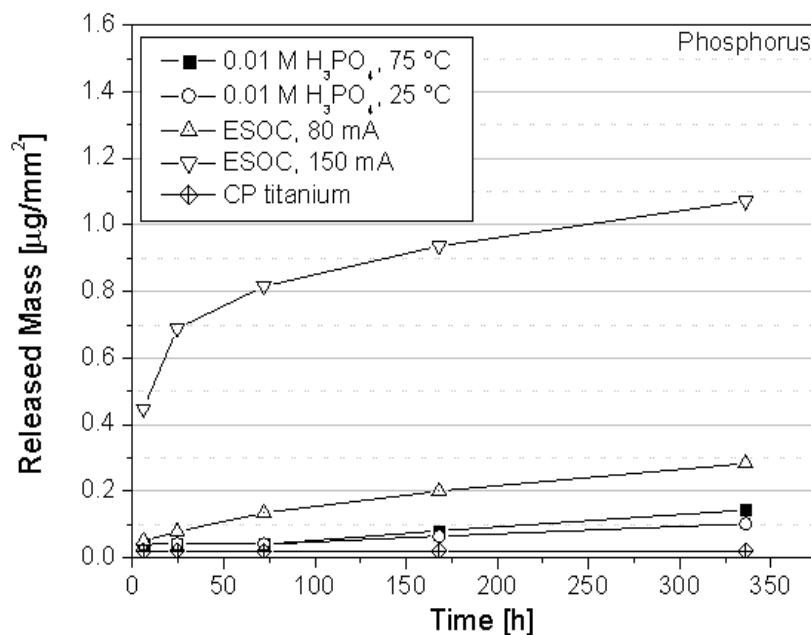


**Fig. 9.2.** Phosphorus mass released over time by five different surfaces. The highest amount of phosphorus is again released by the APC coating produced in ESOC at 150 mA. Less phosphorus is released by APC coatings produced in ESOC at 80 mA and the coatings produced in phosphoric acid.

**Change in the chemical composition due to dissolution.** The changes in calcium and phosphorus level near the surface of the coating the APC coatings are presented in Table 9.2. The calcium content at the surface is reduced by a factor of 4 for the coating produced in ESOC at the higher current. A little less extensive is the reduction for the coating produced in ESOC at the lower current.

**TABLE 9.2.** Calcium and phosphorus concentration before and after the dissolution experiment. The concentrations were measured with XPS.

Parameter set	Calcium (before)	Calcium (after)	Ratio for calcium	Phosphorus (before)	Phosphorus (after)	Ratio for phosphorus
	[atom-%]	[atom-%]	before/after	[atom-%]	[atom-%]	before/after
ESOC (150 mA)	16	4	4	12	6	2
ESOC (80 mA)	11	4	2.8	10	10	1
H <sub>3</sub> PO <sub>4</sub> (25 °C)				16	5	3.2
H <sub>3</sub> PO <sub>4</sub> (75 °C)				18	9	3

The decrease of the phosphorus content is less pronounced. This may be due to the fact that the phosphate released into the EDTA-solution is not chelating and thus can re-adsorb on the sample surface, which is very likely [181,182].

**Surface morphology after the dissolution experiment.** In the ICP-measurement, an increase in dissolved calcium was detected over time. Titanium was also found to be released from the APC coatings. The morphology of one coating surface after the dissolution experiment is shown in Fig. 9.3.

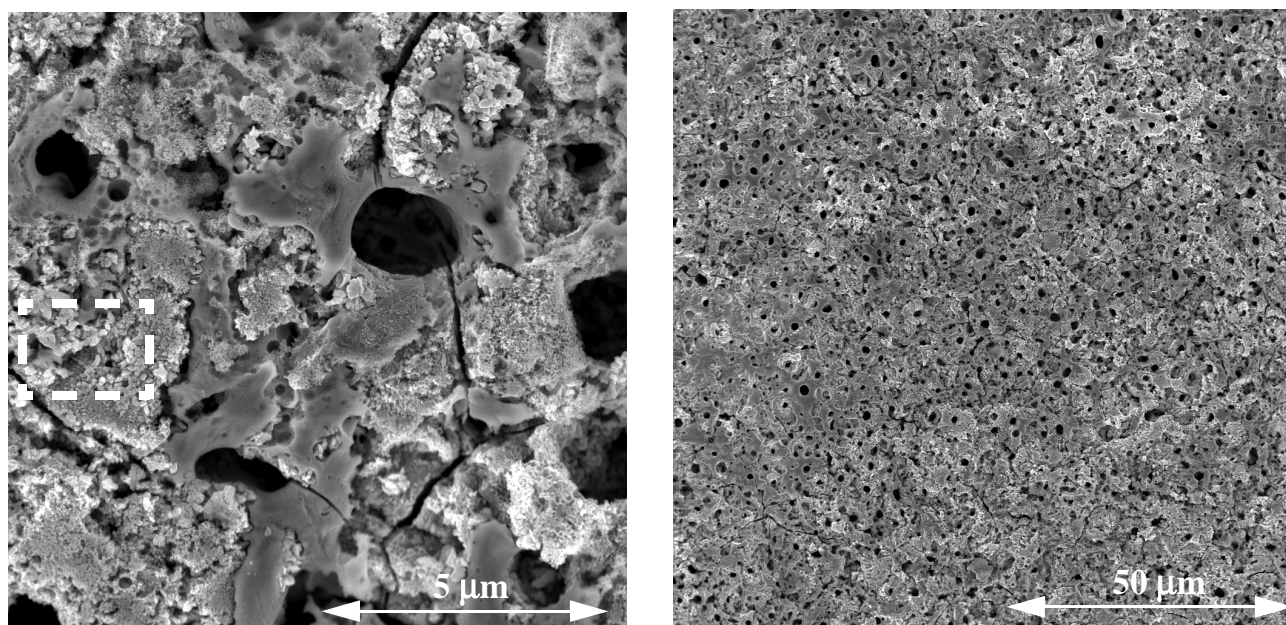


**Fig. 9.3.** SEM micrographs of an APC coating produced in ESOC at 150 mA after the dissolution experiment. The coating has partly dissolved. The rest of the coating remains as a grainy skeleton (rectangle as an example). The overall view (right) shows that the dissolution process is not restricted to certain domains of the coating.

Large parts of the APC coating produced in ESOC have dissolved. Small grains are uncovered as a consequence of the dissolution process. The micrograph in Fig. 9.4 shows the grains at higher magnification. The grains look like small single crystals with a size below 100 nm. Most probably, these crystals are anatase crystals since only anatase was detected with Raman spectroscopy after the dissolution experiment.

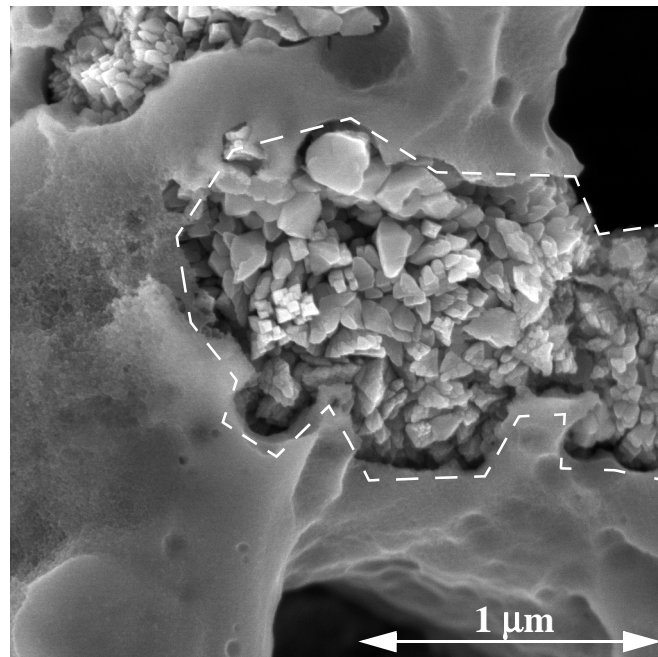


**Fig. 9.4.** SEM micrographs of an APC coating produced in ESOC at 150 mA after the dissolution experiment (Detail). At high magnification, small grains become visible (e. g. inside the polygon).

#### 9.1.4 Discussion

The dissolution behavior of APC coatings produced in two different electrolytes was compared to uncoated CP titanium. As model solution, 1.7 mM EDTA·K<sub>2</sub> was chosen. The experiment was carried out over a duration of two weeks. The changes of the calcium, phosphorus, sodium, and titanium concentration in the EDTA-solution were tracked using ICP-OES.

After the two weeks, significant<sup>1</sup> amounts of calcium and phosphorus were released from the coatings produced in ESOC. The coating produced at higher current released more calcium than the one coated at 80 mA. This finding corresponds with the total calcium amount incorporated in the APC coating increasing with increasing current density (refer to Section 8.3). However, if the total amount of calcium incorporated into the APC coating is compared to the total mass released during the dissolution experiment, it is found that the released mass per square millimeter exceeds the value for the incorporated mass by a factor of more than 2. The chemical digestion was carried out with

1. significant with respect to the detection limit.

samples having a diameter of 13 mm while the dissolution experiment was carried out with smaller samples (diameter of 7 mm). It may be that the upscaling (i. e., the change in current) did not lead to exactly the same coating properties. A comparison of Fig. 8.8 with Fig. 8.2 shows that for example the surface topography is not exactly the same. Therefore, the coating morphology and, connected to the morphology, the *integral* chemical composition may therefore be different. A further reason for the different calcium contents found may be related to the chemical digestion procedure. Between the digestion and the ICP-measurement, calcium may have precipitated out of the solution, even though no particles could be identified by eye. The digestion procedure for APC coatings has been established in the course of this thesis and still can be further optimized in the future.

The second very important element released during the dissolution experiment was phosphorus (most probably in the form of phosphate). The most phosphorus is released by the coating prepared in ESOC at the higher current. Similar to calcium, the total phosphate mass released exceeds the value found for the total incorporated phosphorus amount (refer to Chapter 8). In the case of the coatings produced in phosphoric acid, much less phosphorus has dissolved during the experiment in comparison to the coatings produced in ESOC. The coating produced at an electrolyte solution temperature of 75 °C released slightly more phosphorus than the coating produced at 25 °C. The released mass after two weeks ( $0.15 \mu\text{g}/\text{mm}^2$  and  $0.1 \mu\text{g}/\text{mm}^2$  respectively) is within the range of the integral phosphorus content determined by the chemical digestion (see Section 7.2). The fact that the values for the released mass from the coating prepared in phosphoric acid correspond to the total incorporated mass (determined by digestion) is an indication that the chemical digestion procedure has to be improved if coatings containing calcium are analyzed. This could possibly be done by chelation of calcium between the digestion and the analysis with ICP.

It was certainly not expected that titania, as the main component of the APC coatings, would dissolve during the dissolution. The ICP-OES measurement should not be misinterpreted. The plasma torch of the spectrometer is not only capable of exciting dissolved ions but also of decomposing small particles and exciting their constituents. As shown by the SEM micrographs in this section, it looks as if a soluble matrix has dissolved from the APC coating, exposing small agglomerates of crystals. These crystals can be released into the solution and may therefore be

responsible for the measured titanium content in the solution. In order to confirm this hypothesis a dynamic light scattering experiment was carried out with one of the solutions containing titanium. The experiment was carried out at the Physics Department of the University of Fribourg, Fribourg, Switzerland. Romer and Schurtenberger detected particles with an average size of about 100 nm [200] in the solution, which is in agreement with the size of the crystal agglomerates shown in Fig. 9.4. The model solution used is an extreme way of testing the solubility of CaP because virtually any CaP-phase will dissolve in such an environment. *In vivo*, I would expect a slower and less complete dissolution. However, titania particles may be released as the APC coating dissolves. Since the size of these particles is less than one micrometer, the particles will be transported away by macrophages, for example [89], probably not causing any damage to the patient.

The dissolution experiment revealed interesting facts about the structure of the APC coatings. The coating consists of more than one phase. The matrix is formed by a phase that is soluble in a EDTA. This matrix is probably amorphous. Embedded in the matrix, small anatase crystals are found. They are grouped into agglomerates that are distributed over the surface.

It can be concluded from the dissolution experiment that the APC coatings produced in ESOC are able to supply calcium and phosphorus to the surrounding tissue if the calcium concentration around the implant to which the coating was applied is below the saturation concentration.

---

## 9.2 A Standard Osteoblast Cell-Culture Study

The new electrolyte system ESOC contains EDTA at a concentration of 0.12 M. During the APC process, temperatures of several thousand Kelvin locally lead to the decomposition of the chemical compounds present in the electrolyte solution. It is possible that during the re-solidification of the coating material new phosphate-containing organic compounds are formed. The newly formed organic compounds could have adverse effects on the biocompatibility of the APC coatings produced in ESOC. In order to compare the biocompatibility (under the aspect of non-cytotoxicity)

of the APC coatings with approved titanium and calcium phosphate surfaces, cell culture tests were carried out. The tests were performed together with the accredited laboratories of Prof. Dr. Roger Thull at the University of Würzburg, Germany.

The surfaces were tested for 13 d with a cell line of human osteoblasts (hFOB 1.19 [201]). At several points in time, the following properties of the cells and biomolecules expressed by the cells were assayed:

- Cell growth
- Cell viability
- Total amount of proteins on the samples
- Alkaline phosphatase activity

Four different APC coatings were used in the cell tests: Two coatings produced in ESOC<sup>1</sup> and two different coatings produced in diluted phosphoric acid as reference surfaces<sup>2</sup>. The APC surfaces have been characterized in Section 7.2 and Section 8.3. As standard surfaces, uncoated and cleaned CP titanium and tissue-culture polystyrene were used. In order to compare the APC coatings with state-of-the-art coatings, two different hydroxyapatite surfaces were supplied by the industrial partners. The first HA-surface coating was a sol-gel coating consisting of titania and HA [121]. The second coating supplied was chemically deposited HA coating.

Detailed results of these cell-culture experiments can be found in the report compiled by Thull and coworkers [202]. The resulting changes in relative cell number on the eight different surfaces over time are shown in Fig. 9.5. On tissue-culture polystyrene, the number of cells is rising from the beginning while on CP titanium, all APC coatings, and the sol-gel HA-coating, the number of cells starts increasing only after day 5. The cell numbers on CP titanium and the APC coatings produced in ESOC are very similar throughout the experiment indicating that the new coatings are *not* cytotoxic. On the chemically deposited HA coating, the number of cells stays very low throughout

- 
1. Disc-shaped samples with 13 mm diameter and a thickness of 1 mm, coated at 25 °C, for 90 s at currents of 200 mA and 290 mA respectively.  $\gamma$ -Sterilisation: ca. 34 kGy.
  2. Disc-shaped samples with 13 mm diameter and a thickness of 1 mm, coated in 0.01 M H<sub>3</sub>PO<sub>4</sub> for 90 s at a current of 290 mA at temperatures of 25 or 75 °C respectively.  $\gamma$ -Sterilisation: ca. 34 kGy.
-

the experiment duration. The reasons for the low numbers are not known. The same tendencies have been found for the cell viability, the total amount of proteins on the samples, and the alkaline phosphatase activity. In brief, the results for the coatings produced in ESOC were very similar to the results for uncoated CP titanium. Tissue culture polystyrene leads to slightly better results.

In conclusion, all APC coatings approved to be free of any cytotoxic properties and may therefore be valuable alternatives to commonly used biomaterials and surfaces commonly used. A more differentiated statement is expected from the first *in vivo* study, which is presented and discussed in the next section.

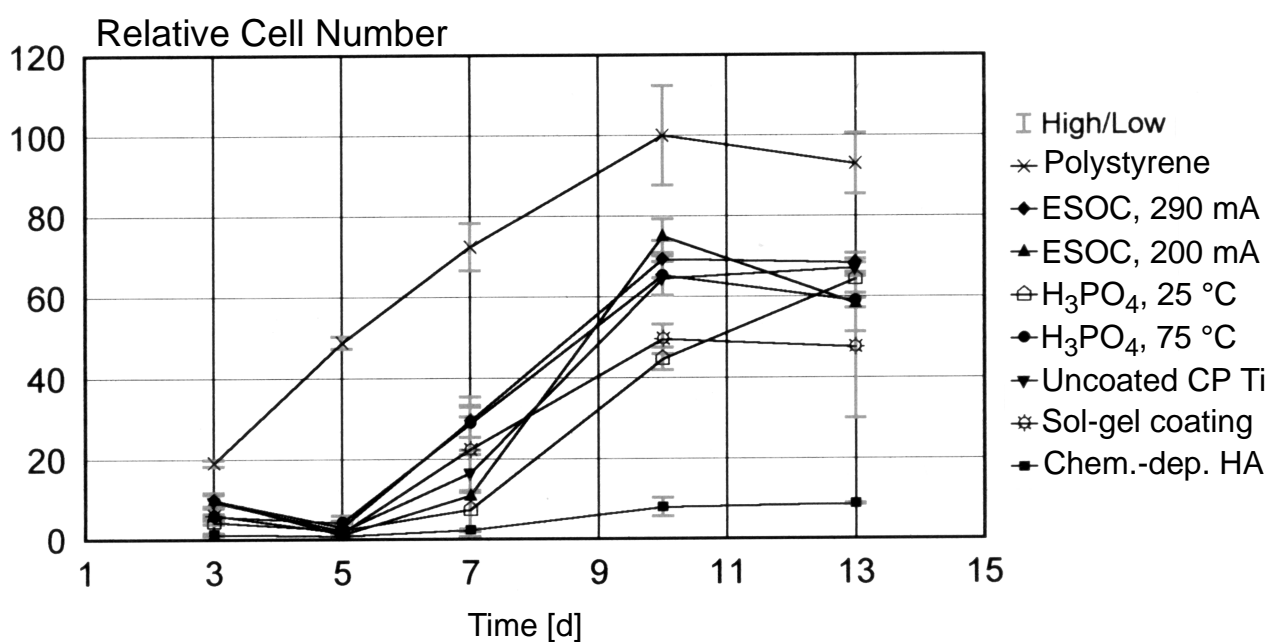


**Fig. 9.5.** Relative change in cell number (normalized to the cell number on polystyrene on day 10) over time (normalized to the cell number on polystyrene at day 10). Tissue-culture polystyrene results in the highest numbers of cells (highest proliferation rate). Similar cell numbers are found on APC layers coated in ESOC and on uncoated CP titanium surfaces.

### 9.3 *The Unloaded in Vivo Study*

The successful outcome of the cell culture study allowed for a first animal study. This study has been carried out in collaboration with the Interface Biology Group of Dr. R. G. Richards, AO Research Institute, Davos, Switzerland. The practical work has been carried out by Patrick Schlegel (as his dissertation).

As an animal model the White Alp sheep was chosen. Cortical screws were implanted into the tibiae of the sheep in a mechanically unloaded position. The aim was to gather information about the general biocompatibility APC coatings in comparison to hydroxyapatite coatings and CP titanium surfaces. Detailed results can be found in the dissertation of Patrick Schlegel [203]. The following experimental part deals mainly with the adaptation of the APC coating process for the cortical screws and gives brief summary of the experimental conditions of the animal study. Furthermore, Section 9.3.2 contains a summary of the results of the animal study. Finally, the conclusions of the first *in vivo* study will be given in Section 9.3.3.

#### 9.3.1 Experimental

APC coatings produced in two different electrolytes were used for the *in vivo* study: APC coatings produced in ESOC at two different current densities (249 and 360 mA at 25 °C) and APC coatings produced in 0.01 M phosphoric acid at two different electrolyte temperatures (25 and 75 °C at 360 mA). The process duration was 90 s for all APC coatings. Prior to the coating process, the cortical screws (Synthes Cortex Screw Ref. 414.016) were cleaned according to the procedure described in Section 4.2. Fig. 9.6 shows an example of a cortical screw.



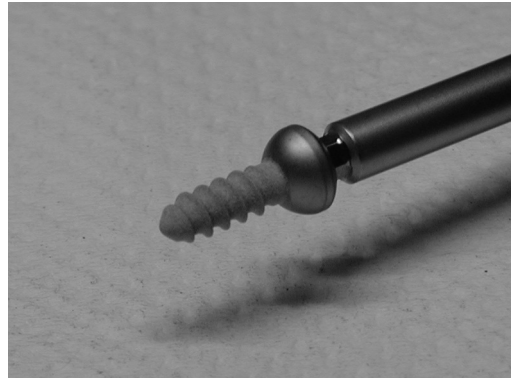


**Fig. 9.6.** Example of a cortical screw as used for the animal study (with VPS coating).

The APC process was adapted for the screws in the same way it was done for the different disc-shaped samples. In a galvanostatic regime the applied current was changed to a value where the time and voltage at which first spark became visible matched with the values for the disc-shaped samples. In ESOC a current of 360 mA applied to one screw corresponded to 150 mA applied to one disc-shaped sample with a diameter of 7 mm, while 249 mA corresponded to 80 mA.

The coating procedure was carried out manually. The change in geometry from the disk-shaped samples to the screws had as a consequence that about 20 % of the coating procedures failed. In most of these 'failed' procedures the voltage rose too slowly and the voltage at the end of the process was up to 60 V lower than the 200 V measured for successful procedures (refer to Section 8.2). The screws obtained in these cases were excluded from the animal study. Reasons for the relatively high rate of failure may be found in material inhomogeneities or varying micro-topographies (with their origin in the machining process). For a production on an industrial scale these influences would have certainly to be investigated more thoroughly.

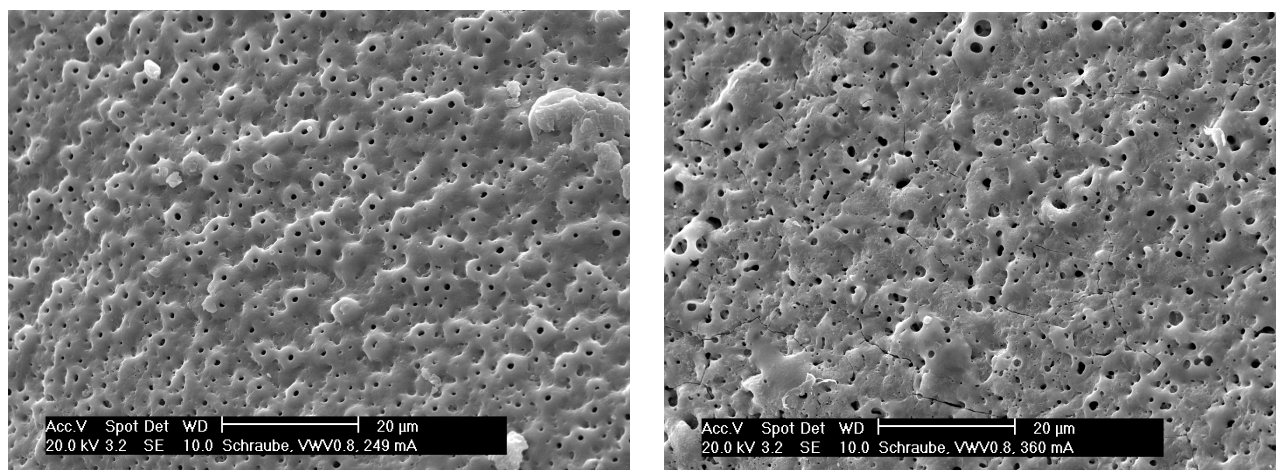


**Fig. 9.7.** SEM micrographs of two coatings produced on corticalis screws in ESOC. The left micrograph shows a area in a thread valley of screw coated at 249 mA. The right micrograph shows a thread valley of screw coated at 360 mA. The most obvious difference between the two coatings is the amount of cracks. More cracks are present on the coating produced at higher current density.

Fig. 9.7 and Fig. 9.8 show representative micrographs of the APC surfaces used in the animal study. In Fig. 9.7 two coatings produced in ESOC are shown. If coated at the higher current (360 mA, 90 s, 25 °C, called VWV-360) the coating structure contains more cracks and the pores are not as regularly distributed over the coating in comparison to the other coating (249 mA, called VWV-249) produced in ESOC. In Fig. 9.8 two different coatings produced in 0.01 M phosphoric acid (360 mA, 90s) are shown (left: 25 °C, called H3PO4-25; right: 75°C, called H3PO4-75). The coating produced at 75 °C has bumpy topography, while if coated at 25 °C the topography of the surface is rather flat with holes distributed over the surface. These holes are not APC pores (refer to Section 7.1). At electrolyte concentrations as low as 0.01 M phosphoric acid, the APC structure (a single breakdown event) becomes very small and the pore is no longer present.

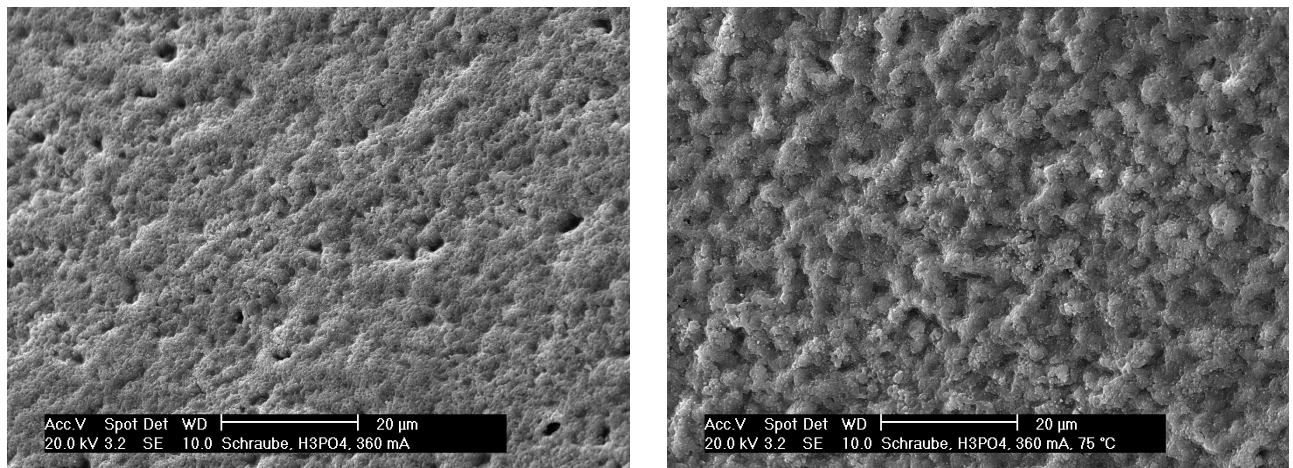


**Fig. 9.8.** SEM micrographs of two coatings produced on corticalis screws in 0.01 M orthophosphoric acid. The left micrograph shows a coating produced at 25 °C, while the coating on the right micrograph was produced at 75 °C electrolyte solution temperature.

The coatings produced in phosphoric acid served as non-soluble standard APC layer in comparison. Additionally, CP titanium screws without CaP coating (called UNT) served as positive control and two different calcium phosphate coatings (called VPS and bmim) served as negative control in the *in vivo* study. The VPS coating is a non-soluble hydroxyapatite coating, while the bmim coating is a chemically deposited soluble hydroxyapatite coating. Prior to the implantation, all screws were  $\gamma$ -sterilized (35.2 kGy).

### 9.3.2 Results

The results as well as the detailed experimental procedure of animal study are part of the dissertation of Patrick Schlegel [203]. In this section a summary of his work reproduced with the kind support of Dr. R. G. Richards, ARI Davos, and Patrick Schlegel.

The cortex screws were implanted into the cis-cortex of the white alpine sheep tibiae. A complete set of Synthes® 4.5mm cortex screws, length 16mm, TiCP, ref: 414.016 (4 APC-coated, 2 hydroxyapatite-coated, and one uncoated but anodized CP titanium screw) were implanted on the left and right tibia of each sheep. The location of each individual screw type was varied in each sheep, so that each screw had been placed once in each location of the template. Fig. 9.9 shows a tibia after the insertion of the screws, within the template.

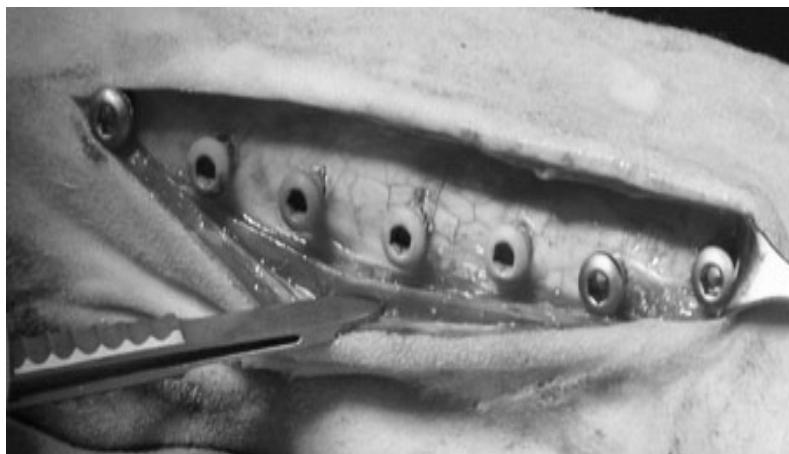


**Fig. 9.9.** Sheep tibia with inserted cortex screws.

---

X-rays of the implantation site were taken at two-week intervals starting on the day of surgery. The thickness of the cortex on each screw surface was monitored over time. Fig. 9.10 shows the cortex thickening over the 12 weeks after implantation for all seven screw types. As a tendency, the increase of the cortex thickness with time is faster for APC-coated screws than for the hydroxyapatite-coated screws (from week 4 to 6). After 12 weeks the thickness of the cortex of the screw type coated in ESOC at the lower current was significantly higher than that of the hydroxyapatite-coated screws. The difference between cortex thickness of the screw type coated in ESOC at higher current and the hydroxyapatite-coated screws was not significant.

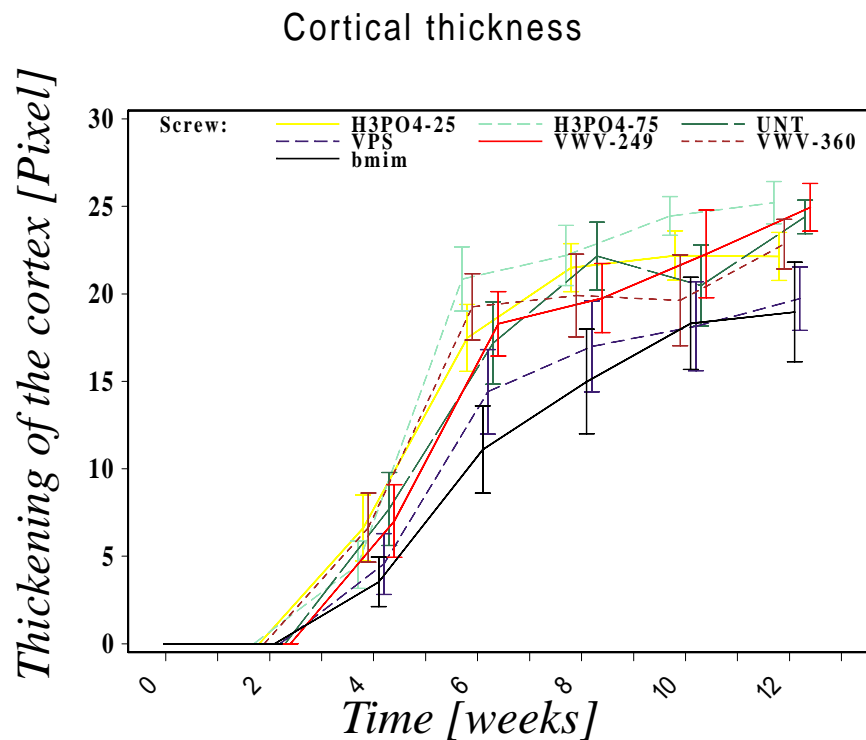


**Fig. 9.10.** Increase of the cortex thickness over time for the different surfaces. The thickness was measured on cross-sections with X-rays. The values are averages of 7 tibiae  $\pm$  standard deviations.

In order to evaluate the implant anchorage, induced by the different surface types, the insertion and extraction torques were measured initially and after 12 weeks at sacrifice. Fig. 9.11 shows the average values for the extraction torque of the seven screw types. The screw types coated with hydroxyapatite (VPS and bmim) exhibited significantly higher extraction torques than all other surfaces. The four surfaces coated with the APC method exhibited significantly higher extraction torques than the uncoated anodized CP titanium surface (UNT). These differences may be attributed to variation between the screw types of coating thickness, varying from zero on the uncoated CP titanium, to a few micrometers with the APC surfaces to 60 to 80  $\mu\text{m}$  with the hydroxyapatite coatings. This increase will produce a pre-load on the screws giving a tighter fit of the implant in the bone, which is known to increase osseointegration and therefore increase the amount of torque required for extraction. To produce screws with these various coatings with only a 1-2 $\mu\text{m}$  in diameter difference would be extremely expensive, since the base screw on which the coatings would be made would have to firstly be made with only 1-2 $\mu\text{m}$  tolerance and vary by the thickness of the applied

coating, which is currently not technically possible (current screw tolerances are between 0.05-0.08 mm). The accuracy of the coating thickness would also have to be produced with a high accuracy of 1-2 $\mu$ m, which is also currently technically not possible.

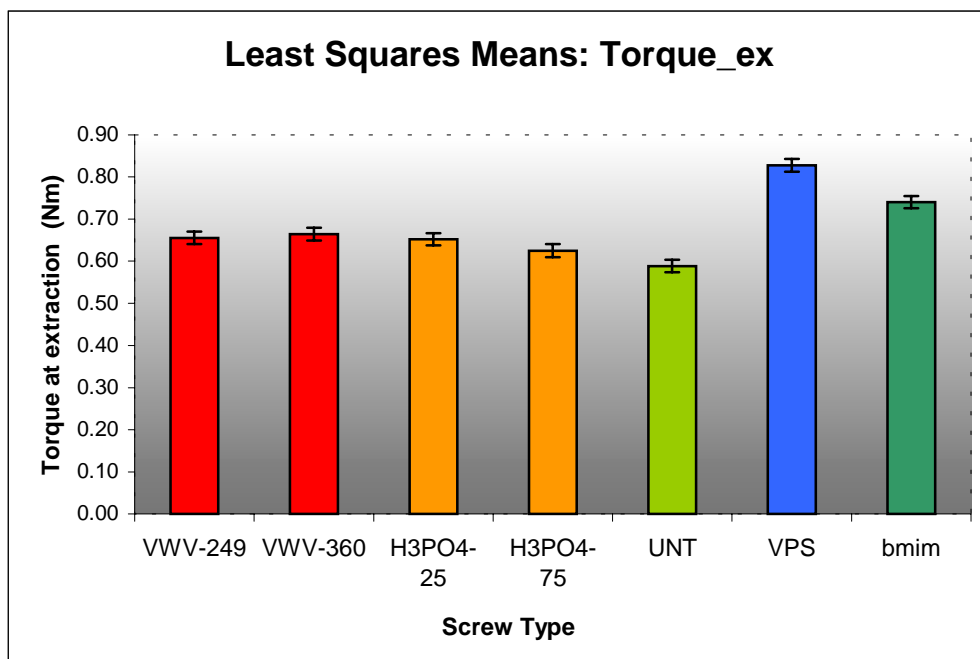


**Fig. 9.11.** Extraction Torque 12 weeks after implantation. The values are least square means, which are adjusted for animal variations and position of the screw in the tibia by statistical analysis.

Bone apposition onto the surfaces of the various screw types at 12 weeks was measured after sacrifice and histological preparation with bright field light microscopy on stained thin sections. No significant difference among the tested screw types was observed in the area of remodeling of the original bone, as well as in the area of the new bone formation towards the screw tips on the endosteal side. Nevertheless, the screws coated in ESOC with the APC-method (VWV-360 and VWV-249) were found to have more implant/calcified bone contact than the other surfaces. Encapsulation of the implant with fibrous tissue was not observed with any screw type tested. The fraction of calcified bone in contact with the implants is shown in Fig. 9.12 for the remodeling of the original cortex. Similar results were found for the new bone formation region (towards the tip the screw in the medullary canal).

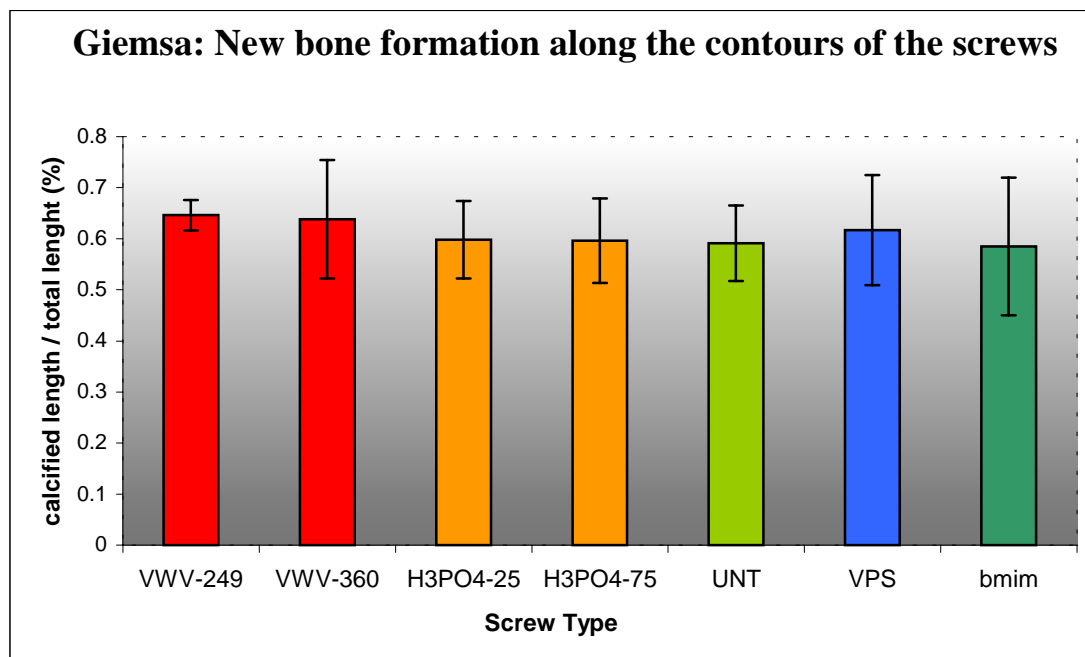


**Fig. 9.12.** Fraction of calcified bone along the contours of the screws. The values are averages of seven tibiae  $\pm$  standard deviation.

### 9.3.3 Conclusions

The screws coated with the APC method in ESOC proved to be biocompatible for bone remodeling and formation. Regarding bone growth induction and the apposition onto the implant surface, the coatings produced in ESOC behaved as well as commercial hydroxyapatite coatings. The unloaded model with the screw does not appear to be sensitive enough to show differences that may occur in clinical situations with other types of implants. If a steel screw as a positive (bad) control had also been used a difference may well have been observed.

Furthermore, the mechanical properties the APC coatings are clearly superior to hydroxyapatite coatings (VPS and bmim) (refer to Chapter 8). However, the anchorage of the hydroxyapatite coating, VPS and bmim, are stronger than that of all APC coatings, but this is very likely to be due to the influence of the coating thickness on the pre-load and therefore anchorage of the implant.





---

# *Investigations on the APC*

## *Process Mechanism*

---

---

### *10.1 Process Mechanism: What is Known*

As described in Chapter 3, the anodic plasma-chemical process (APC) consists of three main process phases. The anodization phase, the breakdown phase, and the APC layer formation phase. During the anodization phase, an oxide film on the surface of the anode is formed as the main reaction, while oxygen evolution may compete as a side reaction on the titanium surface (interface material/electrolyte) [145]. As a matter of fact, the formed oxide layer contains small amounts of anions of the electrolyte solution. Due to the incorporation of impurities or flaw formation in the anodic oxide, another side reaction has to be considered (reported to occur on aluminum), which does take place near the interface metal/oxide, it is the formation of oxygen bubbles within the anodic oxide. Such bubbles are considered to be responsible for pitting and breakdown phenomena [142]. Titanium oxide films exhibit a higher electronic conductivity than aluminum oxide, the oxidation reaction from  $O^{2-}$  to  $O_2$  is therefore assumed to be even more likely to occur during the anodic oxidation of titanium.

The present level of mechanistic understanding of the oxide film breakdown is not really satisfying due to the fact that many important factors (such as mechanical stresses, incorporation of flaws, oxygen film formation, oxygen evolution, etc.) were left aside by Albella et al. for the sake of computability [148]. Since too many factors are likely to play a decisive role in the breakdown process, the process is commonly described in a phenomenological way rather than a consistent

mathematical model. Shimizu and coworkers have investigated the occurrence of breakdown events on aluminum in borate solution [144]. They found isolated locations at the surface where the anodic oxide film had broken down, as well as radial cracks in the oxide films starting from the breakdown location. The most interesting finding of the study is the detection of the first breakdown events (with respect to voltage) at locations where flaws were present in the oxide film. According to the authors, one possible kind of flaw may consist in oxygen cavities inside the anodic oxide layer.

The cited work was carried out on high-purity aluminum surfaces. Much less information is currently available on titanium. Hence, a high-resolution scanning electron microscopy study was carried out to obtain phenomenological information about the APC process mechanism on CP titanium and to allow for the comparison between the published findings on aluminum and the results of this thesis on CP titanium surfaces.

## 10.2 High-Resolution SEM Study of the different stages of the APC Process

### 10.2.1 Experimental

**Sample preparation.** 50  $\mu\text{m}$  thick CP titanium foil (Goodfellow, No LS218178 LC,  $\geq 99.6$  wt-% purity) was cut to sample size (see Fig. 10.1) using standard scissors. The samples were square shaped with an attached narrow stripe for the electrical contacting.

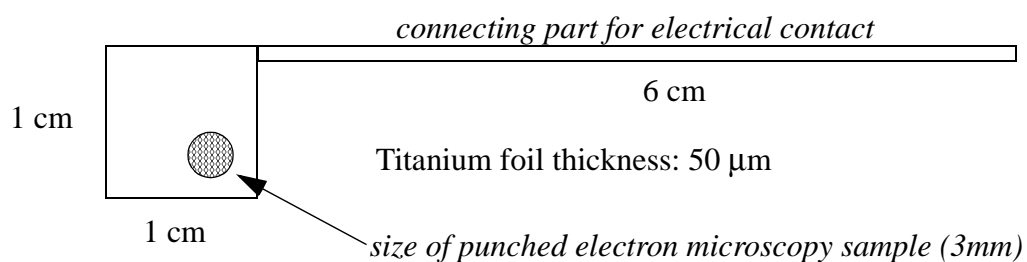


**Fig. 10.1.** Titanium foil sample for HRSEM study. Circular shaped samples with 3 mm of diameter were punched out of the square-shaped part of the sample after applying the APC-coating.

The samples were degreased and etched as described in Section 4.2. After the cleaning the samples were wrapped into aluminum foil for storage.

The samples were coated a) in the newly developed ESOC electrolyte (containing Ca, PO<sub>4</sub> at pH 14), and b) in 0.01 M orthophosphoric acid. To obtain information about the process mechanism, the coating process was stopped at different voltages between 0 and the final voltage after 90 s of APC treatment. All experiments were performed at a constant current density of 250 mA.

After coating, the samples were carefully rinsed with ultra-pure water and subsequently allowed to dry. For the HRSEM, circular-shaped samples with a diameter of 3 mm were punched out of the coated sample with a standard punch device for transmission electron microscopy sample preparation.

The 3 mm samples were sputter coated with a very thin layer of tungsten in a Balzers MED 010 table-top, high-vacuum coating device. After inserting the samples into the coating chamber, the chamber was evacuated down to a pressure of  $5 \cdot 10^{-5}$  mbar. Then, the pressure was increased to the sputter pressure of  $5 \cdot 10^{-2}$  mbar by supplying pure argon gas. Tungsten was sputtered onto the samples up to a thickness of 1 nm. The thickness of the sputter coating was monitored by a quartz crystal balance.

**Investigation method.** In order to achieve a high lateral resolution of 2-3 nm with SEM several prerequisites have to be met (the principle of scanning electron microscopy has been discussed in Chapter 6):

- The electron source has to be very bright (high current per solid angle) and the energy distribution of the emitted electrons must be very narrow in order to minimize the effective electron probe size at the sample [176]. A typical electron source meeting these prerequisites is the cold field emission gun (FEG). In contrast to the widespread heated tungsten hairpin source, FEGs exhibit a brightness up to a thousand times higher and an energy spread lower by a factor 3 to 5 [176]. To further reduce the probe diameter, the acceleration voltage has to be high (> 20 kV). All these measures together allow for an effective electron probe size of 0.7-1 nm (Hitachi S-5200).
- The volume information in the electron signal has to be minimized. This is somehow contradictory to the prerequisite above, since the information volume increases with increasing acceleration voltage. However, a method to avoid this problem has been demonstrated among others by

Hermann and Müller [204]. They showed that if materials with a low density (such as organic materials) are coated with a very thin film (1 to 3 nm) of a heavy metal, the resulting secondary electron (SE) signal is determined by SEs excited by the incident primary electron beam (SE1) and not by secondary electrons that are excited by backscattered electrons (SE2). The metal layer has to be of high density in order to reduce the escape depth of the SEs to approx. one nanometer. In such a thin layer the production of multiply scattered primary electrons is very unlikely (3.8 nm for electrons with 30 keV electrons in gold [205], page 83). As a consequence, the amount of backscattered primary electrons in the metal layer is low. Thus, most of the incident electrons from the electron beam pass the metal layer without being backscattered. As soon as they enter the low-density material underneath the metal layer, the mean free path of the primary electrons is increased by factor of more than 10 ([205], page 83). With respect to the heavy metal layer, the primary electrons are distributed due to scattering processes over a large volume. They may leave the sample surface again as backscattered electrons (BSE) and thereby excite secondary electrons (SE2). The number of these BSE is relatively low in materials with low density and low atomic number compared to the very localized SE1 yield amplified by the heavy metal layer. The heavy metal coating can be seen as an artificial density step in the material, which concentrates the SE1. Without coating, the SE1 signal would contain a higher information volume (since the mean free path is increased with decreasing density or atomic number) and it would continuously be superimposed by the SE2 signal. Working at low acceleration voltages would reduce the information volume but is inevitably associated with a broadening of the primary electron beam.

The investigations have been carried out with a Hitachi S-900 in-lens SEM with field emission gun. The working distance was 0.3 mm. The acceleration voltage was 30 kV and an beam current of 100 pA was applied. The findings were cross-checked with uncoated samples in order to exclude artefacts from the sputter procedure and the deposited metal layer.

### **10.2.2 Results**

**The titanium surface before anodization.** Two SEM micrographs of CP titanium surfaces before anodization are provided in Fig. 10.2. The cleaning of the samples with HF/HNO<sub>3</sub> has the side effect that grain boundaries and other imperfections of the metal are etched faster than the bulk of the grain

so that grain boundaries become visible as grooves on the surface [30]. The micrograph at higher magnification shows oxide domes grown at a grain boundary [206].

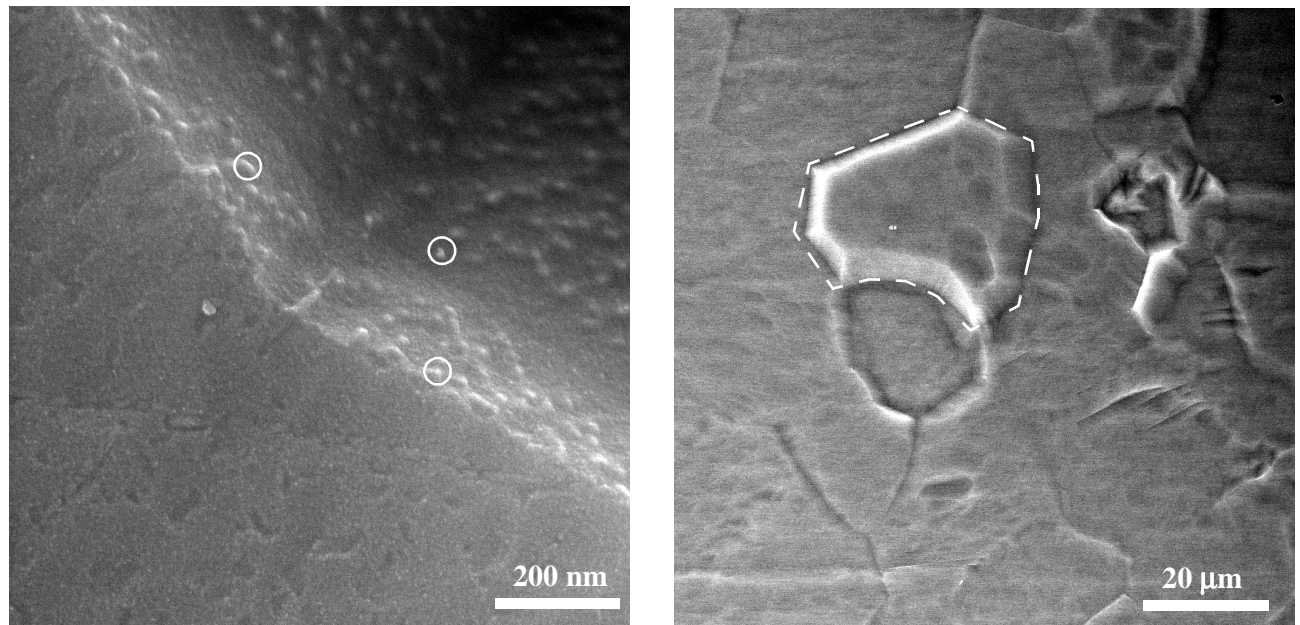


**Fig. 10.2.** SEM micrographs of a cleaned CP titanium surface prior to the anodization treatment. On the left micrograph, a grain boundary is shown at high magnification. It shows local oxide dome formation (examples marked with circles) [206]. On the right micrograph, the grain structure of the CP titanium substrate is visible due to the etching with HF/HNO<sub>3</sub> (polygon).

**Phosphoric acid.** The different phases of the APC process in orthophosphoric acid are shown in Figs. 10.3 to 10.7. The anodization process was stopped at 50, 100, 150, 200, and 350 V respectively. In Fig. 10.3 the titanium surface was anodized to 50 V. At a high magnification (left micrograph) one can see that the anodic oxide has formed inhomogeneously in the form of island-like structures, growing first perpendicular to the surface and subsequently spreading laterally. The islands touch each other at some point and grow together. In Fig. 10.4, the anodization process was stopped at 100 V at which state the islands have more or less coalesced. Additionally, blisters have formed underneath the oxide film at many sites of the surface. They occur in the bulk grain areas as well as at the grain boundaries. Some of the blisters are open and allow a view into the hollow and empty inside of the blister. The high magnification micrograph in Fig. 10.4 reveals that the grown anodic

oxide is not homogeneous and dense bulk oxide but contains a certain degree of porosity underneath the surface of the oxide (marked on the image with a rectangle).

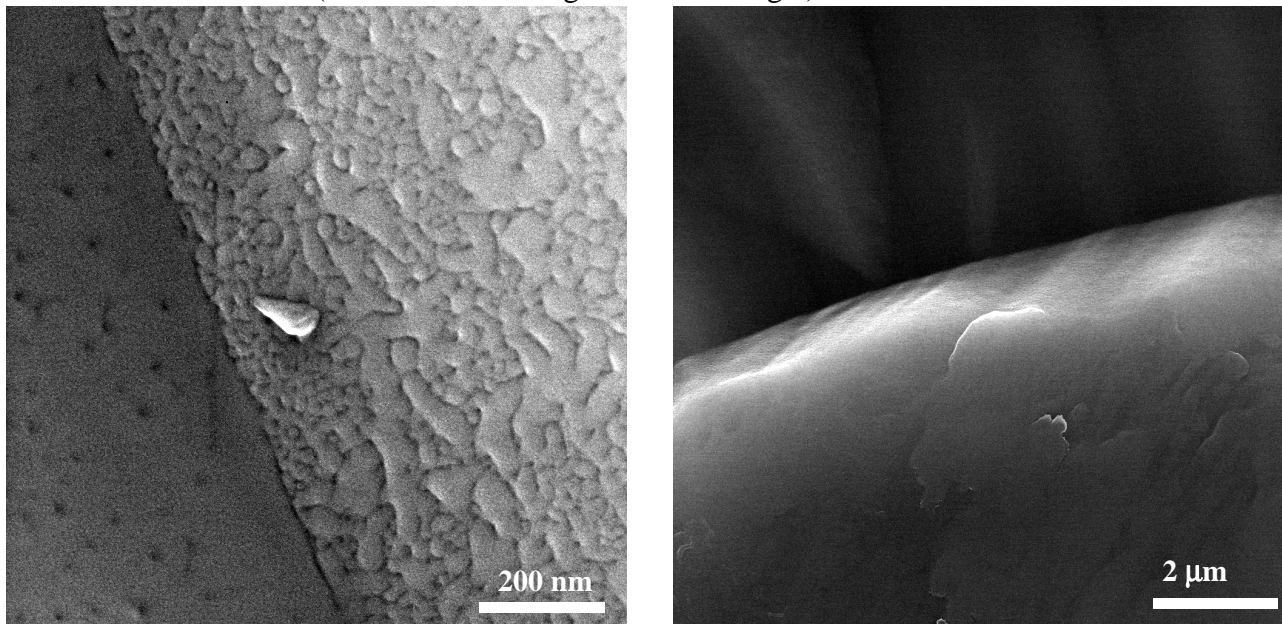


**Fig. 10.3.** CP titanium surface anodized to 50 V (250 mA, 25 °C) in 0.01 M phosphoric acid. The left picture shows the oxide growth near a grain boundary. The oxide grows irregularly over the surface.

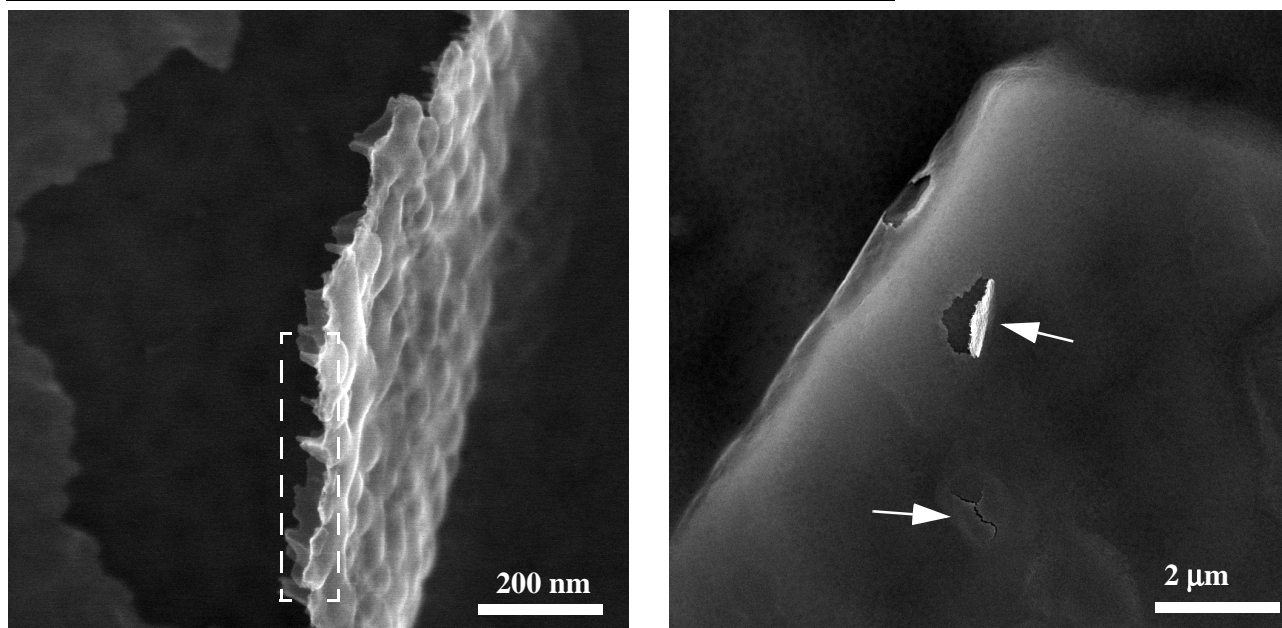


**Fig. 10.4.** CP titanium surface anodized to 100 V (250 mA, 25 °C) in 0.01 M phosphoric acid. At 100 V blister-like parts of the anodic oxide film have delaminated from the substrate. A detailed view of one of the blisters is provided for in the left picture (corresponding to that at the upper arrow in the overview picture) The thickness of the oxide film is not constant and it seems that the film itself is porous underneath its surface (rectangle).

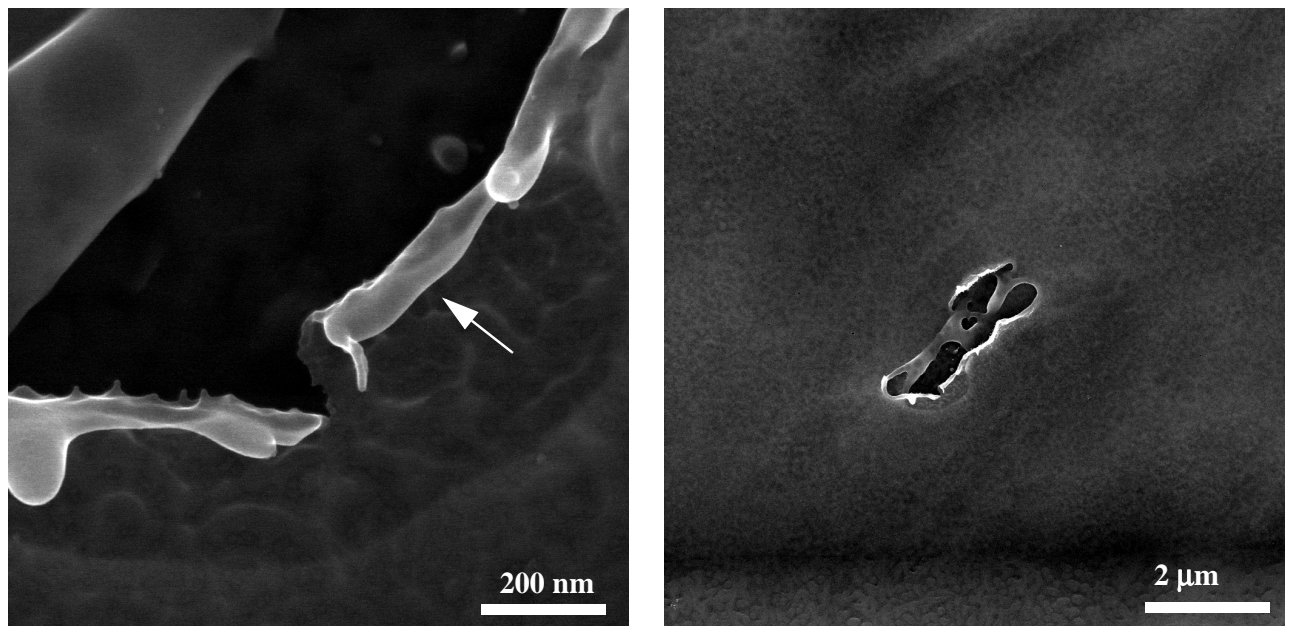


**Fig. 10.5.** CP titanium surface anodized to 150 V (250 mA, 25 °C) in 0.01 M phosphoric acid. The two micrographs show an isolated breakdown. It is located at a blister-like structure, which has weakened the anodic oxide layer. The micrograph on the left shows a detail of the breakdown, where it becomes evident that the oxide film has locally fused.

If the process is stopped at 150 V, first and isolated breakdown events occur (Fig. 10.5). The rounded edges of the oxide at the breakdown site indicate that the oxide was fused temporarily (arrow). At this stage, the location of the breakdown event correlates with the blisters. At 200 V (Fig. 10.6), the breakdown events have spread over the surface, possibly starting from a single blister. At high magnification (micrograph on the left side of Fig. 10.6), the typical APC structures emerge characterized by round breakdown sites with small holes from evaporating electrolyte in the center. The overall impression is that the coating is still incomplete and the thickness of the oxide at the healed sites is comparable to the anodic oxide around the breakdown. Anodizing to 350 V results in the typical oxide that have been reported in Chapter 7. The surface is completely and evenly covered with an APC layer. Starting from the nanometer level, there are surface features in the range of several nanometers, hundreds of nanometers, and several micrometers superimposed on each other, resulting in a complex surface topography.

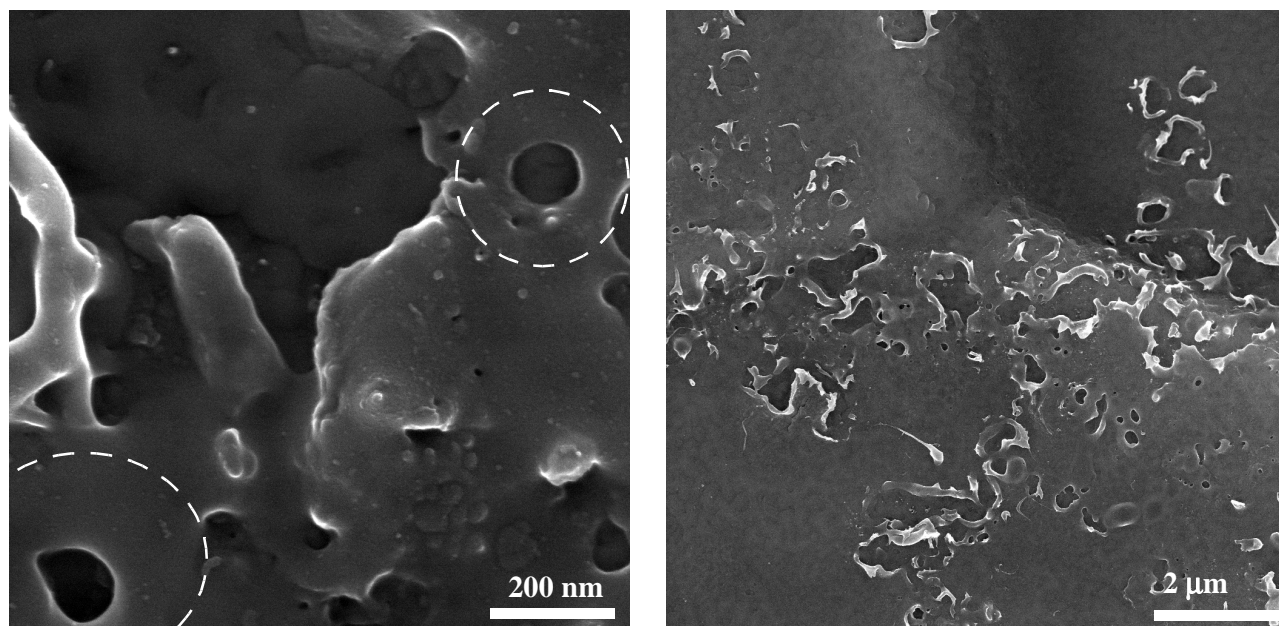


**Fig. 10.6.** CP titanium surface anodized to 200 V (250 mA, 25 °C) in 0.01 M phosphoric acid. The micrograph on the left side shows the typical APC structure characteristics (rounded breakdown structures with pore from evaporating electrolyte, (circles)). The overview on the right side shows that the APC process has not yet covered the whole surface.

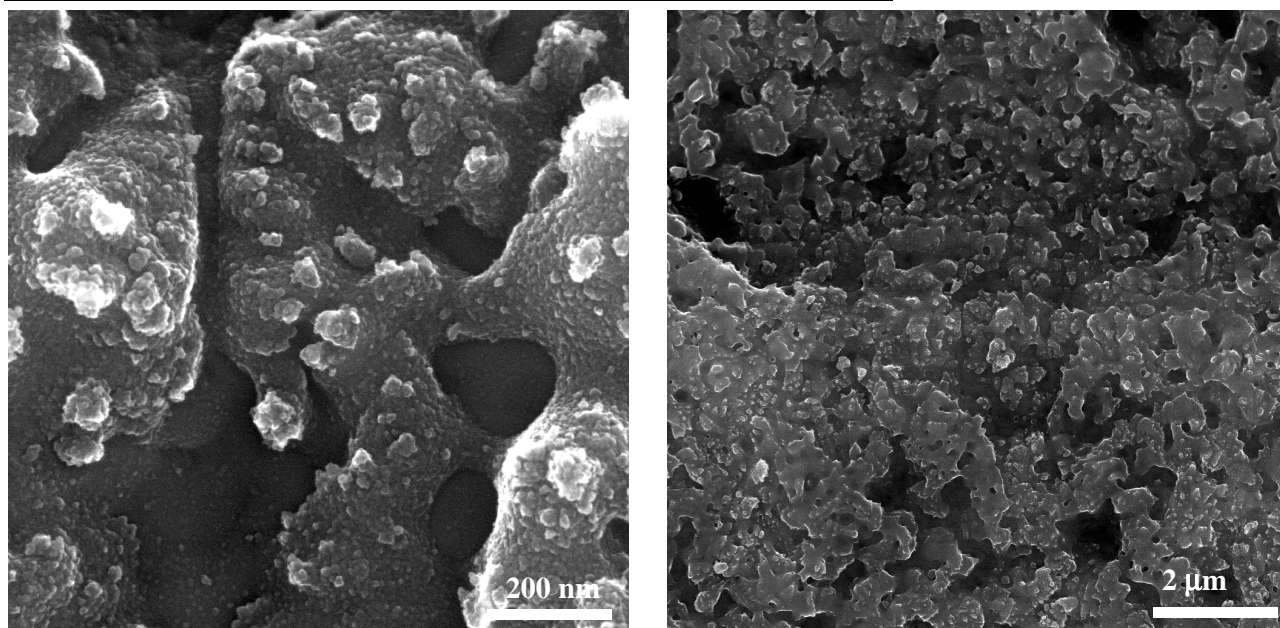


**Fig. 10.7.** CP titanium surface anodized to 350 V (250 mA, 25 °C) in 0.01 M phosphoric acid. At 350 V an APC layer with peak and valley structures on different length scales has developed: in the range of a few nanometers, hundreds of nanometers (both on the left picture) and in the range of micrometers (picture on the right side).



**ESOC electrolyte.** Different stages of the APC process with the ESOC electrolyte have been investigated analogously to the investigation performed with orthophosphoric acid. Unlike the phosphoric acid, ESOC contains higher concentrations of salts. Therefore the oxide film breaks down at lower voltages [149,156]. Using the ESOC electrolyte it was also investigated what changes in the surface structure of the APC coating would occur if the process was not stopped after 90 s but continued up to about 220 V, where the process became unstable and the voltage started to fluctuate within a range of more than 20 V.

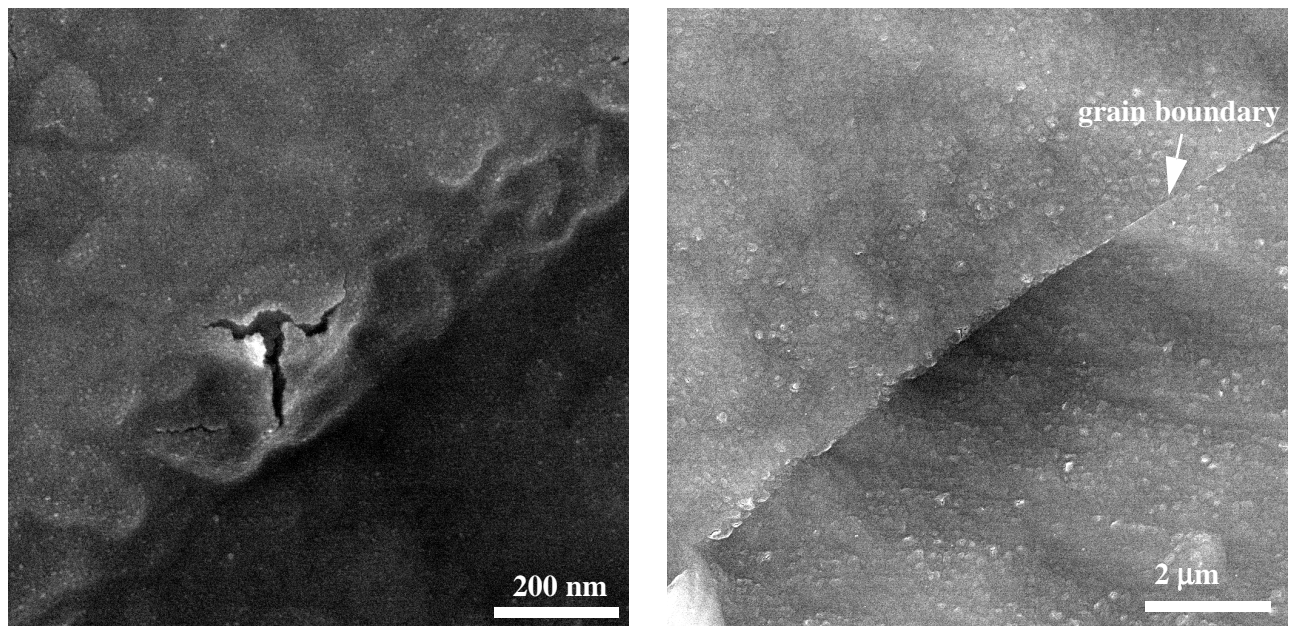


**Fig. 10.8.** CP titanium surface anodized to 20 V (250 mA, 25 °C) in ESOC electrolyte. Already at 20 V, first blisters appear on the titanium surface anodized in ESOC. Compared to the blisters grown in phosphoric acid, the blisters grown in ESOC are smaller.

The first pair of micrographs (Fig. 10.8) shows a sample anodized galvanostatically to 20 V at 250 mA. Already at this low voltage, blisters have formed at the surface. However, compared to the phosphoric acid electrolyte, the blisters formed in ESOC are smaller. The blisters look as if they had grown out of the oxide domes that were originally present on the titanium surfaces prior to anodization (Fig. 10.2). As the blisters formed in phosphoric acid, the blisters formed in ESOC are present not only at grain boundaries but also in the bulk grain area.

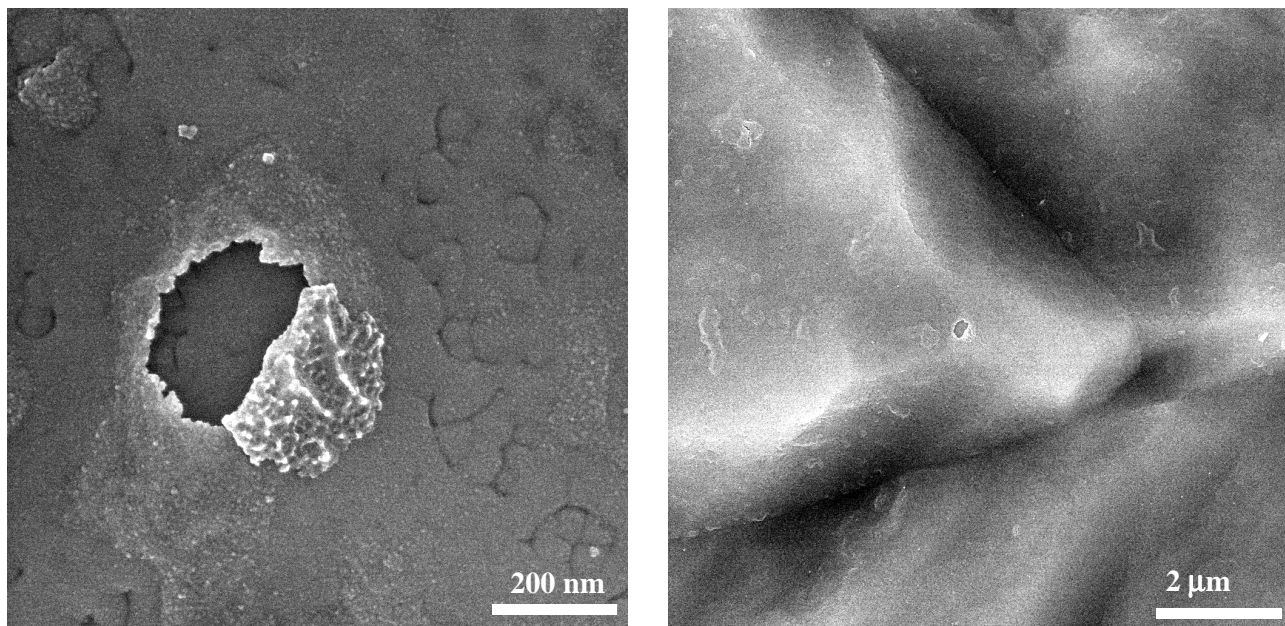


**Fig. 10.9.** CP titanium surface anodized to 40 V (250 mA, 25 °C) in ESOC electrolyte. At 40 V the topography has become coarser (with respect to the surface at 20 V). On the left-hand side a blister has burst and a lid-like part has folded back allowing for a view of the inner side of the oxide layer.

If the process is stopped at 40 V (Fig. 10.9), the island-like oxide structures touch each other and coalesce, similar to the situation with the phosphoric electrolyte. It is important to note that the blister has not burst by cracking but by folding back of the blister lid. The backfolded lid provides information on the interface between the anodic oxide film (lid) and the substrate. Interestingly enough, this interface is neither flat nor does it show the typical characteristics of a ceramic fracture. It rather indicates that the anodic oxide film was porous already before the large blister had formed. At about 60 V, first breakdown events become visible on the surface. The left micrograph of Fig. 10.10 shows a single breakdown at high magnification. The breakdown is located at an opened blister and shows the characteristic rounded oxide structures (arrow on left micrograph of Fig. 10.10) indicating the presence of temperatures beyond the melting temperature of the oxide. At 80 V (Fig. 10.11) the density of breakdown events has significantly increased, while the thickness of the healed oxide is still qualitatively comparable to the thickness of the anodic oxide film before the breakdown (estimated from the SEM micrographs).

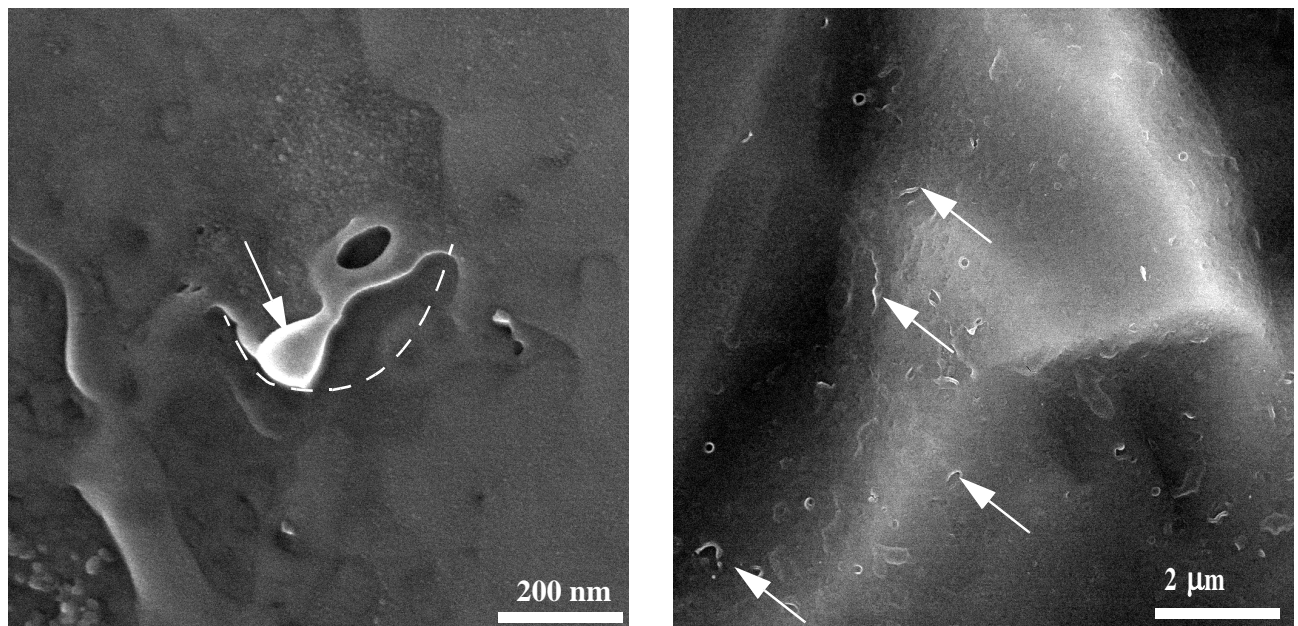


**Fig. 10.10.** CP titanium surface anodized to 60 V (250 mA, 25 °C) in ESOC electrolyte. Around 60 V, first breakdown events are present on the surface. They are indicated by the rounded structures of the blister edges, which show that the material had fused (left image, dashed line: form of the blister before the breakdown). The breakdown events at this stage are isolated and are distributed all over the sample surface (overview image on the right, arrows).

The typical APC layer structure is found for samples anodized to 112V (Fig. 10.12), even though a single breakdown event is small with respect to the surfaces shown in Chapter 8. An estimation of the layer thickness is now no longer possible, since the APC coating covers the sample surface completely.

When preparing the samples for the cell culture and the animal study (both Chapter 9), the APC process was stopped after 90 s at a voltage of 180 to 200 V. Therefore the micrographs from a sample anodized to 190 V (Fig. 10.13) represent the final appearance of titanium surfaces coated in ESOC throughout this PhD thesis. The structure of the APC layer coarsens between 112 V and 190 V. Cracks are present at 190 V, probably due to thermal stresses in the APC layer. Furthermore, the smooth surface of the breakdown sites (not considering now the principal topography of a breakdown), is roughened by the formation of fine structures of nanometer size. This superimposed topography is even more pronounced if the process is not stopped at 190 V but at 220 V.

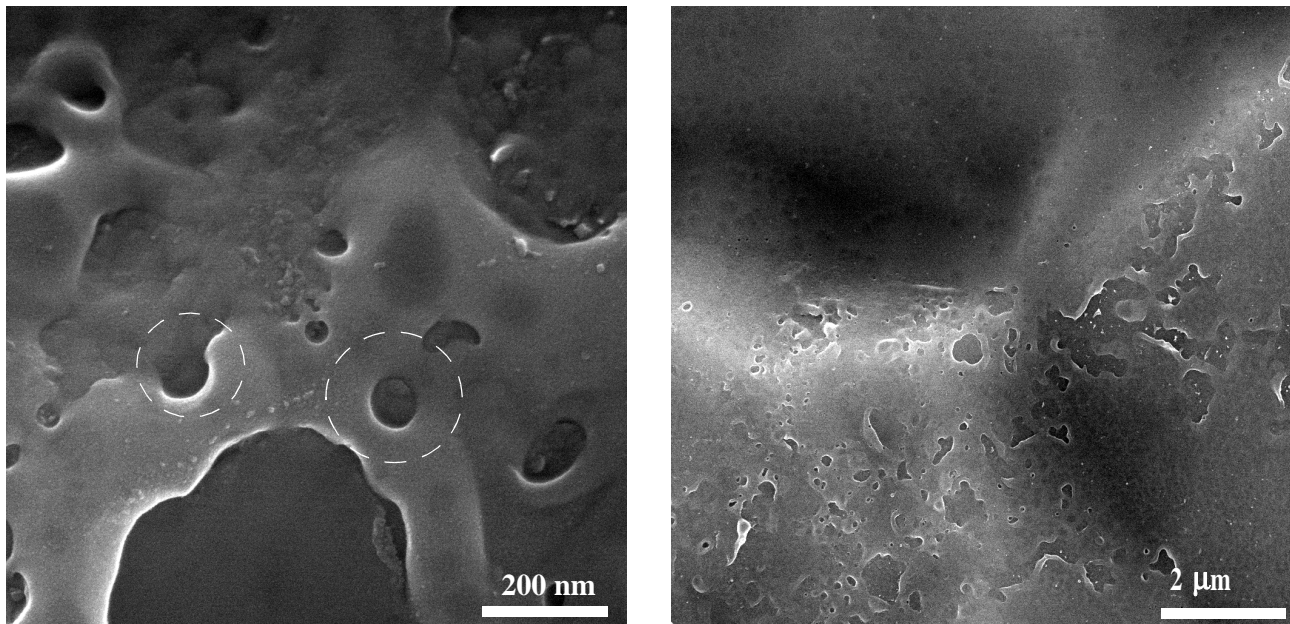


**Fig. 10.11.** CP titanium surface anodized to 80 V (250 mA, 25 °C) in the ESOC electrolyte. At 80 V the surface is covered completely with breakdown events, but the local healing process did not yet lead to a thick APC coating. Typical APC structures are marked with circles. The pores are due to evaporating electrolyte.

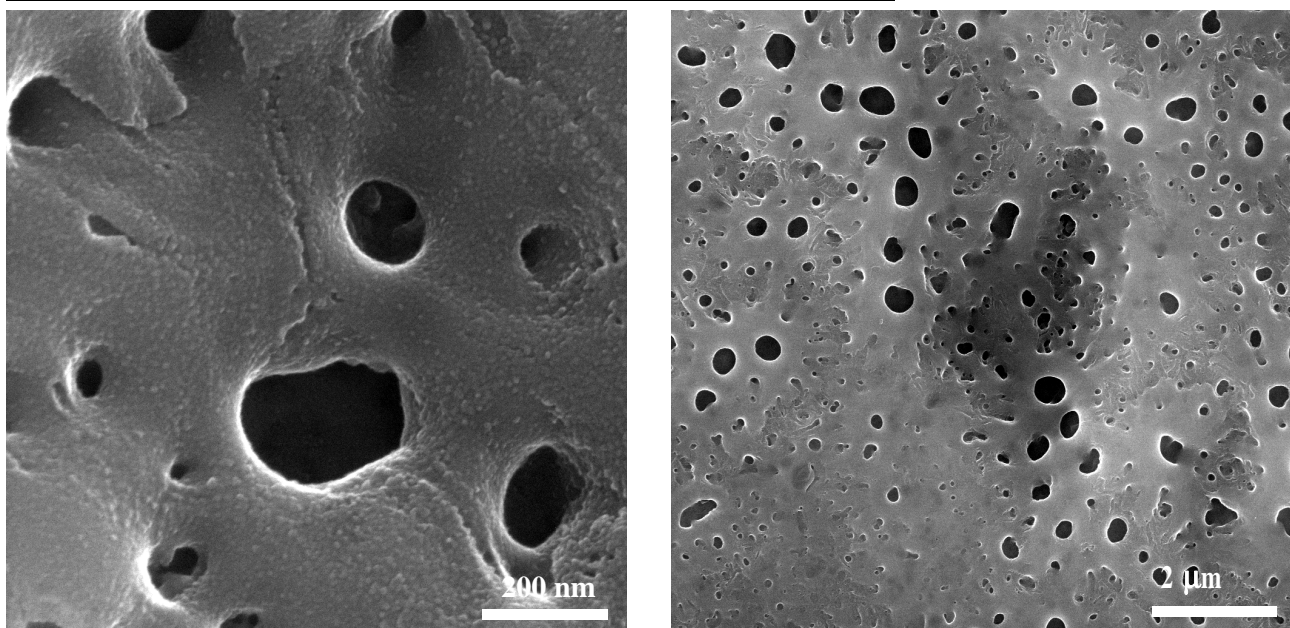


**Fig. 10.12.** CP titanium surface anodized to 112 V (250 mA, 25 °C) in ESOC electrolyte. At 112 V a confluent APC layer has formed on the surface.

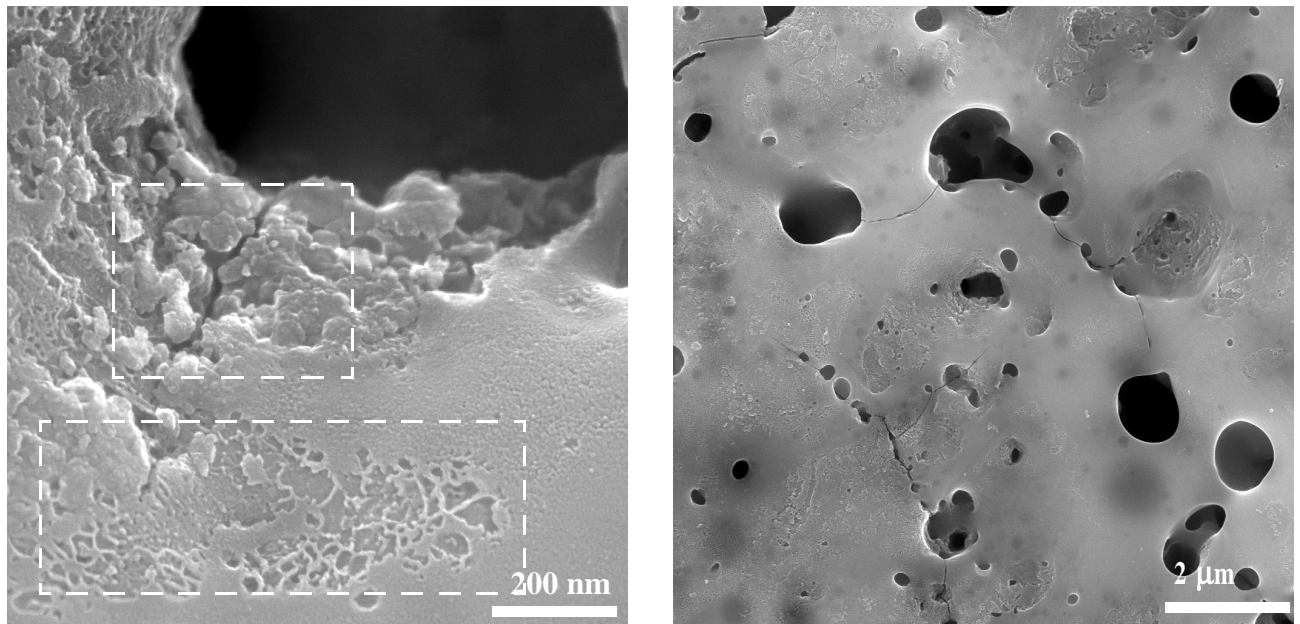


**Fig. 10.13.** CP titanium surface anodized to 190 V (250 mA, 25 °C) in ESOC electrolyte. The APC process was usually stopped at about 190 V (refer to Chapters 8 & 9). Compared to the micrographs taken on surfaces anodized to 112 V, the APC coating has become coarser. Additionally, fine structures are superimposed on the breakdown sites (rectangles), which increases the roughness of the coating on the nanometer level.

If anodized to about 220 V (Fig. 10.14), the APC layer is covered with cracks. The surface around the pores is no longer smooth but porous itself and appears at some points as a honeycomb-like structure. The process at this stage is neither stable nor reproducible. The voltage/time-curve for the surface shown in Fig. 10.14 is plotted in Fig. 10.15. The voltage drops temporarily from about 220 V down to below 50 V. It is, however, not possible to correlate the voltage drops with any feature present on the surface after the coating procedure.

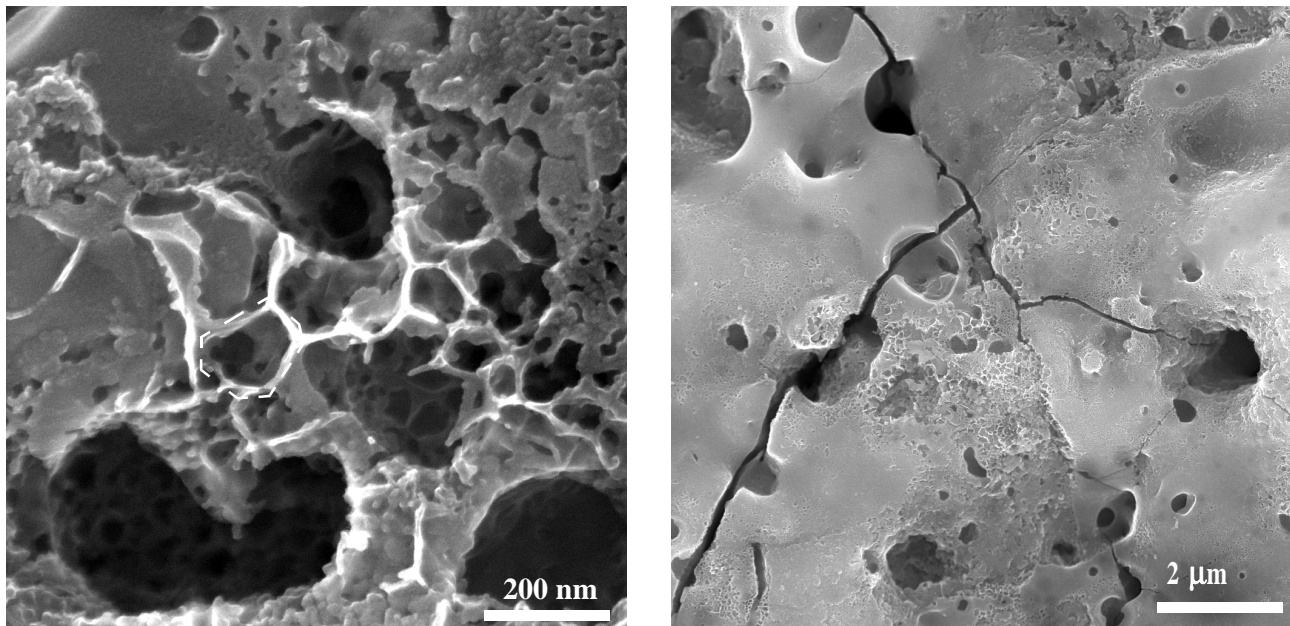


**Fig. 10.14.** CP titanium surface anodized to 220 V (250 mA, 25 °C) in ESOC electrolyte. At this stage cracks become the dominant features on the surface, probably due thermal stresses in the APC layer. In addition, honeycomb-like structures could be found at some of the breakdown locations (polygon).

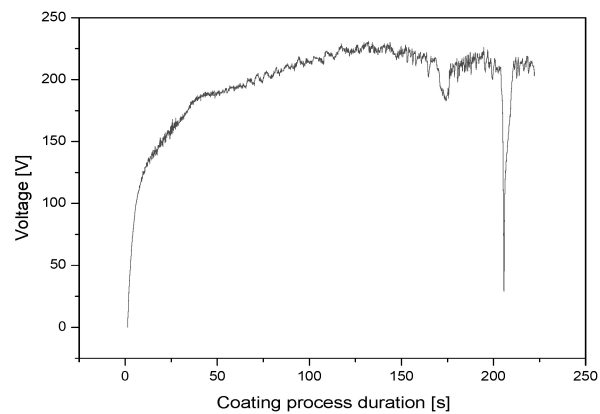


**Fig. 10.15.** Voltage/time curve for the surface shown in Fig. 10.14. At this extreme time conditions, the process becomes unstable. The voltage drops from 220 V down to below 50 V.

### 10.2.3 Discussion

Based on literature [156] and experimental observations during the study, the breakdown voltage,  $V_B$ , for titanium in 0.01 M phosphoric acid was expected to be around 300 (own experiments) to 350 V ([156]). The breakdown voltage values were assessed by taking the voltage at which the first sparks appeared. The present SEM study proves that this way of assessing  $V_B$  results in values for  $V_B$  that are too high. The first breakdown events occur at much lower voltages (as low as 150 V) in the case of titanium in 0.01 M phosphoric acid. This is half of the value reported in the literature. The same is true for titanium anodized in ESOC. My own observations on the first visible spark yielded values for  $V_B$  of about 115 V. The correct value is between 50 and 60 V (assessed by SEM). Probably, the amount of light emitted at breakdown events at 60 V for ESOC, and 150 V for phosphoric acid respectively, is too small to be recognized by the human eye. Further difficulties to identify the sparks arise from oxygen evolution at the anode during the anodization phase of the process, which screens the sparks.

Irrespective of the electrolyte, blisters appeared at the surface of the anodized titanium samples at voltages as low as 20 V for samples anodized in ESOC and less than 100 V in phosphoric acid. Only little is known about these blisters appearing on the surface during the anodization of titanium. Two possible explanations for their appearance are set forth here.

1. The specific volume of the oxide formed during the anodization is larger than the specific volume of the consumed metal. The so-called Pilling-Bedworth (PB) ratio (ratio of the specific volume of the oxide to specific ratio of the consumed metal) for  $TiO_2/Ti$  is 1.93 [149]. If the PB ratio is larger than unity, compressive stresses occur in the oxide during the anodization. According to Parkhutik [149], the compressive stresses can lead to layer formation in the oxide, subsequent delamination, and eventual cracking of the delaminated oxide (if the tensile stresses that are induced by the delamination exceed the elastic limit of the oxide). However, no explanation is found for the failure of the blister shown in Fig. 10.9.
2. Crossland and coworkers reported the formation of oxygen bubbles within the oxide layer during the anodization of aluminum near the metal/film interface [142]. They identified flaws (impurities or second phase particles) as locations where the oxidation of  $O^{2-}$  to molecular oxygen took place [142].

Since the electronic conductivity of titania is higher than that of alumina, the oxygen formation is even more favorable for titania. The extensive formation of oxygen near the interface metal/anodic oxide layer could lead to locally very high mechanical stresses and therefore to blisters. The kind of mechanical stresses that occur in the case of blister formation are not compressive stresses but tensile stresses. In the case of tensile stresses induced by oxygen formation, the failure of the blister with the formation of a lid seems plausible. However, on titanium and under the anodization conditions set up for the APC process, it has not yet been confirmed that the blisters contain indeed oxygen.

Scharnweber investigated the blister formation on titanium by transmission electron microscopy [207]. He found that the interface blister/substrate is not located at the metal/oxide-interface but at the interface between natural oxide layer and anodic oxide layer. The author also claims that the blisters occur due to molecular oxygen formation at the interface between the natural and the anodic oxide film.

In order to find evidence for the second explanation, a simple experiment was performed based on the following assumption [208]:

- A cavity is required to enable the formation of molecular oxygen. This cavity may be an irregularity around an inclusion or at a grain boundary. It may even be an accumulation of dislocations due to mechanical deformation of the metal.

Hence, cleaned CP titanium foil was plastically deformed at defined points with a micro-hardness tester in order to produce local accumulations of dislocations. The deformed foil was subsequently anodized in ESOC up to voltages where blisters occurred. However, the investigation of these surfaces in the SEM did not reveal any correlation between hardness imprints (i. e., local deformation) and blister formation.

It is evident from the reported investigation with high-resolution SEM that the first breakdown events occur at open blisters. After the blister has opened by cracking of its surface, a new interface between electrolyte and sample is created inside the blister, where the oxide is not as thick as the rest of the primary anodic oxide film of the sample. Due to the applied voltage the inside of the blister is



suddenly oxidized in the same way as the detached oxide of the blister was oxidized before. Fig. 10.16 depicts a section through a blister on the sample surface. A potential location for the dielectric breakdown is the interface between the detached blister oxide and the oxide inside the blister (rectangle), which has formed after the electrolyte had contacted the inner part of the blister.

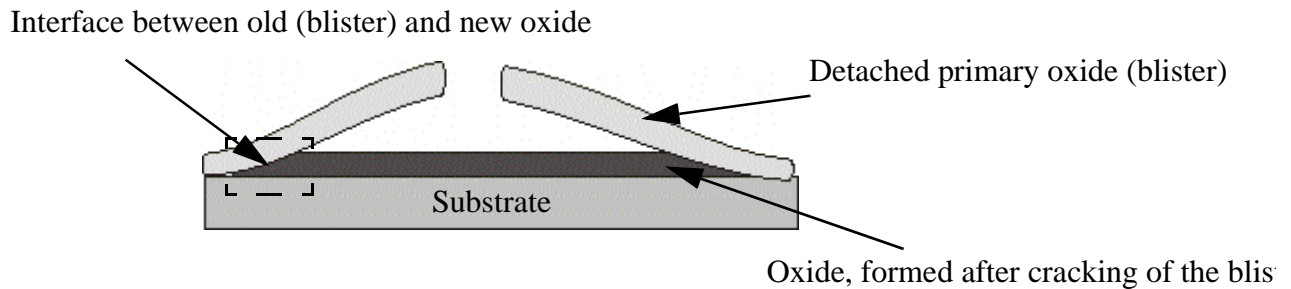


**Fig. 10.16.** Schematic cross section through a blister. After the inside of the opened blister is electrically contacted with electrolyte, new oxide is formed inside the blister (dark grey). An interface between old (blister) oxide and new oxide is created. This interface is probably the location of the first breakdown events.

Two conclusions may be drawn: Admittedly, both mechanisms, blister formation due to the high PB-ratio (for Ti/TiO<sub>2</sub>) with subsequent compressive stresses and blister formation due to oxidation of oxygen cations, may take place. The compressive stresses may induce a first detachment of the oxide film forming a small cavity and enabling the formation of molecular oxygen. The further increase of the blister volume may be mainly driven by the high oxygen pressures inside the blister. Secondly, one can clearly make a statement concerning the location of the first breakdown events. The first breakdown events are located at cracked blisters.

### 10.3 A Proposal for the APC Process Mechanism

Wirtz, Brown, and Kriven divided the APC process into three phases: (phase1) conventional anodization phase, (phase 2) breakdown of the anodic oxide film, and (phase 3) healing and layer formation phase [20]. This classification has to be modified for phases 1 and 2 based on my own experimental findings. During the anodization phase blister-like structures are formed (see Section 10.2.2), which weaken the anodic oxide and act as weak points [20,144] in the anodic oxide film. the first breakdown events clearly take place much earlier than reported in the literature [156].

However, due to the low voltage, their energy is insufficient to form an APC coating. With increasing voltage the breakdown events contain more and more energy, which leads to the fusion of the metallic substrate material and the desired incorporation of electrolyte constituents. The details of film formation in phase 3 remain unclear after the SEM investigation. It was not possible by SEM to find a border between APC coated and uncoated areas. The results suggest that the APC layer formation process is a continuous process rather than being divided into distinct phases.

In summary, the proposed process mechanism can be described as a logical sequence of individual events that occur on the anode surface:

1. As soon as a positive voltage is applied to the sample, a conventional anodic oxide layer starts to grow on the surface.
2. As the oxide grows, blister-like structures may form locally.
3. At a certain voltage at which the electron current locally exceeds a critical value (see Chapter 3), the first dielectric breakdown events occur. These breakdown sites coincide with the blister-like structures and result in the formation of an oxide film with a thickness similar to the anodic oxide around the breakdown site.
4. As the voltage increases further, the single breakdown events contain an increasing amount of energy so that the amount of fused material rises as well. The healed sites are thus turned into local APC structures.
5. Thermal stresses around the breakdown sites cause the formation of cracks and additional breakdown events around the initial breakdown site.
6. Starting from the primary breakdown site(s)<sup>1</sup>, an avalanche of secondary breakdowns spread over the whole sample surface area up to the point where the APC layer completely covers the surface.
7. Steps 4 to 6 may happen repeatedly as the voltage increases, resulting in the layer being destroyed locally and healed again with the formation of a coarser structure.

---

1. The breakdown cascade starts at many different sites on the surface simultaneously.

8. Strongly depending on the electrolyte composition, the APC process terminates at the voltage where arc discharges start to occur. This kind of discharge consumes most of the current applied to the sample, since the electrical resistance in the arc is much lower than that of the surrounding oxide. Under galvanostatic anodization conditions, arc discharges cause the voltage to drop to a level of a few volts (see Fig. 10.15). The oxide layer near the arc discharge is destroyed due to the high heat impact.

A schematic drawing of the process mechanism is shown in Fig. 10.17, attempting to fit the sequence of events into the three-phase process description of Wirtz, Brown, and Kriven [20]. The voltage/time curve shown is characteristic for all electrolytes investigated in the course of this thesis. The slope of the curve decreases monotonically with coating time. Up to the point of breakdown the decrease can be explained by the increasing portion of electron current (due to impact ionization, refer to Section 3.2.2) within the constant overall current. Thus, the current consumed by oxide formation decreases and consequently the voltage (directly dependant on the oxide thickness) rises at an increasingly lower rate. After the first breakdown has taken place, oxide growth and breakdown events occur simultaneously, while in phase 3 the APC process (i. e., breakdown events with subsequent healing of the oxide locally) dominates. In phase 2 the slope of the voltage/time curve is changing from the oxide growth slope to the slope characteristic for APC layer formation (phase 3). Since higher voltage implies the presence of a thicker dielectric oxide film, the difference in slope between phase 1 and phase 3 reflects a lower oxide formation rate during the APC layer formation phase (phase 3) in comparison to the anodic oxide formation phase (phase 1).

The high-resolution SEM study successfully illustrated the early stages of the APC process, in particular, the location of the first breakdown events. However, the propagation of the breakdown events over the surface could not be documented since no distinct border between APC coated and non-coated area could be found.

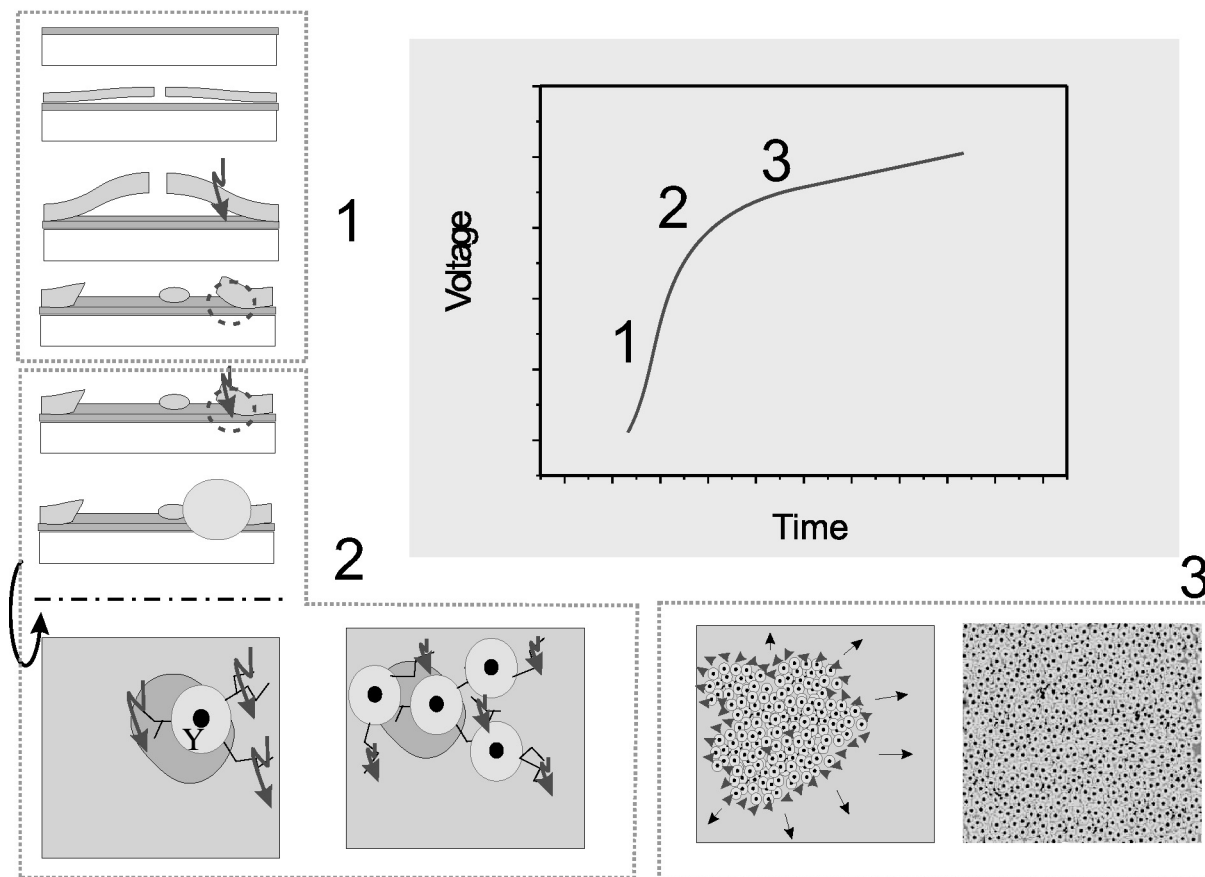


**Fig. 10.17.** Scheme of the proposed film formation mechanism. At the top right a characteristic voltage/time curve for an APC process is shown. The insets to the left and the bottom depict the different events that take place during the process (left/top drawings are cross sections through a sample, while the other insets are surface views). Numbers 1 to 3 depict the three process phases according to Wirtz, Brown and Kriven [20]. According to the high-resolution SEM study the events taking place during the three phases are as follows: (phase 1) formation of an anodic oxide layer, blister formation (as discussed in Section 10.2.3), and first breakdown events without formation of thick oxide layer; (phase 2) breakdown events with higher energy resulting in a thicker oxide with APC structure (yellow [Y] with black pore in the middle), while cracks due to thermal stresses around the healed breakdowns induce further breaking down of the oxide film; (phase 3) the breakdown events spread avalanche-like over to the surface until the whole sample is coated.

---

In this work, the anodic plasma-chemical coating process was investigated in the context of coating CP titanium implant surfaces. The influence of the APC coating process parameters on the APC process and the resulting surface properties was investigated first using the standard electrolytes orthophosphoric acid and calcium orthophosphate. The most important parameter for the dielectric breakdown of the anodic oxide film was found to be in the electrolyte concentration. With increasing electrolyte concentration, the voltage at which first sparks became visible decreased in accordance with the predictions by Albella and coworkers [148]. The influence of the electrolyte temperature on the dielectric breakdown is weak.

The surface topography of the coating depends on the current applied during the coating procedure, the electrolyte concentration, and, to a small extent, on the electrolyte solution temperature. Generally, coatings produced at higher currents, higher electrolyte concentrations, and lower temperatures resulted in coarser surface structures, while the area per breakdown event increased. The only crystalline phases detected in the APC coatings produced in the two standard electrolytes was anatase ( $\text{TiO}_2$ ). No calcium phosphate phases were found in coatings produced in the calcium orthophosphate electrolyte system.

The chemical composition at the surface of the APC coating is again mainly influenced by the electrolyte concentration. With increasing concentration of the electrolyte in solution, increased

amounts of ions from the electrolyte are incorporated into the APC coating, while the phosphorus content in the APC coating assessed by XPS (for both electrolyte system) can be varied only to a small extent, ranging from 16 atom-% in the case of 0.01 M orthophosphoric acid to some 20 atom-% in 0.25 M orthophosphoric acid (assessed by XPS). The concentrations of calcium in coatings produced with the calcium orthophosphate electrolyte slightly increased with the electrolyte concentration. Interestingly, the Ca/P ratio at the coating surface increased as well, even though the ratio in the electrolyte solution is held constant. Finally, the observation that the ratio at the surface is approx. 0.3 while the overall Ca/P ratio of the entire coating is only 0.05 (using ICP-OES for the determination of the integral composition) is believed to be important. The chemical elements incorporated from the electrolyte into the APC coating were found to be well distributed across the coating and not only adsorbed at the coating surface. However, the chemical composition of APC coatings produced in the calcium orthophosphate electrolyte was confined to low levels of calcium and low Ca/P ratios. The restrictions found were

- the low solubility of calcium, and
- the positive charge of the  $\text{Ca}^{2+}$  ions in solution.

The mentioned restrictions were overcome with the new electrolyte system (ESOC). In this electrolyte system the solubility of calcium in solution was increased by the addition of a chelating agent (EDTA). Secondly, the net charge of the Ca-EDTA chelate was changed from net positive/neutral to net negative by increasing the pH of the electrolyte solution to a value of 14. These two measures allowed for a significant increase of the amount of calcium incorporated into the APC coatings and of the Ca/P ratio in the APC coatings. The absolute content of calcium at the surface was increased by a factor of more than two, while the phosphorus content could be reduced to values smaller than the calcium content resulting in Ca/P ratios above 1 at the coating surface. The integral Ca/P ratio could be increased to 0.8. If the different process parameters are compared with each other, the applied current turned out to be the most important. As for the other electrolyte systems, higher currents during the coating process resulted in coarser coating morphologies, while the chemical composition at the surface was independent of the applied current. The crystal structure of the APC coatings produced in ESOC was found to be similar to coatings produced in the standard

---

electrolytes. Only for coatings produced at high currents and/or elevated electrolyte temperatures was an additional band in the Raman spectra, typical for amorphous calcium phosphates found.

The solubility of the calcium phosphates incorporated into the APC coating was tested using a diluted EDTA solution. The dissolution experiment was carried out at 37 °C for 14 d. Significant amounts of calcium and phosphorus were released from coatings produced in the new electrolyte right from the first few hours of the experiment up to the end of the experiment after 14 d exposure. However, possibly due to the strong complexation by EDTA, not only calcium and phosphate were dissolved but also titania particles were found to be released into the solution. Valuable information about the general morphology of the APC coatings was found with SEM after the coatings had undergone the solubility tests, indicating the presence of an amorphous matrix containing calcium and phosphorus. Embedded in this matrix are clusters of anatase crystals with an average size of some 100 nm.

The APC process mechanism was investigated in a phenomenological approach. The process was interrupted at different stages of the coating procedure, and the corresponding samples were investigated using high-resolution SEM. Even at very low voltages (during the anodization phase), the anodic oxide layer delaminated locally and formed open blister-like structures. First breakdown events were found to occur at such blisters. The delamination could be caused by either compressive stresses in the anodic oxide film, the formation of molecular oxygen at the interface oxide/substrate metal or, most probably, a combination of both. The breakdown voltage was found to be much lower than predicted by literature or my own visual observations. Usually, the occurrence of visible sparks is used to determine the breakdown voltage. However, the high-resolution SEM investigations showed that first breakdown events take place at about half the voltage predicted by the visible-spark-criterion for the electrolytes investigated (ESOC and 0.01 M orthophosphoric acid). At such low voltages the energy contained in one breakdown event may be too small to cause visible sparks. In summary, the results achieved in this work suggest a modified mechanism for the APC process. The main difference to the published proposals for the APC mechanism is the view that the process does not follow a sequence of events but that oxide growth, film breakdown, and APC layer formation occur simultaneously. In fact, the primary breakdown events are localized phenomena not

consuming the entire current applied. Processes, such as anodic oxide growth and oxygen evolution at the interface electrolyte/anodic oxide, are still ongoing in this phase. Furthermore, the complete coverage of the sample with an APC layer does not (necessarily) mean that the APC process stops. After a first confluent APC layer has been completed, the process re-starts at an increased energy level resulting in a new and thicker APC layer, which completely replaces the previous one.

A number of questions remain unanswered. The investigation on the APC process mechanism was clearly focussed on the empirical work and the conclusions that may be drawn from the experimental results. The integration of the findings from the high-resolution SEM study into a mathematical model has not yet been carried out mainly as a consequence of complexity of the system and the many factors that influence the anodic plasma-chemical growth mechanism. However, it would be interesting to put more effort into the investigation of the dielectric breakdown in order to be able to tune the resulting chemical composition and to minimize parasitic side reactions, such as oxygen evolution. The emphasis of future investigations should be placed on

- the investigation of blister formation; it is still somewhat unclear how the blisters are formed, and
- the incorporation (rate and mechanism) of anions from the electrolyte into the anodic oxide at the beginning of the APC process, since these anions play an important role in the cascade of events during the breakdown event.

The development of the new electrolyte system resulted in increased levels of calcium and phosphate in the APC coatings. However the Ca/P ratio is still below the desired value of about 1.7. Opportunities to further improve the Ca/P ratio and the absolute concentration of calcium in the APC coatings may be found with other chelating agents, e. g. through increased electrostatic interaction during the coating procedure. Furthermore, it could be useful to find chelating agents with lower  $pK_a$  values of the acidic sites compared to EDTA that would allow the design of electrolytes with lower pH. This may be relevant since the excessive oxygen evolution observed during the APC process in ESOC is possibly related to the very high pH used.



---

An *in vitro* study was carried out with four different APC coatings<sup>1</sup>, state-of-the-art calcium phosphate coatings, and uncoated CP titanium surfaces. Cell cultures of human fetal osteoblasts (hFOB 1.19 [201]) were used to test cell number, cell viability, total protein content, and cell differentiation (alkaline phosphatase activity) on the coatings during a period of two weeks. The results did not reveal any adverse effects (i. e. cytotoxicity) of the APC coatings on the tested parameters in comparison to other calcium phosphate coatings and uncoated CP titanium surfaces.

A possible use of APC coatings produced in ESOC for biomedical purposes has certainly to be evaluated further. APC coatings were applied to screws and proved to be easily applicable to more complex 3-dimensional shapes than disks. These screws were tested *in vivo* for biocompatibility in a sheep model. APC coatings produced in ESOC were compared to APC coatings produced in phosphoric acid, uncoated CP titanium screws, and two commercially available hydroxyapatite coatings. Cortical screws were implanted into the tibiae of the sheep. After 12 weeks the sheep were sacrificed. The APC coatings obtained in ESOC expressed a good biocompatibility and the amount of bone that grew onto the implant surface as well as the bone growth rate were comparable to those of the hydroxyapatite coatings.

The APC coating technique has two big advantages in comparison to the commercially available calcium phosphate coatings: it is very cost-effective and it can be used to coat complex 3D-shaped implants. This gives the possibility to apply calcium phosphate coatings to implant devices, such as pins for external fixation of bone fractures, where it is too costly to use plasma-sprayed hydroxyapatite (besides the adhesion problems with plasma-sprayed coatings). Compared to uncoated implants the APC coating produced in ESOC may lead to faster healing, induce the growth of new bone. Therefore, APC coatings may have beneficial effects especially in the case of osteoporotic bone. The possibility to coat complex shapes could allow for the homogeneous coating of implants, such as cages for spinal fusion, for patients with damaged bones (for example after bone cancer treatments). However, the first animal study was carried out without mechanical loading of the implant after the insertion, while all the implants mentioned above are mechanically loaded. It is known that the healing process at the implantation site may be significantly influenced by

---

1. APC coatings produced in the new electrolyte system (ESOC) and 0.01 M orthophosphoric acid were used for the study.

mechanical stresses that arise in a 'loaded situation'. A 'loaded' animal study is currently being carried out at the AO Research Institute in Davos. It is expected that from this study more distinct differences between the different coatings and the uncoated implants can be obtained. The next step after the animal studies should then be a clinical study with human patients.

APC has proved to be a valuable method for coating titanium implants even if the implants have complex 3D-shape. The coatings developed in this PhD thesis have been shown to result in excellent mechanical properties. In a calcium-deficient environment, the APC coatings produced in ESOC may dissolve, thus, partly accelerating the healing process. Furthermore, the coating setup is simple and the APC process itself is robust and tolerant to small changes in the coating parameters.

1. Lee TK, Haynes RJ, Longo JA, Chu JR. Pin removal in slipped capital femoral epiphysis: The unsuitability of titanium devices. *Journal of Pediatric Orthopaedics* 1996; **16** (1): 49-52.
2. Moller K, Sollerman C, Geijer M, Branemark PI. Osseointegrated silicone implants - 18 patients with 57 MCP joints followed for 2 years. *Acta Orthopaedica Scandinavica* 1999; **70** (2): 109-115.
3. Lundborg G, Branemark PI, Rosen B. Osseointegrated thumb prostheses: A concept for fixation of digit prosthetic devices. *Journal of Hand Surgery-American Volume* 1996; **21A** (2): 216-221.
4. Steinemann SG. Titanium - the material of choice? *Periodontology 2000* 1998; **17**: 7-21.
5. Shackelford JF. Bioceramics - A historical perspective. Bioceramics. Zurich-Uetikon: Transtec Publications Ltd, 1999: 1-4.
6. Ducheyne P, Qiu Q. Bioactive ceramics: the effect of surface reactivity on bone formation and bone cell function. *Biomaterials* 1999; **20** (23-24): 2287-2303.
7. Shackelford JF. Bioceramics - Current status and future trends. Bioceramics. Zurich-Uetikon: Transtec Publications Ltd, 1999: 99-106.
8. de Groot K, Klein CPAT, Wolke JGC, de Blicke-Hogersvorst JMA. Chemistry of calcium phosphate bioceramics. In: Yamamuro T, ed. Calcium phosphate and hydroxylapatite ceramics. Boca Raton [etc.]: CRC Press, 1990: 3-16.
9. Barrere F, Stigter M, Layrolle P, van Blitterswijk CA, de Groot K. In vitro dissolution of various calcium-phosphate coatings on Ti6Al4V. Bioceramics. Zurich-Uetikon: Trans Tech Publications Ltd, 2000: 67-70.
10. Saadalla ME, Ahad N, Gibson IR, Shelton JC. Comparison between commercial calcium phosphate bone cements. Bioceramics 14. Zurich-Uetikon: Trans Tech Publications Ltd, 2002: 331-334.
11. Berger G, Gildenhaar R. Resorbable Bone Substitution On the Basis of Calcium Phosphates. *Materialwissenschaft und Werkstofftechnik* 1995; **26** (7): 379-385.
12. Fulmer MT, Ison IC, Hankermayer CR, Constantz BR, Ross J. Measurements of the solubilities and dissolution rates of several hydroxyapatites. *Biomaterials* 2002; **23** (3): 751-755.
13. Ducheyne P, Cuckler JM. Bioactive Ceramic Prosthetic Coatings. *Clinical Orthopaedics and Related Research* 1992; (276): 102-114.

14. Gross KA, Phillips MR. Identification and mapping of the amorphous phase in plasma-sprayed hydroxyapatite coatings using scanning cathodoluminescence microscopy. *Journal of Materials Science-Materials in Medicine* 1998; **9** (12): 797-802.
15. Li P, deGroot K, Kokubo T. Bioactive  $\text{Ca}_{10}(\text{PO}_4)_6(\text{OH})_2\text{-TiO}_2$  composite coating prepared by sol-gel process. *Journal of Sol-Gel Science and Technology* 1996; **7** (1-2): 27-34.
16. Gruner H. Thermal spray coatings on titanium. In: Brunette DM, Tengvall P, Textor M, Thomsen P, eds. *Titanium in Medicine*. Berlin & Heidelberg: Springer-Verlag, 2001: 375-416.
17. Kim HM, Miyaji F, Kokubo T, Nakamura T. Effect of heat treatment on apatite-forming ability of Ti metal induced by alkali treatment. *Journal of Materials Science-Materials in Medicine* 1997; **8** (6): 341-347.
18. Cigada A, Cabrini M, Pedefferri P. Increasing of the Corrosion-Resistance of the Ti6Al4V Alloy By High Thickness Anodic-Oxidation. *Journal of Materials Science-Materials in Medicine* 1992; **3** (6): 408-412.
19. Lausmaa J. Mechanical, thermal, chemical, and electrochemical surface treatment of titanium. In: Brunette DM, Tengvall P, Textor M, Thomsen P, eds. *Titanium in Medicine*. Berlin & Heidelberg: Springer-Verlag, 2001: 231-267.
20. Wirtz GP, Brown SD, Kriven WM. Ceramic coatings by anodic spark deposition. *Materials & Manufacturing Processes* 1991; **6** (1): 87-115.
21. Güntherschulze A, Betz H. Neue Untersuchungen über die elektrolytische Ventilwirkung. *Zeitschrift für Physik* 1932; **78**: 196-210.
22. Kurze P, Knofler W. Anodic-Oxidation under Spark Discharge (Anof) - a New Coating Procedure in Medical Technology. *Zeitschrift für klinische Medizin-ZKM* 1986; **41** (3): 219-222.
23. Williams DF. *The Williams Dictionary of Biomaterials*. 1 ed. Liverpool: Liverpool University Press, 1999.
24. Park JB, Lakes RS. *Biomaterials: An Introduction*. 2nd ed. New York: Plenum Press, 1992.
25. Windler M, Klabunde R. Titanium for Hip and Knee Prostheses. In: Brunette DM, Tengvall P, Textor M, Thomsen P, eds. *Titanium in Medicine*. Berlin & Heidelberg: Springer-Verlag, 2001: 703-746.
26. Nötzli H. Personal Communication: Personal experiences with total hip joint replacements, Zurich: 2001.
27. Collings EW. Physical metallurgy of titanium alloys. In: Boyer R, Welsch G, Collings EW, eds. *Materials Properties Handbook: Titanium Alloys*. Materials Park, OH: ASM Intl., 1994: 3-122.
28. Boyer R, Welsch G, Collings EW. Titanium Datasheets. In: Boyer R, Welsch G, Collings EW, eds. *Materials Properties Handbook: Titanium Alloys*. Materials Park, OH: ASM Intl., 1994: 125-262.
29. Textor M, Sittig C, Frauchiger VM, Tosatti SGP, Brunette DM. Properties and biological significance of natural oxide films on titanium and its alloys. In: Brunette DM, Tengvall P, Textor M, Thomsen P, eds. *Titanium in Medicine*. Berlin & Heidelberg: Springer-Verlag, 2001: 171-230.
30. Sittig C. Charakterisierung der Oxidschichten auf Titan und Titanlegierungen sowie deren Reaktionen in Kontakt mit biologisch relevanten Modellösungen; Diss. ETH Nr. 12657. Ph. D.-Thesis: Federal Institute of Technology, Zurich, 1998.
31. Kaesche H. Die Spannungsrisskorrosion der Titanwerkstoffe - Stand der Forschung. Symposium Strangpressen 1970 (Rieder Symposienreihe). *Zeitschrift für Metallkunde* 1973; **64** (9): 593-605.
32. Zwicker U. Titan und Titanlegierungen. In: Köster W, ed. *Reine und angewandte Metallkunde in Einzeldarstellungen*. Berlin & Heidelberg: Springer Verlag, 1974.
33. Sittig C, Hahner G, Marti A, Textor M, Spencer ND, Hauert R. The implant material, Ti6Al7Nb: surface microstructure, composition and properties. *Journal of Materials Science-Materials in Medicine* 1999; **10** (4): 191-198.

- 
34. Velten D, Biehl V, Aubertin F, Valeske B, Possart W, Breme J. Preparation of TiO<sub>2</sub> layers on cp-Ti and Ti6Al4V by thermal and anodic oxidation and by sol-gel coating techniques and their characterization. *Journal of Biomedical Materials Research* 2002; **59** (1): 18-28.
35. Wennerberg A, Albrektsson T, Andersson B. Design and surface characteristics of 13 commercially available oral implant systems. *International Journal of Oral & Maxillofacial Implants* 1993; **8**: 622-633.
36. Gasser B. Physiko-chemische Oberflächenanalysen sowie biomechanische und biologische Aspekte aus Reintitan und im Hinblick auf eine physiologische Funktionsweise. Diss Nr. 1204. Ph. D.-Thesis: University of Fribourg, Fribourg, 1998.
37. Freese H. Metallurgy and technological properties of titanium and titanium alloys. In: Brunette DM, Tengvall P, Textor M, Thomsen P, eds. *Titanium in Medicine*. Berlin & Heidelberg: Springer-Verlag, 2001: 25-51.
38. Okazaki Y, Rao S, Tateishi T, Ito Y. Cytocompatibility of various metal and development of new titanium alloys for medical implants. *Materials Science and Engineering A - Structural Materials Properties Microstructure and Processing* 1998; **243** (1-2): 250-256.
39. Wintermantel E, Ha SW. *Biokompatible Werkstoffe und Bauweisen*. Berlin & Heidelberg: Springer Verlag, 1996.
40. Kim TI, Han JH, Lee IS, Lee KH, Shin MC, Choi BB. New titanium alloys for biomaterials: A study of mechanical and corrosion properties and cytotoxicity. *Bio-Medical Materials and Engineering* 1997; **7** (4): 253-263.
41. Sittig C, Textor M, Spencer ND, Wieland M, Vallotton PH. Surface characterization of implant materials cp Ti, Ti-6Al-7Nb and Ti-6Al-4V with different pretreatments. *Journal of Materials Science-Materials in Medicine* 1999; **10** (1): 35-46.
42. Okazaki Y, Tateishi T, Ito Y. Corrosion resistance of implant alloys in pseudo physiological solution and role of alloying elements in passive films. *Materials Transactions Jim* 1997; **38** (1): 78-84.
43. Finet B, Weber G, Cloots R. Titanium release from dental implants: an in vivo study on sheep. *Materials Letters* 2000; **43** (4): 159-165.
44. Bianco PD, Ducheyne P, Cuckler JM. Titanium serum and urine levels in rabbits with a titanium implant in the absence of wear. *Biomaterials* 1996; **17** (20): 1937-1942.
45. Imam MA, Fraker AC. Titanium alloys as implant materials. In: Brown SA, Lemons JE, eds. *Medical applications of titanium and its alloys: the materials and biological issues*; STP 1272. West Conshohocken, PA: ASTM, 1996: 3-16.
46. Vörös J, Wieland M, Ruiz-Taylor L, Textor M, Brunette DM. Characterization of titanium surfaces. In: Brunette DM, Tengvall P, Textor M, Thomsen P, eds. *Titanium in Medicine*. Berlin & Heidelberg: Springer-Verlag, 2001: 87-144.
47. Boyan BD, Dean DD, Lohmann CH, Cochran DL, Sylvia VL, Schwartz Z. The titanium-bone cell interface in vitro: the role of the surface in promoting osteointegration. In: Brunette DM, Tengvall P, Textor M, Thomsen P, eds. *Titanium in Medicine*. Berlin & Heidelberg: Springer-Verlag, 2001: 561-586.
48. Massaro C, Rotolo P, De Riccardis F, Milella E, Napoli A, Wieland M, Textor M, Spencer ND, Brunette DM. Comparative investigation of the surface properties of commercial titanium dental implants. Part I: chemical composition. *Journal of Materials Science-Materials in Medicine* 2002; **13** (6): 535-548.
49. Kasemo B, Lausmaa J. Surface Science Aspects on Inorganic Biomaterials. *Crc Critical Reviews in Biocompatibility* 1986; **2** (4): 335-380.
50. Ratner BD. A perspective on titanium biocompatibility. In: Brunette DM, Tengvall P, Textor M, Thomsen P, eds. *Titanium in Medicine*. Berlin & Heidelberg: Springer-Verlag, 2001.
51. Kilpadi KL, Chang PL, Bellis SL. Hydroxylapatite binds more serum proteins, purified integrins, and osteoblast precursor cells than titanium or steel. *Journal of Biomedical Materials Research* 2001; **57** (2): 258-267.
52. Suzuki R, Frangos JA. Inhibition of inflammatory species by titanium surfaces. *Clinical Orthopaedics and Related Research* 2000; (372): 280-289.

53. Tengvall P, Lundström I. Review paper: Physico-chemical considerations of titanium as a biomaterial. *Clinical Materials* 1992; **9**: 115-134.
54. Tengvall P, Elwing H, Sjöqvist L, Lundström I, Bjursten LM. Interaction Between Hydrogen-Peroxide and Titanium - a Possible Role in the Biocompatibility of Titanium. *Biomaterials* 1989; **10** (2): 118-120.
55. Tengvall P, Lundström I, Sjöqvist L, Elwing H, Bjursten LM. Titanium-Hydrogen Peroxide Interaction - Model Studies of the Influence of the Inflammatory Response On Titanium Implants. *Biomaterials* 1989; **10** (3): 166-175.
56. Lincks J, Boyan BD, Blanchard CR, Lohmann CH, Liu Y, Cochran DL, Dean DD, Schwartz Z. Response of MG63 osteoblast-like cells to titanium and titanium alloy is dependent on surface roughness and composition. *Biomaterials* 1998; **19** (23): 2219-2232.
57. Boyan BD, Lohmann CH, Dean DD, Sylvia VL, Cochran DL, Schwartz Z. Mechanisms involved in osteoblast response to implant surface morphology. *Annual Review of Materials Research* 2001; **31**: 357-371.
58. Hambleton J, Schwartz Z, Khare A, Windeler SW, Luna M, Brooks BP, Dean DD, Boyan BD. Culture Surfaces Coated with Various Implant Materials Affect Chondrocyte Growth and Metabolism. *Journal of Orthopaedic Research* 1994; **12** (4): 542-552.
59. Windeler SW, Bonewald L, Khare A, Boyan BD, Mundy GR. The influence of sputtered bone substitutes on cell growth and phenotypic expression. In: Davies JE, ed. *The bone-biomaterial interface*. Toronto: University of Toronto Press, 1991: 205-213.
60. Ameen AP, Short RD, Johns R, Schwach G. The Surface-Analysis of Implant Materials .1. The Surface-Composition of a Titanium Dental Implant Material. *Clinical Oral Implants Research* 1993; **4** (3): 144-150.
61. Wieland M. Experimental Determination and quantitative evaluation of the surface composition and topography of medical implant surfaces and their influence on osteoblastic cell-surface interactions. Diss ETH No. 13247. Ph. D.-Thesis: Federal Institute of Technology, Zurich, 1999.
62. Shi HQ, Tsai WB, Garrison MD, Ferrari S, Ratner BD. Template-imprinted nanostructured surfaces for protein recognition. *Nature* 1999; **398** (6728): 593-597.
63. Clark P, Connolly P, Curtis ASG, Dow JAT, Wilkinson CDW. Cell Guidance by Ultrafine Topography In vitro. *Journal of Cell Science* 1991; **99**: 73-77.
64. Curtis A, Wilkinson C. New depths in cell behaviour: reactions of cells to nanotopography. *Cell Behaviour: Control and Mechanism of Motility*. London: PORTLAND PRESS LTD, 1999: 15-26.
65. Curtis A, Wilkinson C. Nanotechniques and approaches in biotechnology. *Trends in Biotechnology* 2001; **19** (3): 97-101.
66. Brunette. The effect of surface topography on cell migration and adhesion. In: Ratner BD, ed. *Surface Characterisation of biomaterials*. Amsterdam: Elsevier Science Publishers B. V., 1988: 203-217.
67. Brunette DM. Principles of cell behavior on titanium surfaces and their application to implanted devices. In: Brunette DM, Tengvall P, Textor M, Thomsen P, eds. *Titanium in Medicine*. Berlin & Heidelberg: Springer-Verlag, 2001: 485-512.
68. den Braber ET, de Ruijter JE, Ginsel LA, von Recum AF, Jansen JA. Quantitative analysis of fibroblast morphology on microgrooved surfaces with various groove and ridge dimensions. *Biomaterials* 1996; **17** (21): 2037-2044.
69. den Braber ET, de Ruijter JE, Smits HTJ, Ginsel LA, von Recum AF, Jansen JA. Quantitative analysis of cell proliferation and orientation on substrata with uniform parallel surface micro-grooves. *Biomaterials* 1996; **17** (11): 1093-1099.
70. Boyan BD, Sylvia VL, Liu YH, Sagun R, Cochran DL, Lohmann CH, Dean DD, Schwartz Z. Surface roughness mediates its effects on osteoblasts via protein kinase A and phospholipase A(2). *Biomaterials* 1999; **20** (23-24): 2305-2310.

- 
71. Boyan BD, Hummert TW, Dean DD, Schwartz Z. Role of material surfaces in regulating bone and cartilage cell response. *Biomaterials* 1996; **17** (2): 137-146.
72. Martin JY, Dean DD, Cochran DL, Simpson J, Boyan BD, Schwartz Z. Proliferation, differentiation, and protein synthesis of human osteoblast-like cells (MG63) cultured on previously used titanium surfaces. *Clinical Oral Implants Research* 1996; **7** (1): 27-37.
73. Kieswetter K, Schwartz Z, Hummert TW, Cochran DL, Simpson J, Dean DD, Boyan BD. Surface roughness modulates the local production of growth factors and cytokines by osteoblast-like MG-63 cells. *Journal of Biomedical Materials Research* 1996; **32** (1): 55-63.
74. Brunette DM. Spreading and Orientation of Epithelial-Cells on Grooved Substrata. *Experimental Cell Research* 1986; **167** (1): 203-217.
75. Wennerberg A. On surface roughness and implant incorporation. Ph. D.-Thesis: University of Gothenburg, Gothenburg, 1996.
76. Buser D, Schenk RK, Steinemann S, Fiorellini JP, Fox CH, Stich H. Influence of Surface Characteristics On Bone Integration of Titanium Implants - a Histomorphometric Study in Miniature Pigs. *Journal of Biomedical Materials Research* 1991; **25** (7): 889-902.
77. Wieland M, Haenggi P, Hotz W, Textor M, Keller BA, Spencer ND. Wavelength-dependent measurement and evaluation of surface topographies: application of a new concept of window roughness and surface transfer function. *Wear* 2000; **237** (2): 231-252.
78. Wieland M, Textor M, Spencer ND, Brunette DM. Wavelength-dependent roughness: A quantitative approach to characterizing the topography of rough titanium surfaces. *International Journal of Oral & Maxillofacial Implants* 2001; **16** (2): 163-181.
79. Baier RE, Meyer AE, Natiella JR, Natiella RR, Carter JM. Surface properties determine bioadhesive outcomes: methods and results. *Journal of Biomedical Materials Research* 1984; **18** (4): 327-55.
80. Baier RE, Meyer AE. Surface Analysis. In: von Recum AF, ed. Handbook of biomaterials evaluation: scientific, technical, and clinical testing of implant materials. New York: Macmillan Publishing Company, 1986: 97-108.
81. Wennerberg A, Bolind P, Albrektsson T. Glow-Discharge Pretreated Implants Combined with Temporary Bone Tissue Ischemia. *Swedish Dental Journal* 1991; **15** (2): 95-101.
82. Davies JE. The importance and measurement of surface charge species in cell behaviour at the biomaterial interface. In: Ratner BD, ed. Surface Characterisation of biomaterials. Amsterdam: Elsevier Science Publishers B. V., 1988: 219-234.
83. Davies JE, Causton B, Bovell Y, Davy K, Sturt CS. The Migration of Osteoblasts over Substrata of Discrete Surface-Charge. *Biomaterials* 1986; **7** (3): 231-233.
84. McKellop HA, Rostlund T, Ebramzadeh E, Sarmiento A. Wear of Titanium 6-4 Alloy in Laboratory Tests and in Retrieved Human Joint Replacements. In: Brunette DM, Tengvall P, Textor M, Thomsen P, eds. Titanium in Medicine. Berlin & Heidelberg: Springer-Verlag, 2001: 748-770.
85. Hutchings R. A Review of Recent Developments in Ion-Implantation for Metallurgical Application. *Materials Science and Engineering a-Structural Materials Properties Microstructure and Processing* 1994; **184** (2): 87-96.
86. Thull R. Semiconductive properties of passivated titanium and titanium based hard coatings on metals for implants--an experimental approach. *Medical Progress Through Technology* 1990; **16** (4): 225-234.
87. Thull R, Grant D. Physical and chemical vapor deposition and plasma-assisted techniques for coating titanium. In: Brunette DM, Tengvall P, Textor M, Thomsen P, eds. Titanium in Medicine. Berlin & Heidelberg: Springer-Verlag, 2001.
88. La Budde JK, Orosz JF, Bonfiglio TA, Pellegrini VD, Jr. Particulate titanium and cobalt-chrome metallic debris in failed total knee arthroplasty. A quantitative histologic analysis. *Journal of Arthroplasty* 1994; **9** (3): 291-304.
-

89. Willert HG, Buchhorn HB, Semlitsch M. Particle disease due to wear of metal alloys. In: Morrey BF, ed. Biological, material, and mechanical considerations of joint replacement. New York: Raven Press, 1993: 129-146.
90. Zeiler G, Thull R. Physikalisch-chemische Oberflächenprozesse und Verankerungsstabilität von zementfreien Titanschaftprothesen. In: Friedebold G, Arbeitskreis Implantate (Deutscher Verband für Materialprüfung), International Association for the Study of Osteosynthesis Deutsche Sektion, Deutscher Verband für Materialprüfung, eds. Bioaktive Werkstoffe - chemische und physikalische Reaktionen 6. Vortragsreihe des Arbeitskreises Implantate, medizinische - technische Zusammenarbeit am 12. November 1985 im Oskar-Helene-Heim in Berlin. Berlin: Dvm, 1986: 229 S.
91. Jones JR, Hench LL. Materials perspective - Biomedical materials for new millennium: perspective on the future. *Materials Science and Technology* 2001; **17** (8): 891-900.
92. Pietrzak WS, Ronk R. Calcium sulfate bone void filler: A review and a look ahead. *Journal of Craniofacial Surgery* 2000; **11** (4): 327-333.
93. Johnson KD, Frierson KE, Keller TS, Cook C, Scheinberg R, Zerwekh J, Meyers L, Sciadini MF. Porous ceramics as bone graft substitutes in long bone defects: A biomechanical, histological, and radiographic analysis. *Journal of Orthopaedic Research* 1996; **14** (3): 351-369.
94. Ratner BD, Hoffmann AS, Schoen FJ, Lemons JE, eds. Biomaterials Science: an Introduction to Materials in Medicine. San Diego, CA: Academic Press, Inc., 1996.
95. Ravaglioli A, Krajewski A. Bioceramics materials · properties · applications. London [etc.]: Chapman & Hall, 1992.
96. Nancollas GH. In vitro study of calcium phosphate crystallization. In: Mann S, Webb J, Williams RJP, eds. Biomineralization chemical and biochemical perspectives. Weinheim: VCH, 1989: 157-180.
97. Kanazawa T. Inorganic phosphate materials. Amsterdam: Elsevier, 1989.
98. Worch H, Scharnweber D. Biologisation of titanium materials. *Zeitschrift für Metallkunde* 1998; **89** (2): 153-163.
99. Ducheyne P, Radin S, Heughebaert M, Heughebaert JC. Calcium-Phosphate Ceramic Coatings On Porous Titanium - Effect of Structure and Composition On Electrophoretic Deposition, Vacuum Sintering and Invitro Dissolution. *Biomaterials* 1990; **11** (4): 244-254.
100. Durucan C, Brown PW. alpha-Tricalcium phosphate hydrolysis to hydroxyapatite at and near physiological temperature. *Journal of Materials Science-Materials in Medicine* 2000; **11** (6): 365-371.
101. Kay JF. Bioactive surface coatings for hard tissue biomaterials. *CRC Handbook of Bioactive Ceramics* 1990; **2**: 111-222.
102. Sanden B, Olerud C, Larsson S. Hydroxyapatite coating enhances fixation of loaded pedicle screws: a mechanical in vivo study in sheep. *European Spine Journal* 2001; **10** (4): 334-339.
103. Schepers E, Declercq M, Ducheyne P, Kempeneers R. Bioactive Glass Particulate Material as a Filler for Bone-Lesions. *Journal of Oral Rehabilitation* 1991; **18** (5): 439-452.
104. Chou L, Marek B, Wagner WR. Effects of hydroxylapatite coating crystallinity on biosolubility, cell attachment efficiency and proliferation in vitro. *Biomaterials* 1999; **20** (10): 977-985.
105. Suzuki T, Yamamoto T, Toriyama M, Nishizawa K, Yokogawa Y, Mucalo MR, Kawamoto Y, Nagata F, Kameyama T. Surface instability of calcium phosphate ceramics in tissue culture medium and the effect on adhesion and growth of anchorage-dependent animal cells. *Journal of Biomedical Materials Research* 1997; **34** (4): 507-517.
106. Lee TM, Wang BC, Yang YC, Chang E, Yang CY. Comparison of plasma-sprayed hydroxyapatite coatings and hydroxyapatite/tricalcium phosphate composite coatings: In vivo study. *Journal of Biomedical Materials Research* 2001; **55** (3): 360-367.
107. Ogiso M, Yamashita Y, Matsumoto T. Microstructural changes in bone of HA-coated implants. *Journal of Biomedical Materials Research* 1998; **39** (1): 23-31.



- 
108. Chang YL, Lew D, Park JB, Keller JC. Biomechanical and morphometric analysis of hydroxyapatite-coated implants with varying crystallinity. *Journal of Oral and Maxillofacial Surgery* 1999; **57** (9): 1096-1108.
109. Koerten HK, van der Meulen J. Degradation of calcium phosphate ceramics. *Journal of Biomedical Materials Research* 1999; **44** (1): 78-86.
110. Cleries L, Fernandez-Pradas JM, Sardin G, Morenza JL. Dissolution behaviour of calcium phosphate coatings obtained by laser ablation. *Biomaterials* 1998; **19** (16): 1483-1487.
111. Frayssinet P, Rouquet N, Tourenne F, Fages J, Hardy D, Bonel G. Cell-Degradation of Calcium-Phosphate Ceramics. *Cells and Materials* 1993; **3** (4): 383-394.
112. Hlavac J. Ceramic coatings on titanium for bone implants. *Ceramics-Silikaty* 1999; **43** (3): 133-139.
113. Ji HX, Ponton CB, Marquis PM. Microstructural Characterization of Hydroxyapatite Coating on Titanium. *Journal of Materials Science-Materials in Medicine* 1992; **3** (4): 283-287.
114. Kuroyama Y, Higashikata M, Nakamura S, Ohgaki M, Akao M, Aoki H. Crystal chemistry and biocompatibility of alpha-TCP produced from beta-TCP by a plasma spraying technique. In: Bonfield W, Hastings GW, Tanner KE, eds. *Bioceramics*: Butterworth Heinemann Ltd., 1991: 65-69.
115. Szmukler-Moncler S, Daculsi G, Delécrin J, Passuti N, Deudon C. Calcium-metallic-phosphates: a new coating biomaterial. In: Doherty PJ, ed. *Advances in Biomaterials 10*. Amsterdam: Elsevier Publisher, B. V., 1992: 377-383.
116. Zeng H, Chittur KK, Lacefield WR. Dissolution/precipitation of calcium phosphate thin films produced by ion beam sputter deposition technique. *Biomaterials* 1999; **20** (5): 443-451.
117. Zeng HT, Lacefield WR. The study of surface transformation of pulsed laser deposited hydroxyapatite coatings. *Journal of Biomedical Materials Research* 2000; **50** (2): 239-247.
118. Kim HM, Miyaji F, Kokubo T, Nishiguchi S, Nakamura T. Graded surface structure of bioactive titanium prepared by chemical treatment. *Journal of Biomedical Materials Research* 1999; **45** (2): 100-107.
119. Langstaff S, Sayer M, Smith TJN, Pugh SM, Hesp SAM, Thompson WT. Resorbable bioceramics based on stabilized calcium phosphates. Part I: rational design, sample preparation and material characterization. *Biomaterials* 1999; **20** (18): 1727-1741.
120. Piveteau L-D. Development of a new concept and of a new method for coating metallic medical implants with bioactive calcium-phosphate; Thesis No. 1184. Ph. D.-Thesis: University of Fribourg, Fribourg, 1998.
121. Piveteau L-D. Sol-Gel Coatings on Titanium. In: Brunette DM, Tengvall P, Textor M, Thomsen P, eds. *Titanium in Medicine*. Berlin & Heidelberg: Springer-Verlag, 2001: 267-282.
122. Shirkhazadeh M. Electrochemical Fabrication of Bioactive Composite Coatings On Ti6Al4V Surgical Alloy. *Materials Letters* 1992; **14** (1): 27-30.
123. Shirkhazadeh M. Direct formation of nanophase hydroxyapatite on cathodically polarized electrodes. *Journal of Materials Science-Materials in Medicine* 1998; **9** (2): 67-72.
124. Huang LY, Xu KW, Lu J. A study of the process and kinetics of electrochemical deposition and the hydrothermal synthesis of hydroxyapatite coatings. *Journal of Materials Science-Materials in Medicine* 2000; **11** (11): 667-673.
125. Born R, Scharnweber D, Roessler S, Stolzel M, Thieme M, Wolf C, Worch H. Surface analysis of titanium based biomaterials. *Fresenius Journal of Analytical Chemistry* 1998; **361** (6-7): 697-700.
126. Arsov LD, Kormann C, Plieth W. In situ Raman-Spectra of Anodically Formed Titanium-Dioxide Layers in Solutions of H<sub>2</sub>SO<sub>4</sub>, KOH, and HNO<sub>3</sub>. *Journal of the Electrochemical Society* 1991; **138** (10): 2964-2970.
127. Kurze P, Krysmann W, Schneider HG. Application Fields of ANOF Layers and Composites. *Crystal Research and Technology* 1986; **21** (12): 1603-1609.
-

128. Lohrengel MM. Thin Anodic Oxide Layers On Aluminum and Other Valve Metals - High-Field Regime. *Materials Science & Engineering R-Reports* 1993; **11** (6): 243-294.
129. Schreckenbach J, Schlottig F, Marx G, Kriven WM, Popoola OO, Jilavi MH, Brown SD. Preparation and microstructure characterization of anodic spark deposited barium titanate conversion layers. *Journal of Materials Research* 1999; **14** (4): 1437-1443.
130. McNeill W, Wick R. Effects of Various Polyvalent Metal Anion Additions to an Alkaline Magnesium Anodizing Bath. *Journal of the Electrochemical Society* 1957; **104** (6): 356-359.
131. Rudnev VS, Yarovaya TP, Boguta DL, Tyrina LM, Nedozorov PM, Gordienko PS. Anodic spark deposition of P, Me(II) or Me(III) containing coatings on aluminium and titanium alloys in electrolytes with polyphosphate complexes. *Journal of Electroanalytical Chemistry* 2001; **497** (1-2): 150-158.
132. Koshkarian KA, Kriven WM. Microstructure and wear characterization of self-lubricating Al<sub>2</sub>O<sub>3</sub> - MoS<sub>2</sub> composite ceramic materials. *New Materials Approaches to Tribology: Theory and Applications* 1989.
133. Ishizawa H, Ogino M. Hydrothermal precipitation of hydroxyapatite on anodic titanium oxide films containing Ca and P. *Journal of Materials Science* 1999; **34** (23): 5893-5898.
134. Ishizawa H, Fujino M, Ogino M. Mechanical and Histological Investigation of Hydrothermally Treated and Untreated Anodic Titanium-Oxide Films Containing Ca and P. *Journal of Biomedical Materials Research* 1995; **29** (11): 1459-1468.
135. Ishizawa H, Ogino M. Characterization of Thin Hydroxyapatite Layers Formed On Anodic Titanium-Oxide Films Containing Ca and P By Hydrothermal Treatment. *Journal of Biomedical Materials Research* 1995; **29** (9): 1071-1079.
136. Ishizawa H, Ogino M. Formation and Characterization of Anodic Titanium-Oxide Films Containing Ca and P. *Journal of Biomedical Materials Research* 1995; **29** (1): 65-72.
137. Ishizawa H, Ogino M. Thin hydroxyapatite layers formed on porous titanium using electrochemical and hydrothermal reaction. *Journal of Materials Science* 1996; **31** (23): 6279-6284.
138. Ishizawa H, Fujino M, Ogino M. Histomorphometric evaluation of the thin hydroxyapatite layer formed through anodization followed by hydrothermal treatment. *Journal of Biomedical Materials Research* 1997; **35** (2): 199-206.
139. Takebe T, Itoh S, Ariake T, Shioji H, Shioyama T, Ishibashi K, Ishizawa H. The effect on immunocytes of anodic oxide titanium after hydrothermal treatment. *Journal of Biomedical Materials Research* 1998; **42** (2): 272-277.
140. Schreckenbach JP, Marx G, Schlottig F, Textor M, Spencer ND. Characterization of anodic spark-converted titanium surfaces for biomedical applications. *Journal of Materials Science-Materials in Medicine* 1999; **10** (8): 453-457.
141. Skeldon P, Shimizu K, Thompson GE, Wood GC. Selective Interfacial Processes and the Incorporation of Electrolyte Species Into Anodic Films On Aluminum. *Philosophical Magazine B-Physics of Condensed Matter Statistical Mechanics Electronic Optical and Magnetic Properties* 1995; **72** (4): 391-400.
142. Crossland AC, Habazaki H, Shimizu K, Skeldon P, Thompson GE, Wood GC, Zhou X, Smith CJE. Residual flaws due to formation of oxygen bubbles in anodic alumina. *Corrosion Science* 1999; **41** (10): 1945-1954.
143. Krysmann W, Kurze P, Dittrich KH, Schneider HG. Process Characteristics and Parameters of Anodic-Oxidation by Spark Discharge (Anof). *Crystal Research and Technology* 1984; **19** (7): 973-979.
144. Shimizu K, Thompson GE, Wood GC. The Electrical Breakdown During Anodizing of High-Purity Aluminum in Borate Solutions. *Thin Solid Films* 1982; **92** (3): 231-241.
145. Vijh AK. Sparking Voltages and Side Reactions During Anodization of Valve Metals in Terms of Electron Tunnelling. *Corrosion Science* 1971; **11** (6): 411-&.

- 
146. DiQuarto F, Piazza S, Sunseri C. A Phenomenological Approach to the Mechanical Breakdown of Anodic Oxide-Films On Zirconium. *Corrosion Science* 1986; **26** (3): 213-221.
147. Ikonopisov S. Theory of electrical breakdown during formation of barrier anodic films. *Electrochimica Acta* 1977; **22**: 1077-1082.
148. Albella JM, Montero I, Martínez-Duart JM. A Theory of Avalanche Breakdown During Anodic-Oxidation. *Electrochimica Acta* 1987; **32** (2): 255-258.
149. Parkhutik VP, Albella JM, Martinez-Duart JM. Electric Breakdown in Anodic Oxide Films. In: Conway BE, Bockris JOM, White RE, eds. Modern aspects of electrochemistry. New York: Plenum Press, 1992: 315-391.
150. Amsel G, Cherki C, Feuillad G, Nadai JP. Influence of Electrolyte on Composition of Anodic Oxide Films on Tantalum. *Journal of Physics and Chemistry of Solids* 1969; **30** (9): 2117-&.
151. Kadary V, Klein N. Electro-Luminescence During the Anodic Growth of Tantalum Pentoxide. *Journal of the Electrochemical Society* 1981; **128** (4): 749-755.
152. O'Dwyer JJ. The Role of Space-Charge in the Theory of Solid-Dielectric Breakdown. *IEEE Transactions on Electrical Insulation* 1984; **19** (1): 1-9.
153. Wolters DR, Vanderschoot JJ. Dielectric-Breakdown in Mos Devices .1. Defect-Related and Intrinsic Breakdown. *Philips Journal of Research* 1985; **40** (3): 115-136.
154. Albella JM, Montero I, Martinezduart JM. Anodization and Breakdown Model of Ta<sub>2</sub>O<sub>5</sub> Films. *Thin Solid Films* 1985; **125** (1-2): 57-62.
155. Albella JM, Montero I, Fernandez M, Gomezaleixandre C, Martinezduart JM. Double Anodization Experiments in Tantalum. *Electrochimica Acta* 1985; **30** (10): 1361-1364.
156. Kalra KC, Singh KC, Singh M. Electrical Breakdown of Anodic Films On Titanium in Aqueous- Electrolytes. *Journal of Electroanalytical Chemistry* 1994; **371** (1-2): 73-78.
157. Briggs D, Seah MP, eds. Auger and X-ray photoelectron spectroscopy. Second , [reprinted] ed. Chichester [etc.]: Wiley [etc.], 1995.
158. Wagner CD, Riggs WM, Davis LE, Moulder JF, Mulienberg GE. Handbook of X-Ray Photoelectron Spectroscopy: Perkin Elmer Corporation, 1979.
159. Scofield JH. Hartree-Slater subshell photoionisation cross-sections at 1254 and 1487 eV. *Journal of Electron Spectroscopy and Related Phenomena* 1976; **8**: 129-137.
160. Payling R. An overview of GD-OES. In: Payling R, Jones DG, Bengtson A, eds. Glow Discharge Optical Emission Spectrometry. Chichester: John Wiley & sons, 1997: 20-47.
161. Delfosse D, Aeberhard M. Tiefenprofilanalyse von technischen Schichten und Oberflächen. *Oberflächen - Polysurface* 1997; (7): 7-10.
162. Bengtson A, Payling R, Jones DG. Quantitative Depth Profiling. In: Payling R, Jones DG, Bengtson A, eds. Glow Discharge Optical Emission Spectrometry. Chichester: John Wiley & sons, 1997: 453-496.
163. Payling R, Aeberhard M, Delfosse D. Improved quantitative analysis of hard coatings by radiofrequency glow discharge optical emission spectrometry (rf-GD-OES). *Journal of Analytical Atomic Spectrometry* 2001; **16** (1): 50-55.
164. Bengtson A, Hånström S. In: Tomellini R, ed. Proceedings of the Fifth International Conference on Progress in Analytical Chemistry in the Steel and Metals Industry. Luxembourg: European Community, 1999: 47-55.
165. Bogaerts A, Gijbels R. Effects of adding hydrogen to an argon glow discharge: overview of relevant processes and some qualitative explanations. *Journal of Analytical Atomic Spectrometry* 2000; **15** (4): 441-449.
166. Müller M. Anodic plasma-chemical surface treatment of titanium for medical implant applications. Diploma-Thesis: ETH Zürich, Zürich, 2002.

167. Pemble ME. Vibrational spectroscopy from surfaces. In: Vickerman JC, ed. *Surface Analysis*. Chichester, UK: John Wiley & Sons Ltd., 1997: 267-311.
168. Meyer N. Personal Communication: Information depth of Raman spectroscopy, Chemnitz: 2001.
169. Balachandran U, Eror NG. Raman spectra of titanium dioxide. *Journal of Solid State Chemistry* 1982; **42**: 276-282.
170. Ohsaka T, Izumi F, Fujiki Y. Raman spectrum of anatase, TiO<sub>2</sub>. *Journal of Raman Spectroscopy* 1978; **7** (6): 321-324.
171. Penel G, Leroy G, Rey C, Bres E. MicroRaman spectral study of the PO<sub>4</sub> and CO<sub>3</sub> vibrational modes in synthetic and biological apatites. *Calcified Tissue International* 1998; **63** (6): 475-481.
172. Ribeiro CC, Barbosa MA, Machado A, Tudor A, Davies MC. Modifications in the molecular structure of hydroxyapatite induced by titanium ions. *Journal of Materials Science-Materials in Medicine* 1995; **6** (12): 829-834.
173. Zhang YH, Chan CK, Porter JF, Guo W. Micro-Raman spectroscopic characterization of nanosized TiO<sub>2</sub> powders prepared by vapor hydrolysis. *Journal of Materials Research* 1998; **13** (9): 2602-2609.
174. Zhao HC, Li XD, Wang JX, Qu SX, Weng J, Zhang XD. Characterization of peroxide ions in hydroxyapatite lattice. *Journal of Biomedical Materials Research* 2000; **52** (1): 157-163.
175. Joy DC. Scanning electron microscopy. In: Lifshin E, ed. *Characterization of Materials*. Weinheim: VCH, 1992: 222-249.
176. Reimer L. Image formation in low-voltage scanning electron microscopy. Bellingham, Washington USA: SPIE Optical Engineering Press, 1993.
177. Windecker R. Optical Autofocusing Profilometer. *Technisches Messen* 1993; **60** (7-8): 267-270.
178. Kalra KC, Singh KC, Singh M. Ionic-Conduction in Anodic Oxide-Films On Titanium in Aqueous- Electrolytes. *Indian Journal of Chemistry Section a-Inorganic Bio-Inorganic Physical Theoretical & Analytical Chemistry* 1994; **33** (4): 308-313.
179. Kalra KC, Singh KC, Singh M. Formation and breakdown characteristics of anodic oxide films on valve metal. *Indian Journal of Chemistry Section a-Inorganic Bio-Inorganic Physical Theoretical & Analytical Chemistry* 1997; **36** (3): 216-218.
180. Hodoroaba VD, Hoffmann V, Steers EBM, Wetzig K. Investigations of the effect of hydrogen in an argon glow discharge. *Journal of Analytical Atomic Spectrometry* 2000; **15** (9): 1075-1080.
181. Busca G, Ramis G, Lorenzelli V, Rossi PF, Laginestra A, Patrono P. Phosphoric-Acid On Oxide Carriers .1. Characterization of Silica, Alumina, and Titania Impregnated By Phosphoric-Acid. *Langmuir* 1989; **5** (4): 911-916.
182. Murrell TS, Nooney MG, Hossner LR, Goodman DW. Growth kinetics of phosphate films on metal oxide surfaces. *Solid-Liquid Electrochemical Interfaces*. Washington: Amer Chemical Soc, 1997: 71-86.
183. Felske A, Plieth WJ. Raman-Spectroscopy of Titanium-Dioxide Layers. *Electrochimica Acta* 1989; **34** (1): 75-77.
184. Hammond CR. Properties of the elements and inorganic compounds. In: Lide DR, ed. *CRC handbook of chemistry and physics*. 75th ed. Boca Raton: CRC Press, 1995.
185. Frauchiger VM. Anodisch-plasmachemische Oberflächenmodifikation von Titanimplantaten. Diploma-Thesis: ETH Zürich, Zurich, 1999.
186. Chang H, Huang PJ. Thermo-Raman studies on anatase and rutile. *Journal of Raman Spectroscopy* 1998; **29** (2): 97-102.
187. Shannon RD, Pask JA. Kinetics of the Anatase-Rutile Transformation. *Journal of The American Ceramic Society* 1965; **48** (8): 391-398.
188. Gauckler LJ. Skript Keramik I-III, Studiengang 'Werkstoffe', ETH Zürich. Zurich, 1994-1996.
-

- 
189. Mitchell PCH, Parker SF, Simkiss K, Simmons J, Taylor MG. Hydrated sites in biogenic amorphous calcium phosphates: An infrared, Raman, and inelastic neutron scattering study. *Journal of Inorganic Biochemistry* 1996; **62** (3): 183-197.
190. Fowler BO, Markovic M, Brown WE. Octacalcium Phosphate .3. Infrared and Raman Vibrational- Spectra. *Chemistry of Materials* 1993; **5** (10): 1417-1423.
191. de Aza PN, Guitian F, Santos C, deAza S, Cusco R, Artus L. Vibrational properties of calcium phosphate compounds .2. Comparison between hydroxyapatite beta-tricalcium phosphate. *Chemistry of Materials* 1997; **9** (4): 916-922.
192. Posset U, Locklin E, Thull R, Kiefer W. Vibrational spectroscopic study of tetracalcium phosphate in pure polycrystalline form and as a constituent of a self- setting bone cement. *Journal of Biomedical Materials Research* 1998; **40** (4): 640-645.
193. Müller Y. to be submitted. Ph. D.-Thesis: ETH Zürich, Zurich, 2002.
194. Healy KE, Ducheyne P. Passive Dissolution Kinetics of Titanium In vitro. *Journal of Materials Science-Materials in Medicine* 1993; **4** (2): 117-126.
195. Ducheyne P, Bianco PD, Kim CS. Bone Tissue-Growth Enhancement By Calcium-Phosphate Coatings On Porous Titanium-Alloys - the Effect of Shielding Metal Dissolution Product. *Biomaterials* 1992; **13** (9): 617-624.
196. Kim CS, Ducheyne P. Compositional Variations in the Surface and Interface of Calcium-Phosphate Ceramic Coatings On Ti and Ti-6Al-4V Due to Sintering and Immersion. *Biomaterials* 1991; **12** (5): 461-469.
197. Healy KE, Ducheyne P. Oxidation-Kinetics of Titanium Thin-Films in Model Physiological Environments. *Journal of Colloid and Interface Science* 1992; **150** (2): 404-417.
198. Healy KE, Ducheyne P. The Mechanisms of Passive Dissolution of Titanium in a Model Physiological Environment. *Journal of Biomedical Materials Research* 1992; **26** (3): 319-338.
199. Tengvall P, Askendal A, Elwing H, Lundström I. A model for the interaction between titanium and living systems. *Biofouling* 1991; **4**: 219-223.
200. Romer S, Schurtenberger P. Personal Communication: Particle size of TiO<sub>2</sub>-particles measured with dynamic light scattering, Fribourg: 2001.
201. Harris SA, Enger RJ, Riggs BL, Spelsberg TC. Development and Characterization of a Conditionally Immortalized Human Fetal Osteoblastic Cell-Line. *Journal of Bone and Mineral Research* 1995; **10** (2): 178-186.
202. Hauck A, Rummel U, Thull R. Biologische in vitro-Prüfungen von OF-modifizierten Proben (FMZ ChemBio 011001). Würzburg: Lehrstuhl für Funktionswerkstoffe der Medizin, Universitätsklinik und Polikliniken für ZMK-Krankheiten, Bayerische Julius-Maximilians-Universität, 2001: 8.
203. Schlegel P. In vivo biocompatibility study of different calcium-phosphate surfaces for implant-bone anchorage. INAUGURAL-DISSERTATION zur Erlangung der Doktorwürde der Veterinär-Medizinischen Fakultät-Thesis: University of Zurich, Zurich, 2002.
204. Hermann R, Muller M. High-Resolution Biological Scanning Electron-Microscopy - a Comparative-Study of Low-Temperature Metal-Coating Techniques. *Journal of Electron Microscopy Technique* 1991; **18** (4): 440-449.
205. Reimer L. Scanning electron microscopy. 2 ed. Heidelberg: Springer-Verlag, 1998.
206. Bearinger JP, Orme CA, Gilbert JL. Direct observation of hydration of TiO<sub>2</sub> on Ti using electrochemical AFM: freely corroding versus potentiostatically held conditions. *Surface Science* 2001; **491** (3): 370-387.
207. Scharnweber D. Personal Communication: Blisters on titanium during anodization, München: 2001.
208. Uggowitzer P. Personal Communication: Possible Origins of Oxide Blisters on CP Titanium Substrates, Zürich: 2001.
-



---

# Curriculum Vitae

## Personal Information

Name:	Vinzenz Max Frauchiger
Date of Birth:	August 12, 1973 in Baden AG
Nationality:	Swiss, Citizen of Wyssachen BE
Marital status:	unmarried

## Education

1999-present	PhD thesis at the Laboratory for Surface Science and Technology, Department of Materials, ETH Zürich, guided by Prof. Dr. N. D. Spencer and Prof. Dr. M. Textor.
1999	Diploma in Materials Engineering, Department of Materials, ETH Zürich.
1993-1999	Student of Materials Engineering, Department of Materials, ETH Zürich
1993	Matura Typus C
1989-1993	Kantonsschule Baden

## Semester and Diploma Works

Nov 1998-Feb 1999	Diploma thesis at the Laboratory for Surface Science and Technology, guided by Dr. M. Textor: <i>Anodic Oxidation by Spark Discharge on CP Titanium Surfaces</i>
-------------------	---

---

Apr 1998-Jul 1998

Semester work at the Institute of Polymers,  
guided by Prof. Dr. P. Schurtenberger:  
*Particle Size Determination by Diffusion Wave  
Spectroscopy*

Nov 1997-Feb 1998

Semester work at the Chair of Nonmetallic Materials,  
guided by Julia Will:  
*Optimization of Bonding Techniques for Ceramics  
Used in Solid Oxide Fuel Cells*

## Internships

Feb 1996-May 1996

ALU Menziken Industrie AG, Menziken AG:  
*Introduction of ISO 14 00x*

Jun 1996-Aug 1996

Tissa Glasweberei AG, Unterkulm AG:  
*Optimization of Polymeric Coatings for Glass fabrics  
Used as Plaster Supports*